22004

NATIONAL LIBRARY
OTTAWA

CANADA

BIBLIOTHÈQUE NATIONALE
OTTAWA

NAME OF AUTHOR........DAVID CECIL SHERIFF WHITE

TITLE OF THESIS........THE MEASUREMENT OF
SUBNANOSECOND NUCLEAR
LIFETIMES.

UNIVERSITY........ALBERTA

DEGREE FOR WHICH THESIS WAS PRESENTED........Ph. D

YEAR THIS DEGREE GRANTED........1974

Permission is hereby granted to THE NATIONAL LIBRARY OF CANADA to microfilm this thesis and to lend or sell copies of the film.

The author reserves other publication rights, and neither the thesis nor extensive extracts from it may be printed or otherwise reproduced without the author's written permission.

(Signed)........

PERMANENT ADDRESS:

ATOMIC ENERGY BOARD
PRIVATE BAG 256
PRETORIA, SOUTH AFRICA

DATED........9 Oct........1974

NL-91 (10-68)

THE UNIVERSITY OF ALBERTA

THE MEASUREMENT OF SUBNANOSECOND NUCLEAR LIFETIMES

by

DAVID CECIL SHERIFF WHITE

A THESIS

SUBMITTED TO THE FACULTY OF GRADUATE STUDIES AND RESEARCH
IN PARTIAL FULFILLMENT OF THE REQUIREMENTS FOR THE DEGREE
OF DOCTOR OF PHILOSOPHY

DEPARTMENT OF PHYSICS

EDMONTON, ALBERTA

FALL, 1974

© DAVID CECIL SHERIFF WHITE 1975

THE UNIVERSITY OF ALBERTA

FACULTY OF GRADUATE STUDIES AND RESEARCH

The undersigned certify that they have read, and recommend to the Faculty of Graduate Studies and Research, for acceptance, a thesis entitled THE MEASUREMENT OF SUB-NANOSECOND NUCLEAR LIFETIMES submitted by David Cecil Sheriff White in partial fulfillment of the requirements for the degree of Doctor of Philosophy.

L. J. McDonald
Supervisor

Douglas M. Sheppard

W. K. Dawson

Richard L. Snyder

Peter R. Smy

T. K. Alexander
External Examiner

Date: Oct 7/1974

ABSTRACT

This research dealt with the measurement of subnanosecond nuclear lifetimes using the pulsed beam delayed-coincidence technique. Measurements were performed on isotopes in the $f\frac{7}{2}$ shell and specifically the isotopes of Titanium and Vanadium. Experimental investigations were also pursued in two other isotopes, ^{59}Ni and ^{65}Zn. Several new lifetimes were determined and confirmation was obtained for some previous values which were measured with different techniques. More information was also obtained on certain levels where previous results are in disagreement.

A new technique has been developed to provide simultaneous data acquisition of both delayed and prompt time distributions. The centroids of the prompt time distributions were used to define the so-called prompt time centroid curve. The Centroid Shift technique was employed to calculate the lifetimes from the centroid shifts of the delayed time distributions with respect to the prompt time centroid curve at the appropriate energies. Additional 'prompt' reference γ-rays were obtained by using a second target. For this purpose, a two-target rotating system was developed. The system has the electronics capable of routing into separate regions of computer memory, information obtained from each target. Thus errors introduced by background

subtractions are minimised since the peak to background ratio is not adversely affected by the presence of the second target.

A major part of the work involved the improvement of the time resolution and study of the timing properties of coaxial Ge(Li) detectors. The significant improvement in the time resolution was achieved through the development of the Triple Constant Fraction Discriminator, an electronic circuit designed to improve the time resolution by a pulse shape discrimination technique. The improvement in the time resolution leads to greater accuracy in the determinations of the centroids of the time distributions, which is the main limitation of the Centroid Shift technique for measuring lifetimes in the tens of picosecond region.

Finally a theoretical description of the energy levels and electromagnetic transition rates of the isotopes studied was performed using the Strong Coupling Symmetric Rotator Model, which included band mixing, and the Intermediate Coupling Model. The predicted level schemes are in good agreement with experimental results and fairly good agreement is obtained between experimental and theoretical electromagnetic transition rates.

ACKNOWLEDGEMENTS

I would like to express my deepest appreciation to my supervisor, Dr. W.J. McDonald, for his encouragement and assistance throughout all phases of this project. His reassuring presence instilled in me the confidence I needed to complete my Ph.D. program.

I am also extremely grateful to Dr. David Hutcheon for his keen interest in this project and the many, many hours of enlightening discussions. I hope that a little of his constructive criticism and ability to understand and come to grips with theoretical and experimental problems has rubbed off on me. His assistance in experimental runs, computer programming for data collection and the final reading of this thesis are much appreciated.

I wish to thank Dr. D,M. Sheppard and Dr. H.S. Sherif for the useful discussions not only concerned with this project but with the many aspects of Nuclear Physics. The Nuclear Physics courses I received from Dr. Sherif provided a tremendous base to my knowledge of Theoretical Nuclear Physics.

I am also grateful to Dr. G.C. Neilson for his assistance in the initial stage of the project and the help of Dr. W.K. Dawson for my working knowledge of the computer systems in the laboratory.

A special thanks goes to the technical and secretarial staff of the Nuclear Research Center, especially

Jock Elliott, Lars Holm, Paul Karvonen and Ron Popik for their invaluable assistance in obtaining running conditions for the van de Graaff. Con Green and Henry Nielsen deserve many thanks for the excellent job in making much of the apparatus required for my experiments.

I wish to thank all of my student colleagues who helped with overnight experimental runs; Rick Hooper, Bob McCamis, Jim Pasos, Jan Soukup and Peter Johnson.

A very special thanks goes to Mrs. Yiu, who did an excellent job of typing the manuscript, in spite of many last minute changes and unreasonable deadlines.

The financial assistance of the National Research Council of Canada and the University of Alberta is gratefully acknowledged. I appreciate the opportunity of coming to Canada to continue my education which the University of Alberta gave to me.

Finally, to my loving wife, Anna, and darling daughter, Vanessa; words cannot describe my feelings to you both.

To Anna and Vanessa
September, 1974

TABLE OF CONTENTS

Chapter Page

1. INTRODUCTION 1

2. THE ANALYSIS OF DELAYED-COINCIDENCE EXPERIMENTS 8
    2.1 The Slope Method 9
    2.2 First Moment or Centroid Shift Method 11
    2.3 Methods of Higher Moments 13
    2.4 Integral Transform Method 16

3. THE IMPROVEMENT IN THE TIME RESOLUTION OF COAXIAL Ge(Li) DETECTORS 21
    3.1 Pulse Shape Analysis 24
    3.2 The Triple Constant Fraction Discriminator 42
    3.3 Experimental Tests of Improved Timing Technique 47

4. THE BEAM PULSING, TARGET ROTATING SYSTEMS AND EXPERIMENTAL METHOD 65
    4.1 The Mobley Compression Pulsed Beam System 65
    4.2 The Rotating Target System 67
    4.3 Target Discriminator 72
    4.4 Experimental Electronics and Methods 77

5. THE FULL ENERGY-COMPTON DILEMMA 88

6. ELECTROMAGNETIC TRANSITION RATES AND PROBABILITIES 109

Chapter Page

7. EXPERIMENTAL RESULTS 116

7.1 Establishment of Suitable 'Prompt' Reference γ-rays 116

7.2 A Lifetime Study of the Isotopes of Titanium and Vanadium 127

a) ^{45}Ti 127

b) ^{47}Ti 132

c) ^{49}Ti 139

d) ^{47}V 142

e) ^{49}V 149

f) ^{50}V 157

g) ^{51}V 160

7.3 ^{59}Ni and ^{65}Zn 168

a) ^{59}Ni 168

b) ^{65}Zn 172

8. THEORETICAL INTERPRETATIONS 180

9. CONCLUSIONS 209

REFERENCES 216

APPENDIX A. A THEORETICAL DESCRIPTION OF THE ONE AND TWO PARTICLE INTERMEDIATE COUPLING MODEL 223

APPENDIX B. THE STRONG COUPLING SYMMETRIC ROTATOR MODEL 238

LIST OF TABLES

Table		Page
1	Lifetime results for ^{64}Cu and the experimental branching ratios for the transitions studied.	126
2	Isotopic analysis and thicknesses of the isotopically enriched Titanium and ^{64}Ni foils	128
3	Lifetime results for ^{45}Ti, ^{47}Ti and ^{49}Ti and the corresponding experimental transition strengths	141
4	Lifetime results for ^{47}V, ^{49}V, ^{50}V and ^{51}V and the corresponding experimental transition strengths	166
5	Lifetime results for ^{59}Ni and ^{65}Zn and the corresponding experimental transition strengths	179
6	Comparison of experimental reduced transition probabilities with the Strong Coupling model calculations for ^{45}Ti, ^{47}Ti and ^{49}Ti	195
7	Comparison of experimental reduced transition probabilities with the Strong Coupling model calculations for ^{47}V, ^{49}V and ^{51}V	197
8	Comparison of experimental reduced transition probabilities with the Intermediate Coupling model calculations for ^{59}Ni and ^{65}Zn	206
9	Reduced matrix elements for the boson creation operators	230

LIST OF FIGURES

Figure		Page
1	Schematic diagram of the various delayed coincidence techniques, data acquisition and display of the prompt, P(t), and delayed, D(t), time distributions.	2
2	The relative statistical error in the meanlife, τ, for the moment methods and the integral transform method as a function of the FWHM of the prompt curve over τ. The prompt curve is assumed to be of the form $\cos^2 \pi x/2a$. (FWHM = a, $N_D = N_P$) (Sp 66).	19
3	Photographs of the preamplifier signals obtained from a 23 c.c. coaxial Ge(Li) detector using a ^{60}Co source.	23
4	Collection of a single electron-hole pair in a double-open-end coaxial Ge(Li) detector.	28
5	Calculated pulse shapes for local interactions at seven different positions along a radius of an ideal double-open-end coaxial Ge(Li) detector.	32
6	Zero-crossing time vs. slope change time, both normalised with respect to the delay time, t_d, for the pulse shapes of fig.5, when applied to a CFPHT. Delay time $t_d = 0.05\ T_{max}$.	35
7	Zero-crossing time vs. slope change time, both normalised with respect to the delay time, t_d, for the pulse shapes of fig. 5, when applied to a CFPHT. Delay time $t_d = 0.10\ T_{max}$.	36
8	Time difference curve obtained when the signals from two CFPHT's set at fractions 0.1 and 0.5, respectively, are applied to a TAC. CFPHT delay time, $t_d = 0.05\ T_{max}$.	38

Figure		Page
9	Time difference curve obtained when the signals from two CFPHT's set at fractions 0.1 and 0.5, respectively, are applied to a TAC. CFPHT delay time, $t_d = 0.10\ T_{max}$.	39
10	Theoretical 'shape' curve obtained from a TAC using the time difference curve of fig. 8, and considering the volume contributions at different radii of a coaxial Ge(Li) detector.	40
11	Theoretical 'shape' curve obtained from a TAC using the time difference curve of fig. 9, and considering the volume contributions at different radii of a coaxial Ge(Li) detector.	41
12	Circuit diagram of the Triple Constant Fraction Discriminator (TCFD).	44
13	Schematic block diagram of the electronic circuit of the TCFD.	45
14	A photograph of the Triple Constant Fraction Discriminator module.	46
15	Block diagram of the bench-testing timing system.	48
16	a) The total time spectrum obtained from ADC R and b) The total 'shape' spectrum obtained from ADC P for a ^{60}Co source.	50
17	Sorted time spectra for seven equal windows set on the 'shape' spectrum between the arrows as indicated in fig. 16b), the system being gated by an energy window on the 1.332 MeV γ-rays of the ^{60}Co source.	51
18	a) The total time spectrum obtained from ADC R and b) The total 'shape' spectrum obtained from ADC P for a ^{22}Na source.	53

Figure Page

19 Sorted time spectra for seven equal windows set on the 'shape' spectrum between the arrows as indicated in fig. 18b), the system being gated by an energy window on the 0.511 MeV annihilation γ-rays of the ^{22}Na source. 54

20 A plot of the FWHM and FWTM against the percentage of the total number of events as sorted time bins are added to the best timing bin from windows set to left and right across the shape spectrum. The system was gated on the 1.332 MeV γ-rays of the ^{60}Co source. 56

21 A plot of the FWHM and FWTM against the percentage of the total number of events as sorted time bins are added to the best timing bin from windows set to left and right across the shape spectrum. The system was gated on the 0.511 MeV peak of a ^{22}Na source. 57

22 FWHM of the prompt time distributions plotted as a function of the inverse of the associated detected energy. The circles represent data from the ^{45}Sc experimental run while the crosses are some data for the ^{35}Cl, ^{37}Cl, ^{39}K experimental run. 59

23 Illustration of some of the ways in which pulses from the Ge(Li) detector are mistimed. Pulses of the form A and B trigger the NOR gate I.C.8 before T_ρ, the arrival time for signals from the zero-crossing comparator, and are correctly timed. Pulses of the form C and D occur later than T_ρ and are thus mistimed. 60

24 a) A logarithmic plot of the total time spectrum obtained for a ^{22}Na source.
b) The same but with the system gated by a window on the 'delta' function peak in the 'shape' spectrum.
The two graphs are displaced by half a division to ensure clarity. 62

Figure Page

25 a) The total 'shape' spectra when resistance $R_1 = 0\,\Omega$ and $R_1 = 870\ \Omega$.
b) Spectra obtained from the 'shape' TAC when the two outputs of the TCFD are set at the same fractions. 64

26 Schematic diagram of the beam transport and Mobley Compression pulsed beam system. 66

27 A photograph of the Rotating Target system. 70

28 A photograph of the Rotating Target system. 71

29 Circuit diagram of the Target Discriminator. 74

30 A photograph of the Target Discriminator module. 75

31 A schematic diagram of the pulse shape logic in the Target Discriminator circuit. 76

32 Block diagram of the experimental electronic arrangement. 78

33 Centroids of the time distributions vs. energy for the ^{64}Ni-^{181}Ta experimental run. Crosses represent centroids from energy windows set on the Compton continuum and circles the centroids for the time distributions of 'prompt' full energy peaks. 81

34 Illustration of the timing error, Δt, introduced by the requirement that a small amount of charge is needed to activate the cross-over diode. 82

35 Time distributions obtained as a collimated γ-ray beam from a ^{22}Na source was moved in steps of 0.5 cm from the centre of the detector to the outer radius, the timing system being gated by an energy window on the 0.511 MeV peak. 90

Figure		Page
36	Time distributions obtained as a collimated γ-ray beam from a ^{60}Co source was moved in steps of 0.5 cm from the centre of the detector to the outer radius, the timing system being gated by an energy window on the 1.332 MeV γ-rays of a ^{60}Co source.	91
37	A plot of the centroids of the time distributions of figs. 35 and 36 vs. the collimated beam position.	93
38	The normalised number of Compton and full energy events, for a given pulse height, plotted as a function of the collimated γ-ray beam position. ^{60}Co, ^{137}Cs, ^{22}Na and RdTh sources were used to obtain the data.	95
39	The calculated percentage contribution to full energy peaks by multiple interacting events (Be 72).	97
40	'Shape' spectra obtained as a collimated γ-ray beam from a RdTh source was moved from the centre of the detector in steps of 0.5 cm to the outer radius, the system being gated by an energy window on the 0.352 MeV γ-rays from the source.	98
41	'Shape' spectra obtained as a collimated γ-ray beam from a ^{137}Cs source was moved from the centre of the detector in steps of 0.5 cm to the outer radius, the system being gated by an energy window on the 0.661 MeV γ-rays from a ^{137}Cs source.	99
42	'Shape' spectra obtained as a collimated γ-ray beam from a ^{60}Co source was moved from the centre of the detector in steps of 0.5 cm to the outer radius, the system being gated by an energy window on the 1.332 MeV γ-rays of a ^{60}Co source.	100
43	Relative peak to Compton ratios, for given pulse heights, plotted as a function of the collimated beam position with only events in the 'good shape' region being selected.	103

Figure Page

44 'Shape' spectra obtained by irradiating the full face of the detector and gating the system on full energy events from one source and the Compton continuum of another, using the same energy window. Spectra are shown for energies 0.661, 1.172 and 1.332 MeV. 104

45 Time distributions obtained as a collimated γ-ray beam from a ^{22}Na source was moved in steps of 1.0 cm from the front face to the back face of the detector crystal, the timing system being gated on the 0.511 MeV peak. 107

46 A plot of the centroids of the time distributions vs. collimated beam positions along side of detector crystal, the system being gated by energy windows at 200, 300 and 511 keV. 108

47 Experimental level schemes for ^{181}Ta and ^{165}Ho. The γ-ray transitions of interest are shown by bolder lines. 118

48 Centroids of the time distributions for full energy events using the ^{64}Ni foil and the ^{181}Ta-^{165}Ho foil combination. 121

49 Experimental level scheme of ^{64}Cu below 927 keV. 122

50 Experimental results for lifetime determinations in ^{64}Cu using the ^{64}Ni and ^{47}Ti foils. 125

51 Experimental level scheme and previous lifetime results for the states in ^{45}Ti. 129

52 Experimental results for lifetime determinations in ^{45}Ti. 131

53 Experimental level scheme and previous lifetime results for the states in ^{47}Ti. 133

54 Experimental results for lifetime determinations in ^{47}Ti and ^{47}V. 135

Figure Page

55 Experimental level scheme and previous Doppler shift lifetime results for ^{48}Ti and ^{51}Cr. 137

56 Experimental results of lifetime determinations in ^{49}Ti. 140

57 Experimental level scheme and previous lifetime results for ^{47}V. 143

58 Experimental results for lifetime determinations in ^{47}V. 145

59 Relative angular distributions for the 58 and 88 keV γ-ray transitions in ^{47}V. 146

60 Experimental level scheme and previous lifetime results for states in ^{49}V. 150

61 Logarithmic plot of the delayed time distribution of the 153 keV → g.s. transition in ^{49}V. 152

62 The delayed time distribution for the 90 keV → g.s. transition in ^{49}V before and after the subtraction of the tail contribution due to the 153 → 90 keV decay. 153

63 Experimental results for the determination of the lifetime of the 90 keV level in ^{49}V. 156

64 Experimental results for lifetime determinations in ^{50}V. The insert shows the level scheme of ^{50}V. 158

65 Experimental level scheme and previous lifetime results for ^{51}V. 161

66 Experimental results for the determination of the lifetime of the 320 keV level in ^{51}V. 162

67 Experimental results for the determination of the lifetime of the 928 keV level in ^{51}V. 164

Figure Page

68 Experimental level schemes for ^{59}Ni and ^{65}Zn and previous lifetime results for excited states of ^{59}Ni. 169

69 Experimental results for lifetime determinations in ^{59}Ni. 170

70 Experimental results for lifetime determinations in ^{65}Zn, using a copper foil and the ^{64}Ni-^{181}Ta foil combination. 173

71 Experimental results for lifetime determinations in ^{65}Zn using a copper foil and the ^{181}Ta-^{165}Ho foil combination. 174

72 Experimental results for lifetime determinations of the higher energy levels in ^{65}Zn. 177

73 Experimental level schemes of the even-even Titanium and Chromium isotopes. 184

74 The excitation energies of the positive parity levels in ^{45}Ti, ^{45}Sc, ^{47}V and ^{49}V plotted as a function of J(J+1). 185

75 Experimental and theoretical level schemes of ^{45}Ti. 188

76 Experimental and theoretical level schemes of ^{47}Ti. 189

77 Experimental and theoretical level schemes of ^{49}Ti. 190

78 Experimental and theoretical level schemes of ^{47}V. 191

79 Experimental and theoretical level schemes of ^{49}V. 192

80 Experimental and theoretical level schemes of ^{51}V. 193

81 Experimental and theoretical level schemes of ^{59}Ni. 202

82 Experimental and theoretical level schemes of ^{65}Zn. 205

83 Experimental level schemes and previous lifetime results for the states in ^{48}V. 215

CHAPTER 1

INTRODUCTION

The knowledge of the lifetime of a nuclear state is important in the determination of the electromagnetic transition matrix elements for comparison with predictions based on theoretical nuclear models. These matrix elements which involve an overlap of the wavefunctions of the states between which the transition occurs are more sensitive to the details of the nuclear model than many other quantities which could be measured. To date, there is only a limited knowledge of the wavefunctions of nuclear levels and this essentially in the low mass region. Thus there is interest in the measurement of lifetimes of nuclear states to obtain more knowledge about the form of the wavefunctions.

For lifetime determinations in the range $10^{-3} > \tau > 10^{-12}$ secs, the most common method is the so-called delayed-coincidence technique which involves the detection of the times of population and decay of the state whose lifetime is to be measured. In the most widely used arrangement, scintillator photomultiplier combinations determine both the time of emission and the energy of the radiations announcing the birth and decay of the state as illustrated in fig. 1. The current literature contains many examples

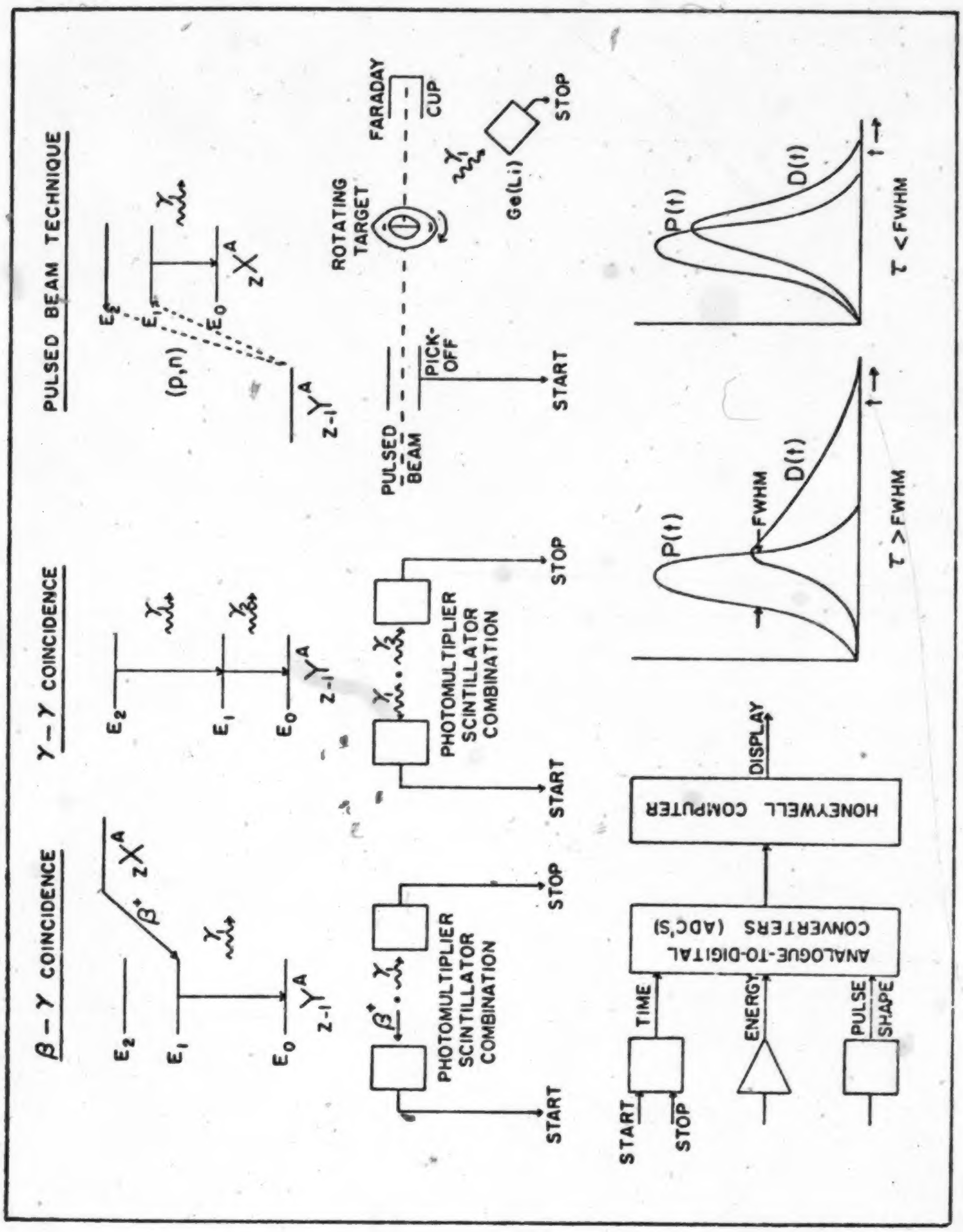
β − γ COINCIDENCE
γ − γ COINCIDENCE
PULSED BEAM TECHNIQUE
E2
E1
E0
β+
γ1
γ2
z-1YA
zXA
(p,n)
PHOTOMULTIPLIER SCINTILLATOR COMBINATION
START
STOP
PULSED BEAM
PICK-OFF
ROTATING TARGET
FARADAY CUP
Ge(Li)
TIME
ENERGY
PULSE SHAPE
ANALOGUE-TO-DIGITAL CONVERTERS (ADC'S)
HONEYWELL COMPUTER
DISPLAY
P(t)
D(t)
FWHM
τ > FWHM
τ < FWHM
t

Fig. 1. Schematic diagram of the various delayed coincidence techniques, data acquisition and display of the prompt, P(t), and delayed, D(t) time distributions.

of γ-γ and β-γ delayed-coincidence measurements. However, this method limits the number of nuclear states that can be investigated due to the poor energy resolution of scintillator detectors and the number of states that are populated by β and γ-ray transitions.

Alternatively, the population of a state can be achieved by using a pulsed beam to excite the state via a nuclear reaction, the timing signals coming from a capacitive beam pick-off before the target and from the detector corresponding to the detection of the radiation from the decay of the state. The University of Alberta has a 7.5MV van de Graaff which has a Mobley Compression System capable of producing every microsecond a beam burst with a width of 0.4ns. This system is ideal for the measurement of lifetimes by direct timing using the delayed-coincidence technique.

With the advent of Lithium drifted Germanium [Ge(Li)] detectors with their superior energy resolution capability, one of the major difficulties associated with the commonly employed scintillator-photomultiplier combinations can be eliminated. However, very little work has been reported utilizing coaxial Ge(Li) detectors for lifetime measurements in delayed-coincidence systems, especially pulsed beam experiments (Ya 69, Wa 70, Ki 71), due to the poor time resolution characteristics of Ge(Li) detectors. It is clear, however, that their extremely good energy resolution would give a great advantage over scintillator detectors for lifetime measurements of excited states in nuclei with complicated decay schemes.

In general, two different time distribution curves are obtained in delayed-coincidence experiments as illustrated in fig. 1. One, the prompt distribution, P(t), is obtained from events in which a state is produced and decays during an interval short compared to the time resolution of the apparatus. The other, called the delayed distribution, D(t), characterises the lifetime to be measured. For lifetimes which are much greater than the time resolution of the apparatus, the delayed distribution exhibits an exponential tail. However, for lifetimes shorter than the time resolution of the measuring apparatus the delayed-coincidence method is restricted to experimental observations of the centroid shift between the delayed and prompt time distribution curves for a given energy.

The accuracy of the centroid shift method, however, is severely limited by the time resolution of Ge(Li) detectors. If electronic noise were the only limitation, timing with Ge(Li) detectors could be very precise, particularly at high energies since the full width at half maximum (FWHM) of the time distribution curves would scale inversely as the detected energy.

However, the time resolution is seriously degraded by the pulse shapes and the pulse rise-time variations which depend on the γ-ray interaction position in the detector intrinsic volume, the detector geometry and the electric field as a function of the position inside the detector.

The purpose of this research was the significant improvement of the time resolution of coaxial Ge(Li) detectors so that lifetimes as short as 10^{-11} secs could be measured using the pulsed beam facility. The Doppler Shift Attenuation Method (DSAM) (Li 63, Wa 63) and the Recoil Distance Method (RDM) (Al 65, Al 70) are other techniques used to measure lifetimes in this region. However, in the range $10^{-12}<\tau<5\times10^{-11}$ secs, the DSAM is restricted to gas targets and the RDM requires high energy heavy ion beams to provide sufficiently large recoil velocities.

The improvement in the time resolution was accomplished through the development of the so-called Triple Constant Fraction Discriminator, an electronic circuit designed to improve the time resolution by a pulse shape discrimination technique (Wh 74, Mc 74).

The accuracy of the centroid shift technique is also determined by the definition of the so-called prompt time distribution centroid curve, a curve through the points representing the centroids of the prompt time distributions plotted against the corresponding energy of the 'prompt' γ-ray. Since a shift from this curve corresponds to a γ-ray with a measurable lifetime, it is essential that the curve be defined accurately in the region of interest. However, in most cases the isotope under study does not have a sufficient number of 'prompt' deexcitation γ-rays in the required energy region. To overcome this problem, a rotating target system was developed. To the rotator are attached two targets, each rotating alternately in and out of the pulsed beam, the one target producing the energy level whose lifetime is to be measured and the other, supplementary reference 'prompt' γ-rays in the energy region of interest.

This simultaneous acquisition of data for the prompt and delayed time distributions is a new development of the technique. In most previous delayed-coincidence techniques alternate experimental runs were done to obtain the prompt and delayed time distributions. Thus errors due to electronic drifts and shifts, and pulsed beam conditions between separate runs, are overcome by our technique. Furthermore, by the definition of the prompt time distribution centroid curve, centroid shifts are calculated with respect to this curve at the appropriate energy whereas previously this was done with respect to a prompt time distribution from a γ-ray of approximately the same energy.

The collection of data by our technique is made possible by a two dimensional sort routine, a software component of the on-line Honeywell 516 computer. Using this routine the total time distribution spectrum can be sorted by setting up to 32 digital windows on the energy spectrum and on that region of the 'pulse shape' spectrum which produces improved time resolution.

A further refinement of the technique was the development of an electronic Target Discriminator module which can rout the information from each target into separate regions of memory of the computer. In this way the peak to background ratio in the energy spectrum is not affected by the presence of the second target, a consideration which is very important for the reduction of errors.

Measurements were performed on isotopes in the f 7/2 shell especially the isotopes of Titanium and Vanadium. Investigations in two other isotopes, ^{65}Zn and ^{59}Ni, also proved fruitful with several lifetime determinations being made. Level schemes and electromagnetic transition probabilities for the isotopes studied were compared with theoretical results obtained from the Intermediate Coupling Model and the Strong Coupling Symmetric Rotator Model, using the Nilsson Hamiltonian to represent the interaction between the last unpaired nucleon and the core.

CHAPTER 2

THE ANALYSIS OF DELAYED-COINCIDENCE EXPERIMENTS

The so-called delayed-coincidence technique is frequently used to determine the lifetimes of excited nuclear states by employing a Time to Amplitude Converter (TAC), which translates time differences into voltage signals, and an Analogue to Digital Converter (ADC) which digitises these signals. There are several different methods of determining the unknown lifetime from the two time distributions experimentally obtained. These are commonly referred to as the prompt and delayed time distributions.

A frequently used method is the so-called slope method (Ne 50), in which a fit of a pure exponential function to that part of the delayed curve well outside the region of the prompt time curve yields the desired decay constant, λ. This method can be applied if the lifetime is sufficiently long to give a significant exponential tail, but otherwise is statistically poor in that only part of the data is used in the evaluation of the lifetime. Statistically, the methods utilizing the moments of the measured time distributions (Ba 50, Su 62) provide a more accurate determination of the lifetime since the entire data are used in the calculations.

The most important of these methods is the first moment or centroid shift method; however, higher moments can also yield information about the lifetimes. Another method which has statistical errors the same magnitude as those of the centroid shift method is the integral transform method (Sp 66A).

A theoretical description of the above methods of analysis is presented below with a discussion of the advantages and disadvantages of each. The prompt and delayed distributions are denoted by P(x) and D(x), and the corresponding histograms obtained from the ADC are denoted by P_i and D_i. P(x) and D(x) are assumed identically zero for $x < 0$ and the number of counts under the two curves (their areas) are N_P and N_D, respectively.

2.1 The Slope Method

The mathematical relation between the two time distributions is the convolution integral

$$D(x) = \frac{N_D}{N_P} \int_0^\infty w(t)\, P(x - t)\, dt \qquad 2\text{-}1$$

where if the decay is a radioactive decay with a mean-life τ ($= 1/\lambda$), the decay function is

$$w(t) = \frac{1}{\tau} \exp(-\, t/\tau) \quad . \qquad 2\text{-}2$$

Substitution of eq. 2-2 in 2-1 gives

$$D(x) = \frac{N_D}{N_P} \int_0^\infty \lambda\, e^{-\lambda t}\, P(x - t)\, dt$$

$$= \frac{N_D}{N_P} \int_0^x P(y)\, \lambda\, e^{-\lambda (x - y)}\, dy \qquad 2\text{-}3$$

where $y = x - t$. Differentiating eq. 2-3 with respect to x gives

$$\frac{dD(x)}{dx} = \lambda \left[\frac{N_D}{N_P} P(x) - D(x)\right] .$$

From this relation follows

$$\frac{d}{dx} [\ln D(x)] = - \lambda \left[1 - \frac{P(x)}{D(x)} \frac{N_D}{N_P}\right] . \qquad 2\text{-}4$$

Consequently, the decay constant can be found from the slope of the logarithmic plot of the delayed curve in the region where $P(x)/N_P$ is negligible compared to $D(x)/N_D$. Thus only that part of the delayed curve which is outside the prompt curve can be used in the evaluation of the lifetime. This restricts lifetime measurements by this method to those which are greater than the time resolution of the apparatus used. The method, however, is insensitive to electronic drifts and the prompt admixtures.

2.2 First Moment or Centroid Shift Method

The n^{th} moment of the delayed time distribution is defined through the formula

$$M_n(D) = \int_0^\infty x^n \, D(x)\, dx \quad . \qquad 2\text{-}5$$

Using n = 1 and substituting in eq. 2-1

$$M_1(D) = \frac{N_D}{N_P} \int_0^\infty x \, dx \int_0^\infty w(t)\, P(x - t)\, dt \; .$$

Substituting $y = x - t$ and rearranging one obtains

$$M_1(D) = \frac{N_D}{N_P} \int_0^\infty y\, P(y)\, dy \int_0^\infty w(t)\, dt + \frac{N_D}{N_P} \int_0^\infty P(y)\, dy \int_0^\infty t\, w(t)\, dt$$

$$= \frac{N_D}{N_P} M_1(P) + N_D\, M_1(w) \; .$$

Since $M_n(w) = n!\, \tau^n$ it follows

$$\tau = \frac{M_1(D)}{N_D} - \frac{M_1(P)}{N_P} \quad . \qquad 2\text{-}6$$

Thus the lifetime to be measured is the centroid shift between the delayed and prompt time distributions. In practice the formula takes the form

$$\tau = \frac{\Sigma x_i\, D_i}{\Sigma\, D_i} - \frac{\Sigma x_i\, P_i}{\Sigma\, P_i} \qquad 2\text{-}7$$

and the statistical error can be calculated using

$$s_A^2 = \left(\frac{\partial f}{\partial a}\right)^2 s_a^2 + \left(\frac{\partial f}{\partial b}\right)^2 s_b^2 + \left(\frac{\partial f}{\partial c}\right)^2 s_c^2 + \ldots \qquad 2\text{-}8$$

where $A = f(a,b,c,\ldots)$ is a function of the independent variables a, b, c, ... Therefore the statistical error in τ is

$$s_\tau^2 = \frac{\Sigma x_i^2 D_i}{N_D^2} - \frac{(\Sigma x_i D_i)^2}{N_D^3} + \frac{\Sigma x_i^2 P_i}{N_P^2} - \frac{(\Sigma x_i P_i)^2}{N_P^3} \qquad 2\text{-}9$$

Equations 2-7 and 2-9 are independent of the origin of the coordinate system and if the particular choice of $\Sigma x_i P_i = 0$ is made expression 2-9 can be transformed using eq. 2-7 and 2-11 to

$$\frac{s_\tau^2}{\tau^2} = \frac{M_2^c(P)}{\tau^2}\left[\frac{1}{N_D} + \frac{1}{N_P}\right] + \frac{1}{N_D} \qquad 2\text{-}10$$

where $M_2^c(P)$ is the normalised second moment of the prompt curve about its own centroid and is a measure of the width of the curve (normalised means adjusted to unit area).

If $M_2^c(P)/\tau^2$ is much larger than unity i.e. the lifetime is small compared to the time resolution of the apparatus, then the statistical error is approximately equal to

$$M_2^c(P)\left[\frac{1}{N_D} + \frac{1}{N_P}\right] \quad .$$

This stresses the importance of good time resolution when short lifetimes are to be measured. It is for this reason that a large section of this thesis is devoted to the improvement of the time resolution of coaxial Ge(Li) detectors.

On the other hand, when τ is large the relative error is approximately $(N_D)^{-\frac{1}{2}}$ and nearly independent of the shape of the prompt curve, the slope method is then better in these cases. The centroid shift method is simple to use and has small statistical errors, however, electronic shifts and drifts play an important role since they give rise to systematic errors. These problems can be overcome if the prompt and delayed time distributions are obtained simultaneously.

2.3 Methods of Higher Moments

Using the definition of the moments eq. 2-5 one obtains

$$M_2(D) = \int_0^\infty x^2 \, D(x) \, dx$$

$$= \frac{N_D}{N_P} \int_0^\infty x^2 \, dx \int_0^\infty w(t) \, P(x - t) \, dt \, .$$

Substituting y = x - t and rearranging

$$M_2(D) = \frac{N_D}{N_P} \Big[\int_0^\infty y^2 \, P(y) \, dy \int_0^\infty w(t) \, dt +$$

$$+ 2 \int_0^\infty y \, P(y) \, dy \int_0^\infty t \, w(t) \, dt + \int_0^\infty P(y) \, dy \int_0^\infty t^2 w(t) \, dt.$$

Therefore using relation 2-6

$$\frac{M_2(D)}{N_D} = \frac{M_2(P)}{N_P} + 2\tau\ [\frac{M_1(P)}{N_P} + \tau]$$

$$= \frac{M_2(P)}{N_P} + 2\tau\ \frac{M_1(D)}{N_D}\ . \qquad 2\text{-}11$$

In an analogous way the relation for the third moment can be obtained and the meanlife from the resulting formulae are:

$$2^{nd}\ \text{moment:}\quad \tau = \frac{N_D}{2M_1(D)}\ [\frac{M_2(D)}{N_D} - \frac{M_2(P)}{N_P}] \qquad 2\text{-}12$$

$$3^{rd}\ \text{moment:}\quad \tau = \frac{N_D}{3M_2(D)}\ [\frac{M_3(D)}{N_D} - \frac{M_3(P)}{N_P}]\ . \qquad 2\text{-}13$$

Again the origin of the coordinate system is arbitrary and by choosing the origin in such a way that $M_1(P) = 0$ the formulae for the statistical errors reduce to simpler forms (Sp 66) as shown below. These are for the second moment

$$\frac{s_\tau}{\tau} = \frac{1}{2}\ [\frac{M_4(P)}{\tau^4\ N_P}\ (\frac{1}{N_D} + \frac{1}{N_P}) - \{\frac{M_2(P)}{\tau^2\ N_P}\}^2\ (\frac{1}{N_D} + \frac{1}{N_P})$$

$$\frac{1}{N_D}\ (\frac{4M_2(P)}{\tau^2\ N_P} + 8)]^{\frac{1}{2}} \qquad 2\text{-}14$$

and for the third moment

$$\frac{s_\tau}{\tau} = \frac{\tau^2}{3(\frac{M_2(P)}{N_P} + 2\tau^2)} [\{\frac{M_6(P)}{N_P \ \tau^6} - (\frac{M_3(P)}{N_P \ \tau^3})^2\}(\frac{1}{N_D} + \frac{1}{N_P})$$

$$\frac{1}{N_D} \{\frac{9M_4(P)}{N_P \ \tau^4} + \frac{36M_3(P)}{N_P \ \tau^3} + \frac{108M_2(P)}{N_P \ \tau^2} + 216\}]^{\frac{1}{2}} \qquad 2\text{-}15$$

Another version of the higher moments was proposed by Sundstrom (Su 62) in which the normalised moments of the delayed and prompt curves (both curves assumed normalised to unit area) are computed with respect to their centroids i.e.

$$M_n^c(g) = \int_0^\infty (x - M_1(g))^n \ g(x) \ dx \quad ;$$

Using this relationship formula 2-16 holds

$$M_i^c(D) = M_i^c(P) + M_i^c(w) \qquad i = 1,2,3 \qquad 2\text{-}16$$

and the meanlife is evaluated from eq. 2-16 to give

2nd moment: $\tau = [M_2^c(D) - M_2^c(P)]^{\frac{1}{2}}$ 2-17

3rd moment: $\tau = \frac{1}{2}[M_3^c(D) - M_3^c(P)]^{\frac{1}{3}}$ 2-18

As pointed out by Weaver and Bell (We 60) the quantity $M_3^c(P)$, the third moment of the prompt curve P(x) about its own centroid, is usually small and frequently negligible so that for many cases it is sufficient to write

$$\tau = \left[\frac{M_3^c(D)}{2}\right]^{\frac{1}{3}} \qquad 2\text{-}19$$

Thus it is possible to evaluate the required lifetime from the shape of the delayed curve with only rough knowledge of the shape of the prompt curve.

The great advantage of the higher moment methods is that if the delayed and the prompt time distribution curves are recorded under different experimental conditions and a pure shift (translation) results, these methods eliminate such effects. Electronic drifts, however, can have serious effects especially for the second moment method as they result in broadening of the two time distribution curves. Also since these methods depend more on the outer less well-defined parts of the curves, these methods suffer from inaccuracy in the determination of accidentals.

2.4 Integral Transform Method

In this method, developed by Sparrman (Sp 66A), the Laplace integral transforms of P(x) and D(x) are defined as

$$L(P) = \int_0^\infty e^{rx}\, P(x)\, dx \qquad 2\text{-}20$$

$$L(D) = \int_0^\infty e^{rx}\, D(x)\, dx \quad . \qquad 2\text{-}21$$

Using the measured distributions P_i and D_i and a selected value of r, numerical values of L(P) and L(D) are obtained by numerical integration. The choice of r is arbitrary except for the condition, $r < \lambda$, the decay constant. Using eq. 2-3 the Laplace integral can be obtained.

$$L(D) = \frac{N_D}{N_P} \int_0^\infty e^{rx} \, dx \int_0^x P(y) \, \lambda \, e^{-\lambda(x-y)} \, dy$$

Changing the order of integration and evaluating the inner most integral yields

$$L(D) = \frac{\lambda}{\lambda - r} \frac{N_D}{N_P} L(P)$$

and hence

$$\tau = \frac{1}{r} \left[1 - \frac{N_D}{N_P} \frac{L(P)}{L(D)}\right] \quad . \qquad 2\text{-}22$$

Using eq. 2-8 the statistical error in τ is given by

$$s_\tau = \frac{c}{r} \frac{L(P)}{L(D)} \left[\left\{\frac{s_{L(P)}}{L(P)}\right\}^2 + \left\{\frac{s_{L(D)}}{L(D)}\right\}^2 + \left\{\frac{s_c}{c}\right\}^2\right]^{\frac{1}{2}} . \qquad 2\text{-}23$$

As $c = N_D/N_P$, $\{s_c/c\}^2$ is easily obtained:

$$\left\{\frac{s_c}{c}\right\}^2 = \frac{1}{N_D} + \frac{1}{N_P} \quad .$$

For the purpose of calculating the errors in L(P) and L(D) the values of L(P) and L(D) are approximated by the sums

$$L(P) = \Sigma\, e^{rn} P_n \quad \text{and} \quad L(D) = \Sigma\, e^{rn} D_n \, .$$

Using eq. 2-8 and the fact $s^2_{D_n} = D_n$, the following expression is obtained

$$s^2_{L(D)} = \Sigma\, e^{2rn} D_n$$

with an analogous expression for $s^2_{L(P)}$. The statistical error, s_τ, therefore depends on r. Sparrman (Sp 66A) has shown that for a minimum statistical error an r-value roughly equal to $\lambda/2$ is the optimum choice in most cases.

To anticipate the statistical errors in the above methods Sparrman and Falk (Sp 66) assumed that the prompt curve was of the form $\cos^2 x\pi/2a$ (FWHM = a) and plotted the relative errors against a/τ as shown in fig. 2. The prompt curve was chosen to have this form since the experimental prompt curves have approximately this form and partly because the convolution integral could be found analytically.

In conclusion the first, second, and third moments can be interpreted in terms of apparent features of the delayed curve as compared to the prompt curve. The first moment is sensitive to the position of the centroids on the time axis, the second moment to the width of the curve, and the third to the asymmetry of the curve.

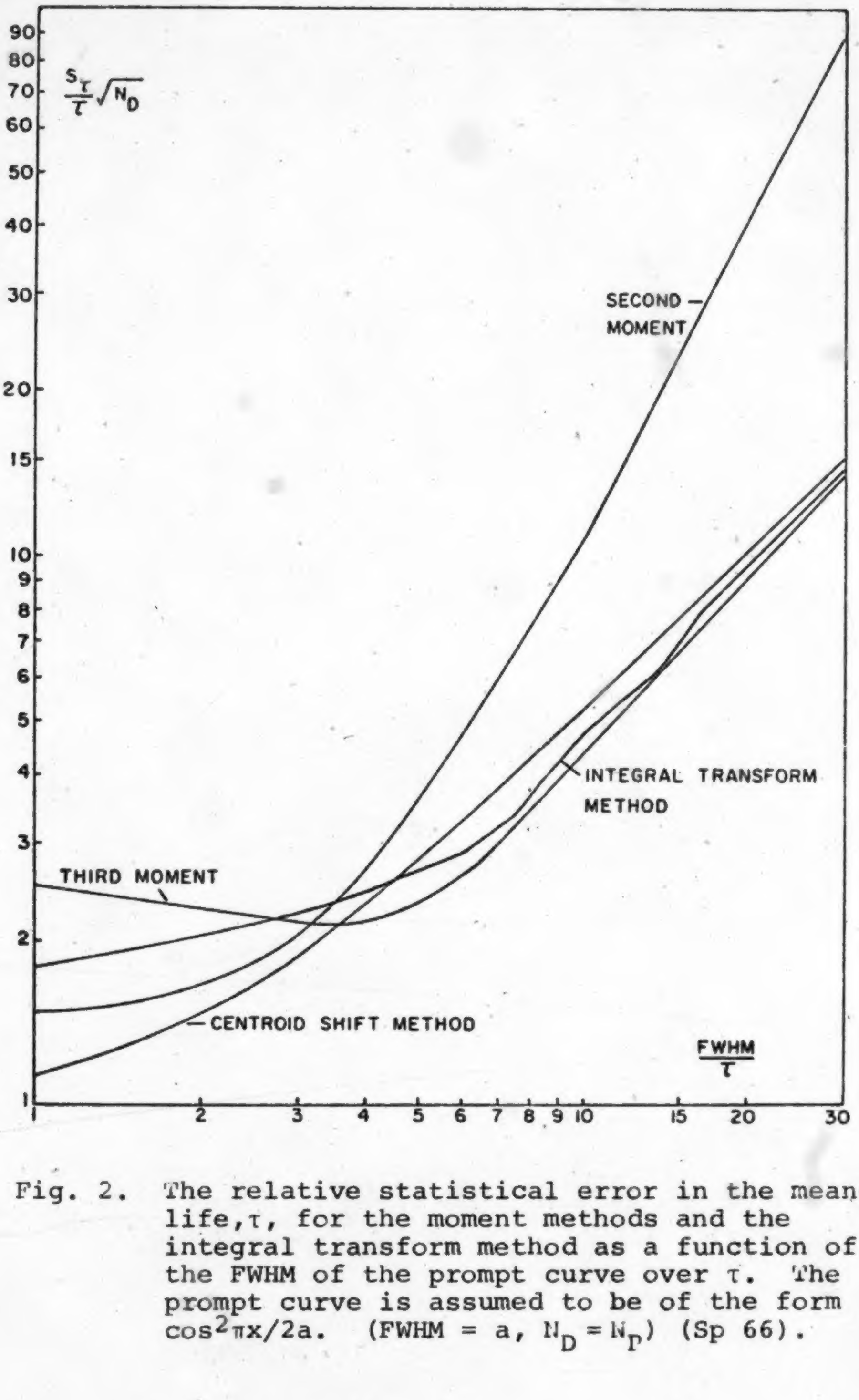

Fig. 2. The relative statistical error in the mean-life, τ, for the moment methods and the integral transform method as a function of the FWHM of the prompt curve over τ. The prompt curve is assumed to be of the form $\cos^2 \pi x/2a$. (FWHM = a, $N_D = N_P$) (Sp 66).

Even higher moments can be employed but the statistical errors of the moments increase with the order and thus only a limited number of moments are useful for practical purposes.

CHAPTER 3

THE IMPROVEMENT IN THE TIME RESOLUTION OF COAXIAL Ge(Li) DETECTORS

The improvement in the time resolution of Ge(Li) detectors is crucial to the measurement of lifetimes shorter than 10^{-10} secs by the Centroid Shift technique. As shown in Chapter 2, when the lifetime to be measured is small compared to the time resolution of the equipment, the statistical error is roughly equal to $M_2^C(P)[1/N_D + 1/N_P]$. $M_2^C(P)$ is the normalised second moment of the prompt curve about its own centroid and N_D and N_P are the total number of counts in the delayed and prompt time distribution curves, respectively. Since $M_2^C(P)$ is a measure of the width of the curve, this stresses the importance of good time resolution when short lifetimes are to be measured.

Ge(Li) detectors, with their extremely good energy resolution, are essential for lifetime measurements in nuclei with complicated decay schemes. However, the time resolution of Ge(Li) detectors is seriously degraded by the pulse shape and pulse rise-time variations which depend on the γ-ray interaction position in the detector intrinsic volume, the detector geometry and the electric field as a function of the position inside the detector. As a result one observes a wide variation of pulse shapes and pulse rise-times as indicated in fig. 3,which is a photograph of the actual signals obtained from the preamplifier of a 23c.c. coaxial Ge(Li) detector.

Several methods (Ch 68, Ja 69, Br 69, Mo 70, Be 72, Ch 72) have been introduced to compensate for the time walk due to rise-time changes in order to improve the time resolution of Ge(Li) detectors. The ARC zero-crossing method (Amplitude and Rise-time Compensation) introduced by Chase (Ch 68) is one of the most successful methods to date for improving the time resolution in Ge(Li) detectors. The method, which uses a Constant Fraction of Pulse Height Trigger (Ge 67), was originally intended for use with scintillator detector pulses which have uniform shapes. Chase has shown that the same electronic technique applied to the Ge(Li) detector pulses does a first order correction to the rise-time variations in the pulses. In fact, it corrects exactly for pulses which have an initial rising portion which is linear. However, the early slope of the time distribution curves are often distorted significantly due to slope changes that occur in the pulses before the zero-crossing of the ARC shaped pulses. Thus a second order correction would be useful to further improve the time resolution of Ge(Li) detectors.

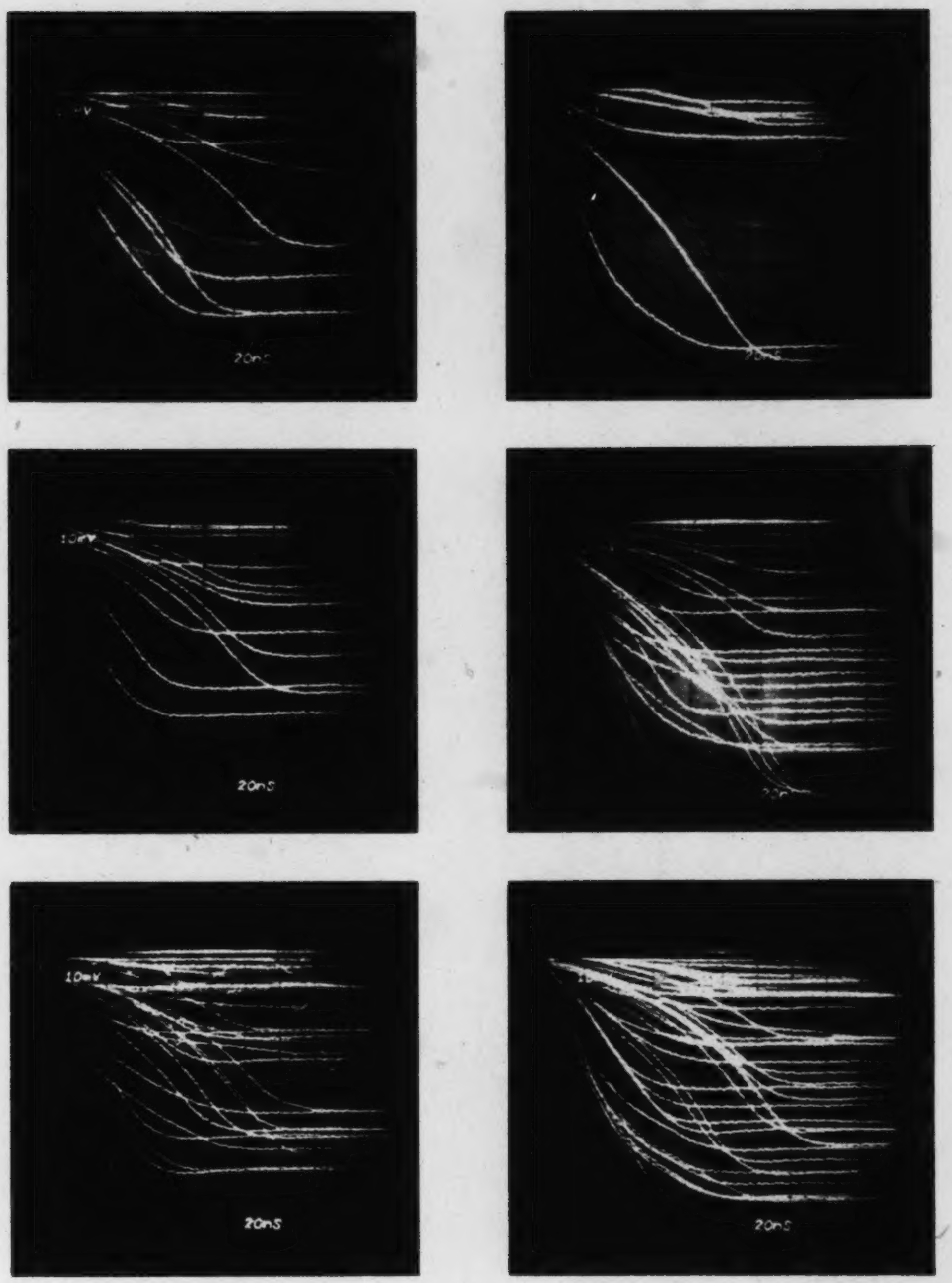

Fig. 3. Photographs of the preamplifier signals obtained from a 23 c.c. coaxial Ge(Li) detector using a ^{60}Co source.

A theoretical base to our technique for improving the time resolution is formed by an analysis of the pulse shapes from coaxial Ge(Li) detectors as a function of the position of irradiation in the detector, and the synthesis of these pulses in a Constant Fraction of Pulse Height Trigger. The results obtained in our investigations, which involve a pulse shape discrimination technique, are considerably better than those of previous methods and are such that lifetimes as short as 10^{-11} secs have been measured by the Centroid Shift technique.

In this work some interesting problems developed which induced a more detailed investigation of the timing properties of coaxial Ge(Li) detectors. The results of this investigation will be discussed later in this chapter and Chapter 5.

3.1 Pulse Shape Analysis

The timing properties of semiconductor detectors are intimately related to the pulse shapes (charge or current pulses) which the detector delivers to the amplifier as a consequence of the detector-radiation interaction. An interaction in the sensitive region of a detector releases a large number of electron-hole pairs which are separated and collected by the electric field present in the intrinsic region. The pulse shapes depend on the charge transit time which is determined by the following major factors (Be 68):

a) The electric field as a function of the position inside the detector sensitive region,

b) the electron and hole mobilities, μ_e and μ_h, which in a given material are functions of the electric field and temperature,

c) the distribution of charge created by the detected radiation which is dependent on the energy and the type of incident radiation.

Other factors such as the noise or charge trapping effects, due to impurities and defects in the semiconductor material, lead to additional requirements for the total collection of the charges. At higher energies the plasma effect, which is the production of secondary electron-hole pairs by the moving charges from the initial interaction, also introduces further complications to the charge collection time.

In the following analysis we consider an ideal coaxial semiconductor detector in which no charge trapping or recombination effects occur. The equation of motion of a carrier is given by the empirical formula stated by Moszyński and Bengtson (Mo 72A)

$$v = v_s/[1 + v_s/\mu\varepsilon] \qquad 3\text{-}1$$

where v is the drift velocity, v_s is the carrier saturation velocity, ε is the electric field and μ is the zero field carrier mobility. However, this formula leads to complicated numerical integration in order to determine the pulse shapes from coaxial detectors. To simplify the mathematics we neglect the carrier velocity saturation effect and assuming that μ is independent of the electric field, we obtain as a first approximation of the empirical formula the equation of motion of a carrier given by (Be 68)

$$v = \mu \varepsilon \quad . \qquad \text{3-2}$$

Sakai et al (Sa 69) have shown that the saturation velocity for both holes and electrons is approximately 1.1×10^7 cm/sec although this limiting velocity is not reached as abruptly for the holes. Electrons reach this saturation velocity at an electric field of about 100 V/mm in Ge(Li) semiconductor material at 77°K. However, much higher fields are required for the holes to reach saturation velocity (Sa 69). Cho and Llacer (Ch 72A) did not observe hole saturation velocity in high purity Ge coaxial detectors at 100-500 V/mm fields. Hence for typical fields in Ge(Li) coaxial detectors eq. 3-2 is a reasonable approximation for the holes but not for electrons. However, since we wish only a qualitative understanding of the problem, eq. 3-2 is used for both the electron and hole motion to obtain conformity on the final pulse shape equation. As will be shown later the form of the pulse shape equation is not affected by considering saturation velocities.

The simplest way to calculate the signal is to consider the energy balance in the system (Go 66). The collection of the carriers corresponds to an energy dissipation in the electrostatic field inside the detector. To maintain the energy stored in the dielectric, a corresponding charge must flow in the external circuit. The collection of a single electron-hole pair is depicted in fig. 4.

Now we have that the energy W stored in the dielectric is equal to $\frac{1}{2}Q^2/C$ where Q is the charge in the detector of capacity C. Therefore,

$$\frac{dW}{dt} = \frac{Q}{C}\frac{dQ}{dt} \quad . \qquad 3\text{-}3$$

The field strength in the case of the double-ended coaxial detector is

$$\varepsilon(x) = -\frac{V}{x \ln(b/a)} \qquad 3\text{-}4$$

where a and b are the inner and outer radii of the interaction zone of the coaxial detector, and V is the applied voltage. Thus the drift velocity for the electrons is

$$v = \frac{dx}{dt} = \frac{V\mu_e}{x \ln(b/a)} \quad . \qquad 3\text{-}5$$

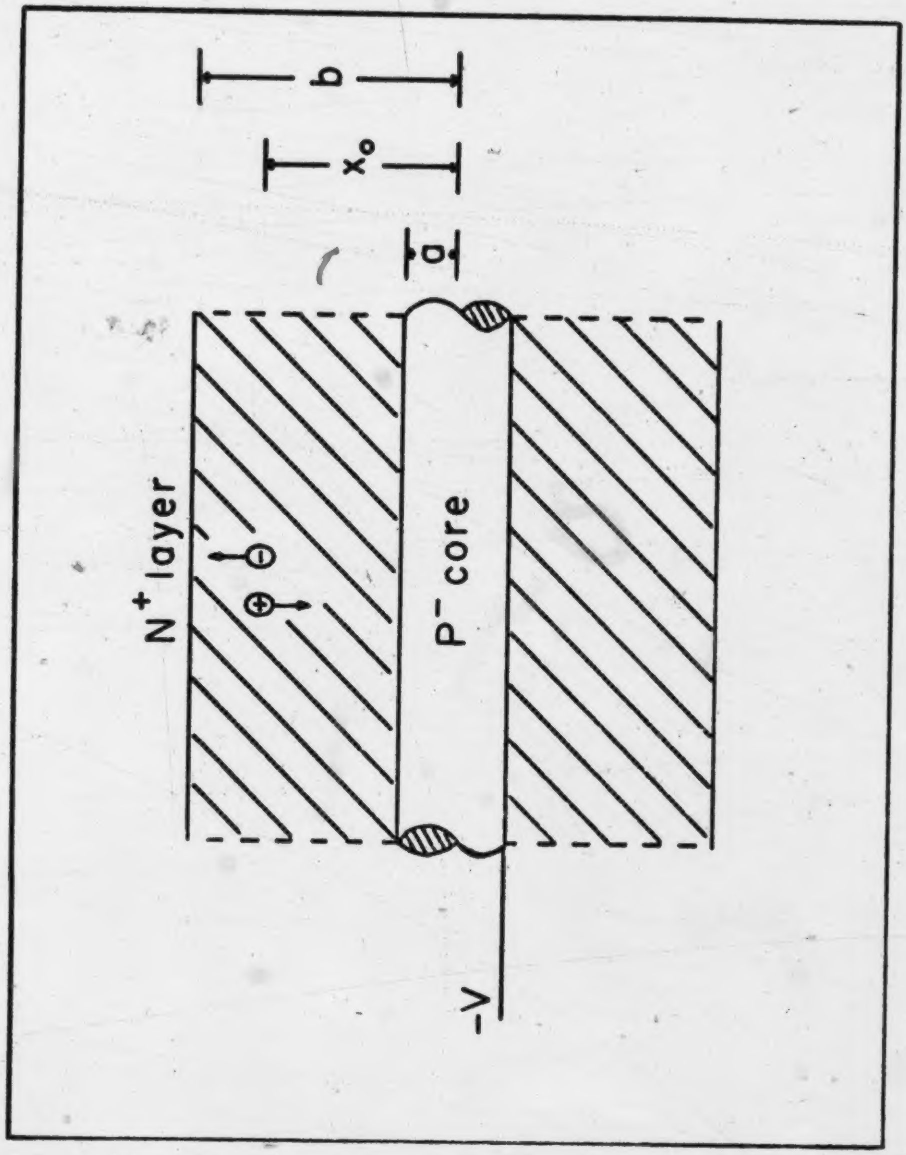
b
x_o
a
N^+ layer
P^- core
−V

Fig. 4. Collection of a single electron-hole pair in a double-open-end coaxial Ge(Li) detector.

Integrating this relation, taking note of the limits of integration, yields for the electrons and holes,

$$x_e(t) = \{x_o^2 + \frac{2t\ \mu_e V}{\ln(b/a)}\}^{\frac{1}{2}} \qquad 3\text{-}6$$

and $$x_h(t) = \{x_o^2 - \frac{2t\mu_h V}{\ln(b/a)}\}^{\frac{1}{2}} \qquad 3\text{-}7$$

respectively. The work done on the electron in time dt is:

$$\text{force} \cdot \text{distance} = \varepsilon(x)\cdot e\cdot v dt \quad .$$

Therefore,

$$\frac{dW}{dt} = e\ \mu_e\ V^2\ \{\frac{1}{x\ \ln(b/a)}\}^2 \quad . \qquad 3\text{-}8$$

Equating eqs. 3-3 and 3-8 we have

$$\frac{dQ}{dt} = I_e(t) = e\ \mu_e\ V\{\frac{1}{x\ \ln(b/a)}\}^2 \qquad 3\text{-}9$$

where $I_e(t)$ is the current due to the motion of the electrons. Similarly for the motion of the holes

$$I_h(t) = -\ e\ \mu_h\ V\{\frac{1}{x\ \ln(b/a)}\}^2 \quad . \qquad 3\text{-}10$$

Substituting $A_e = \mu_e V/\ln(b/a)$ and $A_h = \mu_h V/\ln(b/a)$ into eqs. 3-9 and 3-10, and using eqs. 3-6 and 3-7, the current contributions for each carrier are:

$$I_e(t) = \frac{e\ A_e}{\ln(b/a)}\ \frac{1}{(x_o^2 + 2A_e\ t)} \qquad 3\text{-}11$$

$$I_h(t) = - \frac{e\,A_h}{\ln(b/a)} \; \frac{1}{(x_o^2 - 2A_h\,t)} \quad . \qquad 3\text{-}12$$

By integrating these expressions with respect to t, the charge Q induced by each carrier is given by

$$Q_e(t) = \frac{e}{2\,\ln(b/a)} \ln(1 + \frac{2A_e\,t}{x_o^2}) \qquad 3\text{-}13$$

$$Q_h(t) = - \frac{e}{2\,\ln(b/a)} \ln(1 - \frac{2A_h\,t}{x_o^2}) \quad . \qquad 3\text{-}14$$

At this point another approximation is made in that the mobilities for the electrons and holes are equal ($A_e = A_h = A$) which is a good approximation for Ge(Li) semiconductor material at 77°K. Further, if one assumes that the interaction of a γ-ray with the detector is such that the charge produced, $n_o e$, is localised to a point which is small compared to the detector dimensions, (the range of 1 Mev electrons in Germanium is ∿0.8 mm (St 67)), then the total charge induced is given by

$$Q(t) = \frac{n_o\,e}{2\,\ln(b/a)} \{\ln(1 + \frac{2At}{x_o^2}) - \ln(1 - \frac{2At}{x_o^2})\} \quad . \qquad 3\text{-}15$$

If saturation velocities for both the electrons and holes had been used, eq. 3-15 would have the form

$$Q(t) = \frac{n_o e}{\ln(b/a)} \{\ln(1 + \frac{v_s^e\,t}{x_o}) - \ln(1 - \frac{v_s^h\,t}{x_o})\} \qquad 3\text{-}16$$

which is very similar to that of eq. 3-15.

The maximum collection time, which corresponds to a generation point near one of the two electrode, is given by

$$T_{max} = (b^2 - a^2)/2A$$

where

$$A = \frac{\mu V}{\ln(b/a)} \quad .$$

Substituting for T_{max} in eq. 3-15, one obtains

$$Q(t) = \frac{n_o e}{2 \ln(b/a)} \{ \ln[1 + \frac{(b^2 - a^2)}{x_o^2} \frac{t_e}{T_{max}}] - \ln[1 - \frac{(b^2 - a^2)}{x_o^2} \frac{t_h}{T_{max}}] \} \qquad 3\text{-}17$$

where

$t_e = t$, for $t \leq (b^2 - x_o^2)\ln(b/a)/2\mu V$

$t_e = (b^2 - x_o^2)\ln(b/a)/2\mu V$ for $t > (b^2 - x_o^2)\ln(b/a)/2\mu V$

and

$t_h = t$, for $t \leq (x_o^2 - a^2)\ln(b/a)/2\mu V$

$t_h = (x_o^2 - a^2)\ln(b/a)/2\mu V$ for $t > (x_o^2 - a^2)\ln(b/a)/2\mu V$

Using eq. 3-17, pulse shape calculations for seven different interaction positions within a coaxial Ge(Li) detector, outer radius 1.54 cm and inner radius 0.34 cm, are shown in fig. 5. It is obvious from these curves that the variations in pulse shapes and pulse rise-times are a major factor contributing to the poor timing resolution of coaxial Ge(Li) detectors.

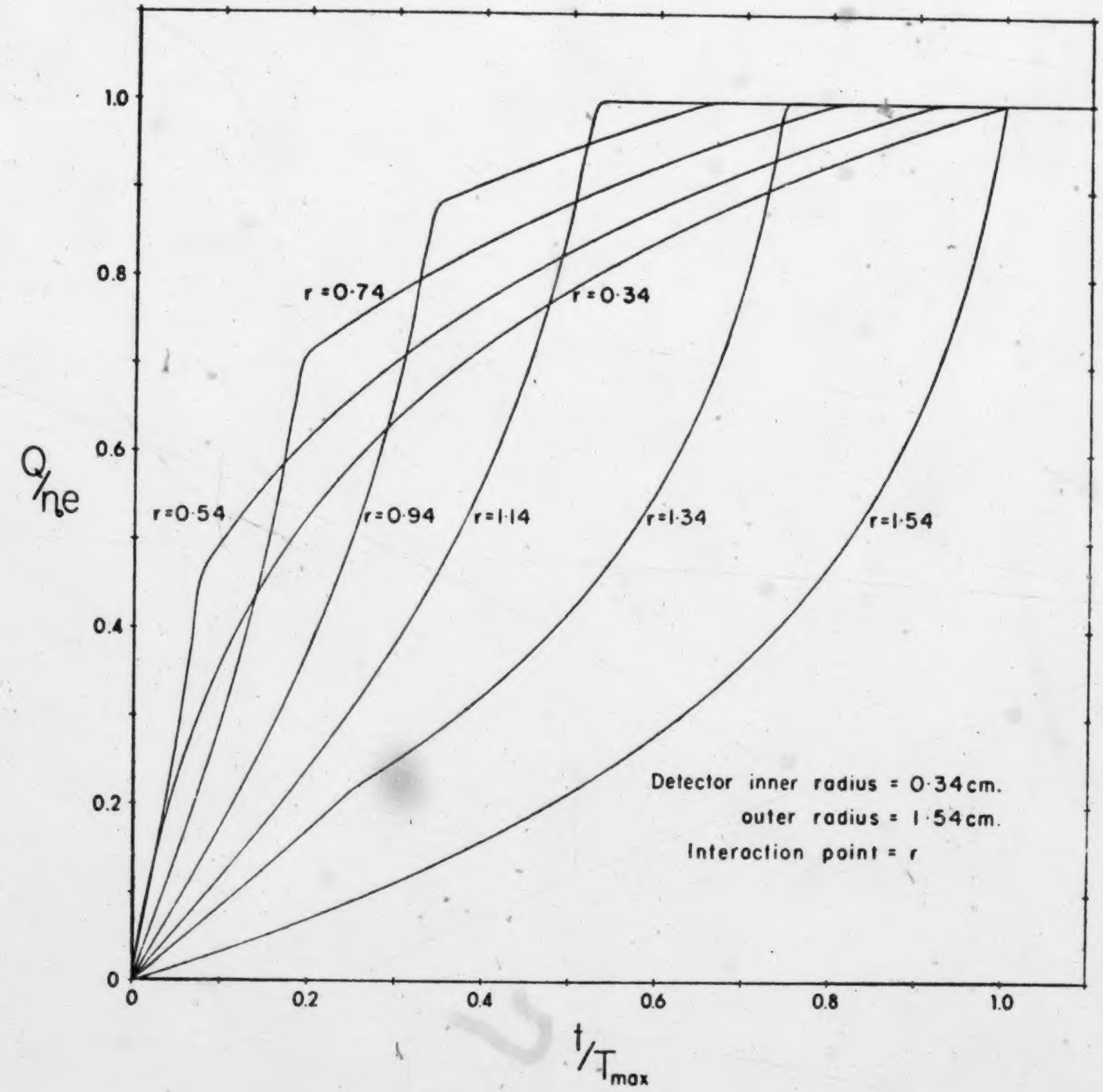

Fig. 5. Calculated pulse shapes for local interactions at seven different positions along a radius of an ideal double-open-end coaxial Ge(Li) detector.

The above pulse shapes are only a good approximation to reality. γ-rays can interact at two or more locations in the detector to produce a charge which is not localised at one point but at several points. This would occur when Compton scattered photons, annihilation quanta, or bremsstrahlung are reabsorbed.

Furthermore, the range of electrons or positrons above 1 MeV is not negligible within a 1 cm detector. Thus, the charge produced by high energy γ-rays and by γ-rays interacting at several locations tends to be distributed in the detector volume. The shape of the pulses resulting from such events will depend upon the the spatial distribution of the charge, including the length of the ionization tracks and their orientation with respect to the collecting electrodes. Thus the resulting pulses are likely to be a superposition of a number of the waveforms as shown in fig. 5. Nevertheless, the actual pulse shapes obtained as shown in fig.3 show a similar variety of shapes as those obtained by the above theoretical calculations.

A signal can be synthesized from the above theoretical pulses by inverting and attenuating it by a factor f, and adding the result to the original pulse delayed by the time t_d. This is the basis of the Constant Fraction of Pulse Height Trigger (Ge 67) (CFPHT) and the Amplitude Rise-Time Compensation technique (ARC) suggested by Chase (Ch 68). Assuming that one has a fast charge amplifier, the timing pulse from the CFPHT is initiated at the zero-crossing point of the synthesized signal

$$E(T) = -f\,\frac{Q(T)}{n_o\,e} + \frac{Q(T - T_d)}{n_o\,e} \qquad \text{3-18}$$

where

$$T = t/T_{max} \quad \text{and} \quad T_d = t_d/T_{max}\ .$$

Using the result, eq. 3-17, we have

$$\begin{aligned} E(T) = -f\,\frac{1}{2\,\ln(b/a)}\,&[\ln\{1 + \frac{(b^2 - a^2)}{x_o^2}\,T\} \\ &- \ln\{1 - \frac{(b^2 - a^2)}{x_o^2}\,T\}] \quad \text{for} \quad T \geq 0 \\ &+ \frac{1}{2\,\ln(b/a)}\,[\ln\{1 + \frac{(b^2 - a^2)}{x_o^2}\,(T - T_d)\} \\ &- \ln\{1 - \frac{(b^2 - a^2)}{x_o^2}\,(T - T_d)\}] \quad \text{for} \quad T \geq T_d. \qquad \text{3-19} \end{aligned}$$

The zero-crossing point of this function was found by successive approximations on a computer for various values of f and T_d. Figs. 6 and 7 show examples of the crossing time t_c versus the slope change time t_s, which is a function of the interaction position in the detector, both normalised to the delay time t_d. For each fraction the curves are made up of two parts, one

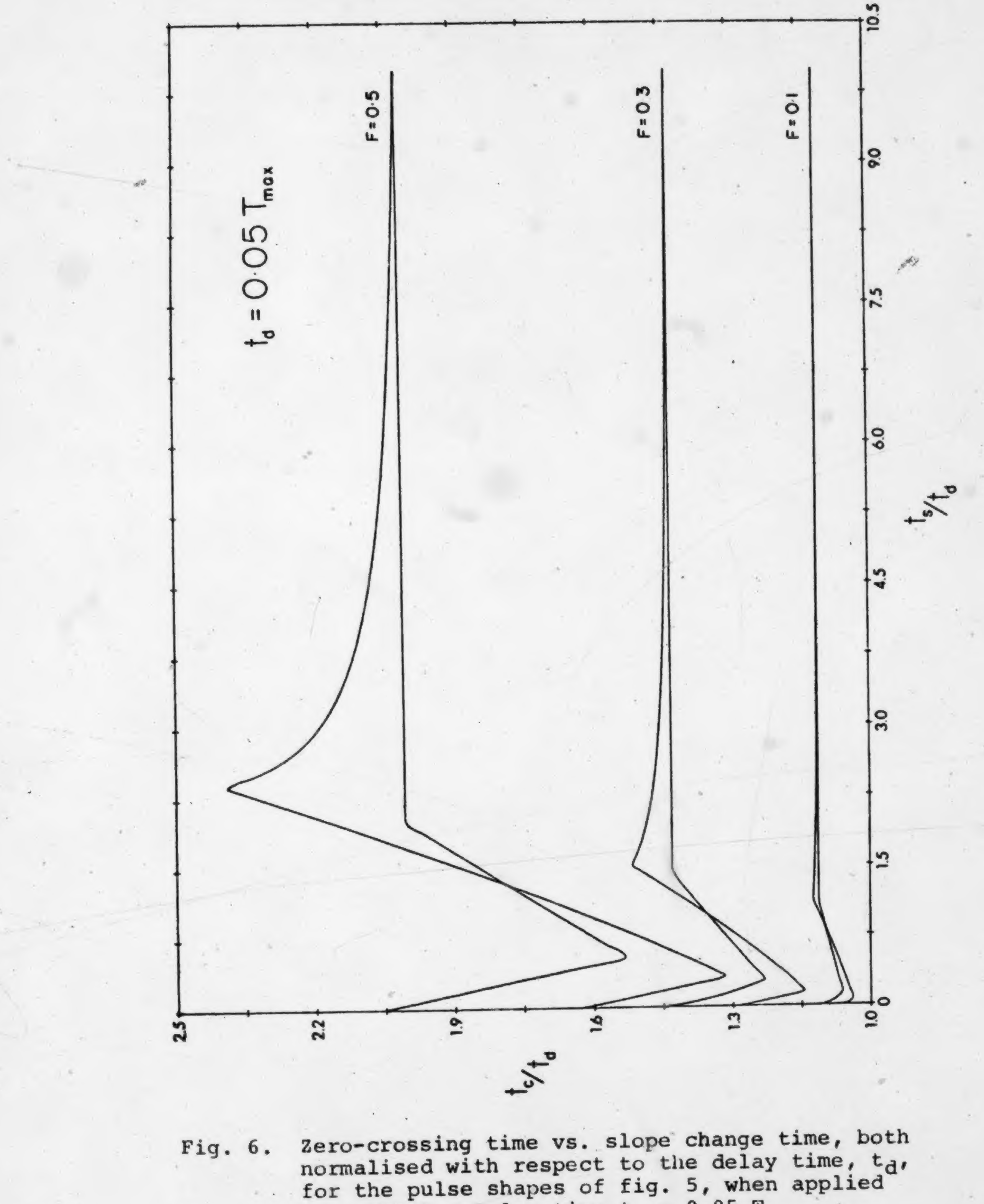

Fig. 6. Zero-crossing time vs. slope change time, both normalised with respect to the delay time, t_d, for the pulse shapes of fig. 5, when applied to a CFPHT. Delay time $t_d = 0.05\ T_{max}$.

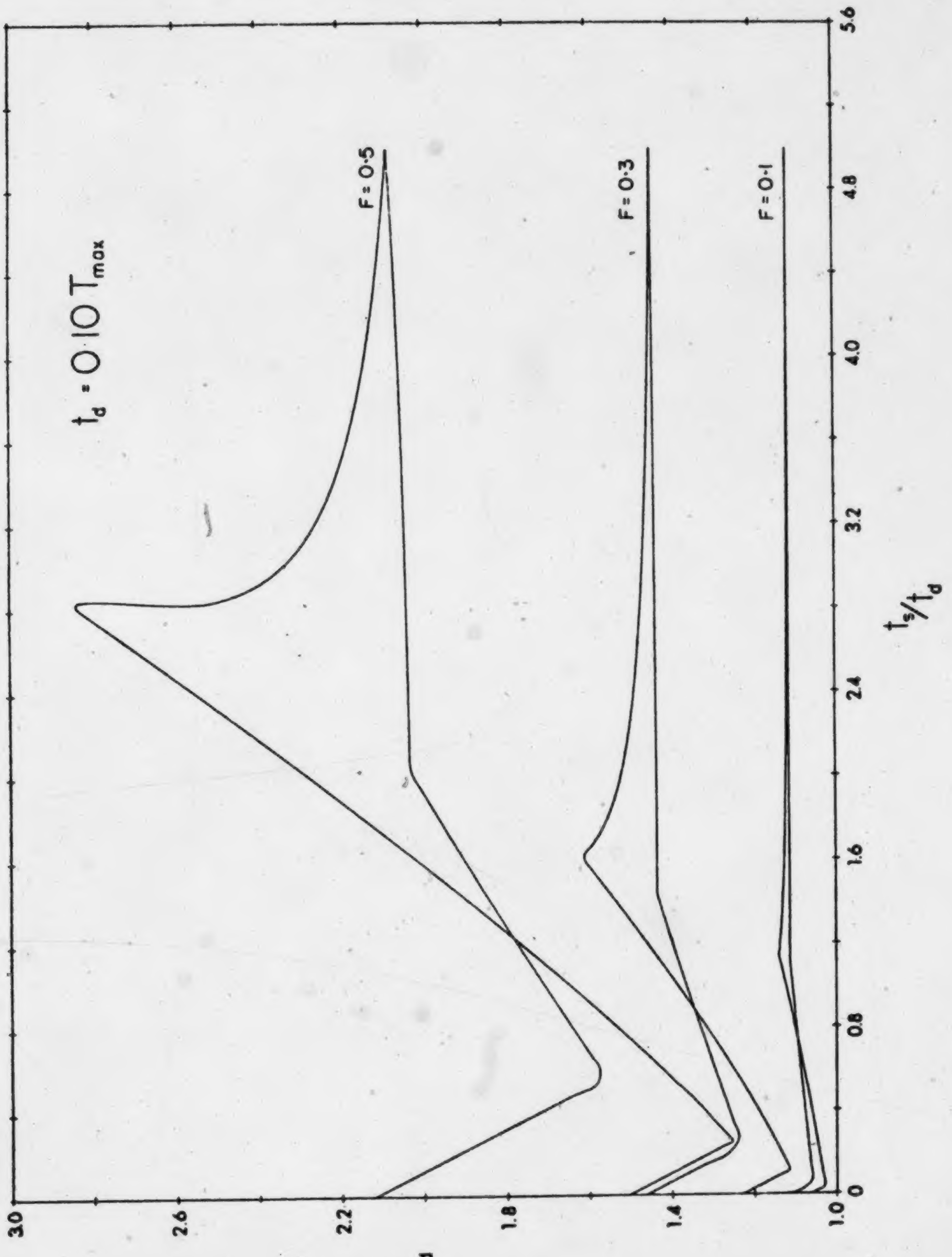

Fig. 7. Zero-crossing time vs. slope change time, both normalised with respect to the delay time, t_d, for the pulse shapes of fig. 5, when applied to a CFPHT. Delay time $t_d = 0.10\ T_{max}$.

corresponding to slope change due to the motion of the holes towards the inner electrode and the other due to the motion of the electrons towards the outer electrode of the detector.

From figs. 6 and 7, the walk of the zero-crossing time with slope change time is well demonstrated. It is this effect that leads to the poor time resolution of coaxial Ge(Li) detectors. It may seem at first glance that the smaller the fraction the better the time resolution. However, at a fraction of 0.1 the attenuated signal is very small and in many cases the same magnitude as the noise in the region of zero-crossing point of the synthesized signal. Hence random triggering of the zero-crossing discriminator occurs leading to very poor time resolution.

It is seen from figs. 6 and 7 that after a certain value of t_s/t_d, the walk is minimal and the improved timing technique to be described effectively takes this region of these zero-crossing time curves to obtain the improved time resolution. This is accomplished by taking the curve for f = 0.1 and subtracting it from the curve for f = 0.5 to obtain time difference curves as illustrated in figs. 8 and 9 for the cases $t_d = 0.05\ T_{max}$ and $t_d = 0.10\ T_{max}$. Experimentally this can be done by using the output from a CFPHT unit set at f = 0.1 to 'START' a Time to Amplitude Converter (TAC), the 'STOP'

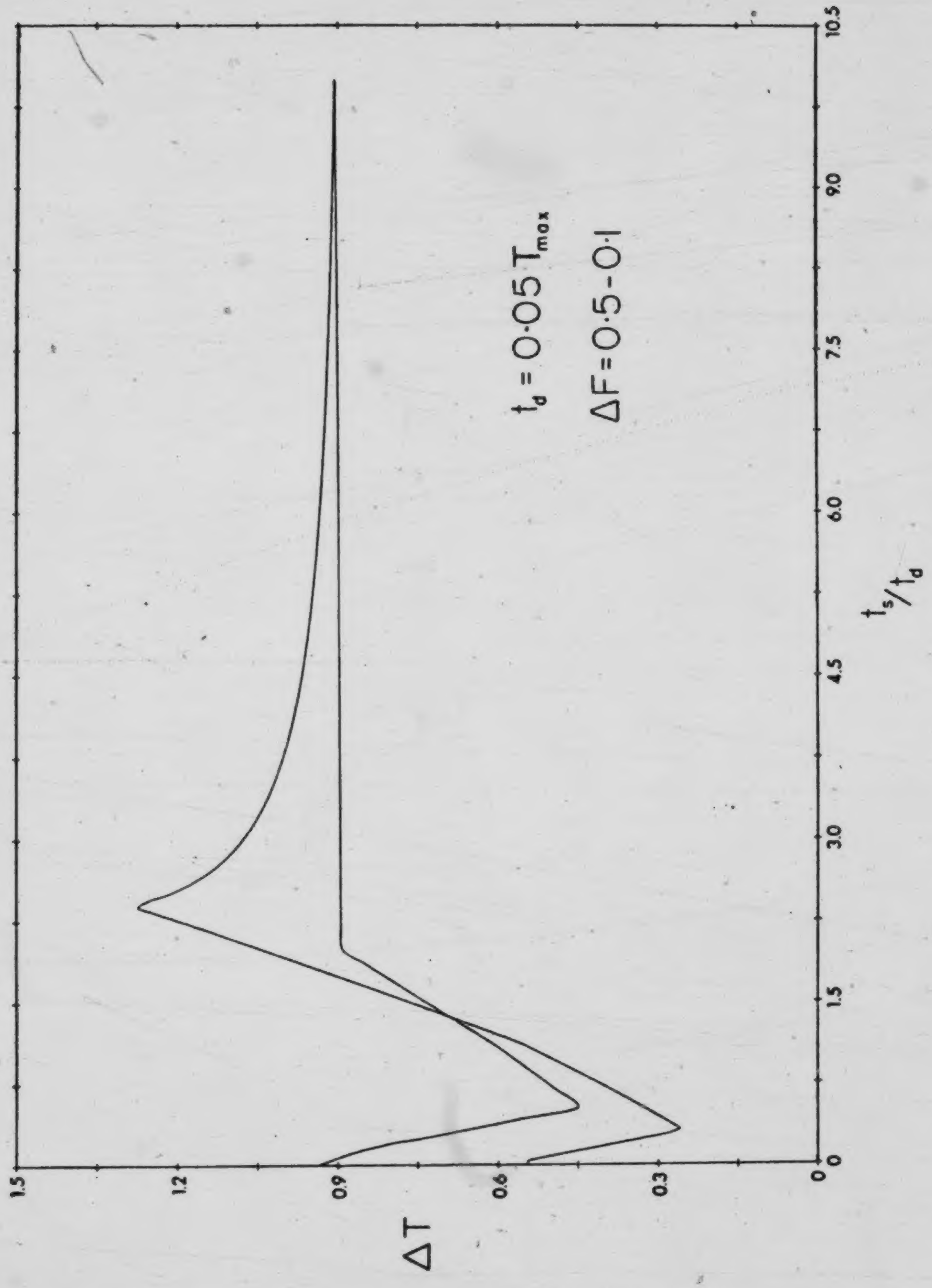

Fig. 8. Time difference curve obtained when the signals from two CFPHT's set at fractions 0.1 and 0.5, respectively, are applied to a TAC. CFPHT delay time, $t_d = 0.05\ T_{max}$.

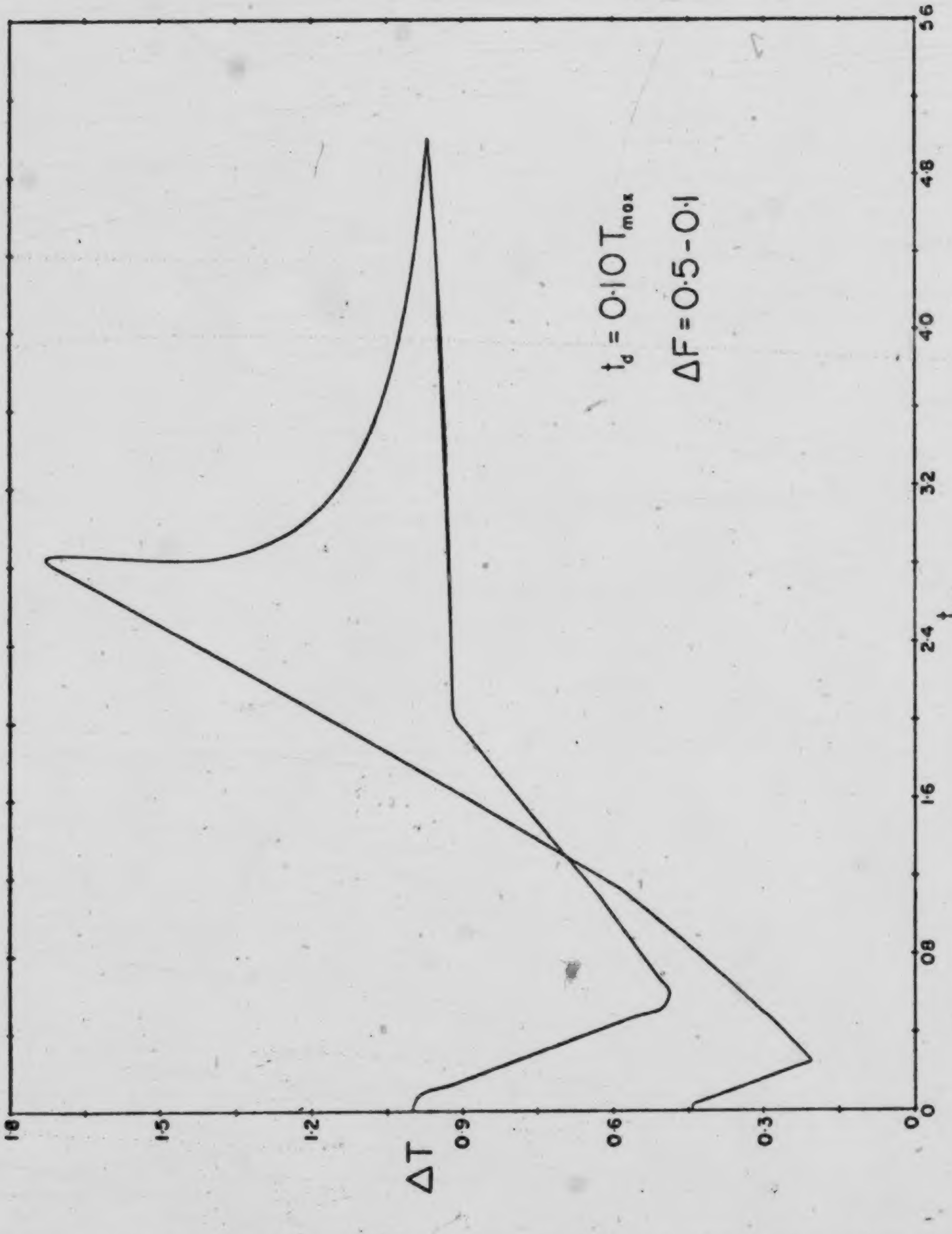

Fig. 9. Time difference curve obtained when the signals from two CFPHT's set at fractions 0.1 and 0.5, respectively, are applied to a TAC. CFPHT delay time, $t_d = 0.10\ T_{max}$.

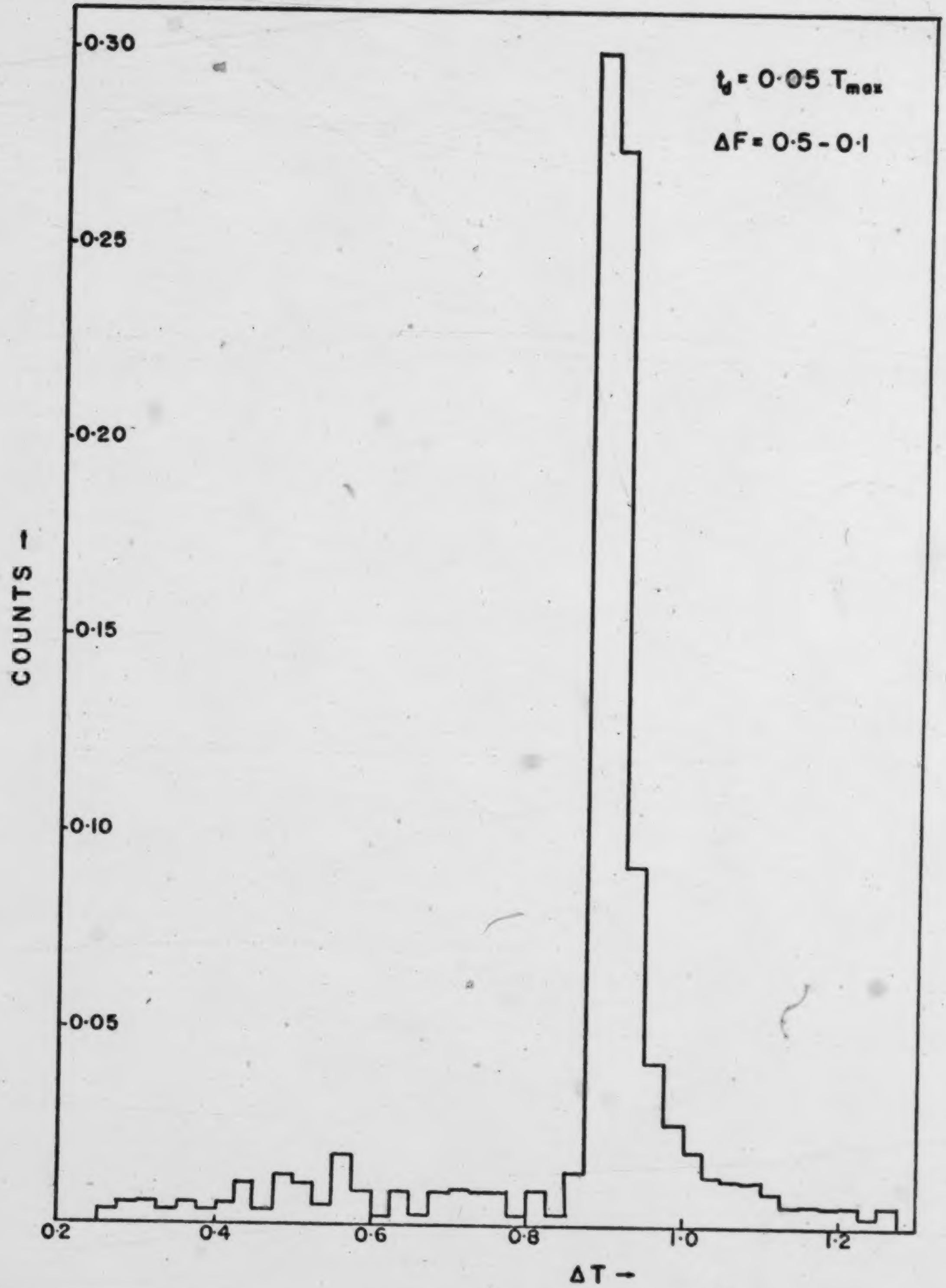

Fig. 10. Theoretical 'shape' curve obtained from a TAC using the time difference curve of fig. 8, and considering the volume contributions at different radii of a coaxial Ge(Li) detector.

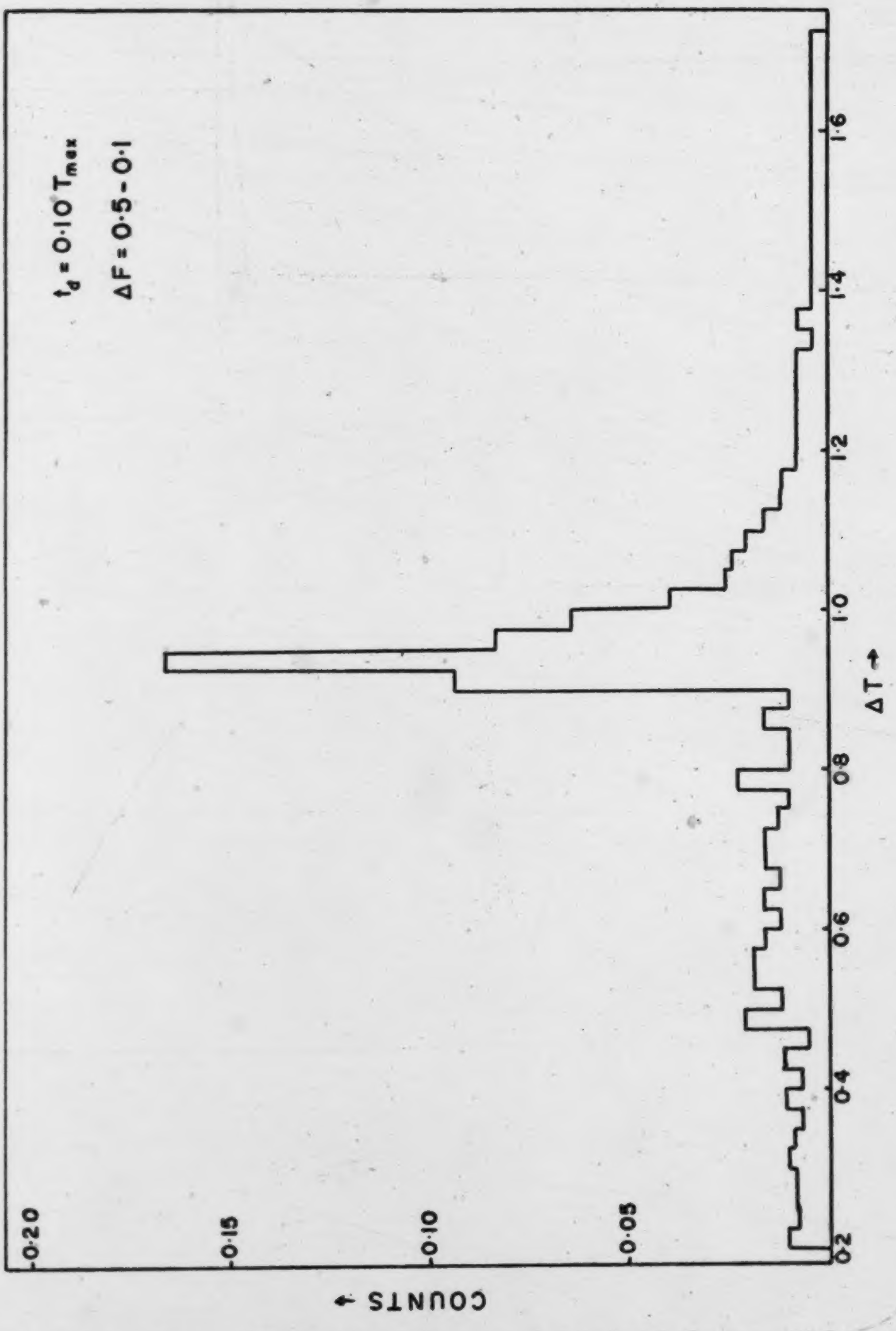

Fig. 11. Theoretical 'shape' curve obtained from a TAC using the time difference curve of fig. 9, and considering the volume contributions at different radii of a coaxial Ge(Li) detector.

for which is obtained from a CFPHT set at f = 0.5. Then by using a Timing Single Channel Analyser (SCA) that portion of the so-called 'shape' spectrum obtained from the TAC which shows minimal walk can be selected by setting the appropriate window in the SCA.

When one considers the volume contribution at different radii of a coaxial Ge(Li) detector, outer radius 1.54 cm and inner radius 0.34 cm, the actual theoretical time difference or 'shape' curves obtained from the TAC are shown in figs. 10 and 11. These curves are not quite the same as those obtained in actual experimental test of the technique for reasons that will be discussed later.

3.2 The Triple Constant Fraction Discriminator

Initially, as described in a recent publication (Wh 74), the improved time resolution of coaxial Ge(Li) detectors was obtained by the above technique by the use of three separate Constant Fraction Discriminators. Two of them were set at fractions 0.1 and 0.5, and their timing outputs were used to 'START' and 'STOP' the 'shape' TAC, respectively.

The output from the third, the setting of which at f = 0.3 gives optimum time resolution without pulse shape selection, was used to obtain the actual time distribution curve from a second TAC.

However, the method suffered from a few drawbacks concerning the settings of the three discriminator units. The following important procedures had to be observed:

a) The threshold level discriminator,

b) The external shaping delays, and

c) The zero-crossing walk adjusts had to be set to precisely the same value on two of the discriminator units. This was achieved by obtaining an effective 'delta' function time spectrum from the 'shape' TAC, both units being set at the same fraction, by careful adjustments on the threshold level and walk adjusts. Even with this procedure, the adjustments might be inadequate if the fraction switch attenuators were not identical in each unit.

These problems were overcome by the development of the Triple Constant Fraction Discriminator (TCFD) which incorporates the use of a common threshold level discriminator, external 50Ω shaping delay, and a common fraction switch attenuator. The circuit diagram is shown in fig. 12. However, the fundamentals of the circuit can more easily be understood from the diagrammatic block circuit, fig. 13.

I.C. 1 is the common threshold level comparator, a 'low' output being obtained between the arrows when the input signal goes below the threshold level. In

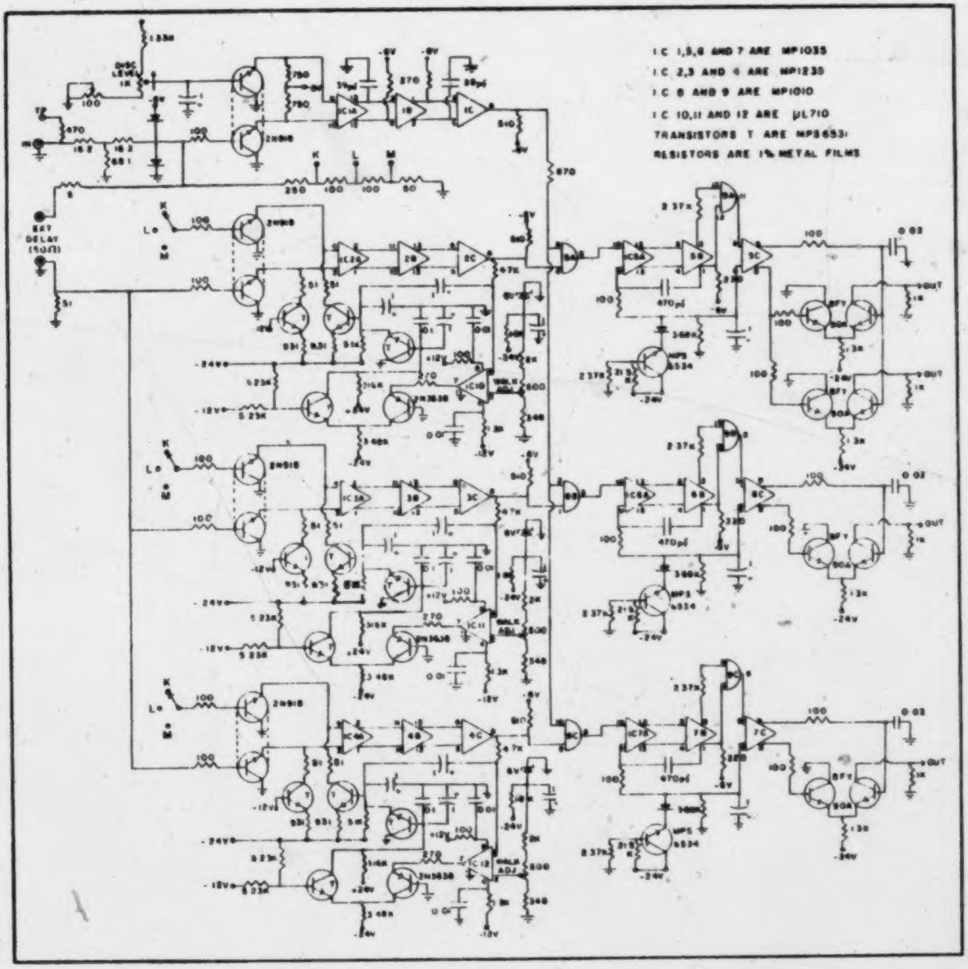
IC 1,5,6 AND 7 ARE MP1035
IC 2,3 AND 4 ARE MP1235
IC 8 AND 9 ARE MP1010
IC 10,11 AND 12 ARE μL710
TRANSISTORS T ARE MPS6531
RESISTORS ARE 1% METAL FILMS
EXT DELAY
OUT

Fig. 12. Circuit diagram of the Triple Constant Fraction Discriminator (TCFD).

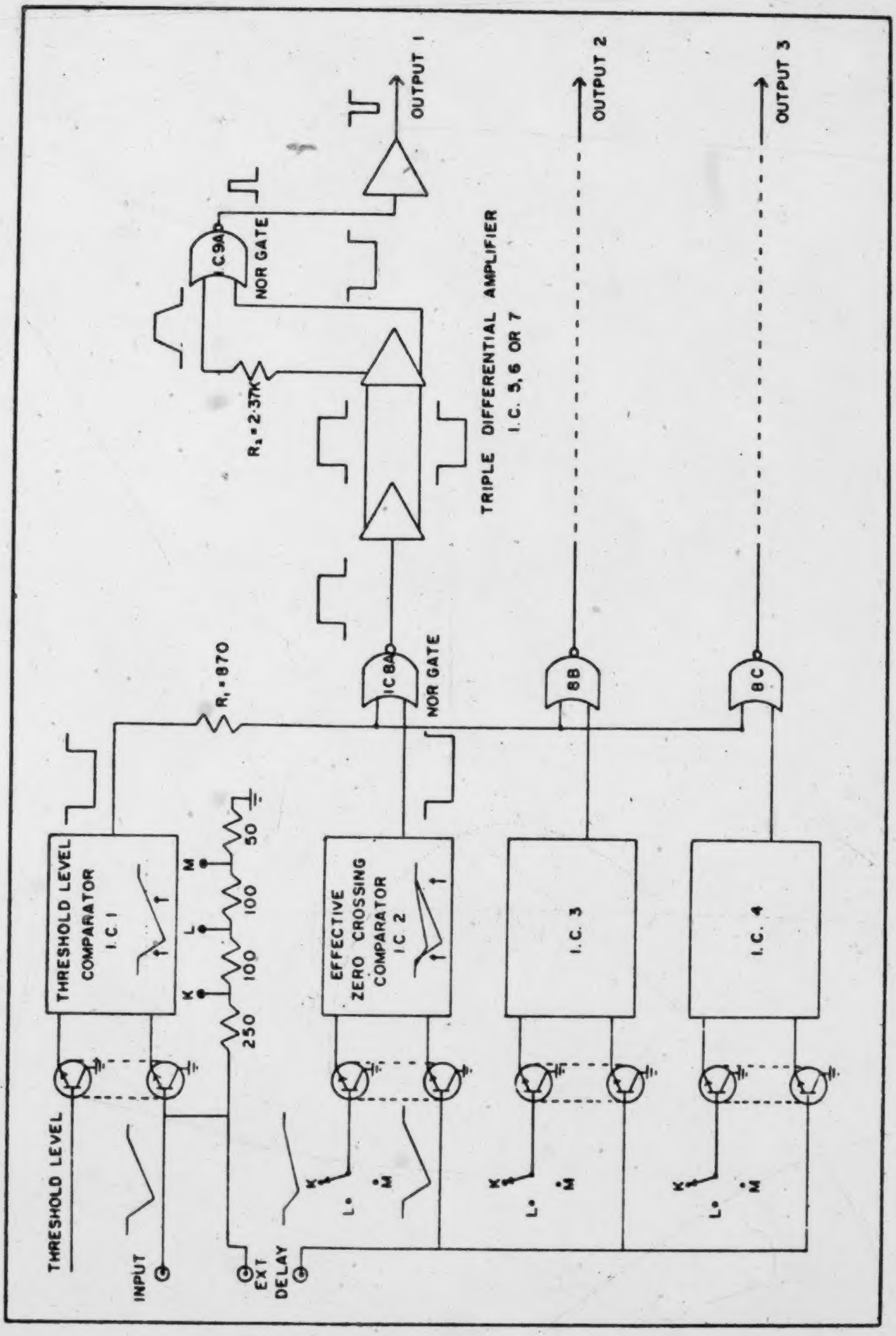
THRESHOLD LEVEL
INPUT
EXT DELAY
THRESHOLD LEVEL COMPARATOR I.C. 1
K
L
M
250
100
100
50
EFFECTIVE ZERO CROSSING COMPARATOR I.C. 2
I.C. 3
I.C. 4
R1 = 870
IC8A
NOR GATE
8B
8C
TRIPLE DIFFERENTIAL AMPLIFIER
I.C. 5,6 OR 7
R2 = 2.37K
IC9A
NOR GATE
OUTPUT 1
OUTPUT 2
OUTPUT 3

Fig. 13. Schematic block diagram of the electronic circuit of the TCFD.

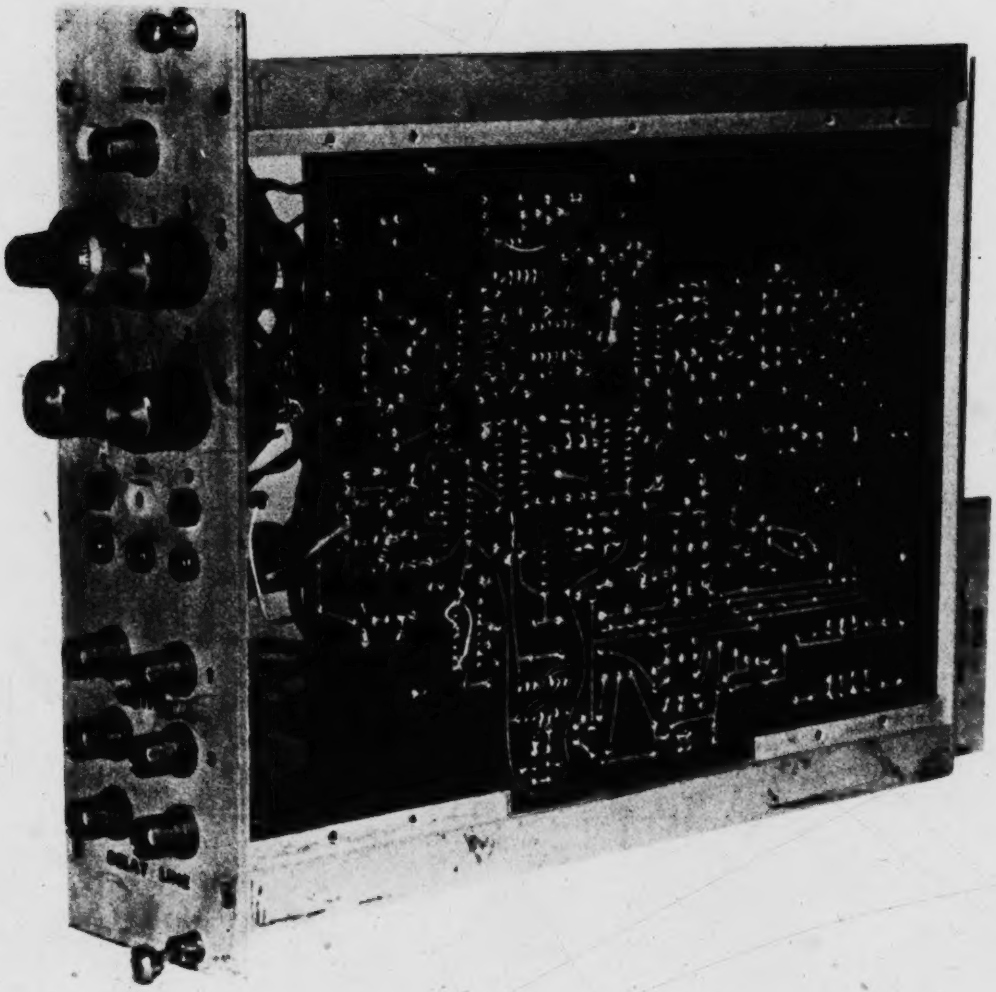

Fig.14. A photograph of the Triple Constant Fraction Discriminator module.

S

I.C. 2, 3 or 4 a comparison is made between the attenuated signal and the original signal delayed a time t_d in the common external 50Ω delay. The I.C. effectively works as a zero-crossing discriminator, a 'low' output being obtained between the arrows at the crossing points as indicated.

The output of the threshold level comparator primes the NOR gate, I.C. 8, where when both inputs are in the 'low' state, the output is 'high'. This signal is then amplified in I.C. 5, 6 or 7, the 'high' output of which is then sent through a 2.37 KΩ shaping resistance R_2. This resistance slows up the rise-time of the signal sufficiently such that it is effectively still in the 'low' state with respect to the switching level, when the 'low' output of I.C. 5, 6 or 7 is applied to the NOR gate I.C. 9. A sharp 15 ns pulse is thus obtained, the length of which is determined by the resistance R_2, and then inverted for use as an output signal. Fig. 14 shows a photograph of the Triple Constant Fraction Discriminator module.

3.3 Experimental Tests of Improved Timing Technique

For bench testing experiments, the TCFD unit was placed in the electronic circuit shown diagrammatically in fig. 15. Timing coincidence was obtained by placing

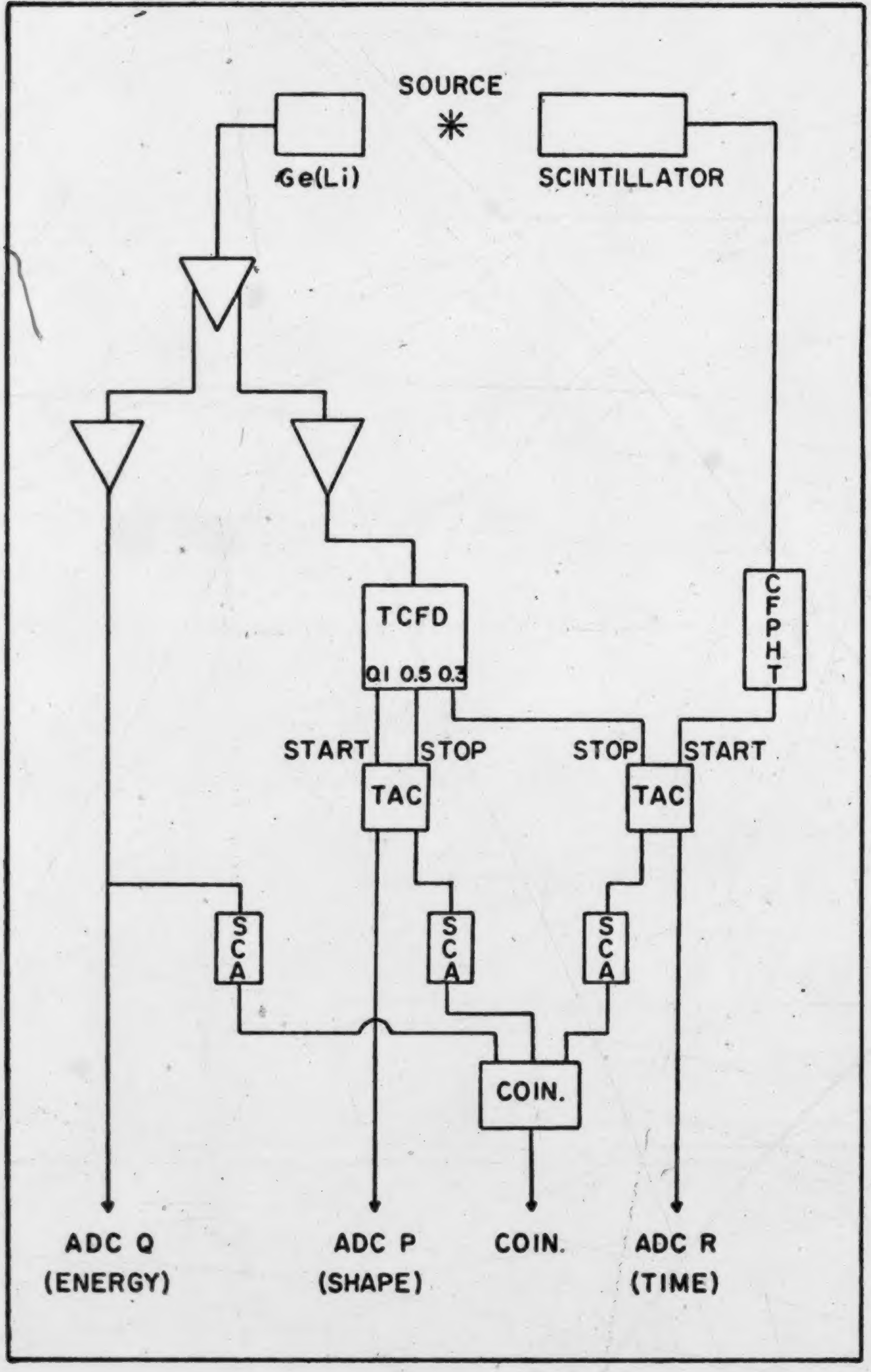
SOURCE
Ge(Li)
SCINTILLATOR
TCFD
0.1 0.5 0.3
CFPHT
START
STOP
STOP
START
TAC
TAC
SCA
SCA
SCA
COIN.
ADC Q
(ENERGY)
ADC P
(SHAPE)
COIN.
ADC R
(TIME)

Fig. 15. Block diagram of the bench-testing timing system.

a ^{60}Co or ^{22}Na source between a 23 c.c. coaxial Ge(Li) detector and a Naton scintillator attached to a C3/1024 fast multiplier tube. One of the signals from the Ge(Li) detector is fed through a linear amplifier and into ADC Q. The other is sent through a Timing Filter Amplifier (TFA) and into the TCFD unit. This unit has three timing outputs each of which can be individually set at any fraction 0.5 (K), 0.3 (L) and 0.1 (M) by using a common fraction switch attenuator as shown in figs. 12 and 13. The output at fraction 0.3 is used to 'STOP' the time TAC. The 'START' signal is obtained from the scintillator. The output of the time TAC is then fed into ADC R. The other two outputs of the TCFD are set at fractions 0.1 and 0.5, 'START' and 'STOP' the 'shape' TAC, respectively, the output of which is fed into ADC P. ADC's P, Q and R require a coincidence signal which is provided by the three timing SCA's and the Universal Coincidence box. The Delay Amplifiers which are used to obtain a coincidence between the signals fed into ADC's P, Q and R and the signal from the coincidence box are not shown in fig. 15.

Fig. 16 shows the total time and 'shape' spectra for the ^{60}Co source as obtained from ADC R and ADC P, respectively. The time spectrum obtained is for all energies and with no 'shape' selection. The FWHM and

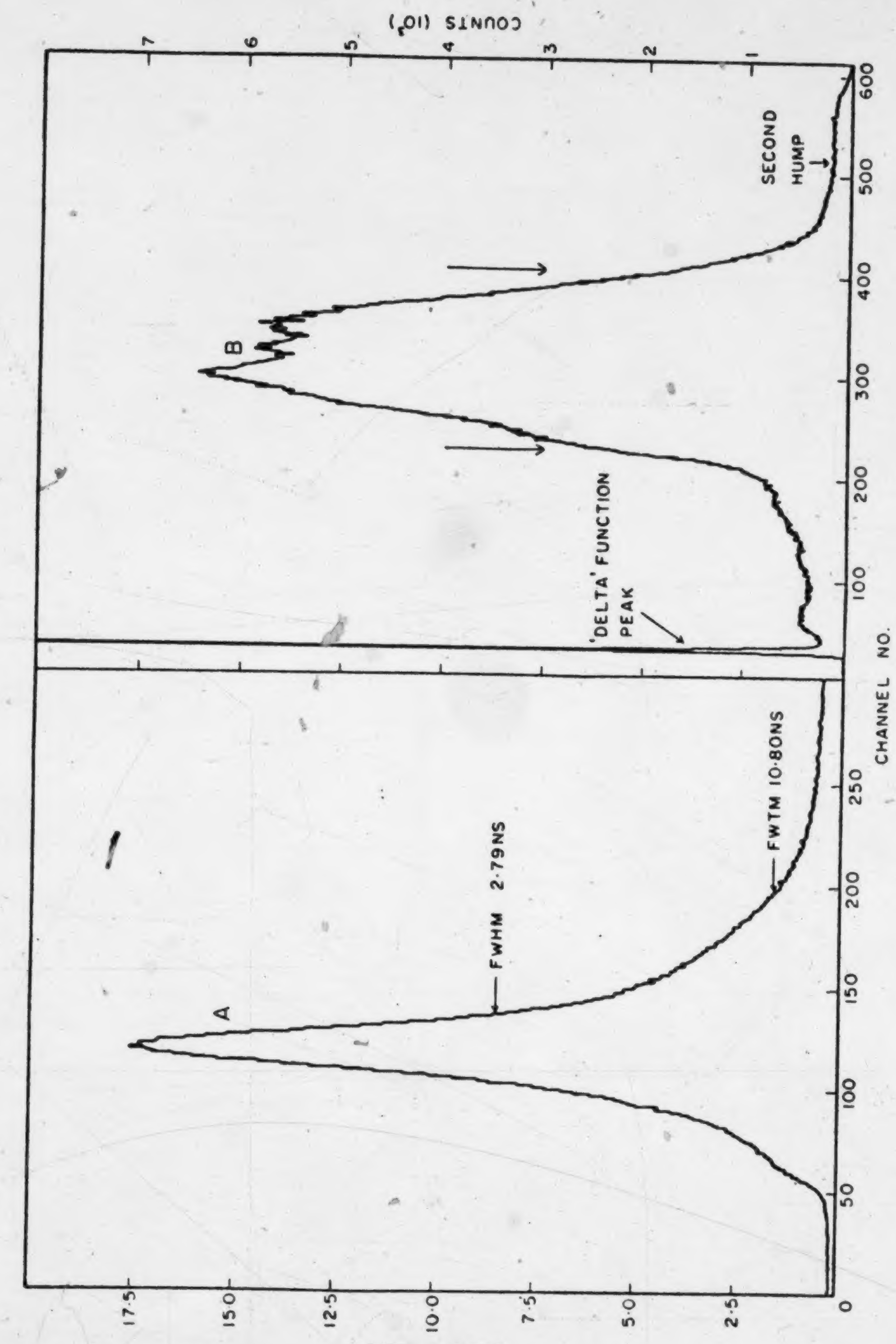

Fig. 16 a) The total time spectrum obtained from ADC R and
b) The total 'shape' spectrum obtained from ADC P for a ^{60}Co source.

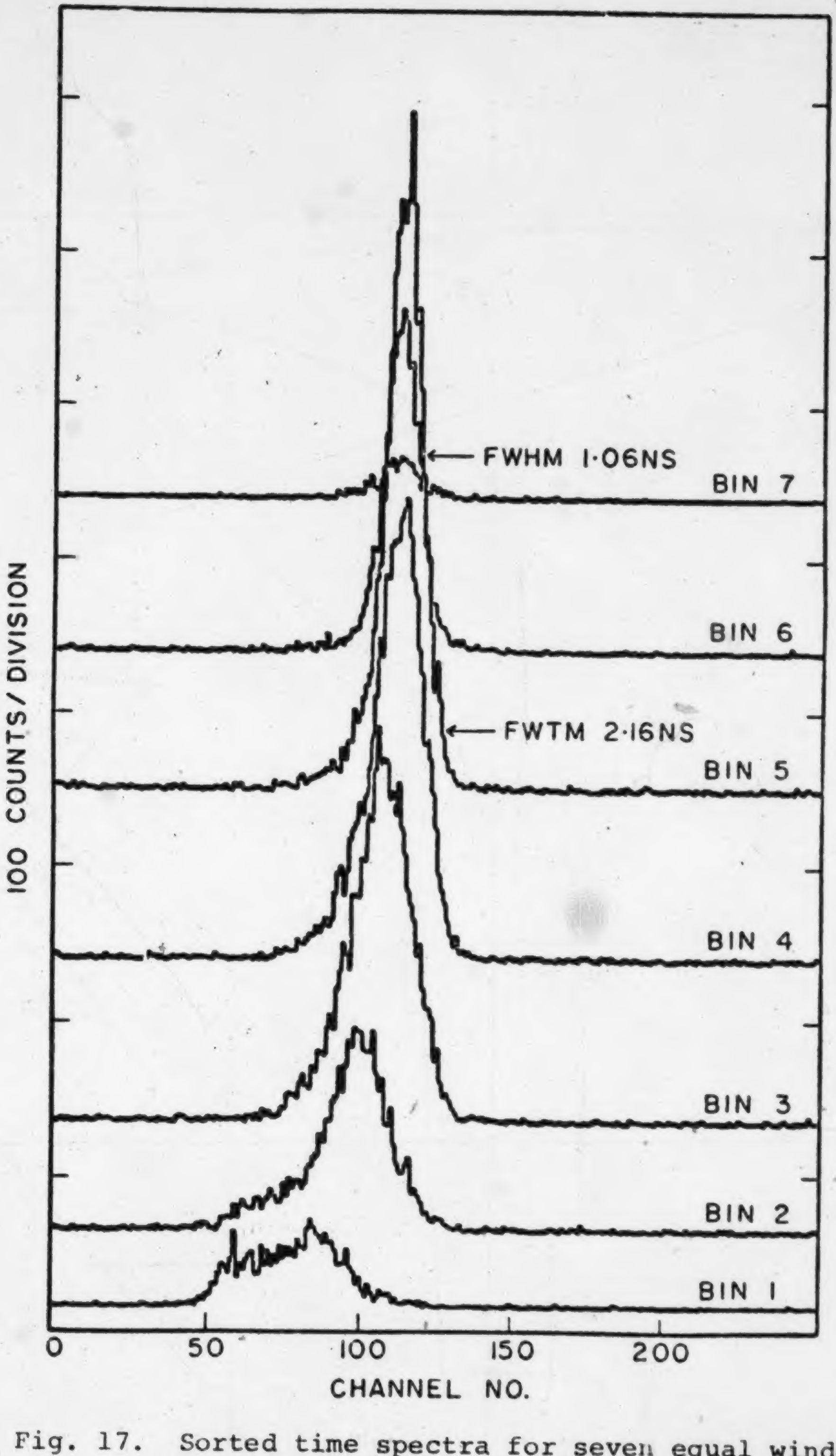

Fig. 17. Sorted time spectra for seven equal windows set on the 'shape' spectrum between the arrows as indicated in fig. 16b), the system being gated by an energy window on the 1.332 MeV γ-rays of the ^{60}Co source.

FWTM are 2.79 ns and 10.80 ns, respectively. Using a two dimensional sort routine, the total time spectrum was sorted into bins according to windows set on the energy and 'shape' spectra. For the ^{60}Co source an energy window was set on the 1.33 MeV peak and 14 equal size windows were set on the 'shape' spectrum. Fig. 17 shows seven of the sorted time spectra for the region between the arrows as indicated in fig. 16. The values of the FWHM and FWTM of the best timing bin, bin 5, are 1.06 ns and 2.16 ns, respectively.

As seen in fig. 17 there is a significant improvement in the time resolution obtained for the ^{60}Co source, especially in the FWTM. The deterioration in the early slope of the time distribution curve which is a feature of the ARC timing technique is completely eliminated by our pulse shape discrimination technique, which is seen to separate this effect mostly into bins 1, 2 and 3.

Similar results were obtained for a ^{22}Na source. Fig. 18 shows the total time and 'shape' spectra as obtained from ADC R and ADC P, respectively. In this case no 'shape' or energy selection was imposed on the system. Again the total time spectrum was sorted according to an energy window set on the 0.511 meV peak and 14 equal size windows on the 'shape' spectrum. Fig. 19 shows seven of the sorted time spectra for the

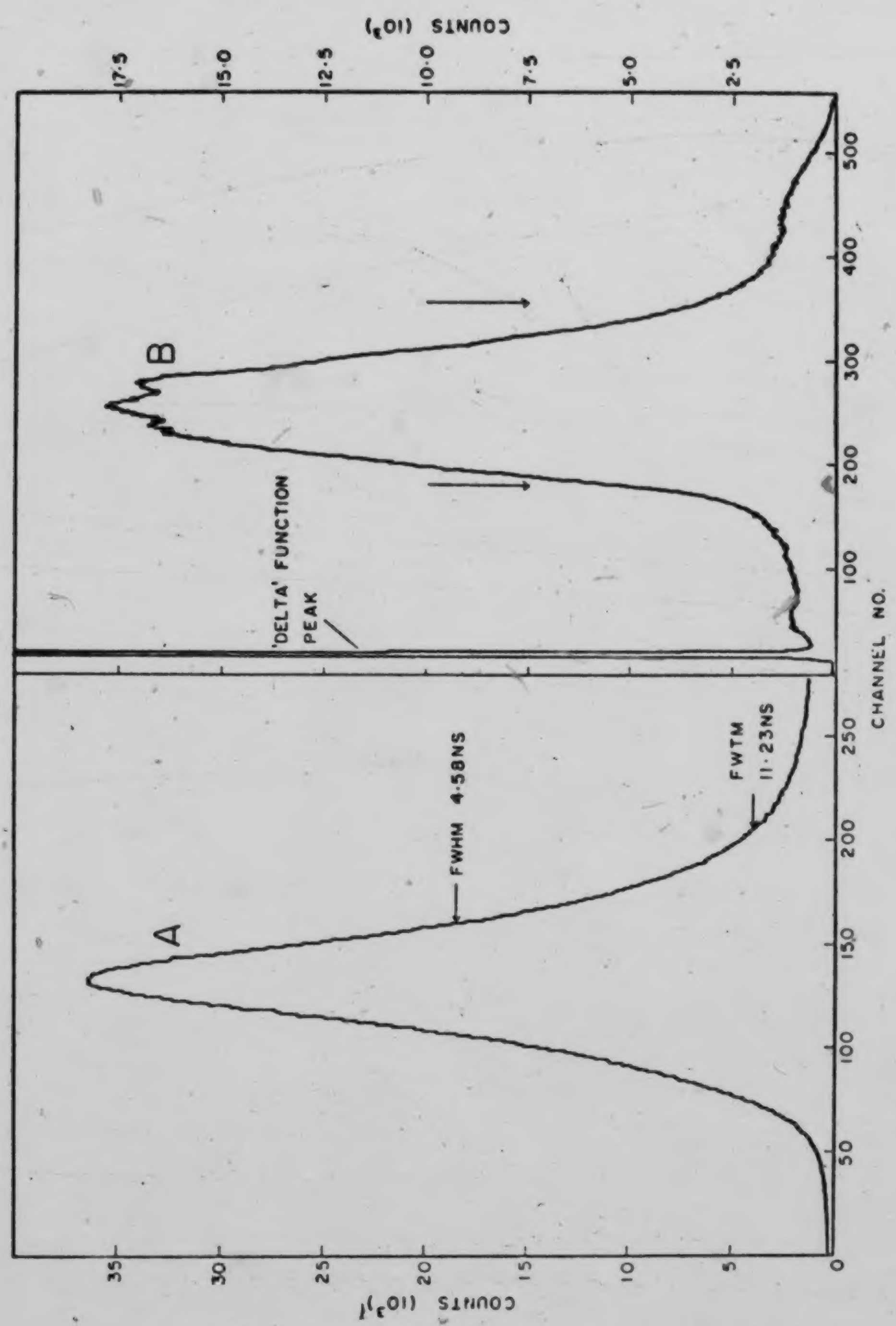

Fig. 18 a) The total time spectrum obtained from ADC R and
b) The total 'shape' spectrum obtained from ADC P for a ^{22}Na source.

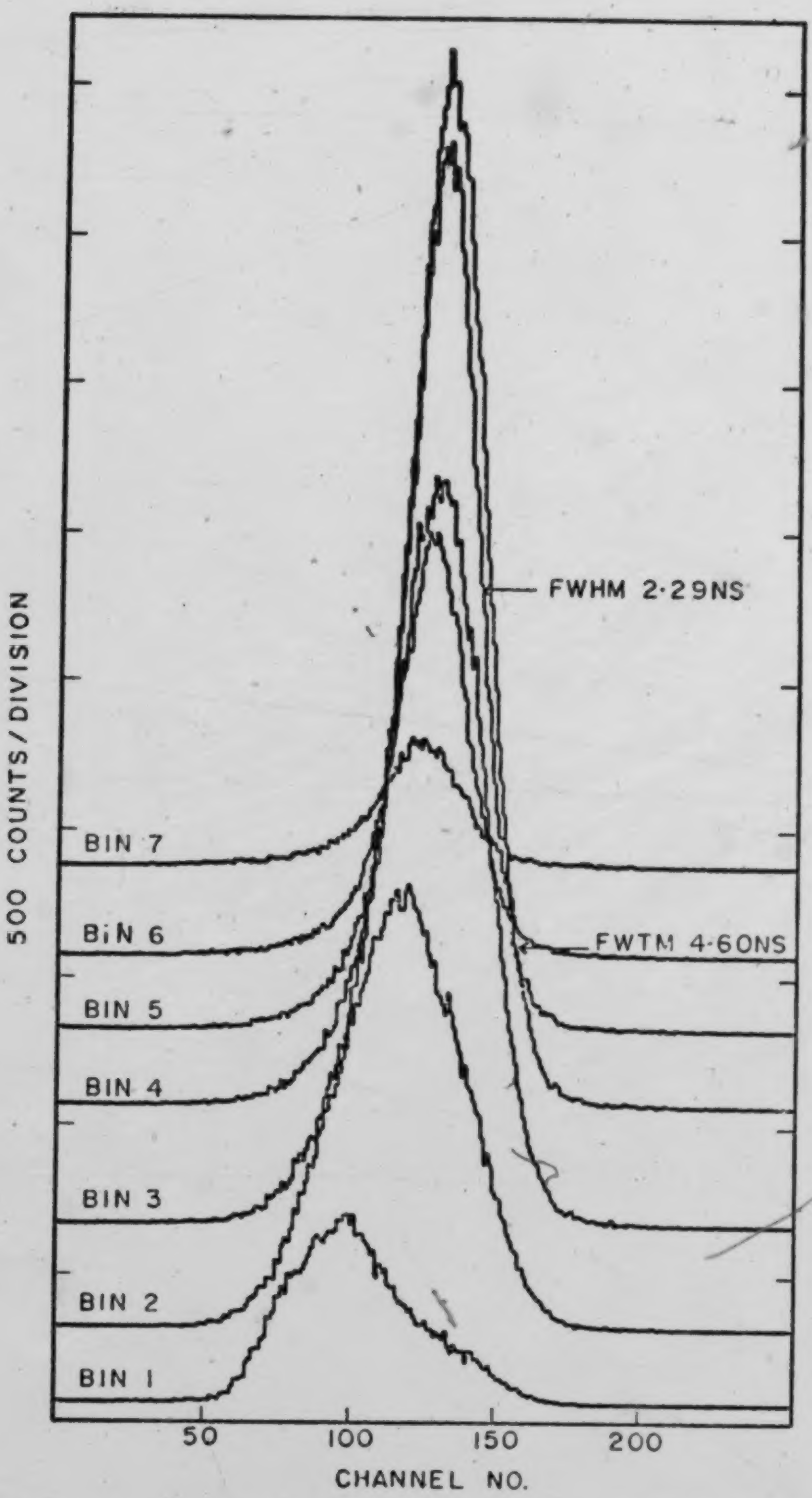

Fig. 19. Sorted time spectra for seven equal windows set on the 'shape' spectrum between the arrows as indicated in fig. 18b), the system being gated by an energy window on the 0.511 MeV annihilation γ-rays of the ^{22}Na source.

region between the arrows as indicated in fig. 18. Again there is a marked improvement in the resolution of the time spectra. Values for the FWHM and FWTM of the best timing bin, bin 5, are 2.29 ns and 4.60 ns, respectively.

A more impressive way of showing the effectiveness of this pulse shape selection technique is a plot of the FWHM and FWTM against the percentage of the total number of events as one adds to the best timing bin, the sorted bins from windows set to the left and right across the shape spectrum. Fig. 20 shows the results for the 1.33 MeV γ-ray of ^{60}Co. Similar results are shown in fig. 21 for the 0.511 MeV peak using a ^{22}Na source.

From these curves it is seen that by a selection of about 50 to 60% of the total number of events a significant improvement in the time resolution can be obtained. This is one of the greatest advantages of the technique that improved timing resolution can be obtained without a serious loss of counting efficiency.

In a recent experimental investigation (Hu 74) the technique was applied to the measurement of lifetimes in ^{35}Cl, ^{37}Cl and ^{39}K using a pulsed proton beam as a method of exciting the states of interest. The improvement in the time resolution was such that lifetimes in the 50 ps region and below were measured and

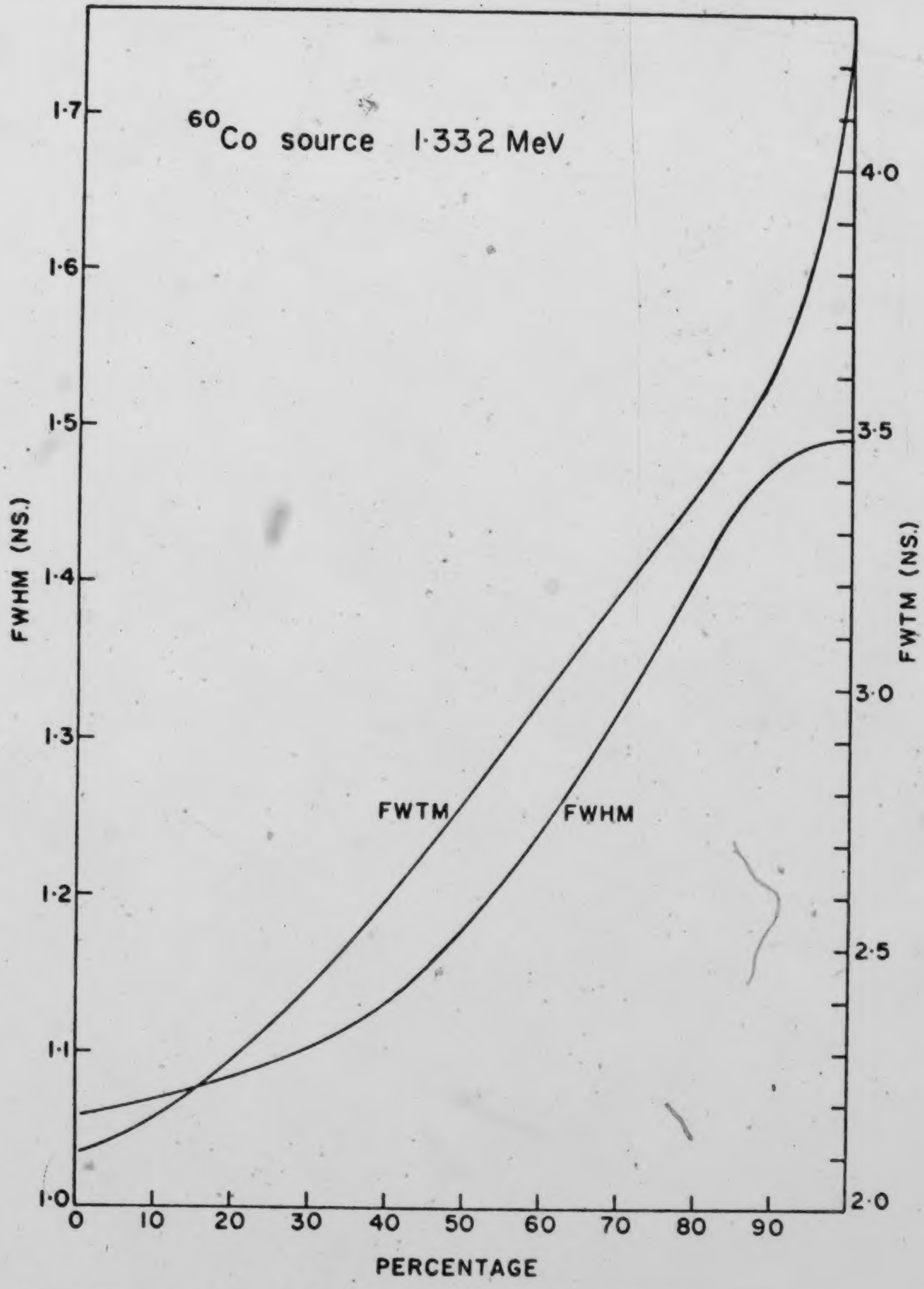

Fig. 20. A plot of the FWHM and FWTM against the percentage of the total number of events as sorted time bins are added to the best timing bin from windows set to left and right across the shape spectrum. The system was gated on the 1.332 MeV γ-rays of the ^{60}Co source.

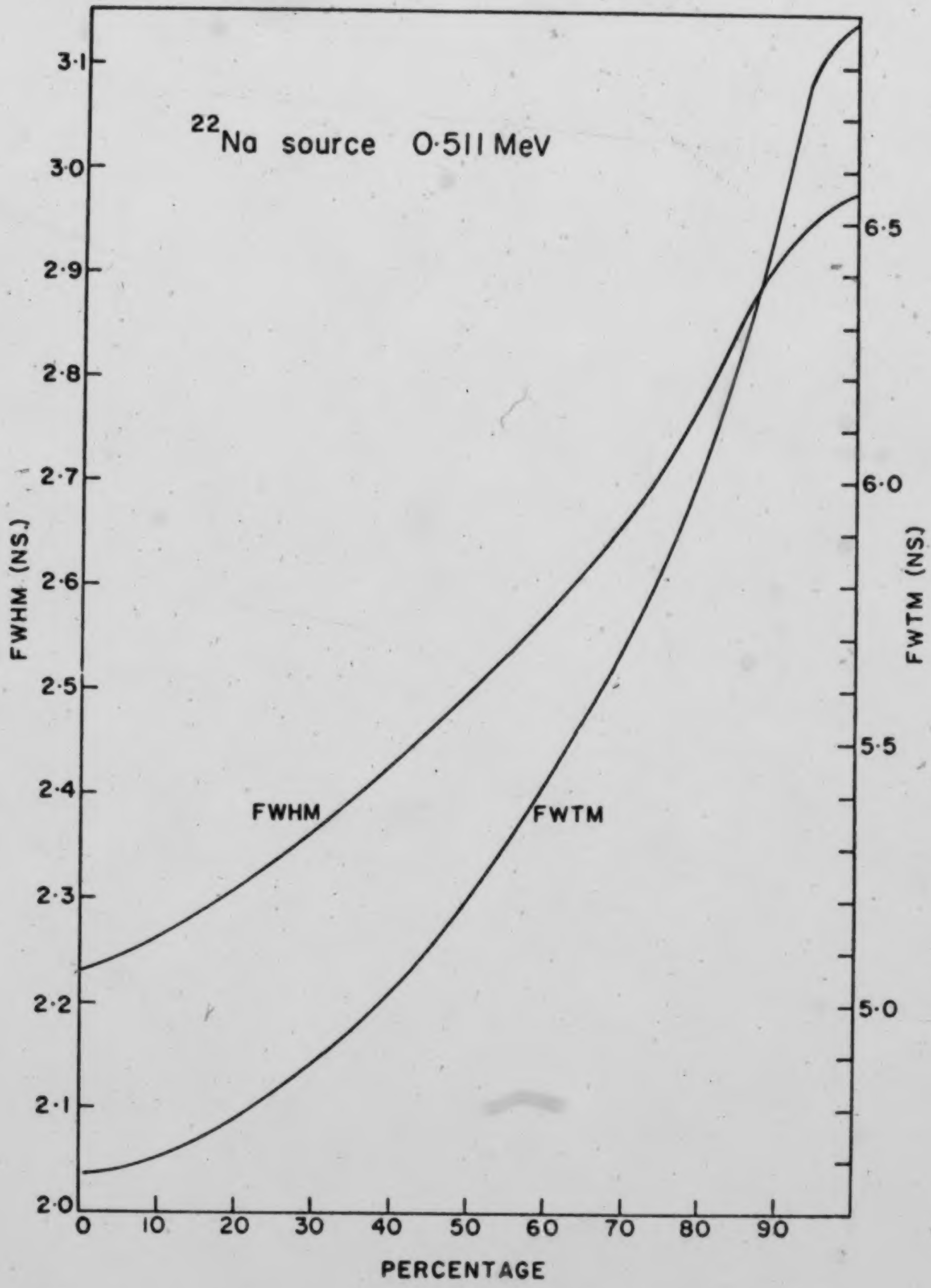

Fig. 21. A plot of the FWHM and FWTM against the percentage of the total number of events as sorted time bins are added to the best timing bin from windows set to left and right across the shape spectrum. The system was gated on the 0.511 MeV peak of a ^{22}Na source.

time resolutions of 800 ps and 650 ps FWHM were obtained in the energy range 2.20 MeV to 3.16 MeV, respectively.

In another application to be discussed in a later chapter, the technique has been used to study lifetimes in ^{45}Ti and ^{45}Sc. The data from this run has been used to show the change in FWHM of the prompt time distribution curves as a function of the inverse of the associated detected energy as plotted in fig. 22. The linearity of the curve indicates the way in which electronic noise is limiting the time resolution. Also shown in fig. 22 is some data from the ^{35}Cl, ^{37}Cl, ^{39}K experiment. It is seen that this data falls on a separate line. It is generally found that the exact position of the line is dependent upon the tuning of the electronic system and the digital window set on the 'shape' spectrum.

Two interesting electronic effects have been found to occur with the Triple Constant Fraction Discriminator. The first effect is that which leads to the 'delta' function peak in the 'shape' spectra as shown in figs. 16 and 18. This peak was found to be related to pulses from the Ge(Li) detector which have poor rise-time characteristics and secondly to those pulses of very small amplitude as illustrated in fig. 23. In these cases the pulses from the zero-crossing comparators prime the NOR gates I.E. 8A, B and C before the

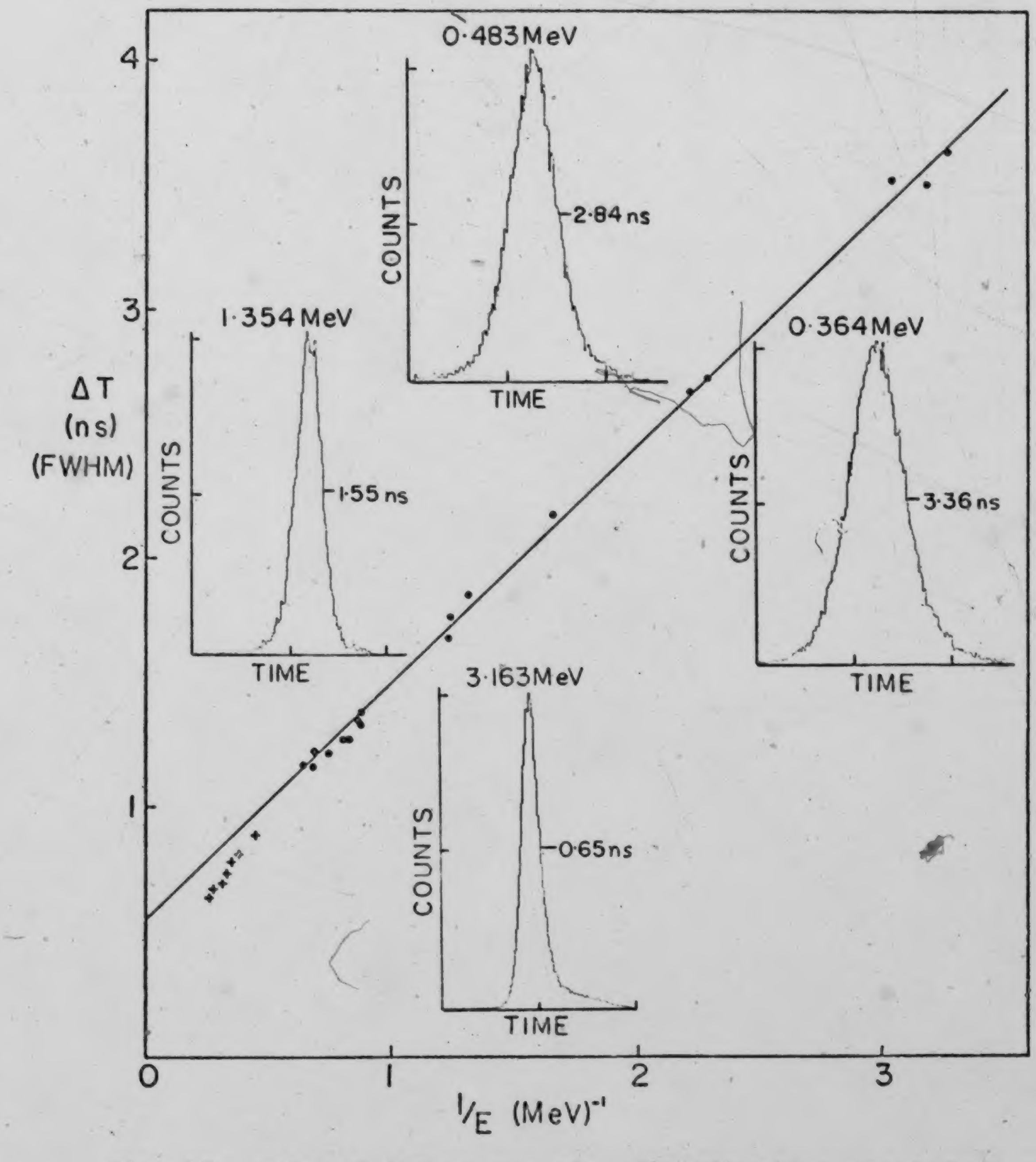

Fig. 22. FWHM of the prompt time distributions plotted as a function of the inverse of the associated detected energy. The circles represent data from the ^{45}Sc experimental run while the crosses are some data for the ^{35}Cl, ^{37}Cl, ^{39}K experimental run.

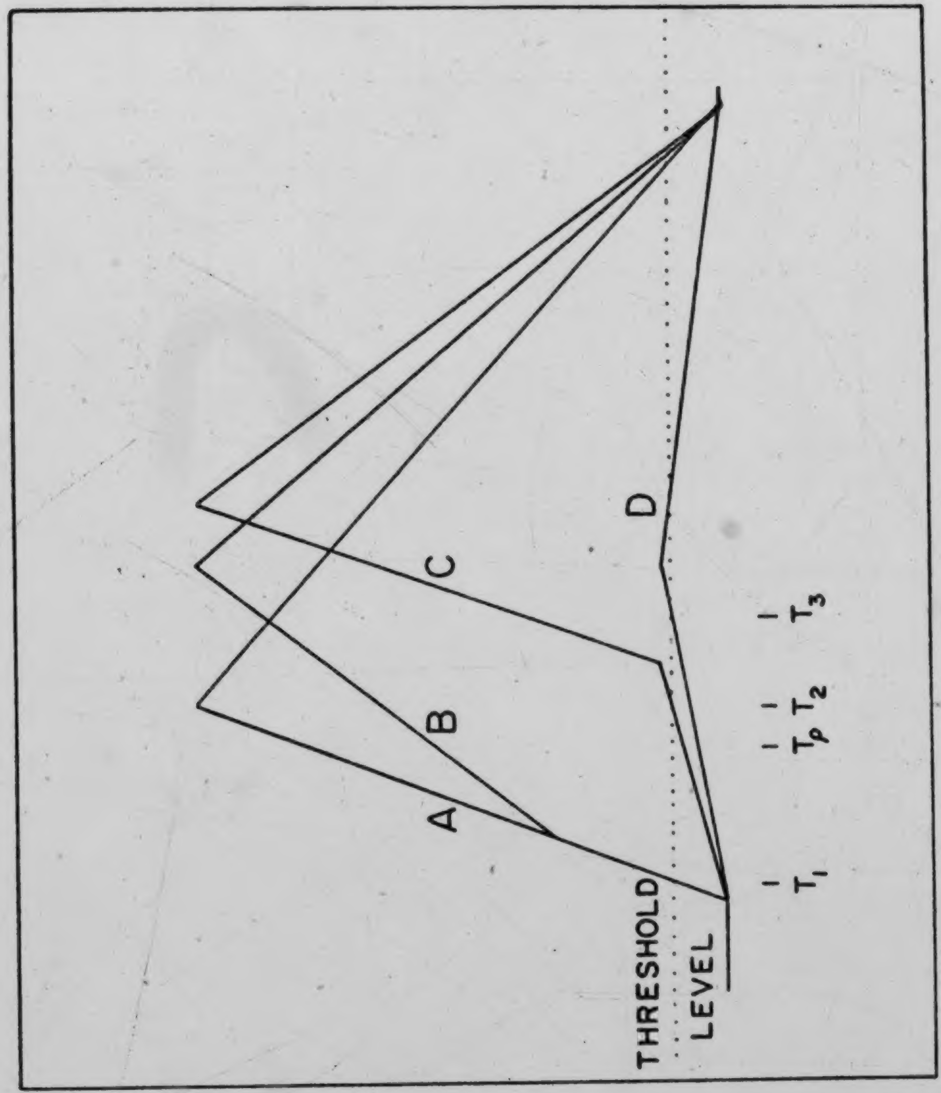

Fig. 23. Illustration of some of the ways in which pulses from the Ge(Li) detector are mistimed. Pulses of the form A and B trigger the NOR gate I.C.8 before T_ρ, the arrival time for signals from the zero-crossing comparator, and are correctly timed. Pulses of the form C and D occur later than T_ρ and are thus mistimed.

arrival of the threshold level pulse. Hence the timing is determined by the latter pulse and since this pulse is common to all three NOR gates a 'delta' function peak is obtained in the shape spectrum.

Fig. 24 shows the results of setting a window on the 'delta' function peak for the total time spectrum obtained from a ^{22}Na source. It is seen that those pulses that give rise to this effect correspond to pulses with poor timing characteristics. Hence with the pulse shape selection technique to improve the time resolution, these events are eliminated.

The second effect is seen in the small second hump in figs. 16 and 18. In general the zero-crossing comparators are continuously being triggered by noise and real events. Therefore, if the threshold level pulse arrives before the attenuated signal has attained a greater amplitude than the noise, the NOR gate will then fire on the threshold level input. As might be expected this effect is mostly restricted to the 0.1 fraction output and occurs with slow rise-time pulses which have poor timing characteristics. It can also occur with very fast rising pulses. The effect can be diminished by increasing the size of the resistance R_1, thereby slowing down the rise-time of the threshold comparator output and increasing the possibility of the attenuated signal rising above the noise level.

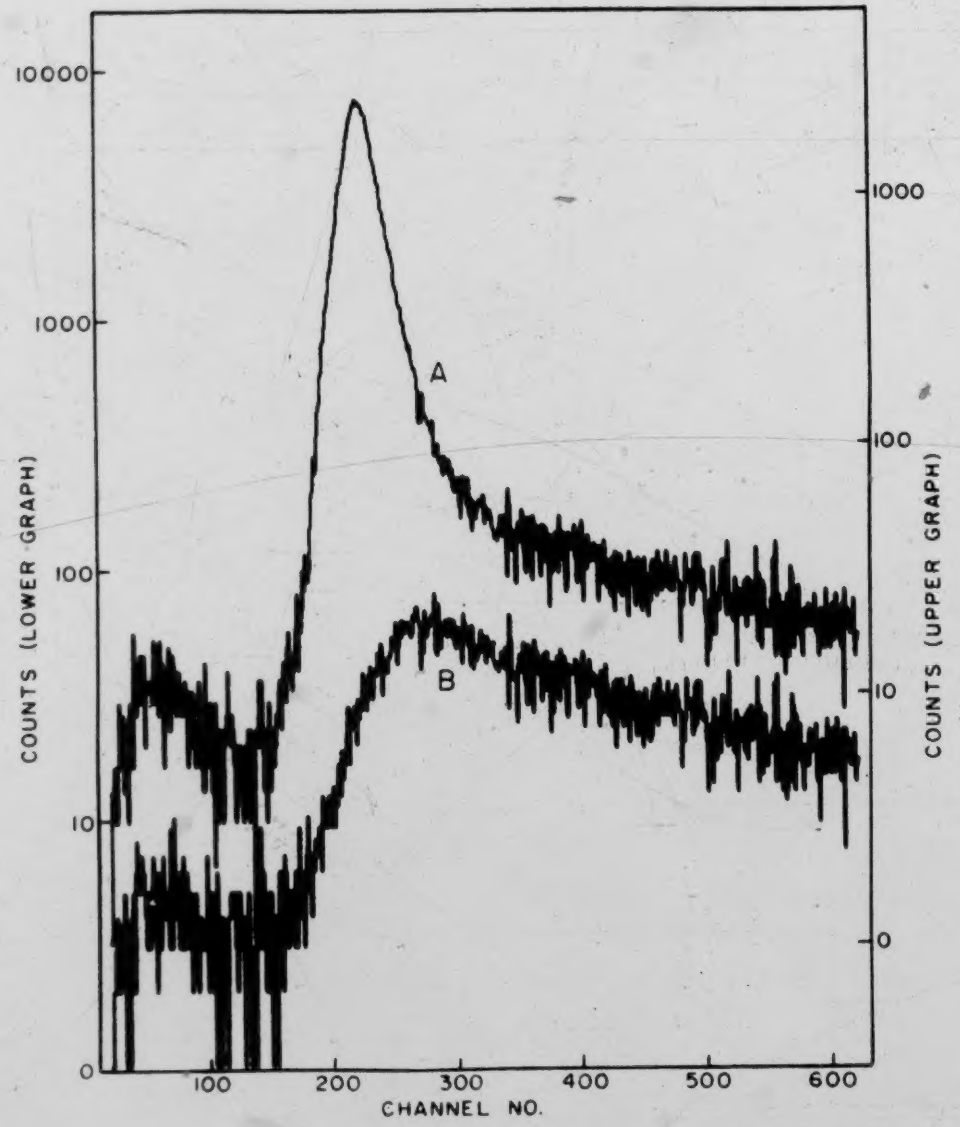

Fig. 24. a) A logarithmic plot of the total time spectrum obtained for a ^{22}Na source.

b) The same but with the system gated by a window on the 'delta' function peak in the 'shape' spectrum.

The two graphs are displaced by half a division to ensure clarity.

Fig.25A shows the effect on this second hump when the resistance R_1 is set equal to zero and when R_1 equals 870 Ω.

A final illustration of the excellent timing characteristics of the Triple Constant Fraction Discriminator is shown in fig. 25B. In this case the two outputs of the TCFD which are fed into the 'shape' TAC are set both at the same fractions. The 'delta' functions (right peaks in each case) obtained, over the range of fraction settings from 0.1 to 0.5, are the desired results of the common threshold level discriminator, external 50 Ω delay and the common fraction switch attenuator. The left hand 'delta' function in each case is the same as that discussed two paragraphs earlier.

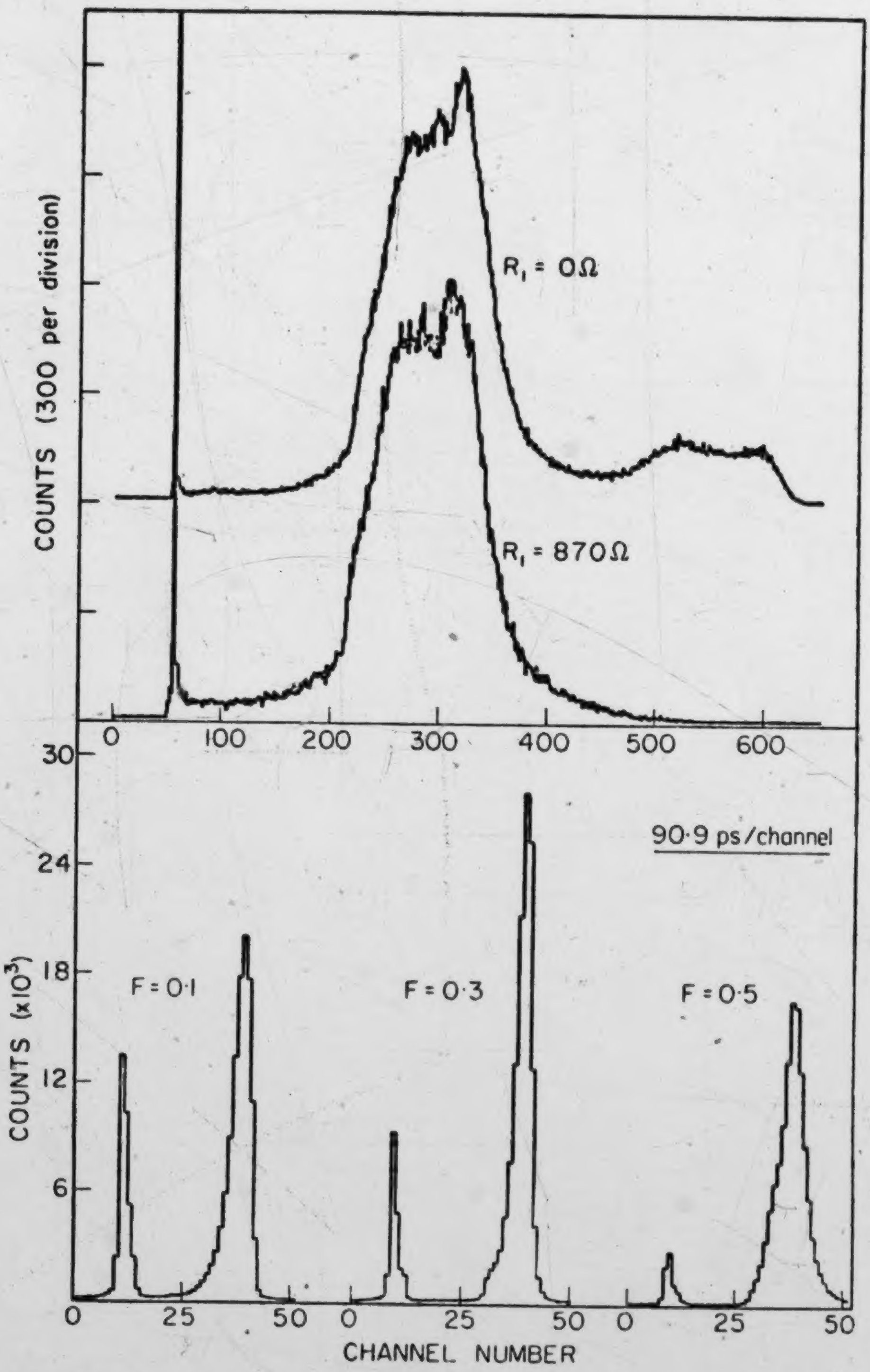

Fig. 25. a) The total 'shape' spectra when resistance $R_1 = 0\ \Omega$ and $R_1 = 870\ \Omega$.
b) Spectra obtained from the 'shape'TAC when the two outputs of the TCFD are set at the same fractions.

CHAPTER 4

THE BEAM PULSING,TARGET ROTATING SYSTEMS AND EXPERIMENTAL METHOD

4.1 The Mobley Compression Pulsed Beam System

In the University of Alberta's 7.5 Mv van de Graaff the pulsed beam is obtained by using both pre-acceleration pulsing and post-acceleration compression as shown schematically in fig. 26. An outline of the system will be given here due to its importance in the experimental technique. However, a more detailed description can be obtained in the Ph.D. thesis of Davies (Da 66).

An ion source located within the high voltage terminal is used to ionise the required gas by a 125 MHz source oscillator and a d.c. ion beam is extracted by means of a probe electric field. An Einzel Lens and Terminal Analysis Magnet are used to focus the beam which can then be pulsed by two sets of R.F. deflection plates set at right angles to each other and driven 90° out of phase by a 1 MHz oscillator. These R.F. deflection plates sweep the beam in an elliptical path over a 1/16 inch aperture, producing a beam pulse of 10 ns width. This beam pulse is then accelerated and further

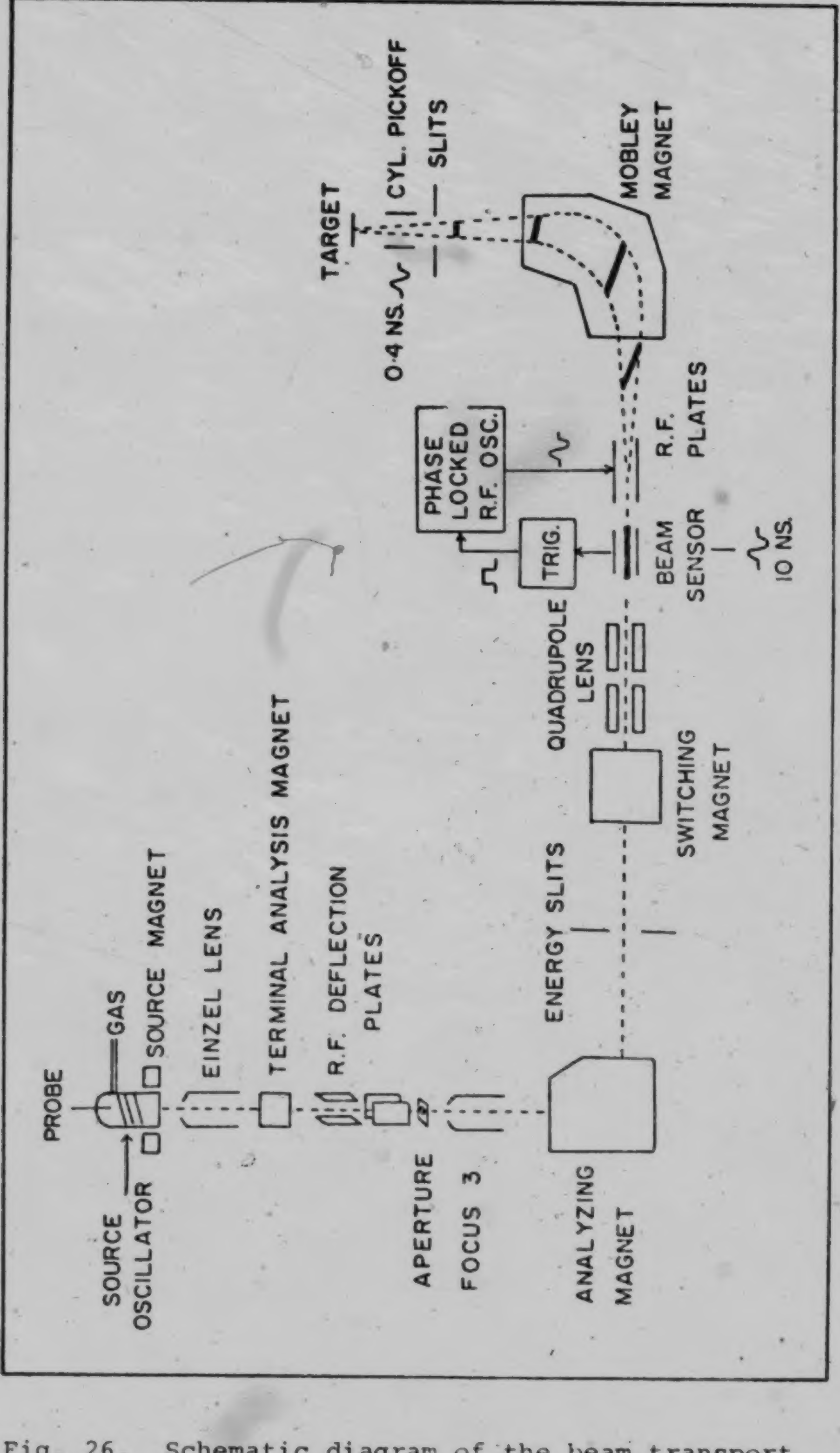
SOURCE OSCILLATOR
PROBE
GAS
SOURCE MAGNET
EINZEL LENS
TERMINAL ANALYSIS MAGNET
R.F. DEFLECTION PLATES
APERTURE
FOCUS 3
ANALYZING MAGNET
ENERGY SLITS
SWITCHING MAGNET
QUADRUPOLE LENS
BEAM SENSOR
10 NS.
TRIG.
PHASE LOCKED R.F. OSC.
R.F. PLATES
MOBLEY MAGNET
SLITS
CYL. PICKOFF
TARGET
0·4 NS.

Fig. 26. Schematic diagram of the beam transport and Mobley Compression pulsed beam system.

focused by Focus 3 and analysed by a 90° magnet to select the desired energy. The beam then passes through a pair of energy stabilising slits 57 inches away from the analysing magnet. These slits feed the corona current central system which stabilises the energy.

A magnetic quadrupole lens then focuses the beam into the first stage of the Mobley compression system. This stage of the system is a pair of deflection plates fed with a phase locked R.F. oscillator of 10 MHz. Phase information is supplied to the oscillator from a cylindrical pick-off in the beam tube just before the R.F. plates.

The second stage is a 90°, 75 inch magnet whose focal points are at the target and the R.F. plates. The beam is swept by the R.F. field such that the particles leaving the deflector plates first, take the longest paths through the magnet while those leaving last take the shortest paths. If the phase and amplitude of the deflector are properly adjusted, all particles will arrive at the target at almost the same time. A final beam pulse with width of 0.4 ns can be obtained at the target.

4.2 The Rotating Target System

As will be seen later, the centroids of the time distribution peaks vary with the energy of the detected γ-ray. This may not pose a problem if the so-called prompt time distribution centroid curve is defined accurately around the energy region of interest by a sufficient number of centroid points obtained from γ-rays whose lifetimes are much shorter than the time resolution of the system (less than, say, 1 ps). However, in most cases the isotope under study does not have a sufficient number of 'prompt' deexcitation γ-rays in the required energy region. It is essential to the accuracy of the results that this problem be overcome. A simple solution is the use of two targets, the one producing the energy level whose lifetime is to be measured and the second, supplementary 'prompt' reference γ-rays.

In most previous delayed coincidence experiments the prompt and delayed time distribution curves were obtained in alternate experimental runs. The errors due to electronic drifts and shifts were minimised by frequent alternation of the measurements with the two sources. This method is obviously cumbersome and thus it is very desirable to obtain the prompt and delayed time distributions simultaneously in order to avoid errors due to electronic drifts and shifts and changes in pulsed beam conditions from one run to the next.

Another important point to be discussed in Chapter 5 is the observed centroid shift for a given energy between the time peaks obtained from events in which the full energy of the 'prompt' γ-rays is deposited in the Ge(Li) detector, and those obtained from Compton events in which part of the energy of the incident 'prompt' γ-rays is deposited. Thus the peak to background ratio is very important in the determination of the true centroid of the background subtracted time distributions and the associated error in this result. Background contributions can be reduced by the use of self-supporting thin targets. The possibility of target fracture by the incident beam is alleviated by the rotation of the target, effectively increasing the target area to the incident beam.

With these points in mind it became necessary to design a twin target rotating system. Two photographs of the rotating target system taken from different angles are shown in figs. 27 and 28. Rotation in the vacuum target chamber is provided by a magnetic coupling capable of 550 r.p.m. which is driven by a 1/8 h.p. variable speed motor. A system of geared pulleys then increases the maximum r.p.m. of the target assembly to 7000, the final drive being accomplished by the friction of an O-ring pulley. The target rotator fits into the inner race of a 5.08 cm bearing which can be

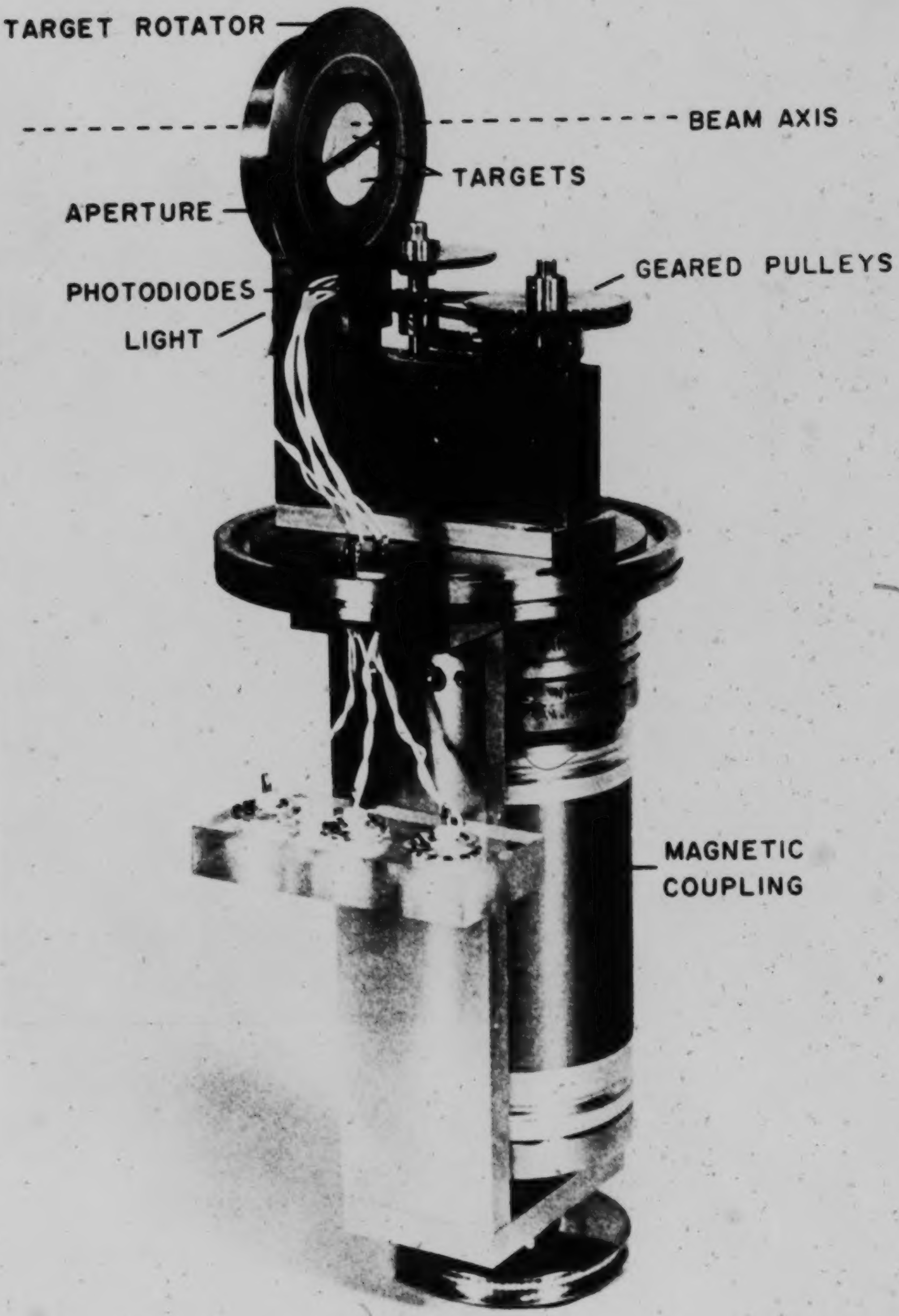
TARGET ROTATOR
BEAM AXIS
TARGETS
APERTURE
GEARED PULLEYS
PHOTODIODES
LIGHT
MAGNETIC COUPLING

Fig.27. A photograph of the Rotating Target System.

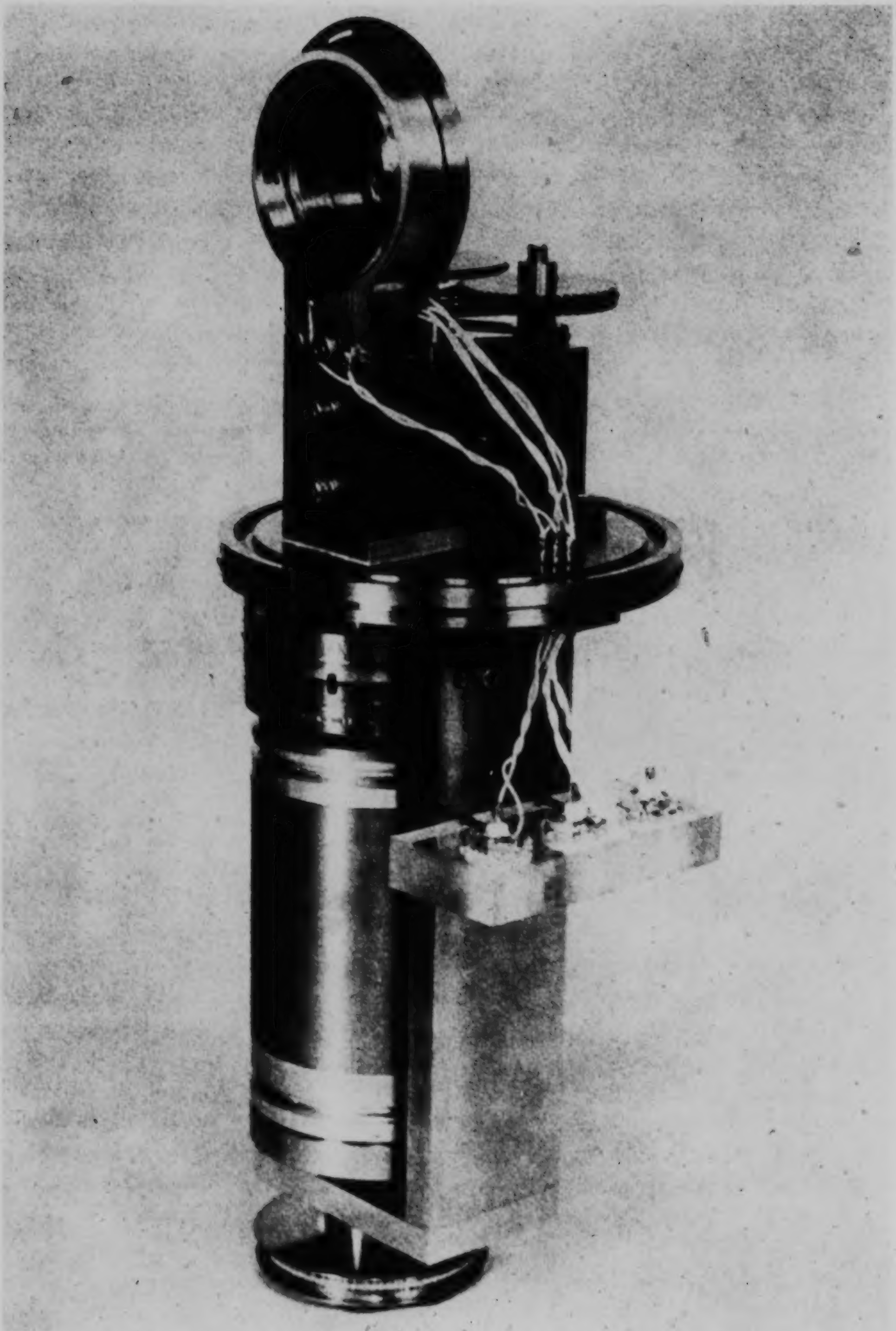

Fig.28. A photograph of the Rotating Target System.

screwed in or out of the main assembly mount to provide the necessary and optimum friction for maximum rotation. It was found that best performance was obtained when the bearings were lubricated with a small amount of Molybdenum Disulphide powder. The target rotator, bearings and bearing mount were made of the same material, steel, to overcome difficulties due to heat expansion which might cause the inner and outer races of the bearings to seize. The system is enclosed in a target chamber which has a 6.35 cm diameter window of 0.12 mm steel so designed that targets can be viewed from 50° to 130° with respect to the beam axis.

4.3 Target Discriminator

When using two targets, each rotating in and out of the beam, it is useful to store the information from each target separately in different regions of the online computer. A separation of the energy spectra from each target means that the peak to background ratio is not adversely affected by the presence of the second target. If the background should also contain the Compton tail of a γ-ray transition from a state whose lifetime is several nanoseconds then the separation of the energy spectra eliminates the problematic effects of this lifetime on the time distribution peaks corresponding to energy windows set on the other spectrum.

To produce this separation of information from each target two slot apertures are machined in the target rotator diametrically opposite at different radii. The targets are made semicircular and screw onto the target rotator. In conjunction with these slots, a light source and two photodiodes are arranged such that as the targets rotate light can pass through either of the slots alternately and be detected by the photodiodes. The beam is collimated by a system of movable slits upstream from the target and is only incident on one target at a time since the axis of rotation of the targets is 0.63 cm off the beam axis.

The outputs from the two photodiodes pass through a kovar connection from the target vacuum chamber and are applied to the so-called Target Discriminator through high input impedance F.E.T. circuits since the photodiodes have a high output impedance. Fig. 29 shows the electronic circuit of the Target Discriminator and fig. 30 a photograph of the actual NIM module. The fundamentals of the Target Discriminator are illustrated in fig. 31. Basically the signals from the photodiodes are amplified, inverted and sent into a flip-flop circuit. The outputs from this and the original inverted pulses are then fed into two separate AND gates as illustrated in fig. 31. The final outputs are high,

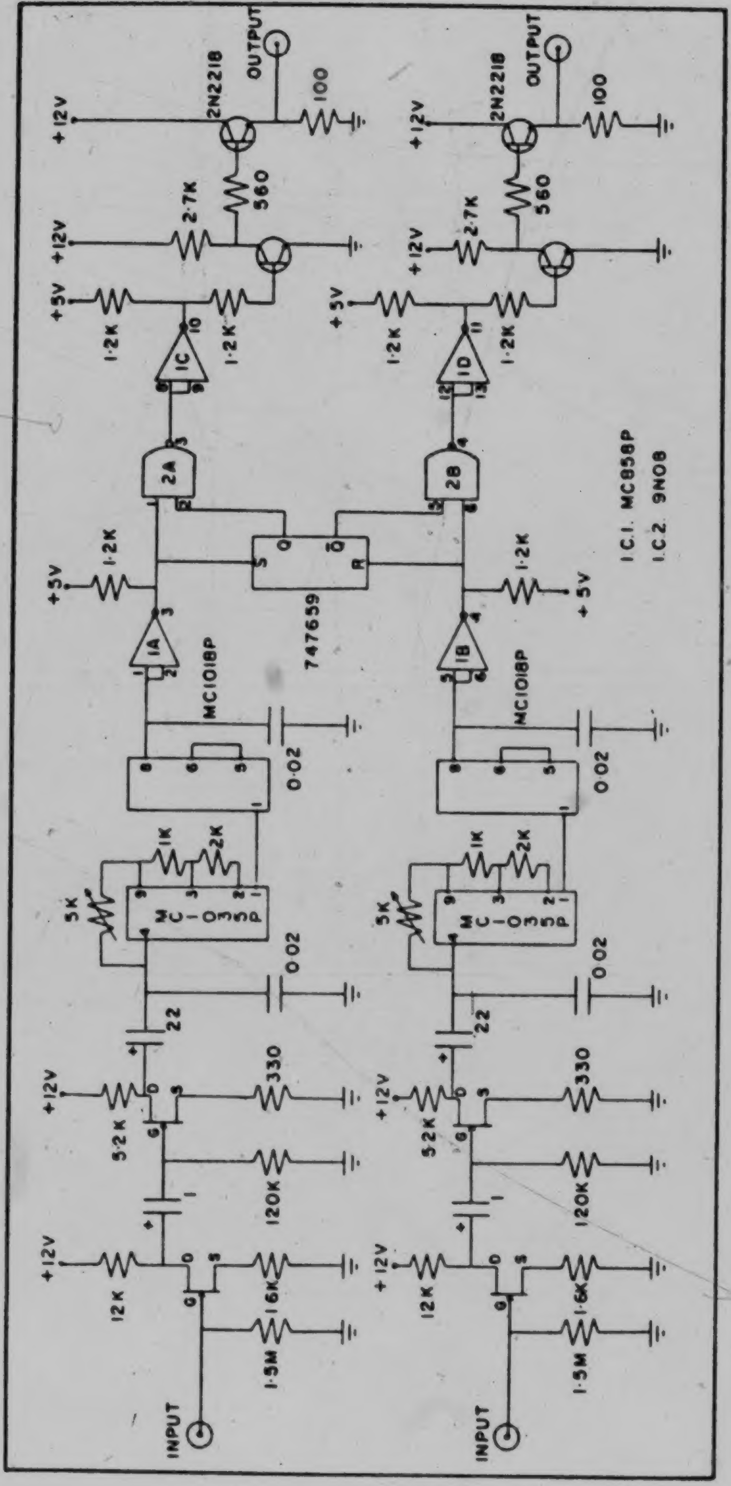
INPUT
1·5M
12K
+12V
1·6K
120K
5·2K
330
22
0·02
5K
MC-0335P
1K
2K
0·02
MC1018P
1A
1B
+5V
1·2K
747659
S
Q
Q̄
R
2A
2B
1C
1D
1·2K
2·7K
560
2N2218
100
OUTPUT
I.C.1. MC858P
I.C.2. 9N08

Fig. 29. Circuit diagram of the Target Discriminator.

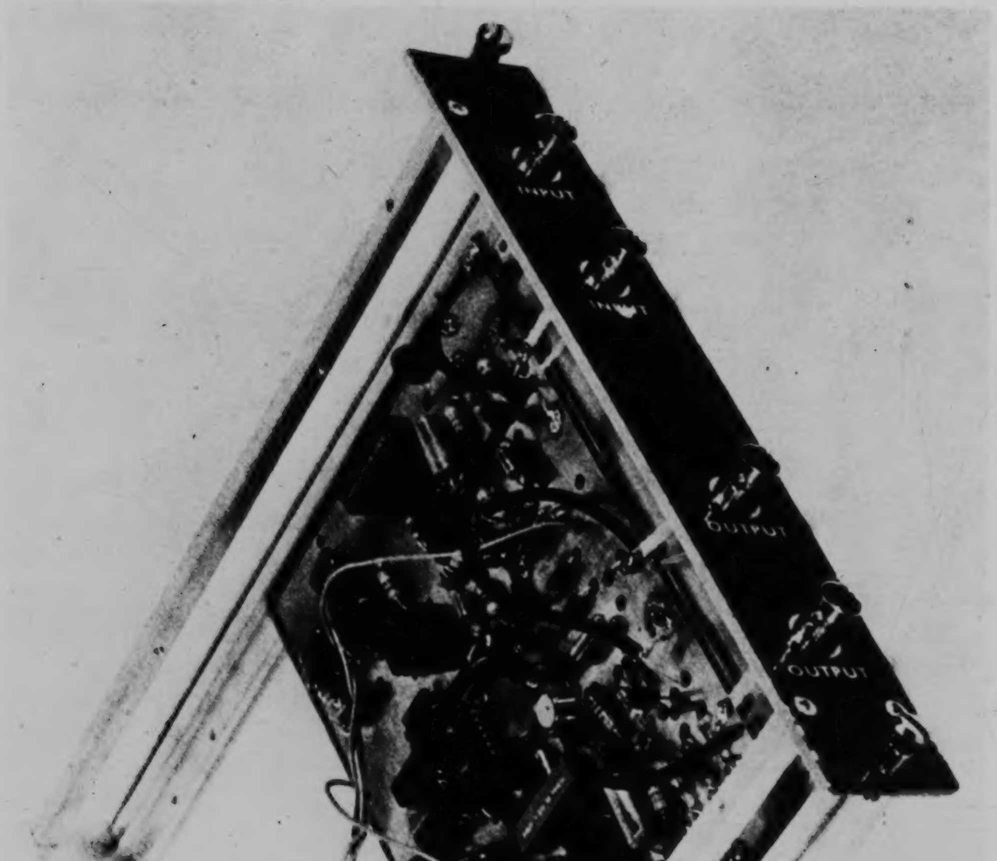
INPUT
OUTPUT
OUTPUT

Fig.30. A photograph of the Target Discriminator Module.

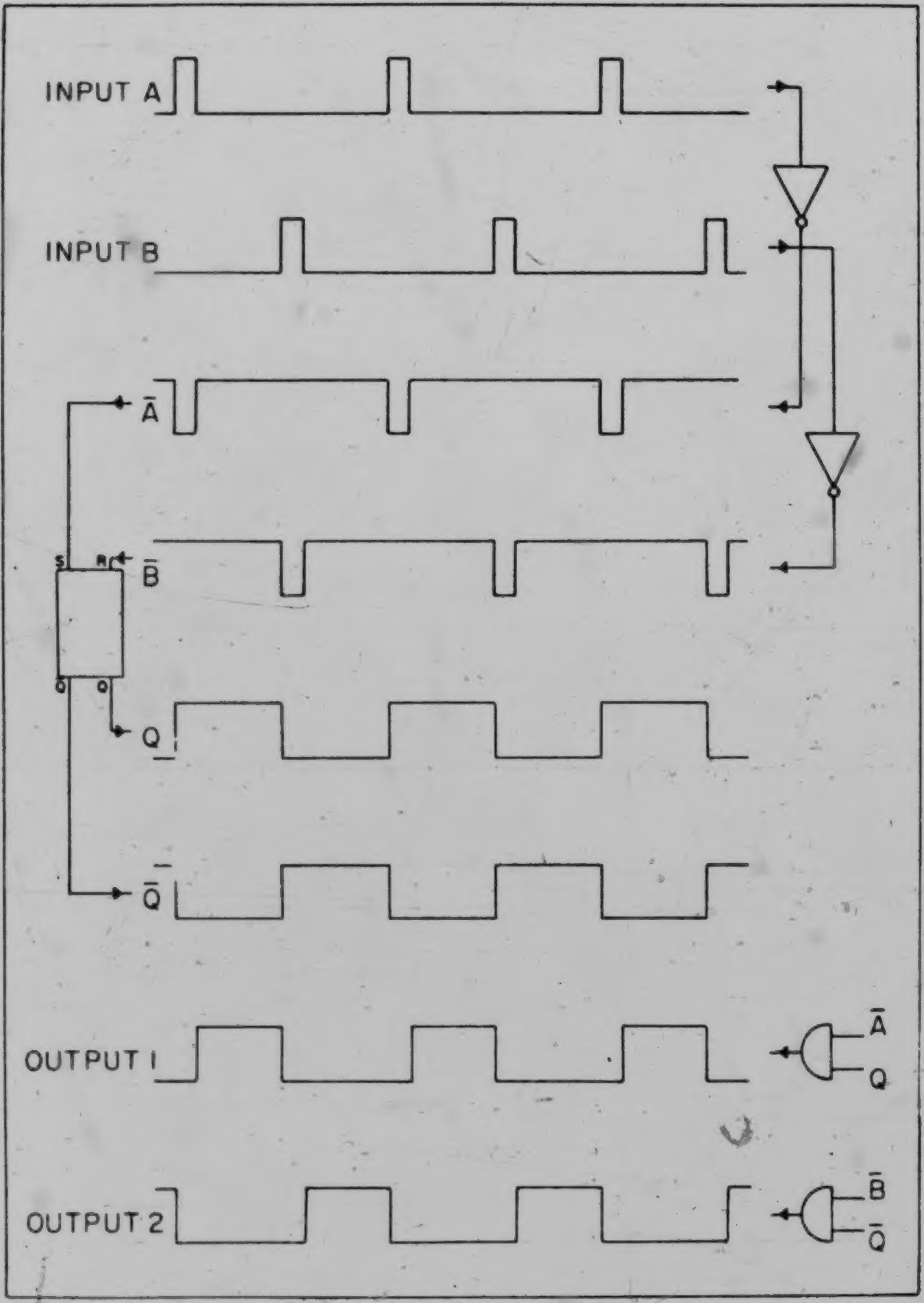
INPUT A
INPUT B
$\bar{A}$
$\bar{B}$
S
R
Q
$\bar{Q}$
Q
$\bar{Q}$
OUTPUT 1
$\bar{A}$
Q
OUTPUT 2
$\bar{B}$
$\bar{Q}$

Fig. 31. A schematic diagram of the pulse shape logic in the Target Discriminator circuit.

amplitude 5 V, or low when the targets are in or out of the beam, respectively. This high output has an amplitude sufficient to trigger a Universal Coincidence box and is thus compatible with other logic signals used for coincidence purposes. It is noticed that both signals are low when the beam is switching targets and thus a complete separation of the energy spectra from each target can be achieved.

4.4 Experimental Electronics and Method

Fig. 32 shows the block diagram of the experimental electronic arrangement. The deexcitation γ-rays, detected using a 23 c.c. coaxial Ge(Li) detector, produce two signals, one of which is sent through a linear amplifier and into ADC P consisting of two regions, each 2048 channels. The other output is fed into the Triple Constant Fraction Discriminator, TCFD, the output of 0.3 fraction being used to 'START' the time TAC. The 'STOP' signal is provided by a capacitive beam pick-off. The output of the time TAC is then fed into ADC R, size 1024 channels.

The other two outputs of the TCFD at fractions 0.1 and 0.5, respectively, 'START' and 'STOP' the 'shape' TAC to produce a 'shape' spectrum in ADC Q, size 1024 channels. The on-line computer, a Honeywell 516, requires a coincidence signal for all three ADC's

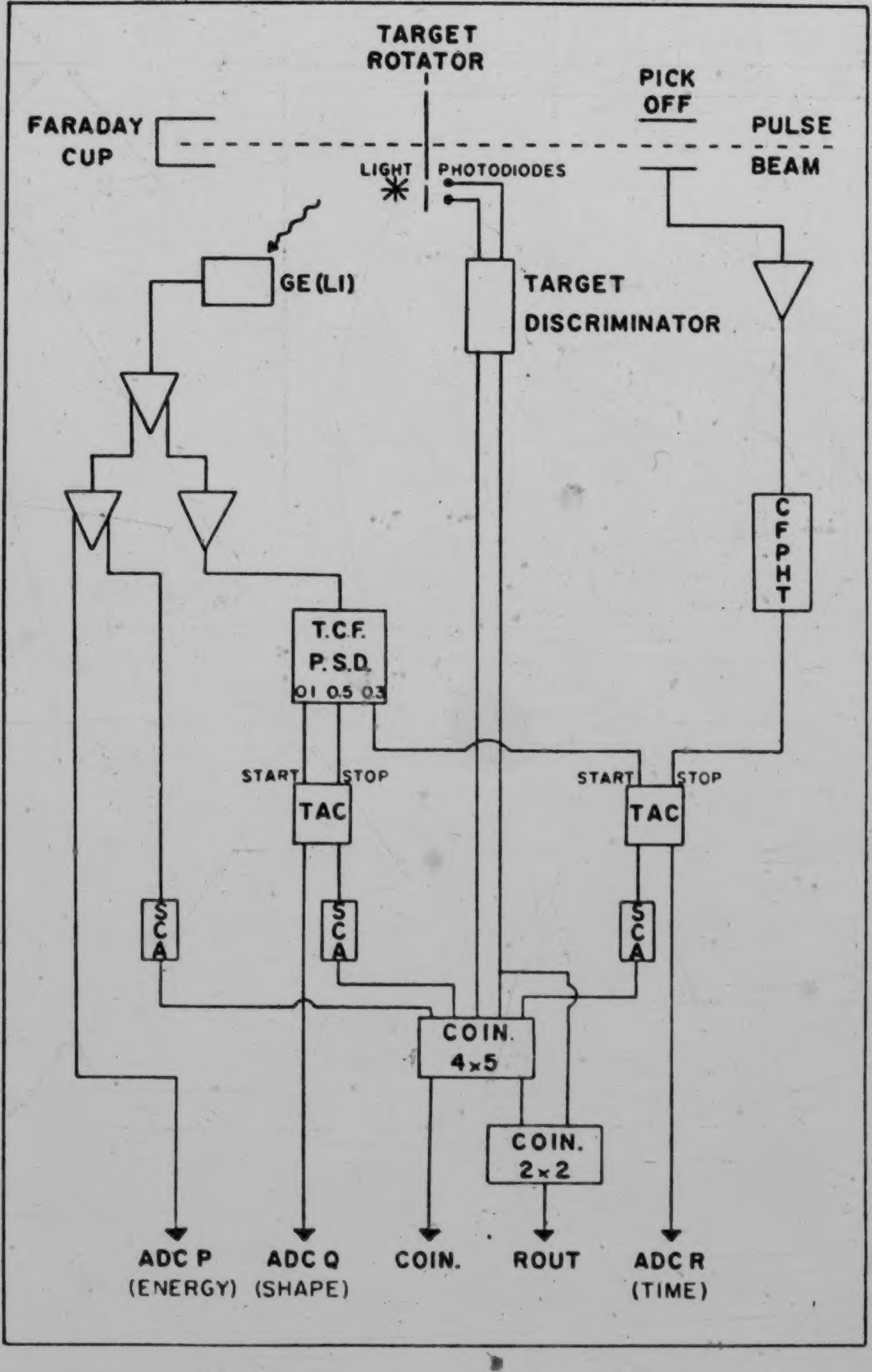
TARGET
ROTATOR
PICK
OFF
FARADAY
CUP
PULSE
BEAM
LIGHT
PHOTODIODES
GE(LI)
TARGET
DISCRIMINATOR
CFPHT
T.C.F.
P.S.D.
0.1 0.5 0.3
START
STOP
TAC
START
STOP
TAC
SCA
SCA
SCA
COIN.
4×5
COIN.
2×2
ADC P
(ENERGY)
ADC Q
(SHAPE)
COIN.
ROUT
ADC R
(TIME)

Fig. 32. Block diagram of the experimental electronic arrangement.

which is provided by the three timing SCA's and a Universal Coincidence box. The coincidence box is set to require 4 out of 5 coincidence signals since the Target Discriminator provides alternate signals when the beam is on one target or the other. The signal from the second coincidence box is used to rout ADC P so that the energy spectrum from each target is stored in the two separate regions of ADC P. Fig.31 does not show the several Delay Amplifiers and Delay boxes necessary to establish a coincidence between the final coincidence signal and those signals fed into ADC P, Q and R.

The acquisition of data into the various regions of memory of the on-line Honeywell 516 computer is accomplished by means of a two dimensional sort routine written by Dr. D.A. Hutcheon. Using this routine the total time spectrum of ADC R is sorted internally by the computer according to digital windows set on the energy spectra of ADC P and on that region of ADC Q, the 'shape' spectrum, which produces improved time resolution. A maximum of 32 digital window combinations can be set on the spectra of ADC P and Q, and the final sorted time spectra corresponding to each window are stored in region X of the computer, a maximum size of 16384 channels.

During an experimental run windows are set on the full energy γ-ray peaks to be investigated, including those peaks to act as 'prompt' references, and on the backgrounds above and below these peaks. The centroids of the resulting sorted time distribution curves were obtained by setting 'begin' and 'end' channels at approximately 5% and 7½% of the peak height of each curve. An average of these two results was then calculated with its associated error. This average should be a more accurate value of the centroid of the curve because setting the 'begin' and 'end' channels is only approximate since the statistics are poor in the outer less well-defined parts of the curves.

The centroids obtained corresponding to energy windows set on the background were then plotted as illustrated by crosses in fig. 33. A background time centroid curve is drawn through these points and the values of the background centroids at the energies of the γ-ray peaks can be interpolated so that background subtractions can be executed. The resulting centroids are then plotted and the 'prompt' reference centroids are fitted with the function described below.

In most CFPHT units, zero-crossing detection is based upon the use of a tunnel diode which does not switch instantaneously but requires an accumulation of a certain amount of charge to activate the diode. This charge is represented by the area under the curve as illustrated in fig. 34, and leads to the timing

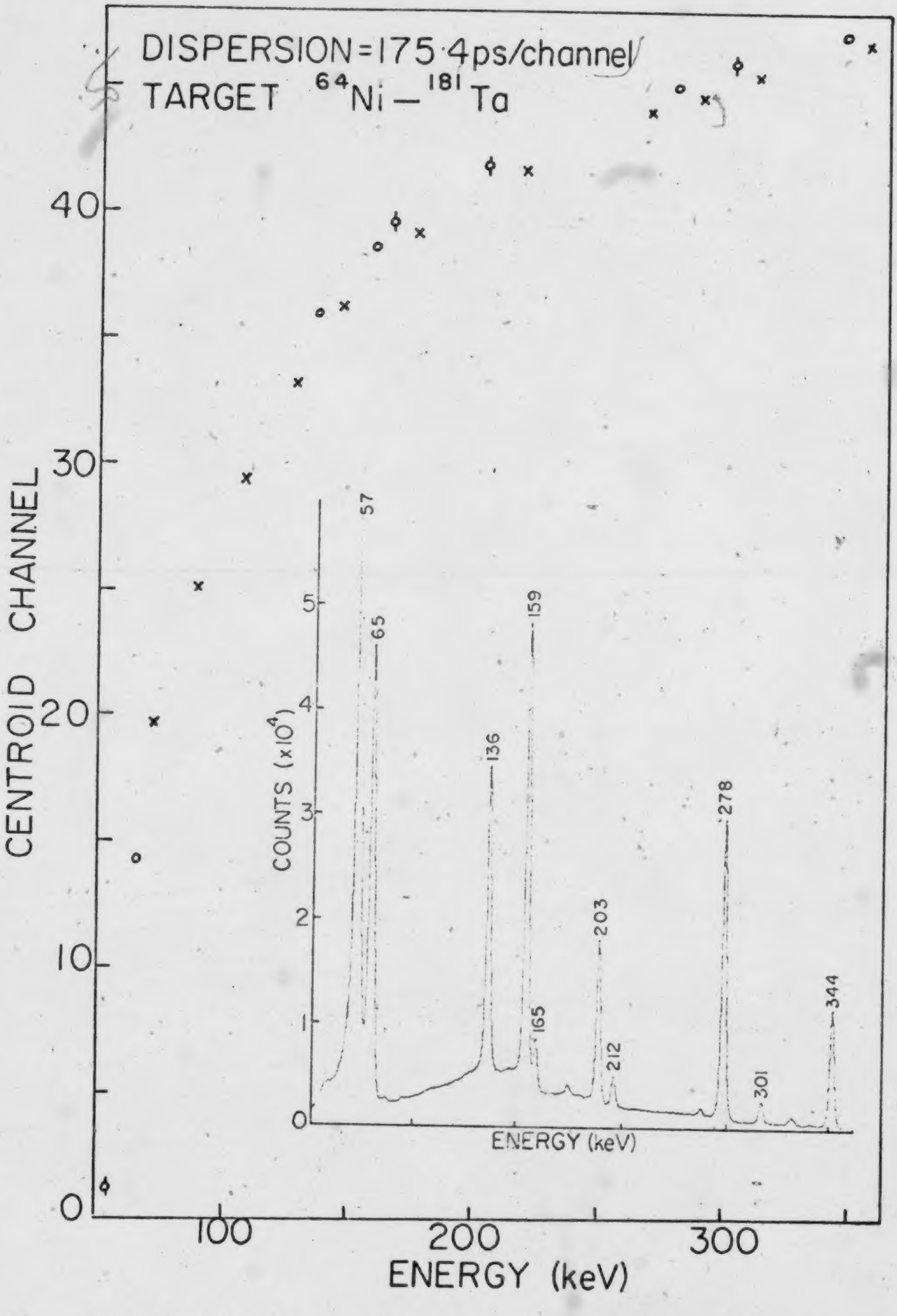

Fig. 33. Centroids of the time distributions vs. energy for the ^{64}Ni-^{181}Ta experimental run. Crosses represent centroids from energy windows set on the Compton continuum and circles the centroids for the time distributions of 'prompt' full energy peaks.

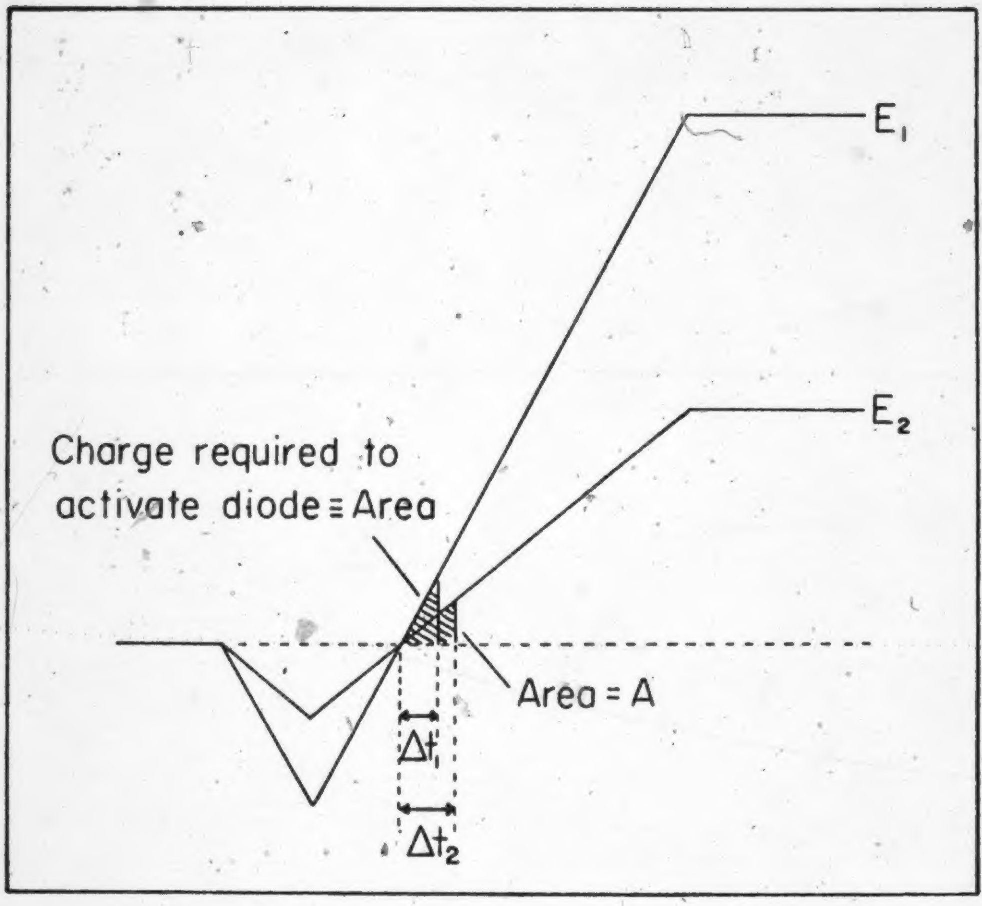
E$_1$
E$_2$
Charge required to activate diode ≡ Area
Area = A
Δt_1
Δt_2

Fig. 34. Illustration of the timing error, Δt, introduced by the requirement that a small amount of charge is needed to activate the cross-over diode.

error, Δt. This is the main factor leading to the walk in the prompt centroid time curve. By considering pulses of different amplitudes i.e. energy E, and the same amount of charge to activate the diode, different triggering times occur as shown in fig. 34. A simple relation can be calculated between Δt and E using linearly rising pulses with equal rise-times:

$$\Delta t = \frac{B}{\sqrt{E}} \quad . \qquad 4\text{-}1$$

Hence, Constant Fraction triggering occurs at a time

$$t = A + \frac{B}{\sqrt{E}} \quad . \qquad 4\text{-}2$$

This relation was used to fit the prompt centroid points with surprising success. An extra term, $C \log_e E$, was added to improve the fit at lower energies since the walk of the prompt time centroid curve is more pronounced in this energy region. However, in most cases the parameter C had a small value. Any centroid which is shifted from this curve corresponds to a γ-ray with a measurable lifetime. The time spectrum ADC R was calibrated using a precision Time Calibrator, ORTEC model 462.

One of the greatest advantages of the above technique is the simultaneous acquisition of data for both the prompt and delayed time distribution curves. Errors due to electronic drifts and shifts which may occur between alternate experimental runs as was the case in previous delayed-coincidence measurements, are thus avoided. Also in previous measurements background subtractions were inaccurate due to the use of scintillator detectors with their poor energy resolution. Our technique goes a long way to solving this problem by the use of the target rotator system. Separation of the spectra from the two targets by the Target Discriminator module prevents increasing the background to peak ratio which is a major factor in producing errors in background subtractions. Due to the extremely good energy resolution of Ge(Li) detectors, digital windows can be placed on the background continuum above and below the γ-ray peak to within a few kev of the peak, to ascertain the true background contribution to the time distribution curves corresponding to energy windows on the γ-ray peaks.

Another advantage is that several levels can be investigated for lifetimes simultaneously and hence the influence on the lifetimes of cascading γ-rays to the levels of interest can be studied. This is especially important if one of the states cascading to the level of interest has a measurable lifetime. Coincidences from other cascades has greatly distorted measurements in previous delayed-coincidence techniques.

Another plus factor of the technique is that centroid shifts are measured relative to the prompt time centroid curve at the appropriate energy. This is important due to the walk in the prompt time centroid curve. An ultimate refinement of the technique would be the development of the timing electronics which produce a walk free prompt time centroid curve.

Simms et al.(Si 61) and Kim and Milner (Ki 71) also recognized the necessity of obtaining the prompt and delayed time distribution curves simultaneously. Simms et al.obtained the desired result by a triple coincidence technique which included β-γ and γ-γ coincidences using plastic scintillators and a NaI detector. However, the method is limited by the number of states that can be excited by β and γ-ray transitions. Another important point which was not considered is the walk of the centroid of the prompt time distributions with the energy of the detected radiation although this effect is less significant with plastic scintillators than with Ge(Li) detectors. Kim and Milner, on the other hand, using a pulsed beam obtained the prompt and delayed time distributions simultaneously by having the energy and time distributions accumulate in a two-parameter analyzer operated in the 512×32 channel mode; 512 channels for energy analysis and 32 channels for the time analysis. Supplementary prompt reference γ-rays were obtained from a second target in a separate experimental run. The main problem of the two parameter analysis is that the time dispersion [0.567 ns/channel] is large compared to lifetimes of the order of 10^{-11} secs and hence the resolution of the time distributions must be good if centroid shifts of the order of a tenth of a channel are to be measured with accuracy. The energy resolution of the detector must also be excellent to resolve γ-ray peaks differing in energy by a few keV since there are only 512 channels for energy analysis. The present technique overcomes these problems by allowing the experimenter more freedom in determining the size of the individual regions of spectra. Also the ability to choose only those γ-ray peaks of interest and to be able to sort the data with respect to another parameter, are additional advantages of the present technique.

There are two major limitations to the technique. The first is the availability of suitable 'prompt' reference γ-rays. The second is the peak to background ratio. It was found that when this ratio decreased below 1:2 large uncertainties were introduced in background subtractions. Hence only γ-rays with reasonable intensities can be studied.

Another background problem is overcome by setting the detector-target distance to about 1 metre so that by time of flight neutrons produced in nuclear reaction at the target can be differentiated from γ-rays. Otherwise the detection of the neutrons leads to a time peak which falls close to or under the time distribution curve obtained from γ-ray detection. This situation is obviously unacceptable. Although the large detector-target distance reduces the count rate considerably, most experimental runs were less than 3 hours.

CHAPTER 5

THE FULL ENERGY - COMPTON DILEMMA

In all the experimental runs performed an interesting feature has been consistently observed. It is found that for a given pulse height there is a centroid shift between the time peaks obtained from events in which the full energy of the 'prompt' γ-rays is deposited in the Ge(Li) detector, and those obtained from Compton scattering of higher energy 'prompt' γ-rays. An ideal 'prompt' γ-ray is that which originates from a level whose lifetime is much less than, say, 5 ps. An example of this effect is shown in fig. 33 from experimental data obtained in the study of lifetimes in ^{64}Cu. For future reference we define the background and prompt centroid time curves as the 'best fit' curves to the centroid points from energy windows set on the Compton background and 'prompt' γ-ray peaks, respectively.

It is noted that for very low energies, those less than 80 kev, the background centroid time curve crosses the prompt centroid time curve. This can be explained by the realisation that the front face of the detector is effectively 'black' to these low energy γ-rays and X-rays. Thus total absorption would occur in a region of poor field characteristics of the detector. Due to these poor fringing fields the collection time of the total charge formed by the γ-ray-detector interaction would be increased and hence the centroids of the time distribution curves for these γ-ray events would be delayed. However, Compton events at the same energy could occur throughout the volume of the detector and hence charge collection times would not be delayed in the same manner.

To investigate the phenomenon at higher energies the timing properties of the coaxial Ge(Li) detector were studied by using collimated γ-ray sources. The first interesting results are shown in fig. 35. In this case, a timing coincidence was set up using a ^{22}Na source and collimating the radiation to the Ge(Li) detector by a 6.3 cm thick lead brick with a hole 0.4 cm in diameter through it. The collimated beam was directed parallel to the axis of the detector crystal and moved in steps of 0.5 cm from the centre to the outer radius of the crystal. Experiments were done with a 23 c.c. coaxial Ge(Li) detector with the intrinsic region of the crystal having dimensions 0.34 cm inner radius and 1.54 cm outer radius. The results shown are for the system gated on the 0.511 MeV peak from the ^{22}Na source. A significant improvement in the time resolution is seen at the centre of the intrinsic region as compared to the regions near the inner and outer electrodes of the

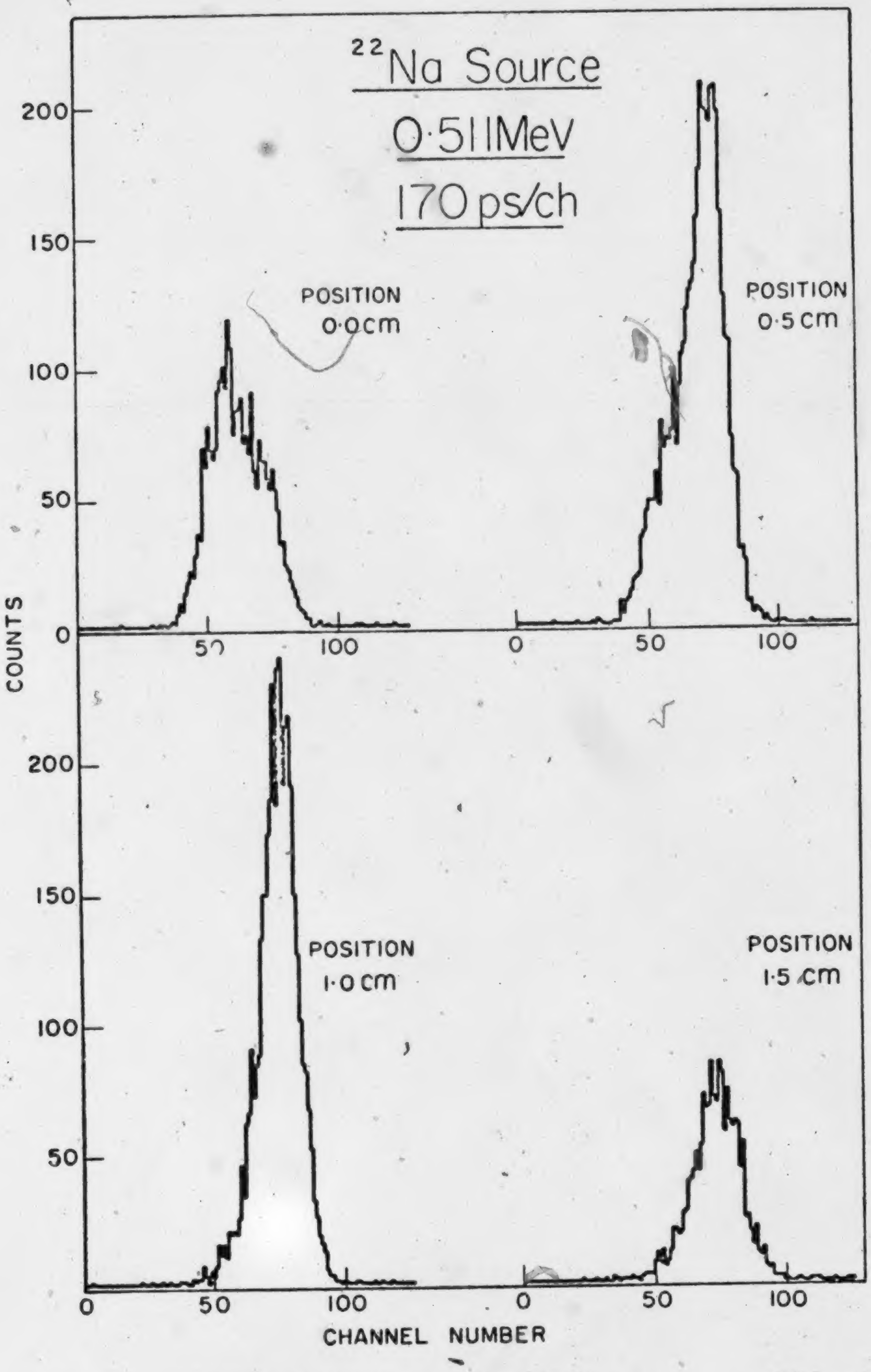

Fig. 35. Time distributions obtained as a collimated γ-ray beam from a ^{22}Na source was moved in steps of 0.5 cm from the centre of the detector to the outer radius, the timing system being gated by an energy window on the 0.511 MeV peak.

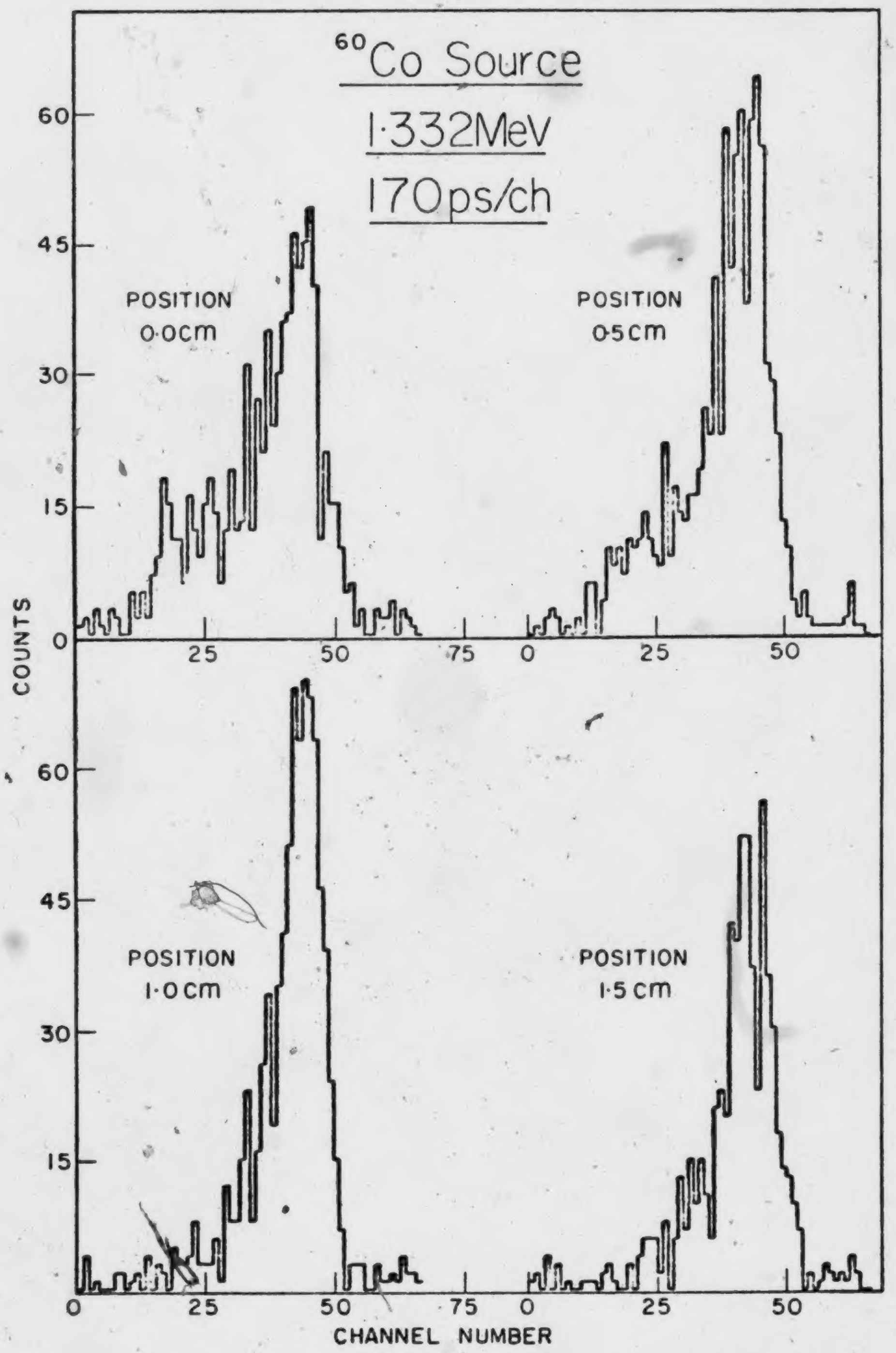

Fig. 36. Time distributions obtained as a collimated γ-ray beam from a ^{60}Co source was moved in steps of 0.5 cm from the centre of the detector to the outer radius, the timing system being gated by an energy window on the 1.332 MeV γ-rays of a ^{60}Co source.

detector. As shown in fig. 5, the centre of the intrinsic region corresponds to pulses that have the shortest rise-times.

Similar results are shown in fig. 36 for a collimated γ-ray beam from a ^{60}Co source with the electronics gated on the 1.33 MeV γ-rays. In this case, however, due to the higher energy γ-rays the lead collimator was not as effective but the same trends are seen that are also observed in fig. 35.

An interesting feature of these curves is that even at the centre of the detector, in a region which should be insensitive, radiation is detected. The deterioration of the early side of the time resolution curves using the ARC timing technique can be explained by events which occur in the central core of the crystal and also in the intrinsic region near the inner electrode. Our technique of pulse shape selection which eliminates these pulses, therefore selects those events which occur in the centre of the intrinsic region i.e. about 1.0 cm from the centre of the crystal.

Fig. 37 shows a plot of the centroids of the time resolution curves of figs. 35 and 36 versus the collimated beam position. The points illustrate that γ-ray-detector interactions occurring towards the outer diameter of the crystal result in events which are timed

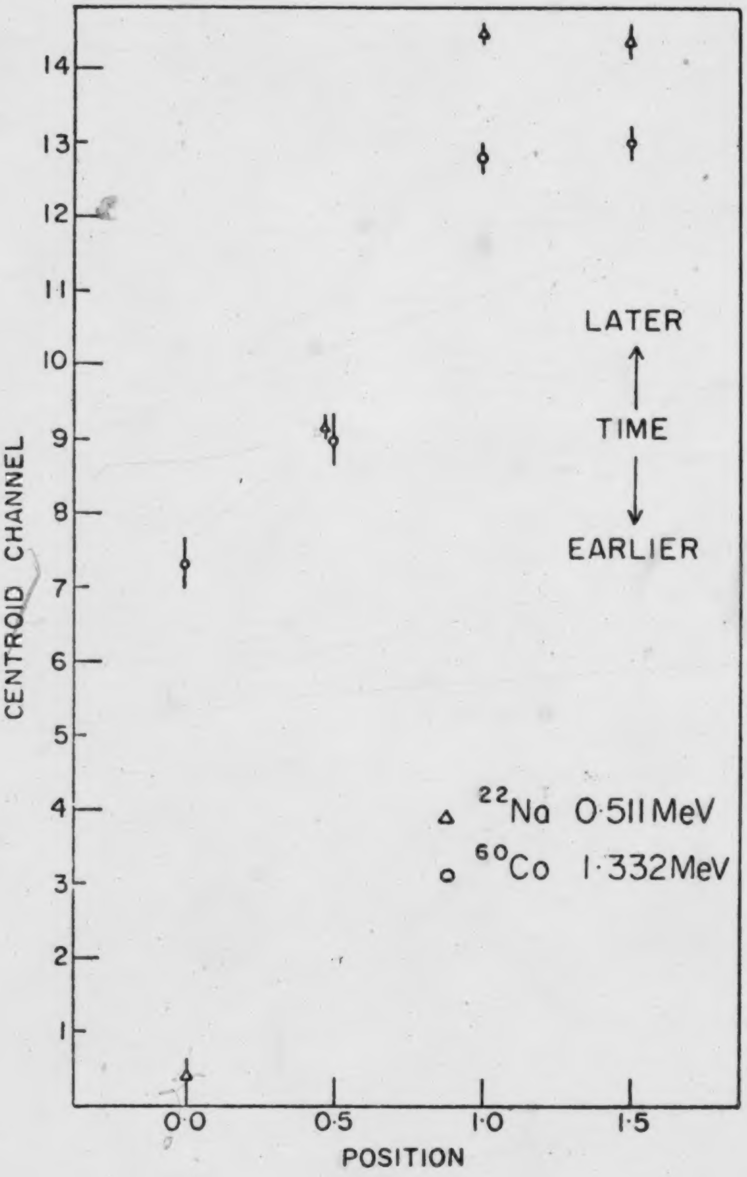

Fig. 37. A plot of the centroids of the time distributions of figs. 35 and 36 vs. the collimated beam position.

later. This is consistent with the theoretical results shown in figs. 6 and 7 which show that the zero-crossing time, t_c, occurs later as the interaction position moves towards the outer radius of the detector.

Using collimated γ-ray beams from ^{60}Co, ^{137}Cs, ^{22}Na and RdTh sources separately, and with no timing coincidence in this case, a comparison between the number of Compton and full energy events at a given pulse height was considered for the four collimated beam positions. The results are shown in fig. 38. They were obtained by setting energy windows on the full energy peaks of a given source and using the same windows to select events from the Compton continua of the other sources where applicable. The graphs are plotted so that at the collimated beam position which shows a maximum, is normalised to unity. From these graphs it is observed that there is a greater proportion of Compton to full energy events in the regions near the inner and outer electrodes of the detector. In each case an approximate background subtraction was done to account for scattering in or transmission through the lead collimator, since perfect collimation is effectively impossible.

These results are not entirely unexpected. In this region most events selected from a Compton continuum almost entirely represent single interactions in

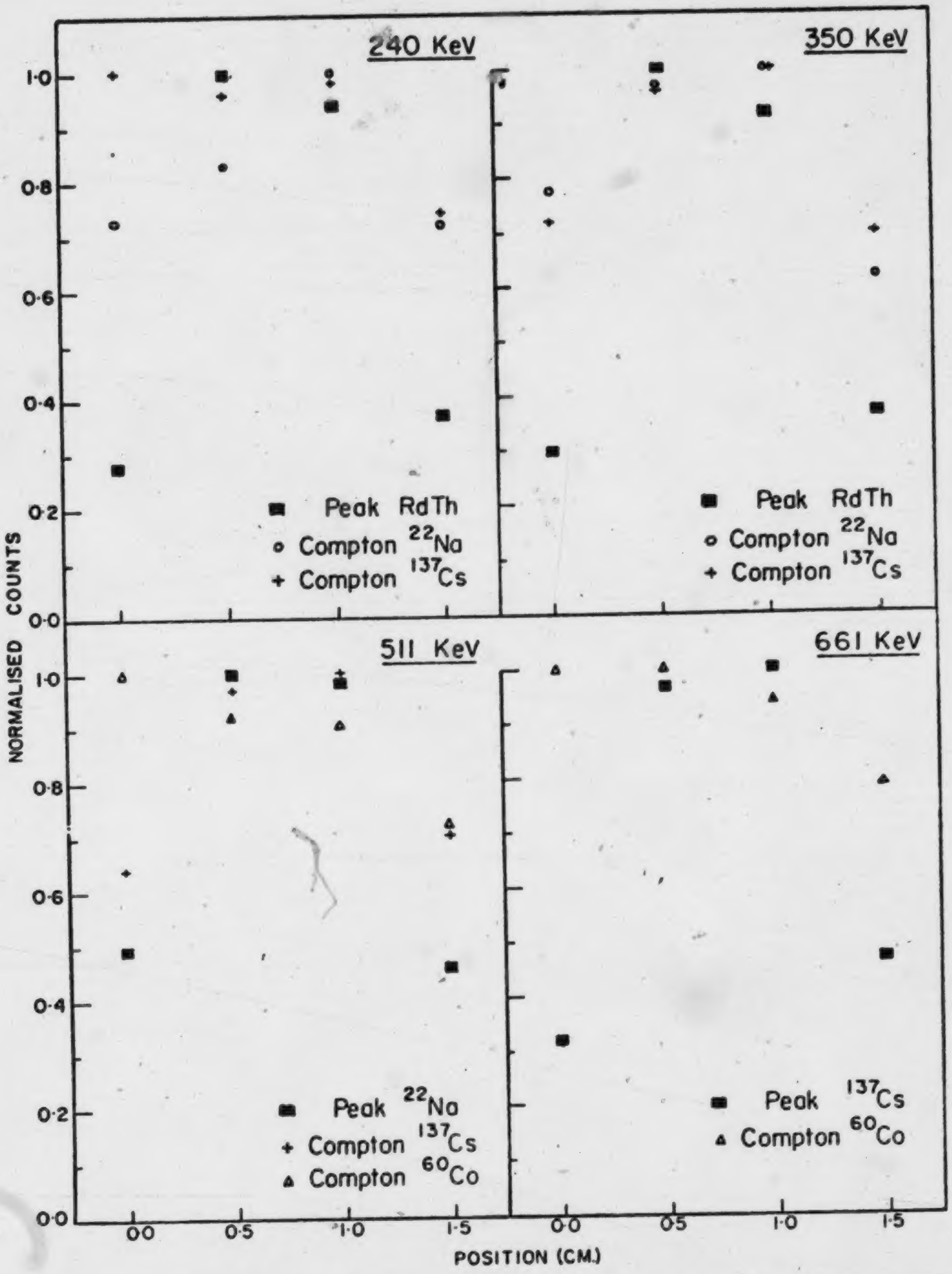

Fig. 38. The normalised number of Compton and full energy events, for a given pulse height, plotted as a function of the collimated γ-ray beam position. ^{60}Co, ^{137}Cs, ^{22}Na and RdTh sources were used to obtain the data.

the detector. However, this is not the case for the full energy events as indicated in fig. 39 which shows the calculated percentage contribution to full energy peaks by multiple scattering events. Bengtson and Moszyński (Be 72) calculated these curves using a Monte Carlo technique and assuming in the Compton scattering problem that 90° was the only possible scattering angle to simplify the calculations.

Thus due to this multiple scattering process there is a greater probability of obtaining a full energy event if the first interaction occurs in the centre of the intrinsic region of the detector. Otherwise subsequent interactions would usually not occur within the detector volume before total absorption of the energy of the initial γ-ray is obtained. This would therefore account for the greater percentage of Compton events occurring near the electrodes of the detector.

Using these results combined with the observations of fig. 37 one would expect to find the centroids of the time distribution curves from Compton events delayed with respect to those obtained from full energy events at the same pulse height.

Since the time resolution is poor near the electrodes one would expect to observe a difference in the shape spectra across the face of the detector using collimated γ-ray beams. Figs. 40, 41 and 42 show the

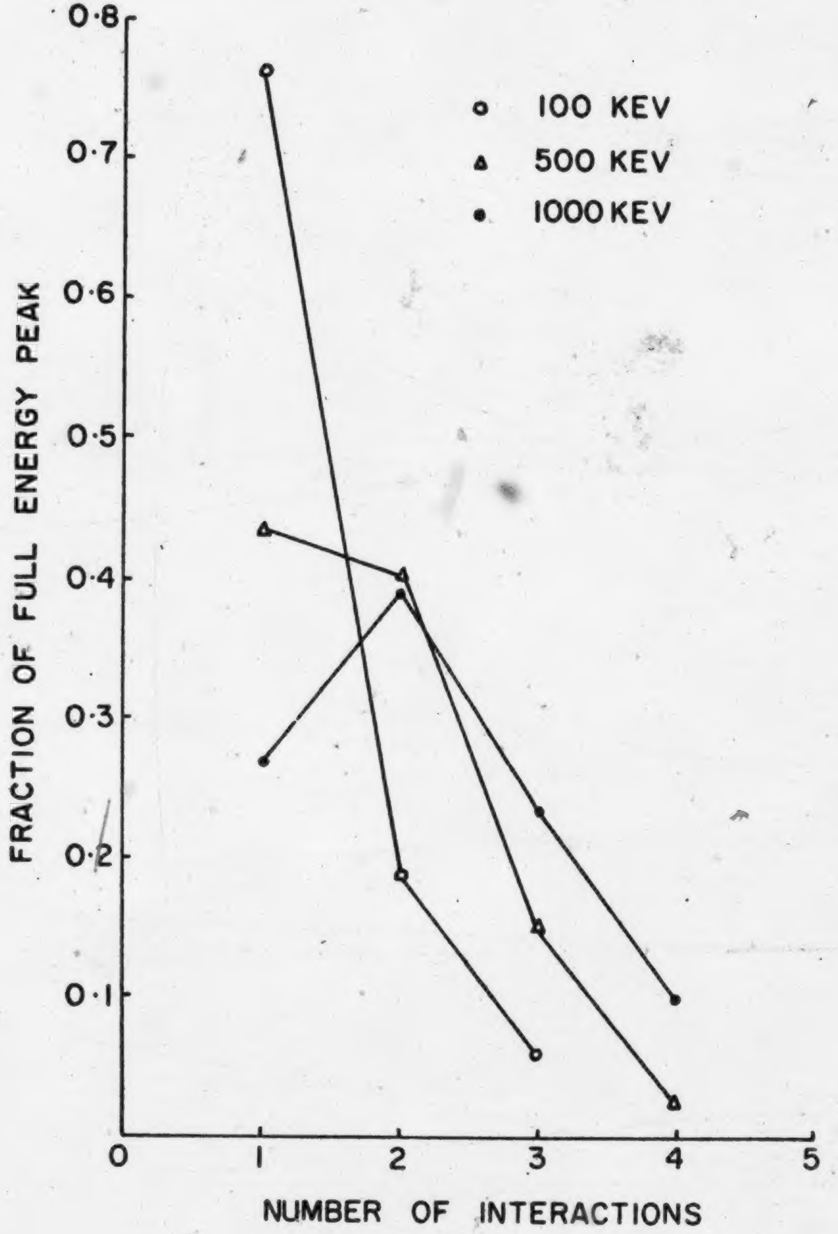

Fig. 39. The calculated percentage contribution to full energy peaks by multiple interacting events (Be 72).

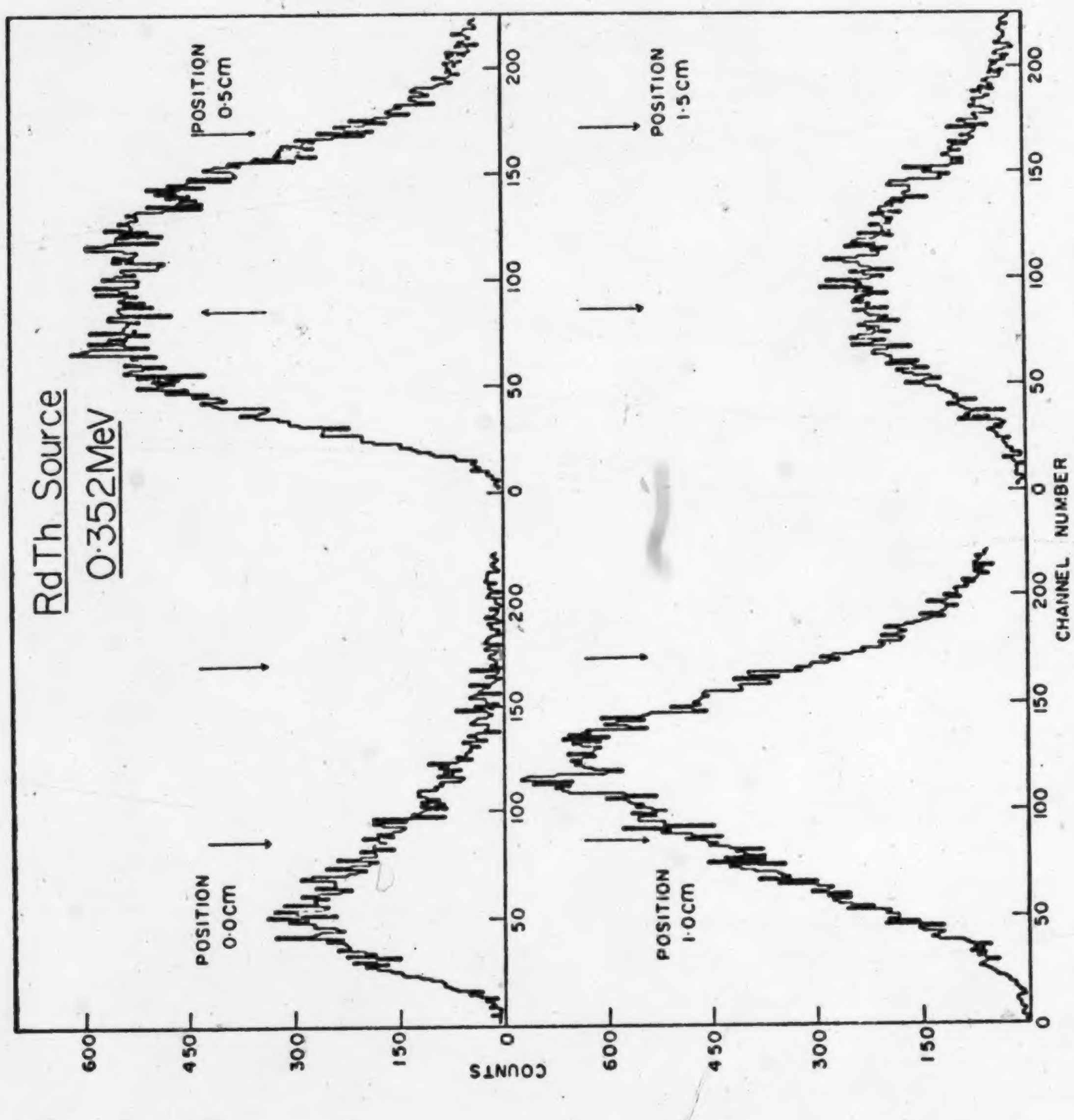

Fig. 40. 'Shape' spectra obtained as a collimated γ-ray beam from a RdTh source was moved from the centre of the detector in steps of 0.5 cm to the outer radius, the system being gated by an energy window on the 0.352 MeV γ-rays from the source.

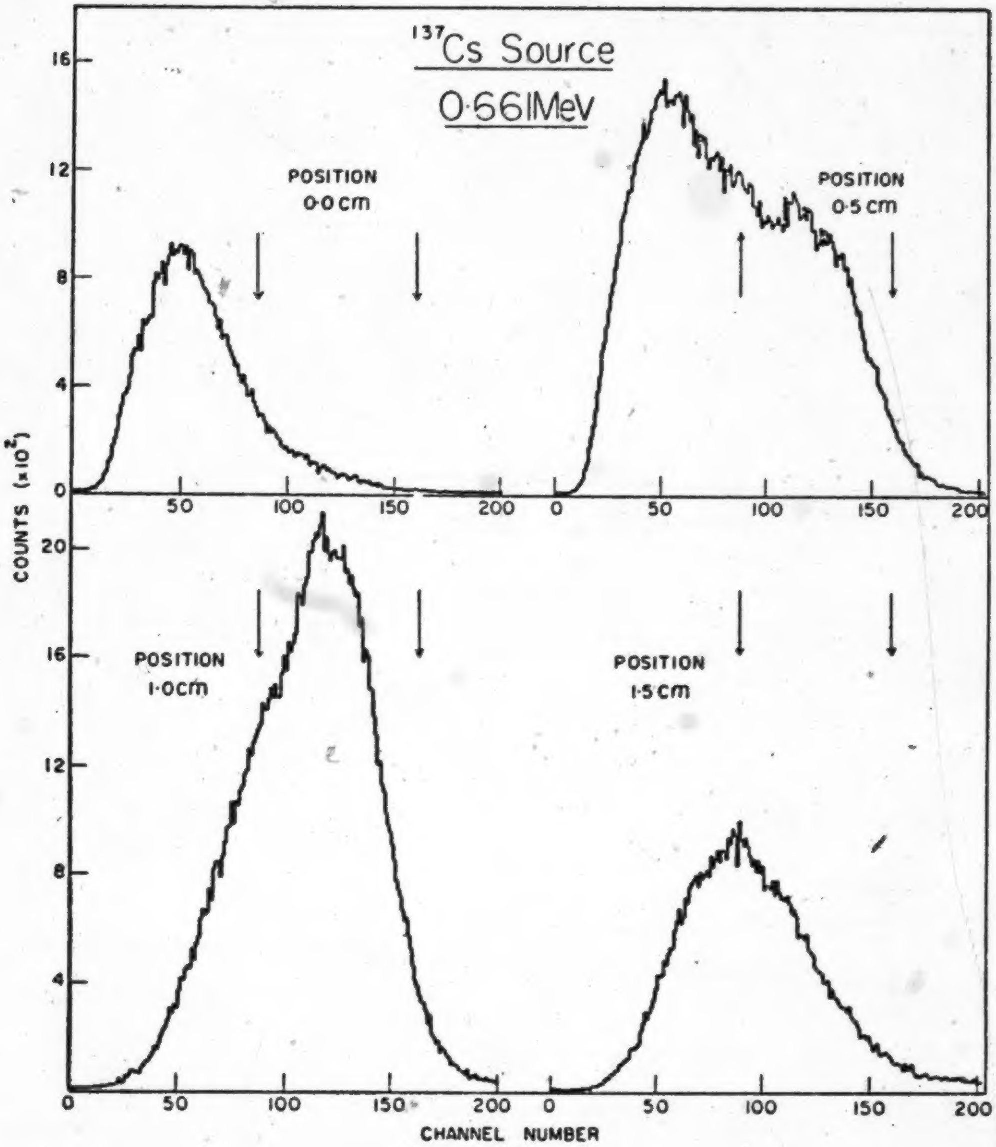

Fig. 41. 'Shape' spectra obtained as a collimated γ-ray beam from a ^{137}Cs source was moved from the centre of the detector in steps of 0.5 cm to the outer radius, the system being gated by an energy window on the 0.661 MeV γ-rays from a ^{137}Cs source.

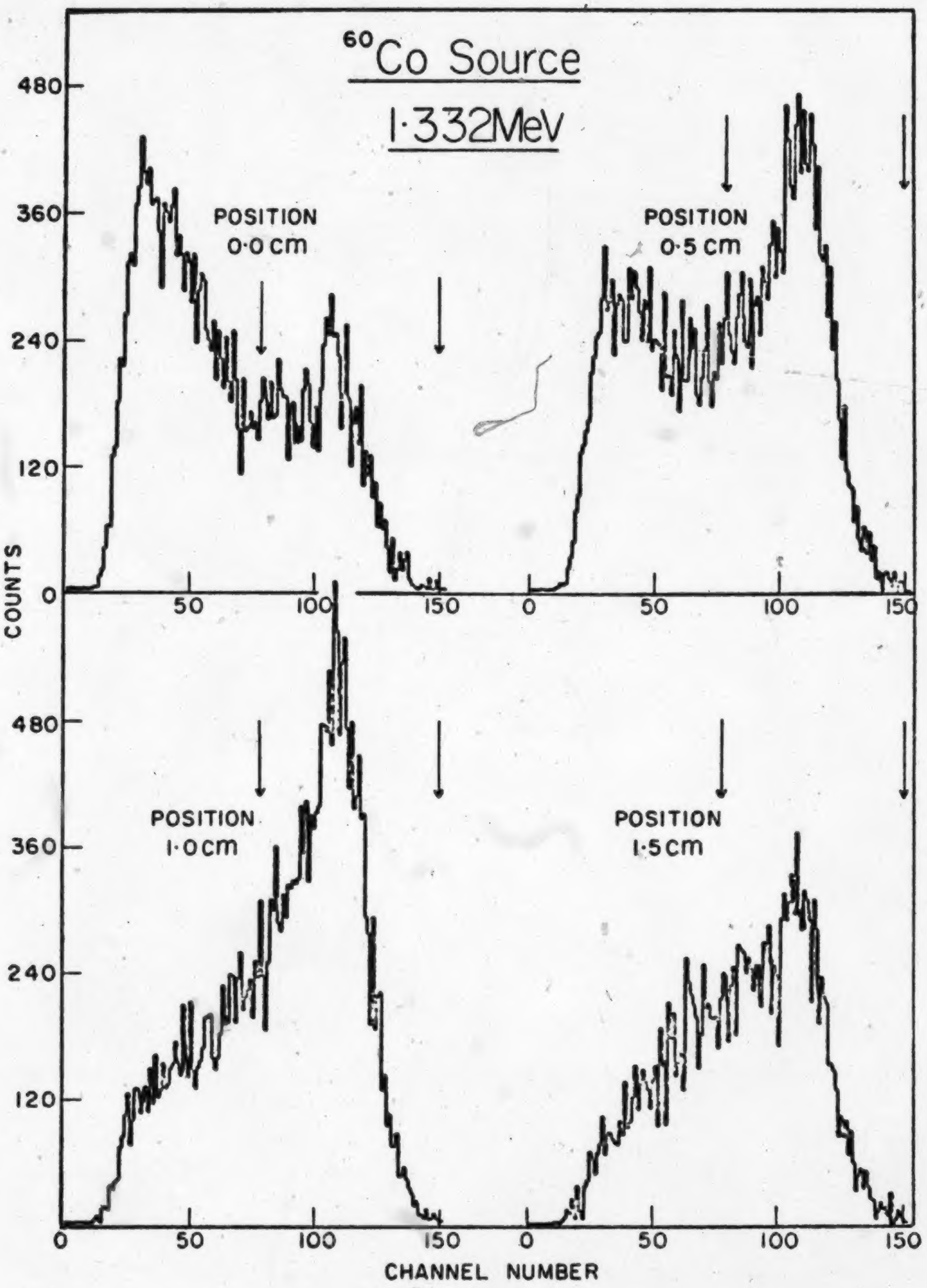

Fig. 42. 'Shape' spectra obtained as a collimated γ-ray beam from a ^{60}Co source was moved from the centre of the detector in steps of 0.5 cm to the outer radius, the system being gated by an energy window on the 1.332 MeV γ-rays of a ^{60}Co source.

shape spectra obtained from the four collimated beam positions at various energies. The figures show results for the 0.352 MeV γ-ray from the RdTh source, the 0.661 MeV γ-ray from the ^{137}Cs source and the 1.332 MeV γ-ray from the ^{60}Co source. Similar results were obtained for other full energy peaks. The arrows on the diagrams illustrate the region used in our pulse shape selection technique and correspond approximately to bins 4 to 7 in figs. 17 and 19, that is those bins which give the most improved time resolution.

These figures show the true significance of the pulse shape selection technique. The technique effectively selects those pulses which occur due to interactions in the centre of the intrinsic region while eliminating a great proportion of those events which occur near the electrodes.

The left hand hump, which could not be theoretically obtained as illustrated in figs. 10 and 11, is seen to come mostly from events which occur in the central core, or in what should be the insensitive region of the detector. Obviously events which occur in this region produce electron-hole pairs which are still collected by the electrodes but with very long collection times which give rise to pulses with poor time resolution characteristics. Thus by drilling out this central core, coaxial Ge(Li) detector should have better time resolution.

Similar shape spectra were obtained for energy windows set on the Compton continua of the sources, however, no significant visual difference could be seen between these spectra and those obtained from full energy events. The slight difference, however, shows up when one normalises the shape spectra for a given energy and collimated beam position and then calculates the total number of events in that region of the shape spectra which gives good time resolution. Fig. 43 shows the results of these calculations plotted as the full energy to Compton ratio, for a given pulse height, versus the collimated beam position. The same trends are shown again as seen in fig. 38 that there is a greater percentage of Compton to full energy events in those regions near the electrodes of the detector.

These slight differences are further accentuated when one considers the volume contributions at a given radius of the detector. The full face of the detector was irradiated with the sources separately and fig. 44 shows the total shape spectra obtained from energy windows set on the full energy peaks and Compton continuum for the same pulse height. Curves are shown for the energies 0.661 MeV, 1.172 MeV and 1.332 MeV, and in each section of fig. 44 the two curves are normalised

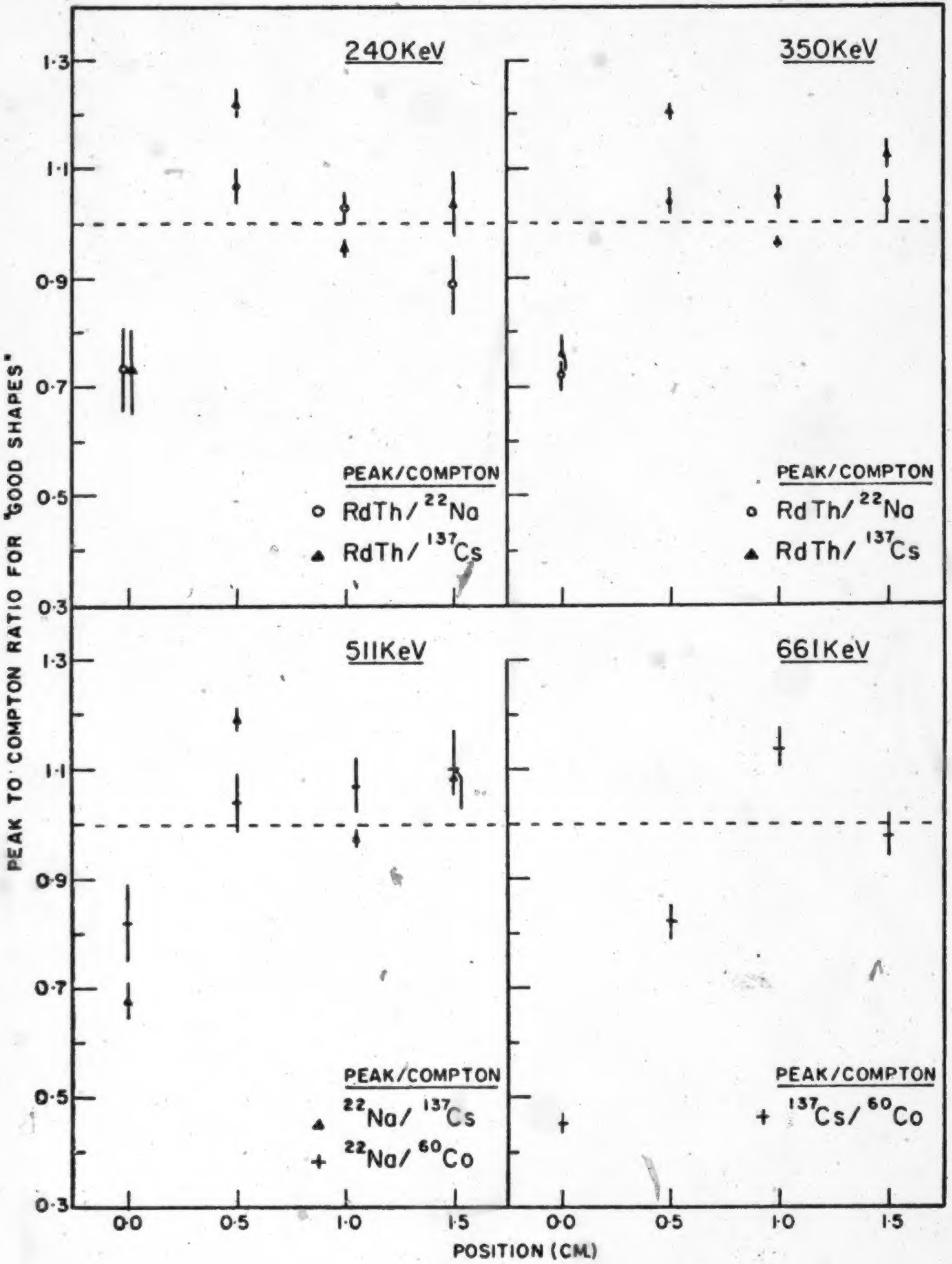

Fig. 43. Relative peak to Compton ratios, for given pulse heights, plotted as a function of the collimated beam position with only events in the 'good shape' region being selected.

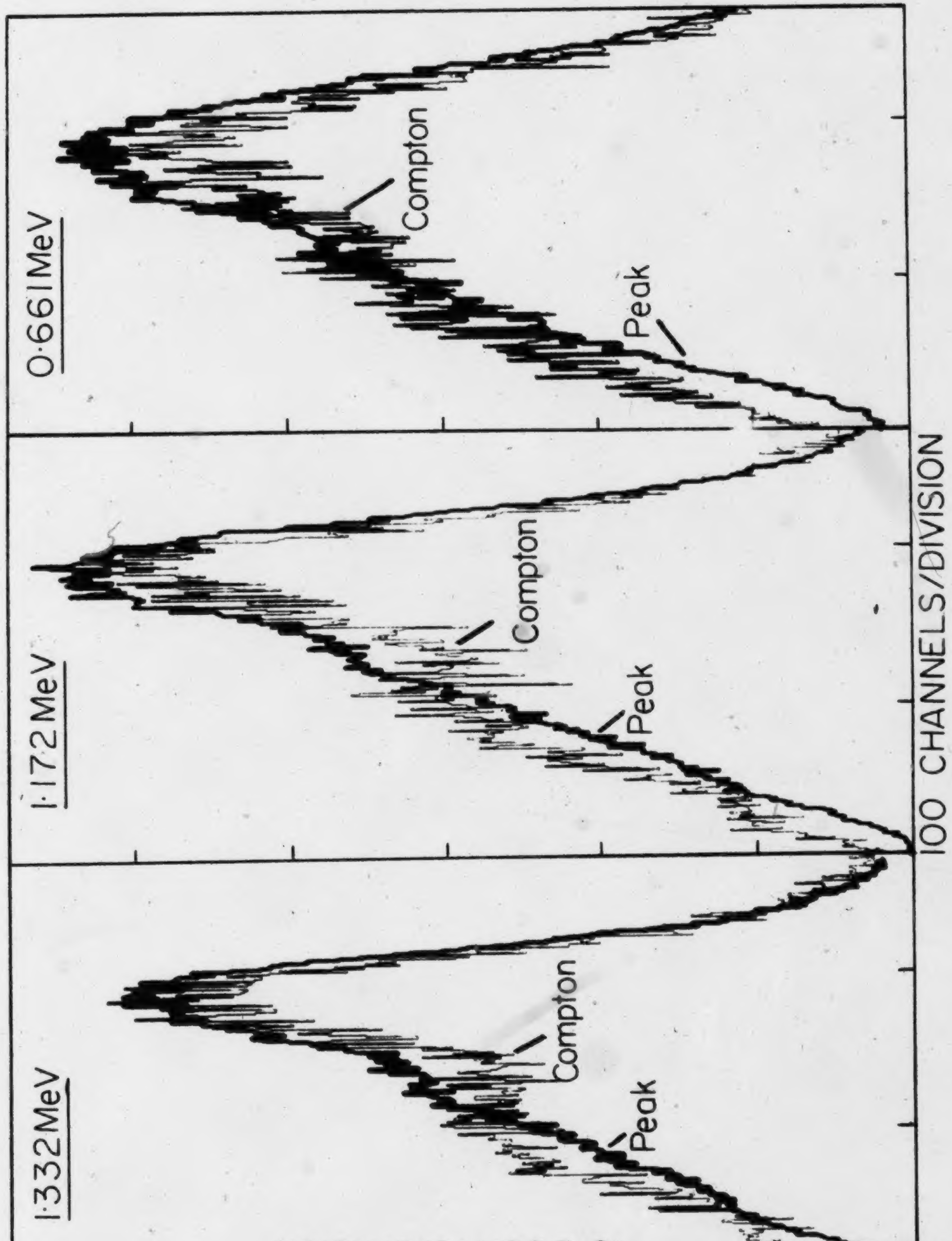

Fig. 44. 'Shape' spectra obtained by irradiating the full face of the detector and gating the system on full energy events from one source and the Compton continuum of another, using the same energy window.

to the same number of counts. It is seen that there is a marked difference in the shape spectra obtained from Compton events compared to those obtained from full energy events especially at higher energies. It is expected that the shape spectra become similar at low energies since in this case γ-rays have a greater probability of depositing all their energy in the detector in a single interaction.

Similar differences between Compton and full energy events have been seen before (St 67, Mo 70, Mo 72) using different techniques. The greater proportion of Compton events in the left side of the shape spectra i.e. the region associated with poor time resolution, can be explained by noting that the regions near the electrodes of a Ge(Li) detector are often poorly compensated, the field therefore being weaker and enhancing carrier recombination and charge trapping effects. Thus γ-rays interacting in these regions often give rise to defective slow-rising pulses with poor time resolution characteristics. Strauss and Larsen (St 67) have stated that much of the continuum at 1.33 MeV was due to these defective pulses.

To finalise the study of the timing properties of coaxial Ge(Li) detectors, a timing coincidence was set up using a collimated beam from a ^{22}Na source, directed at 0.5 cm intervals along the side of the detector, perpendicular to the axis of the crystal.

Fig. 45 shows the time resolution curves obtained with the electronics gated on the 0.511 MeV peak at 1.0 cm intervals from the front face to the back face of the crystal. No shape selection was involved in these results. It is observed that the time resolution is poor at both ends of the detector where the electric field, a fringing field, is poor.

A plot of the centroids of these time distribution curves, and those at other energies, against the position of the collimated beam are shown in fig. 46. This result is quite unexpected, the timing coming earlier at the back face of the detector. It could be that the geometry of the particular detector used resulted in a variation in the electric field along the length of the detector crystal. However, as no measurements have been done to see whether a similar result occurs with other crystals no conclusion is possible.

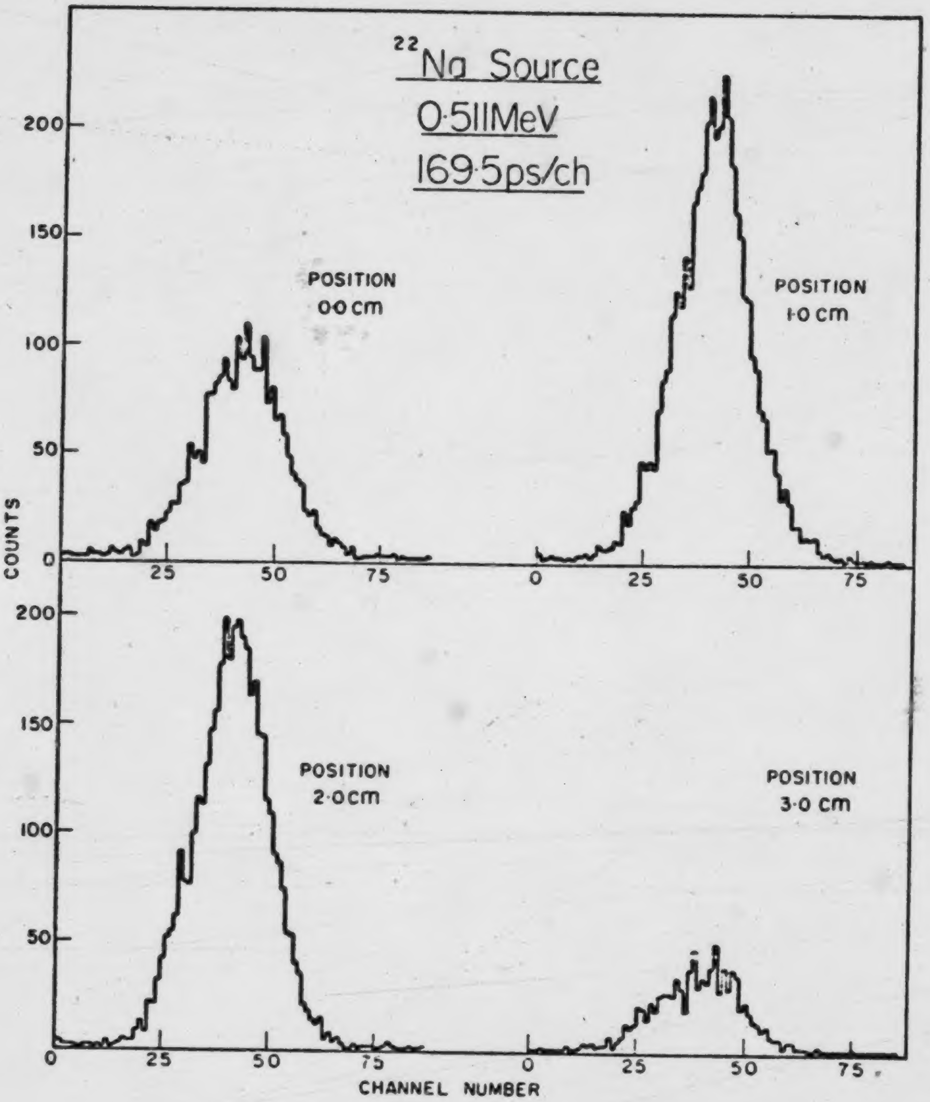

Fig. 45. Time distributions obtained as a collimated γ-ray beam from a ^{22}Na source was moved in steps of 1.0 cm from the front face to the back face of the detector crystal, the timing system being gated on the 0.511 MeV peak.

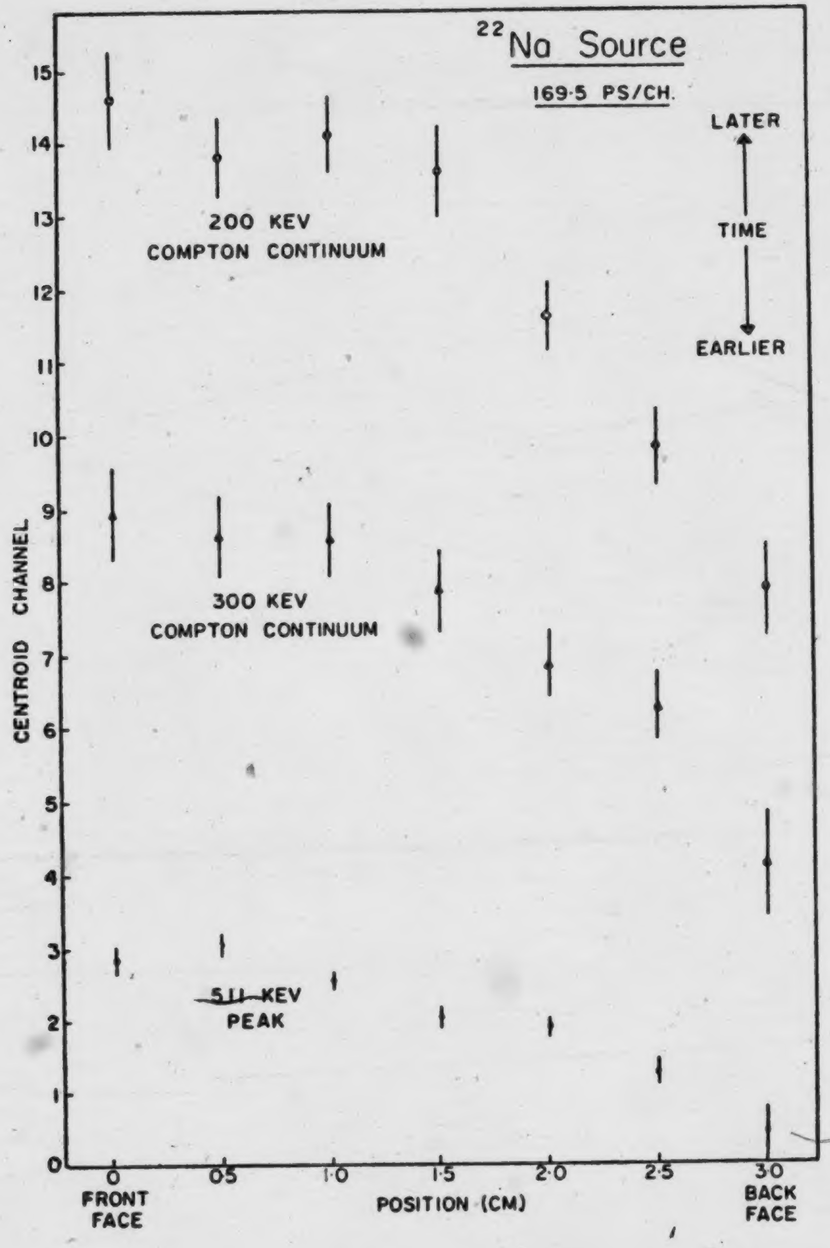

Fig. 46. A plot of the centroids of the time distributions vs. collimated beam positions along side of detector crystal, the system being gated by energy windows at 200, 300 and 511 keV.

CHAPTER 6

ELECTROMAGNETIC TRANSITION RATES AND PROBABILITIES

By Heisenberg's uncertain principle, the meanlife of an excited nuclear state, is defined in terms of the energy width Γ for a γ-decay as

$$\Gamma\tau = \hbar = 0.6582 \times 10^{-15} \text{ eV sec} . \qquad 6\text{-}1$$

The radiative transition probability is the reciprocal of the meanlife

$$T = \frac{1}{\tau} = \frac{\Gamma}{\hbar}$$

which is the sum of the partial transition probabilities

$$T = \sum_{\sigma L} T(\sigma L) \qquad 6\text{-}2$$

where L is the multipolarity of the decay and σ represents the mode, either electric or magnetic.

The partial transition probability of a gamma transition, angular momentum LM and energy E, from the initial level spin J_i to the final level with spin J_f is given by (Mo 65, Sk 66)

$$T(\sigma LM) = \frac{8\pi(L+1)}{L[(2L+1)!!]^2} \frac{1}{\hbar} \left(\frac{E}{\hbar c}\right)^{2L+1} |\langle f|M^{\sigma}_{LM}|i\rangle|^2 \qquad 6\text{-}3$$

where M^{σ}_{LM} is the corresponding multipole operator.

Usually one is not interested in the orientation of either the initial or final state, so one sums over magnetic substates M_f and averages over M_i. Defining the so-called reduced matrix element

$$B(\sigma L,\ J_i \to J_f) = (2J_i + 1)^{-1} \sum_{M_i M_f} |\langle f\ M^{\sigma}_{LM} | i \rangle|^2 \quad . \qquad 6\text{-}4$$

The partial transition probability becomes

$$T(\sigma L) = \frac{8\pi(L+1)}{L[(2L+1)!!]^2} \frac{1}{\hbar} \left(\frac{E}{\hbar c}\right)^{2L+1} B(\sigma L) \qquad 6\text{-}5$$

The electric and magnetic operators for a single particle are given by

$$M^E_{LM} = er^L\, Y^*_{LM} - i\, \frac{g_s \mu_o \omega}{c} (L+1)^{-1}\, \underset{\sim}{\sigma} \times \underset{\sim}{r} \cdot [\mathrm{grad}(r^L\, Y_{LM})]^* \qquad 6\text{-}6$$

and

$$M^M_{LM} = \mu_o \left(\frac{2}{L+1}\, g_\ell\, \underset{\sim}{\ell} + g_s\, \underset{\sim}{s}\right) \cdot [\mathrm{grad}(r^L\, Y_{LM})]^* \ , \qquad 6\text{-}7$$

respectively. The first term in each denotes the contribution due to the orbital motion, while the second term arises from the intrinsic particle spin. μ_o is the nuclear magneton and the g's are the gyromagnetic ratios.

From these equations it follows that any 2^L pole multipole radiation field carries angular momentum L and z-component M and its parity being $(-1)^L$ or $(-1)^{L-1}$ for EL or ML radiation, respectively. Hence from the conservation of angular momentum 2^L pole radiation can occur only between states whose angular momenta obey the selection rules

$$|J_i - J_f| \leq L \leq J_i + J_f$$

and

$$M = M_i - M_f \quad .$$

From the conservation of parity, one has

$$\begin{aligned} \Delta\pi \equiv \pi_i/\pi_f &= (-)^L \quad \text{for EL radiation} \\ &= (-1)^{L-1} \quad \text{for ML radiation} \end{aligned}$$

where π_i and π_f are the parities of the nuclear states involved in the transition.

In order to set a standard for comparison of all experimental transitions, regardless of any model of the states involved, the so-called Weisskopf and Moszkowski units were defined. Since one does not distinguish neutron from proton transitions, for EL transitions involving a single proton, the main contribution to M^E_{LM} is provided by the orbital term. For a central potential the wavefunctions of the initial and final states can be written as a product of a radial function which depends on the details of the potential and a two-component function which contains angle and spin variable but is independent of the details of the potential. Thus the electric multipole matrix element can be written as

$$\langle f|M^E_{LM}|i\rangle = e\int_0^\infty \mathcal{R}_f\, r^L \mathcal{R}_i\, r^2\, dr \int_{4\pi} \Theta^{M_f *}_{\ell_f J_f}\, Y_{LM}\, \Theta^{M_i}_{\ell_i J_f}\, d\Omega$$

where $d\Omega$ refers to integration over all angles and sum over spins. To evaluate the reduced matrix element a 'statistical factor' S is defined as follows:

$$S(J_i\, L\, J_f) = 4\pi(2J_i+1)^{-1} \sum_{M_i M_f} \left|\int_{4\pi} \Theta^{M_f *}_{\ell_f J_f}\, Y_{LM}\, \Theta^{M_i}_{\ell_i J_f}\, d\Omega\right|^2 \qquad 6\text{-}8$$

which simplifies

$$S(J_i\, L\, J_f) = (2J_f + 1)\,(J_i J_f \tfrac{1}{2} - \tfrac{1}{2}|L0)^2 \ . \qquad 6\text{-}9$$

Hence the reduced matrix element becomes

$$B(EL) = \frac{e^2 R^{2L}}{4\pi}\left(\int_0^\infty \mathcal{R}_f \left(\frac{r}{R}\right)^L \mathcal{R}_i\, r^2\, dr\right)^2 S(J_i\, L\, J_f) \ . \qquad 6\text{-}10$$

In order to obtain simple standard units the radial wavefunctions $\mathcal{R}$ for both initial and final states are assumed constant throughout the interior of the nucleus (for $r < a$) and vanish outside (for $r > a$). On the basis of this constant density model, the values of the radial integrals are given as follows:

$$\int_0^\infty \mathcal{R}_f \left(\frac{r}{R}\right)^L \mathcal{R}_i\, r^2\, dr = 3/(L+3) \ . \qquad 6\text{-}11$$

A further assumption is made that the radiation of multipole L occurs between the states $J_i = L + \frac{1}{2}$ and $J_f = \frac{1}{2}$. Hence

$$S(L+\tfrac{1}{2},\ L,\tfrac{1}{2}) = 1 \quad . \qquad 6\text{-}12$$

Thus substituting eqs. 6-11 and 6-12 in eq. 6-10 one obtains the Weisskopf or Moszkowski unit for an EL-transition

$$B_W(EL) = \frac{e^2 R^{2L}}{4\pi} \left(\frac{3}{L+3}\right)^2$$

$$= \frac{1}{4\pi}\left(\frac{3}{L+3}\right)^2 1.2^{2L}\ A^{2L/3}\,[\mathrm{fm}^{2L} e^2] \qquad 6\text{-}13$$

in units of $\mathrm{fm}^{2L} e^2$ where the following relation has been used for the nuclear radius

$$R = r_o\ A^{1/3}$$

and where $r_o = 1.2$ fm and A is the atomic number of the nucleus.

Similarly a Moszkowski unit for magnetic transitions can be calculated:

$$B_M(ML) = \frac{1}{\pi}\left(\mu_p L - \frac{L}{L+1}\right)^2 \left(\frac{3}{L+2}\right)^2\ 1.2^{2L-2}\ A^{(2L-2)/3}$$

$$[\mathrm{fm}^{2L-2}\mu_o^2] \quad . \qquad 6\text{-}14$$

The Weisskopt unit for magnetic transition is a numerical approximation of this Moszkowski unit

$$B_w(ML) = \frac{10}{\pi} \left(\frac{3}{L+3}\right)^2 1.2^{2L-2} A^{(2L-2)/3} [fm^{2L-2} \mu_o^2]. \qquad 6\text{-}15$$

It must be emphasized that the above theoretical estimates are crude and are not expected to represent accurately transitions in actual nuclei. However, they provide a starting point for interpretation of known results.

Several convenient units have been tabulated (Sk 66) for use in the above formulae:

$$\hbar c = 1.973 \times 10^{-11} \text{ MeV cm}$$

$$e^2 = 1.440 \text{ MeV fm}$$

$$\mu_o = 0.01589 \text{ MeV fm}^3 .$$

Another parameter of significant importance in the calculation of partial transition probabilities is the E2/M1 multiple mixing ratio δ which may be defined by the following relations:

$$\delta^2 = \frac{T(E2)}{T(M1)}$$

$$T(M1) = \frac{1}{1 + \delta^2} T$$

$$T(E2) = \frac{\delta^2}{1 + \delta^2} T$$

and

$$T = T(M1) + T(E2) .$$

If the nuclear state should decay by other competing processes such as internal conversion, the radiative decay lifetime τ_γ must be corrected by

$$\tau_\gamma = \tau_{obs}(1 + \alpha_T)$$

where τ_{obs} is the observed lifetime and α_T is the total internal conversion coefficient.

CHAPTER 7

EXPERIMENTAL RESULTS

7.1 Establishment of Suitable 'Prompt' Reference γ-rays

One of the most important problems faced in this research was the definition of the prompt time centroid curve. A sufficient number of centroid points corresponding to γ-ray transitions from states whose lifetimes are short compared to the time resolution of the system, less than say 5 ps, are required. The usefulness of the technique and the validity of the results hinge on finding a solution to this problem.

The shortest lifetimes that can be measured by this technique are of the order of 10 ps, and lifetimes of this magnitude or greater are most frequently encountered in low lying energy levels of nuclei, typically at energies of less than 300 keV. In this energy region the walk of the prompt time centroid curve is pronounced and becomes worse as the energy decreases. Hence, it is absolutely necessary to have sufficient reference 'prompt' γ-rays in this region where, unfortunately, there are very few 'prompt' γ-ray transitions. Unless an isotope is found which has several 'prompt' γ-ray transitions one has to resort to a 'smorgasbord' target consisting of several different isotopes, each having one or two 'prompt' γ-ray transitions, in order to adequately define the prompt time centroid curve. This would lead to problems in target fabrication and also the possibility of many unwanted γ-ray transitions and nuclear reactions.

In some cases states which have measured lifetimes less than 60 ps can be used to help define the prompt time centroid curve by adjusting their centroids amounts equivalent to their measured lifetimes. A literature search yielded two suitable isotopes, ^{181}Ta and ^{165}Ho, each with many γ-ray transition from states with lifetimes of 60 ps or less. Another advantage of these two isotopes is that they occur as 100% of the natural elemental abundance.

Fig. 47 shows the decay schemes of ^{181}Ta (Ro 70, NDS 73) and ^{165}Ho (NDS 74) for the low energy states. For proton beams of less than 5.5 MeV the states which are strongly populated are the 136 and 301 keV levels in ^{181}Ta and the 95 and 210 keV levels in ^{165}Ho. The γ-ray transitions of interest, the 136, 165 and 301 keV transitions in ^{181}Ta and the 95, 115, and 210 keV transitions in ^{165}Ho, are shown in bold ink in fig. 47.

The lifetime of the 136 keV level in ^{181}Ta has been measured using several techniques. Values of 60±5 ps (Bl 60) and 61.4±5.4 ps (Ar 70) were obtained using a microwave beam pulsing system. Steiner et al.

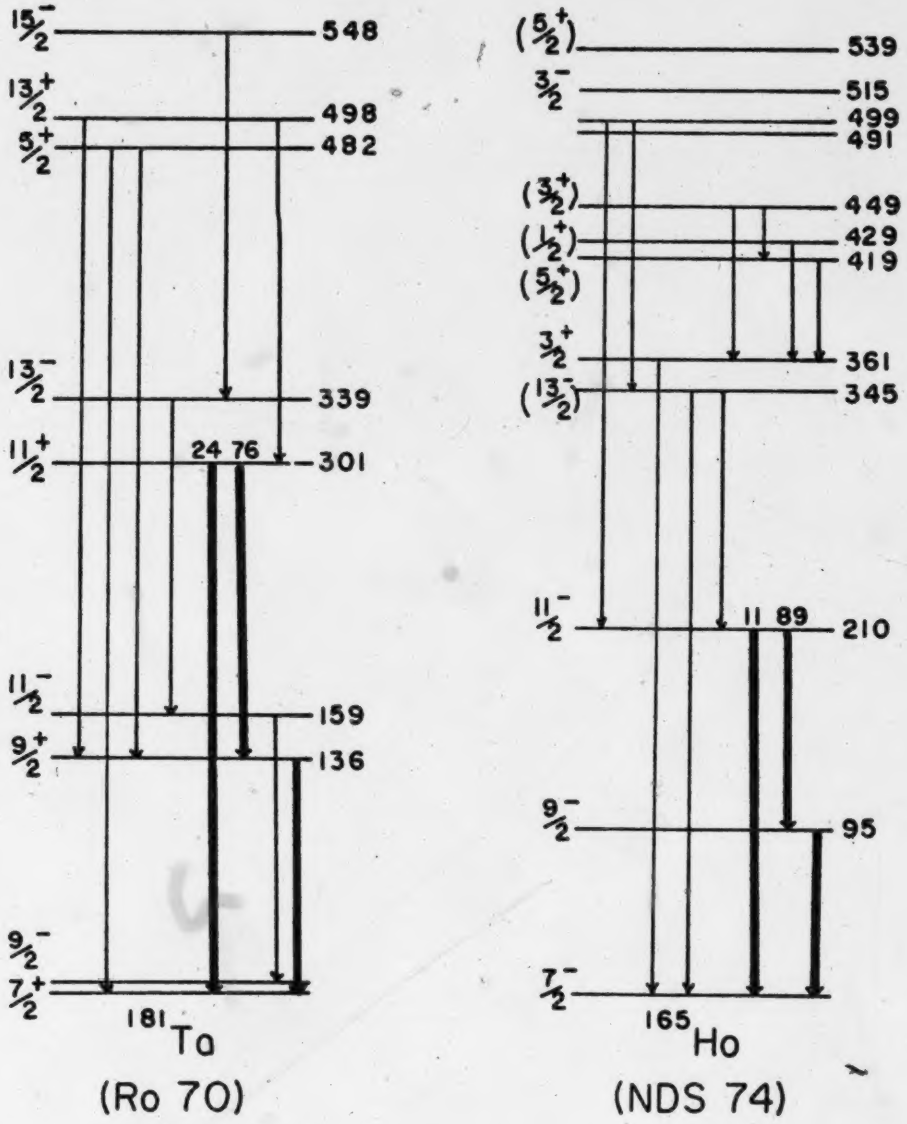
15/2 −
548
13/2 +
498
5/2 +
482
13/2 −
339
24 76
11/2 +
301
11/2 −
159
9/2 +
136
9/2 −
7/2 +
181 Ta
(Ro 70)
(5/2 +)
539
3/2 −
515
499
491
(3/2 +)
449
(1/2 +)
429
419
(5/2 +)
3/2 +
361
(13/2 −)
345
11/2 −
210
11 89
9/2 −
95
7/2 −
165 Ho
(NDS 74)

Fig. 47. Experimental level schemes for ^{181}Ta and ^{165}Ho. The γ-ray transitions of interest are shown by bolder lines.

(St 69) obtained a value of 55±3 ps using the Mössbauer Effect and the weighted mean of several Coulomb Excitation measurements yields a reduced transition probability $B(E2)\uparrow = (2.0\pm0.4)\times10^4\ e^2fm^4$ from which a lifetime of 55±11 ps is calculated (NDS 73). The weighted mean of these results, 57.2±2.3 ps, has been used in this work.

The reported lifetime of the 301 keV level in ^{181}Ta is 21.6±1.7 ps (NDS 73) which has been calculated from an average value of $B(E2)\uparrow = (0.50\pm0.04)\times10^4\ e^2fm^4$.

The lifetime of the 95 keV level in ^{165}Ho has also been measured using several techniques. Armbruster et al. (Ar 70) obtained a value of 40.6±3.4 ps with a microwave beam pulsing system. Blunck et al. (NDS 74) using the Mössbauer Effect obtained a value of 31.7±0.6 ps which is in agreement with the value of 32±1 ps (NDS 74) calculated from the B(E2)↑ result (Ol 60). A weighted mean of 32.0±0.5 ps was adopted for this work.

The lifetime for the 210 keV state in ^{165}Ho is 18.8±1.2 ps (NDS 74) calculated from the measured B(E2)↑ value of (Ol 60) of $(0.63\pm0.04)\times10^4\ e^2fm^4$.

To define the prompt time centroid curve at even lower energies the X-rays of both ^{181}Ta and ^{165}Ho were used. These include the K_α X-rays at 56.28 and 57.54 keV and the K_β X-ray of 65.20 keV in ^{181}Ta and the K_α X-rays of 46.70 and 47.55 keV in ^{165}Ho. X-rays of these energies have very short lifetimes which are illustrated by the measurement of the width of the K_α X-ray transition in ^{197}Au at 68.81 keV to be 54 eV (He 54). This is equivalent to a lifetime of 0.012 fs.

These X-rays together with the γ-ray transitions discussed above define the prompt time centroid curve very well below 165 keV as illustrated in fig. 48. These results were obtained using a 5.0 MeV pulsed proton beam on two targets, one being a 1 mg/cm^2 enriched ^{64}Ni foil and the other composed of two sections consisting of a 110 mg/cm^2 ^{165}Ho foil and a 156 mg/cm^2 ^{181}Ta foil. The centroids at 95, 115, 136, 165, 210 and 310 keV were adjusted to take into account the measured lifetimes of the states from which these transitions occur.

To define the prompt time centroid curve at energies above 150 keV more accurately, a detailed investigation of the lifetimes of the states in ^{64}Cu was performed. ^{64}Cu was chosen because its γ-ray decay scheme (Gr 73) has many transitions between 159 and 600 keV, an important energy region for lifetime investigations. Recently a detailed investigation of the properties of the excited states and γ-ray transitions in ^{64}Cu was done in this laboratory for a Ph.D. dissertation by Green (Gr 73). Fig. 49 shows the level scheme for ^{64}Cu below 927 keV. The states in ^{64}Cu are excited via the ^{64}Ni(p,n)^{64}Cu reaction

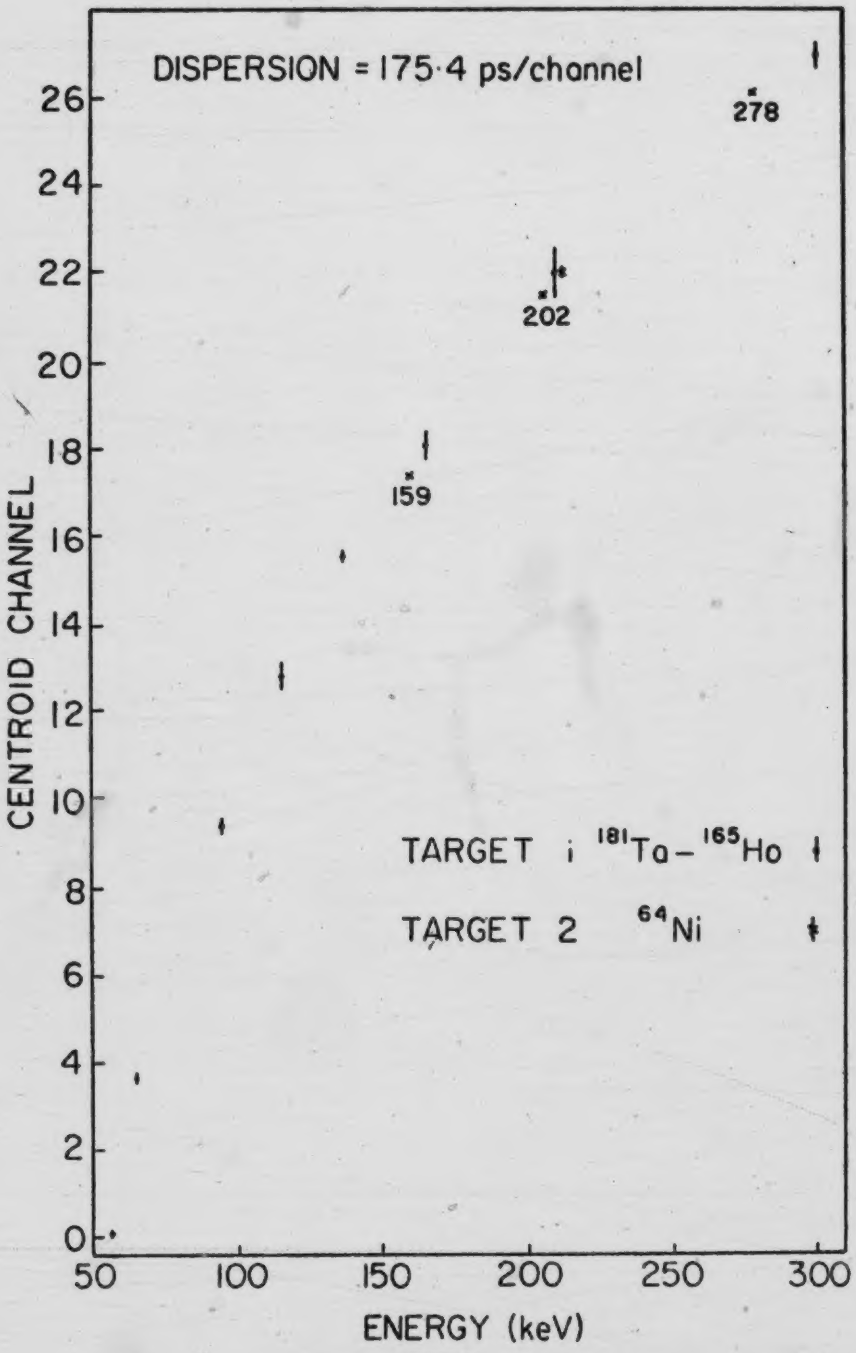

Fig. 48. Centroids of the time distributions for full energy events using the ^{64}Ni foil and the ^{181}Ta-^{165}Ho foil combination.

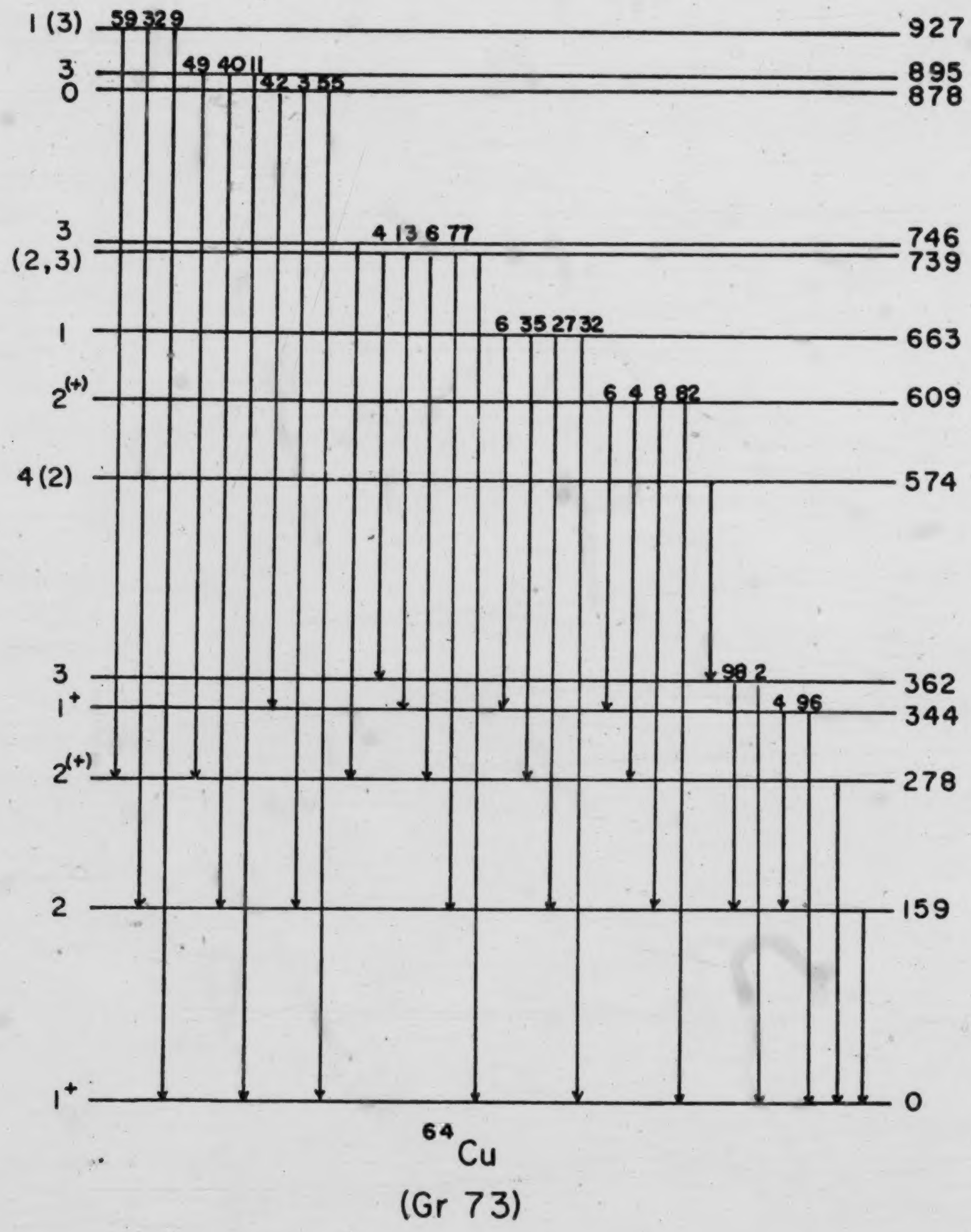
1 (3)
59 32 9
927
3
49 40 11
895
0
42 3 55
878
3
4 13 6 77
746
(2,3)
739
1
6 35 27 32
663
2(+)
6 4 8 82
609
4 (2)
574
3
98 2
362
1+
4 96
344
2(+)
278
2
159
1+
0
64Cu
(Gr 73)

Fig. 49. Experimental level scheme of ^{64}Cu below 927 keV.

which has a Q value of -2.458 MeV. An illustration of the experimental results for the 159, 203, 212 and 278 keV transitions are shown in fig. 48, the centroids being indicated by crosses.

Several other second targets were used in order to provide 'prompt' γ-rays to determine the lifetimes of the levels in ^{64}Cu. The 278 keV level in ^{197}Au which decays to the ground state has a lifetime of 21.6±1.2 ps (NDS 72) which is calculated from the B(E2)↑ and the mixing ratio measurement by McGowan et al.(Mc 71). Thus by using a ^{197}Au foil target the lifetime of the level at 278 keV in ^{64}Cu could be measured.

Two other targets used were NaCl evaporated on ^{181}Ta and natural copper foil. The first excited state at 439 keV in ^{23}Na has a value cited by Endt and van der Leun (En 73) of 1600±80 fs and the first three excited states of ^{63}Cu at 669, 962 and 1327 keV, and ^{65}Cu at 771, 1115 and 1482 keV all have lifetimes less than 1 ps (Wo 70). A final comparison target used was a 1 mg/cm^2 enriched ^{47}Ti foil. The (p,n) reaction excites the states in ^{47}V. The level at 660 keV has been measured to have a lifetime of $4^{+2.8}_{-2}$ ps by the recoil distance technique (Bl 73). This state has three decay modes; a 48% branch to the ground state, a 15% branch to the first excited state via a 572 keV γ-ray and a 37% branch to the third excited state via a 400 keV γ-ray transition.

An example of an experimental run using the ^{64}Ni and ^{47}Ti foils is shown in fig. 50. Eighteen experimental runs were performed to obtain the lifetimes in ^{64}Cu and the results are shown in table 1. The formulation used to calculate the weighted average is that employed in Nuclear Data Sheets: If $x_1 \pm \Delta x_1, x_2 \pm \Delta x_2 \ldots x_n \pm \Delta x_n$ are n independent measurements of a given quantity, the weighted average of these measurements is $\bar{x} \pm \Delta\bar{x}$ where

$$\bar{x} = W \sum x_i/(\Delta x_i)^2$$

and

$$W = \frac{1}{\sum (\Delta x_i)^{-2}}$$

and $\Delta\bar{x}$ is the larger of $(W)^{\frac{1}{2}}$ and $[W\sum\{(\Delta x_i)^{-2}(\bar{x}-x_i)^2\}/n-1]^{\frac{1}{2}}$. In those cases where no centroid shift is observable the result is quoted as an upper limit using the error $\Delta\bar{x}$ as this limit.

The results shown in table 1 indicate that ^{64}Cu is an excellent source of 'prompt' reference γ-rays.

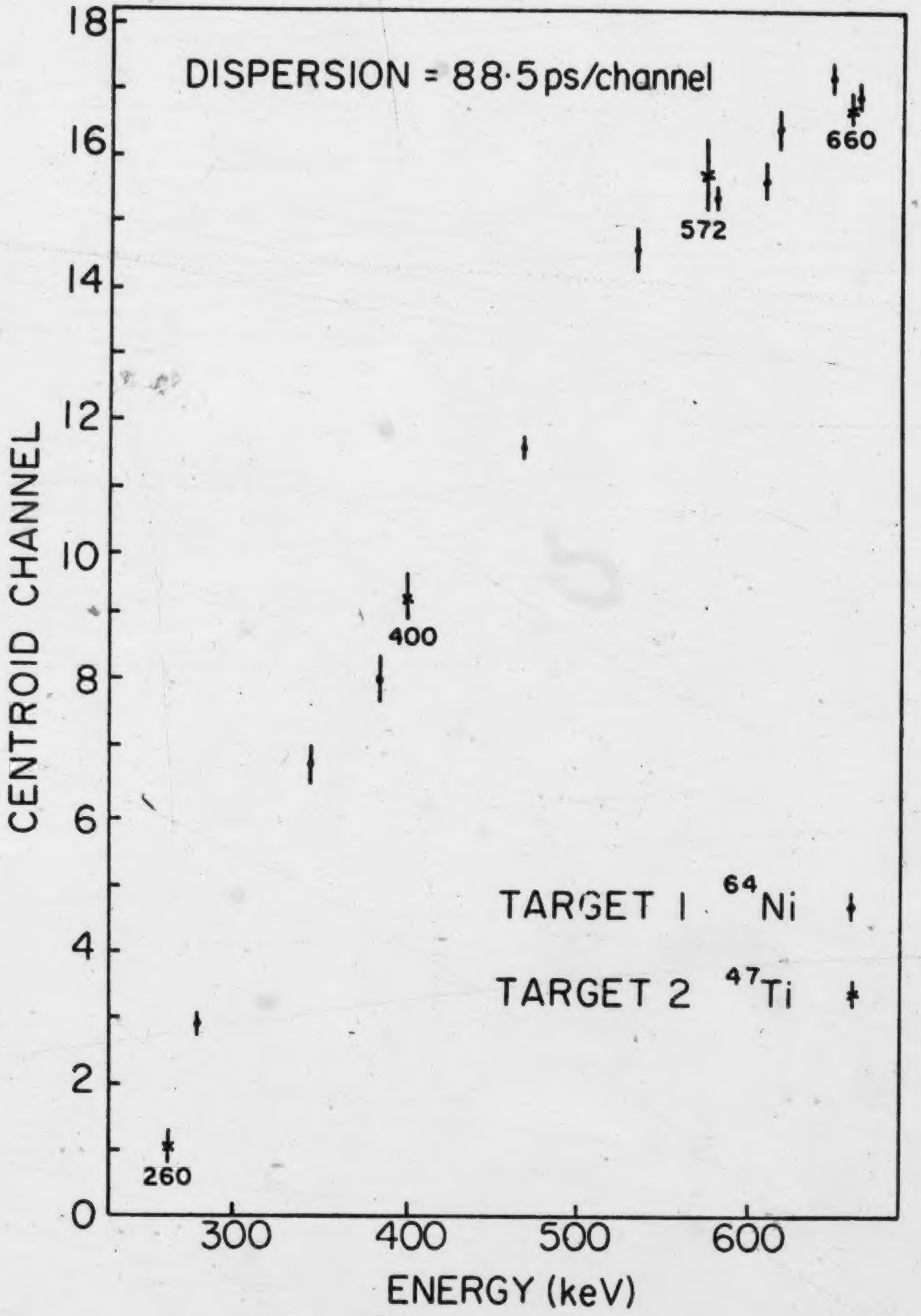

Fig. 50. Experimental results for lifetime determinations in ^{64}Cu using the ^{64}Ni and ^{47}Ti foils.

Table 1

Lifetime results for ^{64}Cu.

Level E_i(keV), I_i^π	Transition to E_f(keV), I_f^π	Branching Ratio (%)	Lifetime (ps)
159 , 2^+	0 , 1^+	100	29.8±5.4
278 , $2^{(+)}$	0 , 1^+	100	6^{+7}_{-6}
344 , 1^+	0 , 1^+	96	<5
362 , 3	159 , 2^+	98	<6
574 , 4(2)	362 , 3	100	9^{+15}_{-9}
609 , 2^+	0 , 1^+	82	<13
633 , 1	0 , 1^+	32	<12
	159 , 2	27	
	278 , $2^{(+)}$	35	
739 ,(2,3)	159 , 2^+	77	<16
746 , 3	278 , $2^{(+)}$	100	<18
878 , 0	344 , 1^+	42	<22
895 , 3	278 , $2^{(+)}$	49	<29
927 , 1(3)	278 , $2^{(+)}$	59	<15

7.2 A Lifetime Study of the Isotopes of Titanium and and Vanadium

The isotopes of Titanium and Vanadium have many low energy excited states whose lifetimes have not been measured or where previous measurements show disagreements in results. It was felt therefore that an investigation of these levels would be useful in obtaining several lifetimes, illustrating the potential of the technique, and would furnish more information on those discrepancies which occur in previous reported measurements.

A complete set of $1\frac{1}{4}" \times \frac{3}{4}"$ rolled isotopically enriched Titanium foils were obtained from Micromatter, Seattle. In addition a ^{64}Ni foil was also obtained. The relevant information on the isotopic analysis and thicknesses is given in table 2.

7.2a ^{45}Ti

The decay scheme for ^{45}Ti as given by Jett et al (Je 68) and Iyengar and Robertson (Iy 71) is shown in fig. 51. Lynch et al (Ly 70) have measured the lifetimes of the first and second excited states to be 4.5±0.5 μs and 17.2±1.0 ns, respectively, using a post acceleration pulsed proton beam. The second excited state has also been measured, using the pulsed proton beam technique, by Blasi et al.(Bl 69) to be 16.6±2.2 ns.

Table 2

Target	Percent Isotopic Composition					Thickness
	A=46	47	48	49	50	mg/cm^2
^{46}Ti	83.8	5.0	9.76	0.73	0.73	1.01
^{47}Ti	1.87	80.1	15.8	1.11	1.1	1.001
^{48}Ti	0.17	0.2	99.36	0.17	0.11	0.981
^{49}Ti	1.33	1.25	14.09	81.61	1.73	1.01
^{50}Ti	1.7	1.3	12.4	1.5	83.2	1.01
	A=58	60	61	62	64	
^{64}Ni	0.92	0.73	0.05	0.38	97.92	0.99

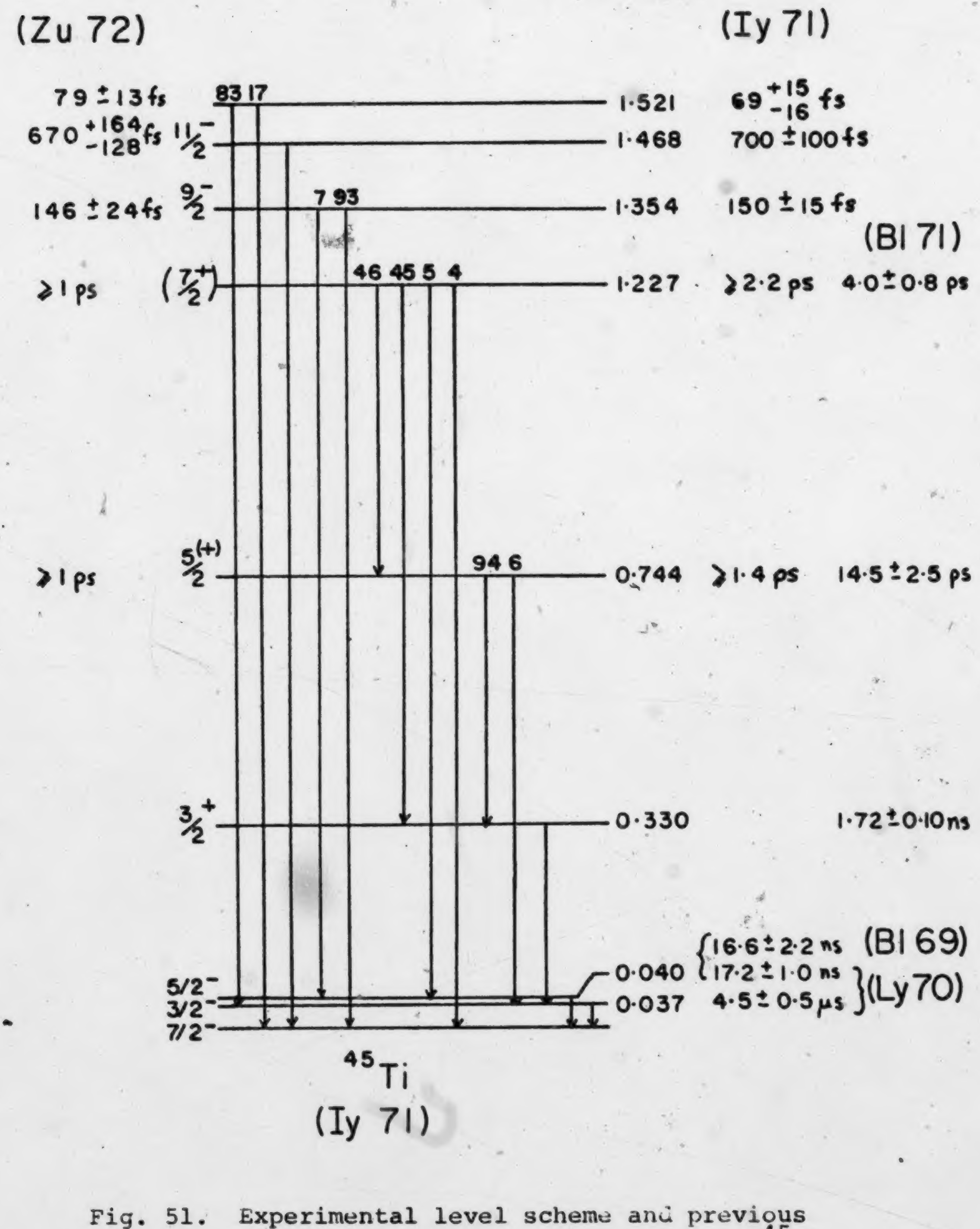
(Zu 72)
(Iy 71)
79 ± 13 fs
83 17
1·521
69 +15 −16 fs
670 +164 −128 fs
11/2−
1·468
700 ± 100 fs
146 ± 24 fs
9/2−
7 93
1·354
150 ± 15 fs
(Bl 71)
≥ 1 ps
(7/2+)
46 45 5 4
1·227
≥ 2·2 ps
4·0 ± 0·8 ps
≥ 1 ps
5/2(+)
94 6
0·744
≥ 1·4 ps
14·5 ± 2·5 ps
3/2+
0·330
1·72 ± 0·10 ns
5/2−
3/2−
7/2−
0·040
0·037
16·6 ± 2·2 ns (Bl 69)
17·2 ± 1·0 ns
4·5 ± 0·5 μs
(Ly 70)
45Ti
(Iy 71)

Fig. 51. Experimental level scheme and previous lifetime results for the states in ^{45}Ti.

The lifetimes of the higher energy levels have been measured by Iyengar and Robertson (Iy 71) and Zuk et al.(Zu 72), both using the Doppler Shift Attenuation Method. Their results are shown in fig. 51. The levels of interest in this work are those which have lower limits i.e. the levels at 330, 744 and 1227 keV. However, these levels have been investigated by Blasi et al.(Bl 71) using the recoil distance technique through the $^{31}P(^{16}O,pn\gamma)^{45}Ti$ reaction at an ^{16}O beam energy of 36 MeV. The following lifetimes were found; 330 keV level, 1.72±0.10 ns; 744 keV level, 14.5±2.5 ps; 1227 keV level, 4.0±0.8 ps.

The two targets used in the investigations were a ^{45}Sc foil, 48 mg/cm^2, and the 1 mg/cm^2 enriched ^{64}Ni foil. Pulsed proton beams of energies 4.2 to 4.5 MeV were used to excite the states in ^{45}Ti and ^{64}Cu via the (p,n) reaction, the Q value for the $^{45}Sc(p,n)^{45}Ti$ reaction being -2.83 MeV. An illustration of the results is shown in fig. 52. The weighted mean of six experimental runs gave a lifetime for the 330 keV level of 1.585±0.020 ns. This result is slightly smaller than that quoted by Blasi et al (Bl 71) of 1.72±0.10 ns. The 293 keV γ-ray transition from the 330 keV level has been found to be isotopic (Iy 71, Zu 72) and therefore no mixing ratio has been found. Assuming the transition to be pure E1, our result

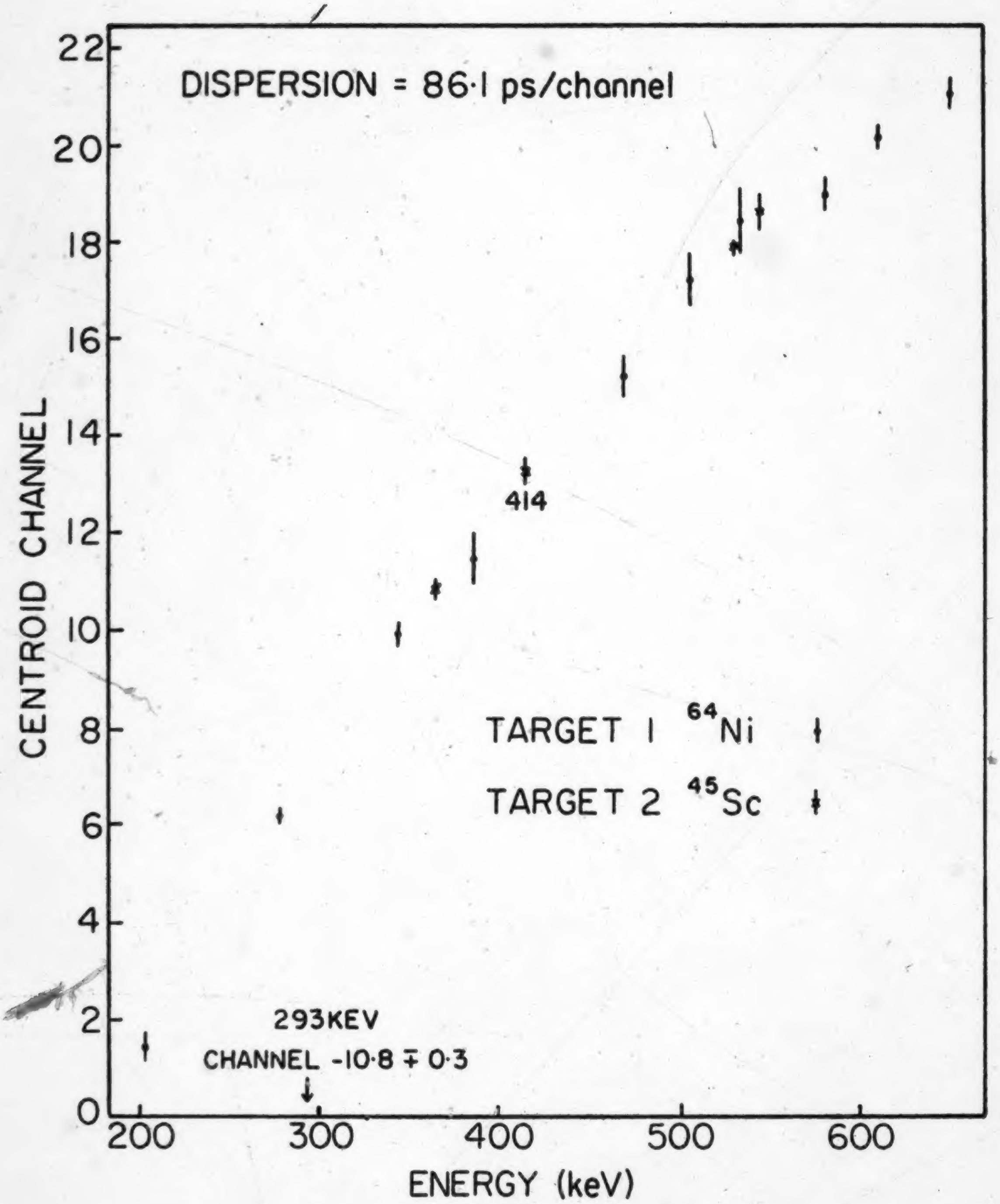

Fig. 52. Experimental results for lifetime determinations in ^{45}Ti.

which yields an experimental E1 transition width $\Gamma(E1) = 4.15 \times 10^{-7}$ eV which using the Weisskopf estimate corresponds to an E1 strength of 1.9×10^{-5} W.u. For a pure M2 mode of decay, the M2 transition strength is 1033 W.u. M2 enhancements of this magnitude are not found, however, the E1 strength is not an unreasonable result and thus the transition is expected to be mainly E1.

No observable shift was seen for the 414 keV γ-ray transition from the 744 keV level and an upper limit of <16 ps was calculated for this level. The parity of the 5/2 spin, 744 keV level is not known, however, Blasi et al.(Bl 71) have suggested a positive parity since this state could be the $5/2^+$ member of a possible rotational band. The 414 keV transition has been found to be isotropic (Iy 71, Zu 72) and thus no mixing ratio has been established. Assuming the lowest mode of decay, a positive parity for the 744 keV level would result in a M1 strength of 0.03 W.u. and a negative parity would lead to an E1 strength of 7.5×10^{-4} W.u. Both these strengths are not uncommon and hence the parity of the state cannot be established from lifetime considerations.

7.2b ^{47}Ti

Fig. 53 shows the decay scheme of ^{47}Ti (We 72). Also indicated are the results of lifetime measurements

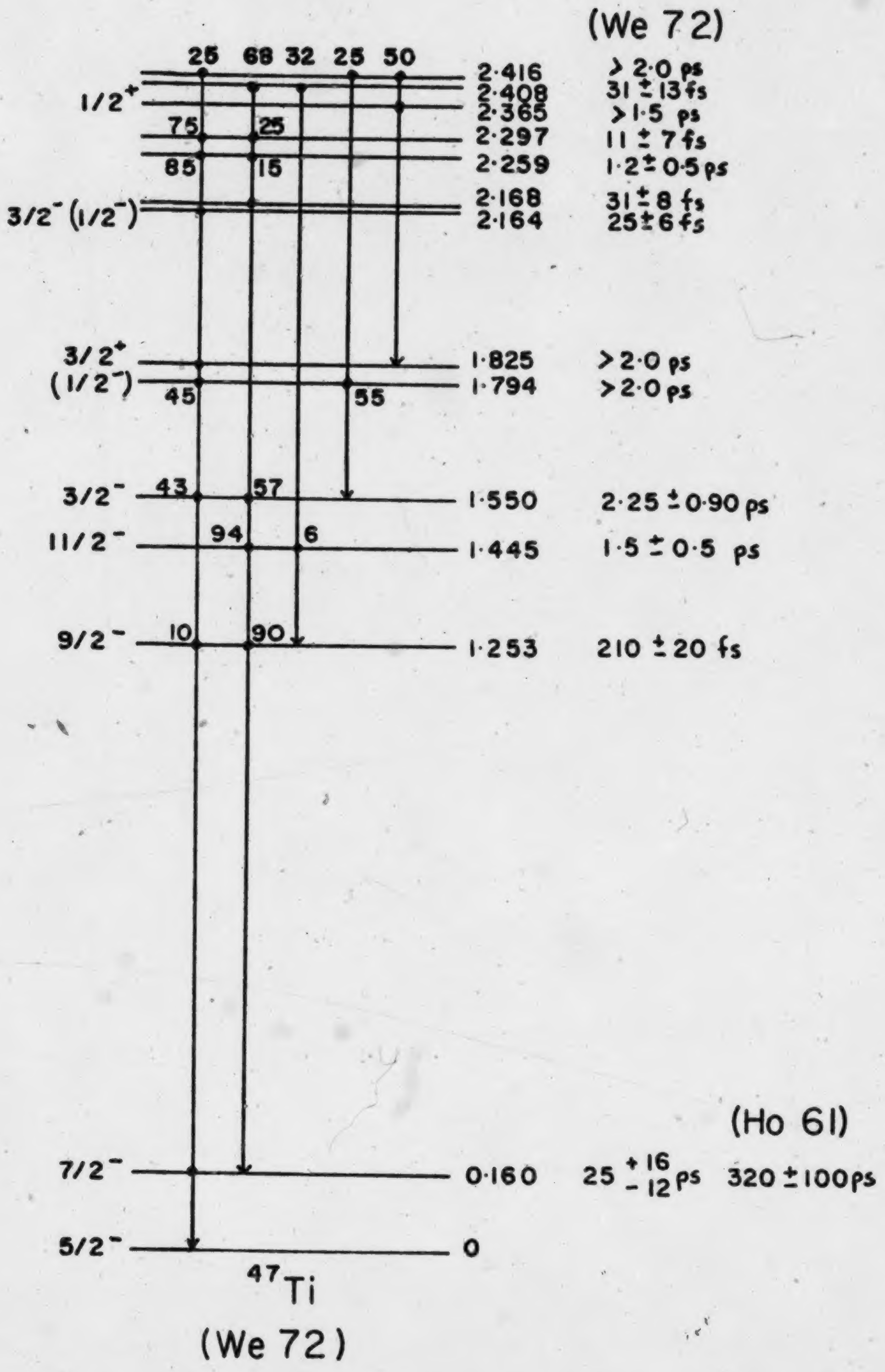
(We 72)
25 68 32 25 50
1/2+
3/2- (1/2-)
2·416 > 2·0 ps
2·408 31 ± 13 fs
2·365 > 1·5 ps
2·297 11 ± 7 fs
2·259 1·2 ± 0·5 ps
2·168 31 ± 8 fs
2·164 25 ± 6 fs
75 25
85 15
3/2+ 1·825 > 2·0 ps
(1/2-) 1·794 > 2·0 ps
45 55
3/2- 43 57 1·550 2·25 ± 0·90 ps
11/2- 94 6 1·445 1·5 ± 0·5 ps
9/2- 10 90 1·253 210 ± 20 fs
(Ho 61)
7/2- 0·160 25 +16 −12 ps 320 ± 100 ps
5/2- 0
47Ti
(We 72)

Fig. 53. Experimental level scheme and previous lifetime results for the states in ^{47}Ti.

using the Doppler Shift Attenuation Method obtained by Weaver et al.(We 72). Of the higher energy levels, the states at 1.794, 1.825, 2.365 and 2.416 MeV are possible candidates for lifetime measurements by our technique. However, the two levels at 2.365 and 2.416 MeV did not provide sufficient yield using the (p,p') reaction reaction to make measurements possible.

For the 160 keV → g.s. transition Weaver et al. (We 72) obtained a mixing ratio of $\delta = 0.027 \pm 0.007$. The B(E2)↑ value for the transition has been determined using Coulomb Excitation by Temmer and Heydenburg (Te 56) and Ritter et al.(Ri 62) who obtained respective values of 396 e^2fm^4 and 280 e^2fm^4 with ±15% errors. These values correspond to a weighted mean value of B(E2)↓ of 239±41 e^2fm^4. Using this result and their mixing ratio, Weaver et al.calculated a lifetime of 25^{+16}_{-12} ps for the 160 keV state. However, Holland and Lynch (Ho 61) using a post acceleration pulsed ^{4}He beam and a NaI(Tl) scintillator detector obtained a lifetime of 320±100 ps for the 160 keV state. A remeasurement of the lifetime of this level is therefore indicated.

Measurements were done on the 160 keV level using the ^{47}Ti foil and the ^{64}Ni foil attached to the 156 mg/cm^2 ^{181}Ta foil. The results of one of the experimental runs are shown in fig. 54. The two points

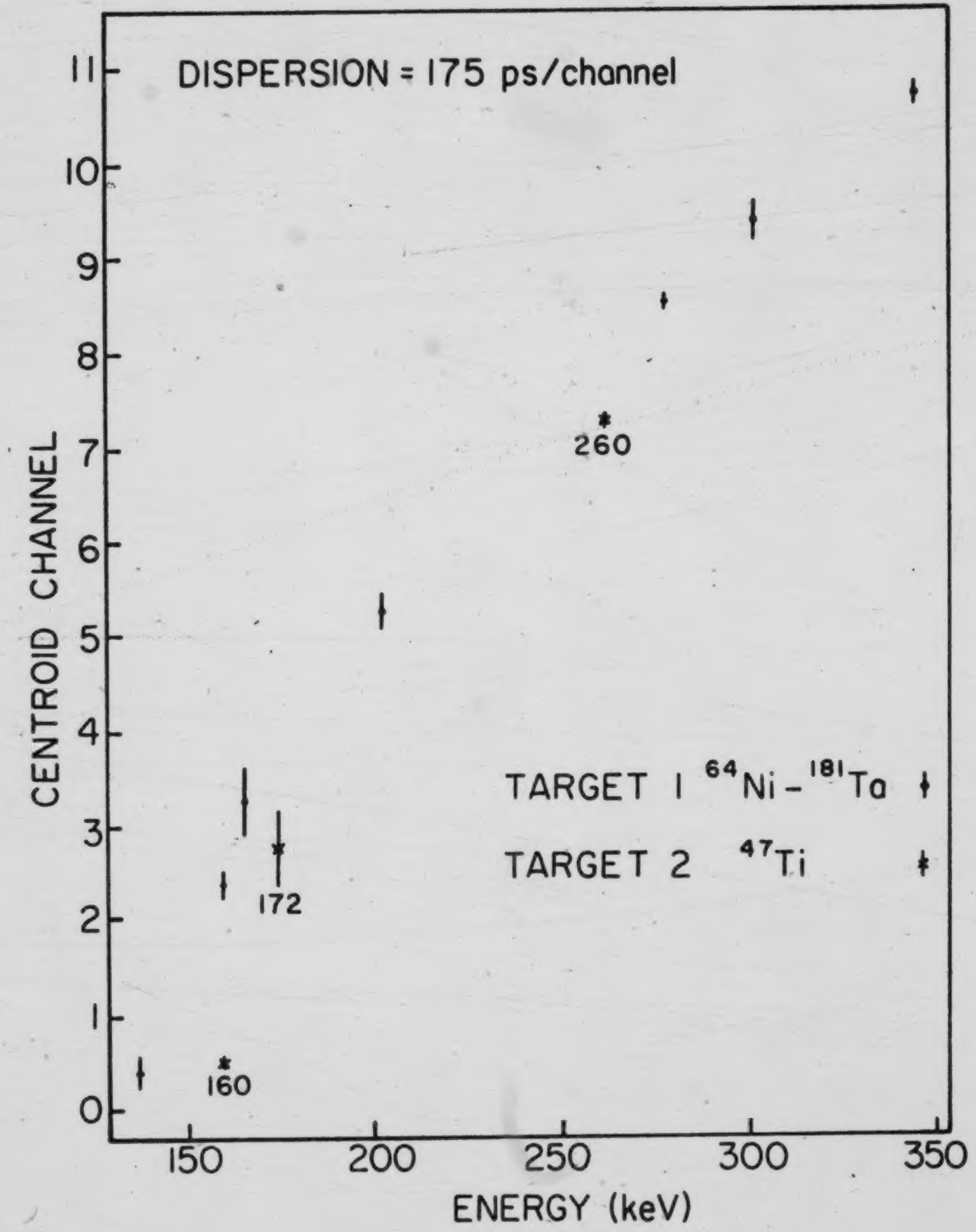

Fig. 54. Experimental results for lifetime determinations in ^{47}Ti and ^{47}V.

at 172 and 260 keV correspond to the decay of the third excited state in ^{47}V which will be discussed in a later section. The weighted mean of eight runs gave a lifetime of 301±8 ps for the 160 keV state which is in agreement with the value obtained by Holland and Lynch.

Using the weighted mean value for the B(E2)↓ and then our result for the lifetime,a mixing ratio of δ = 0.095±0.003 is obtained. From these results the 160 keV → g.s. transition has an E2 strength of 24 W.u. and a M1 strength of 0.03 W.u.

The levels at 1.795 and 1.825 MeV were studied using the ^{47}Ti foil. Two second targets were used, a ^{48}Ti foil and a ^{51}V target prepared by mixing powdered V_2O_5 with benzene and polyurethane and smearing the resulting glue thinly on a piece of gold leaf. This target is commonly referred to as a gloop target. Kavaloski and Kossler (Ka 69) have studied the levels in ^{48}Ti up to 3.74 MeV excitation energy using the Doppler Shift Attenuation Method. Their results and level scheme are shown in fig. 55. Szöghy et al (Sz 73) used the same technique to study the levels in ^{51}Cr below 4.1 MeV excitation. Their results and level scheme are also shown in fig. 55. The ^{51}V(p,n)^{51}Cr reaction Q value is -1.532 MeV, so that the ^{51}V target plus the ^{48}Ti target provide many 'prompt' reference γ-rays for the study of the two levels in ^{47}Ti. As

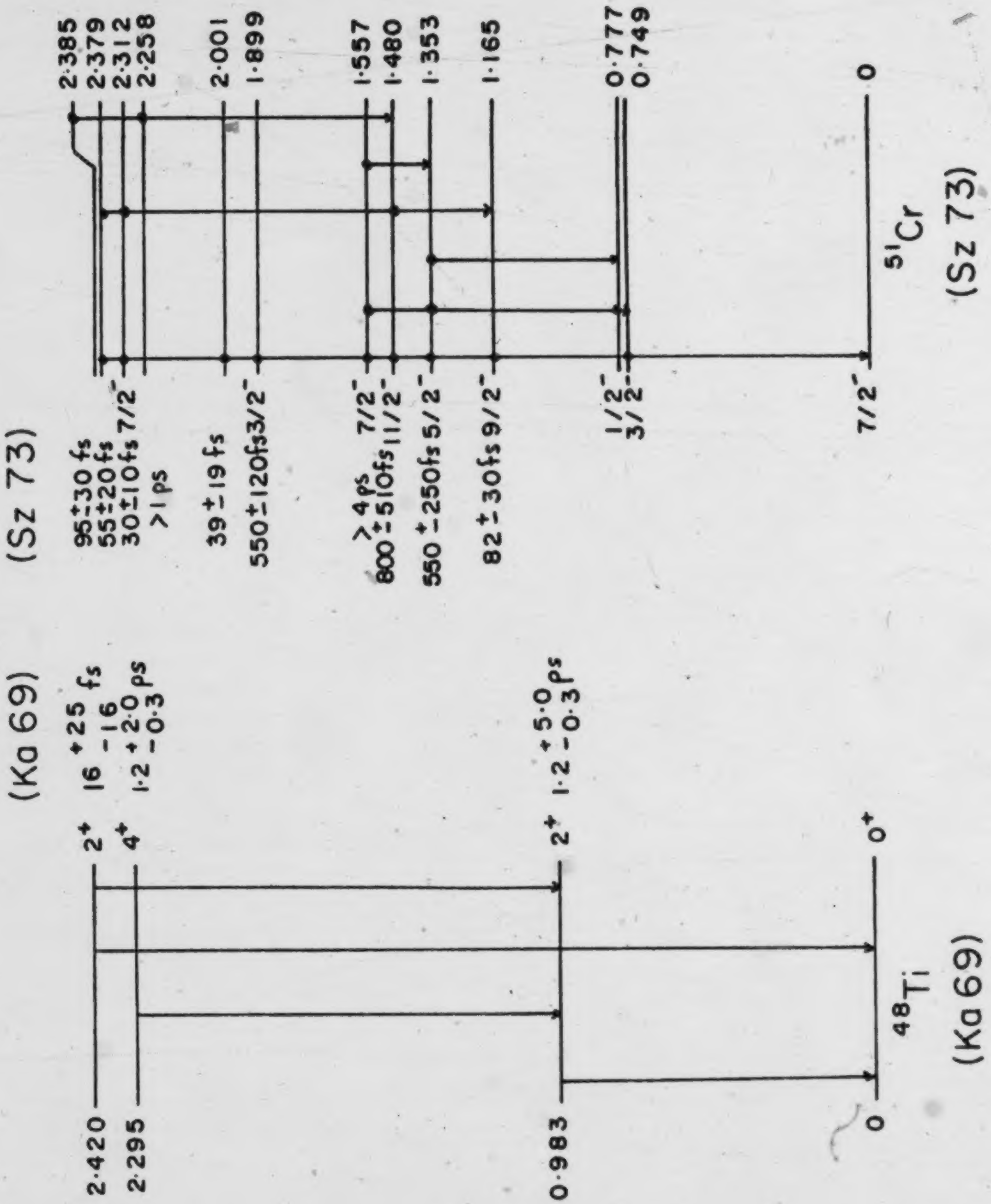
(Ka 69)
2.420
2.295
0.983
0
2+
4+
2+
0+
16 +25 -16 fs
1.2 +2.0 -0.3 ps
1.2 +5.0 -0.3 ps
48Ti
(Ka 69)
(Sz 73)
2.385
2.379
2.312
2.258
2.001
1.899
1.557
1.480
1.353
1.165
0.777
0.749
0
95±30 fs
55±20 fs
30±10 fs 7/2-
>1 ps
39±19 fs
550±120 fs 3/2-
>4 ps 7/2-
800±510 fs 11/2-
550±250 fs 5/2-
82±30 fs 9/2-
1/2-
3/2-
7/2-
51Cr
(Sz 73)

Fig. 55. Experimental level scheme and previous Doppler shift lifetime results for ^{48}Ti and ^{51}Cr.

shown in fig. 53 supplementary 'prompt' γ-rays are also available from the ^{47}Ti target.

The experimental results gave no observable centroid shift for the 1.795 and 1.825 MeV γ-rays and hence upper limits of <23 ps and <10 ps were calculated, respectively, for these levels. Weaver et al have tentatively set a value of spin $1/2^-$ to the 1.795 MeV level. The Weisskopf E2 transition width for the 1.795 MeV transition to the ground state spin $5/2^-$ is 1.51×10^{-4} eV and hence the measured limits on the lifetime correspond to an E2 strength of 0.19 W.u. < (E2) < 2.17 W.u. Weaver et al assign a spin of $3/2^+$ to the 1.825 MeV level with mixing ratios for the ground state transition of either $\delta = 0.219 \pm 0.037$ or $\delta = 2.18^{+0.18}_{-0.16}$. Based on the experimental limits for the lifetimes the first mixing ratio corresponds to limits on the E1 and M2 strengths of 1.16×10^{-5} W.u. < (E1) < 5.96×10^{-5} W.u. and 0.54 W.u. < (M2) < 5.22 W.u., respectively. Similarly for $\delta = 2.18^{+0.18}_{-0.16}$ the following limits are obtained; 1.88×10^{-6} W.u. < (E1) < 1.21×10^{-5} W.u. and 13.6 W.u. < (M2) < 71.9 W.u., respectively. The M2 enhancements obtained for $\delta = 2.18^{+0.18}_{-0.16}$ are rather large so that lifetime considerations indicate that $\delta = 0.219 \pm 0.037$ is the more acceptable mixing ratio for this transition.

7.2c ^{49}Ti

No lifetime information at all has been reported for ^{49}Ti. The level scheme of fig. 56 is that given in Nuclear Data Sheets (NDS 70). Since the ^{49}Ti(p,n)^{49}V Q value is -1.384 MeV, the excited states of ^{49}Ti are not observed using proton inelastic scattering. Hence a 4.0 MeV pulsed deuteron beam was used to investigate the levels in ^{49}Ti. The ^{47}Ti and ^{48}Ti foils were used as the two targets. 'Prompt' reference γ-rays are provided by the ^{47}Ti(d,p)^{48}Ti and the ^{48}Ti(d,n)^{49}V reactions lifetime measurements in ^{49}V are discussed in section 7.2e. The results of one of the experimental runs are shown in fig. 56. No shifts were observed for the 1.381, 1.585 and 1.762 MeV γ-ray transitions in ^{49}Ti. Thus upper limits for the lifetimes of these levels are:

1.381 MeV level < 5 ps

1.585 MeV level < 11 ps

1.762 MeV level < 14 ps.

The 0.342 MeV γ-ray transition from the 1.723 MeV level to the first excited state at 1.381 MeV could not be studied since no suitable 'prompt' reference γ-rays could be found in this energy region using the pulsed deuteron beam.

All the experimental results obtained for the Titanium isotopes are shown in table 3 together with

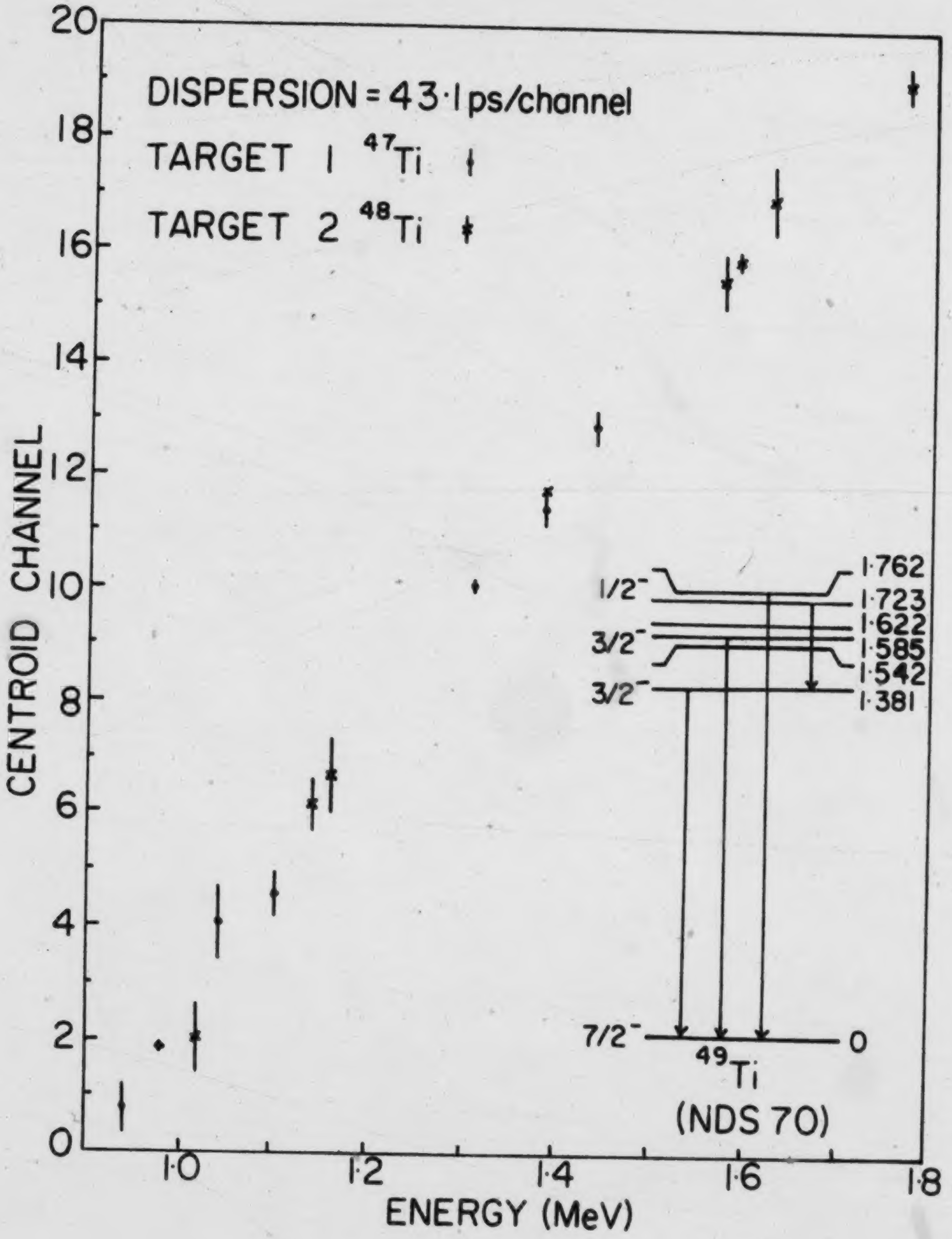

Fig. 56. Experimental results of lifetime determinations in ^{49}Ti.

Table 3

Lifetime results for ^{45}Ti, ^{47}Ti and ^{49}Ti and the corresponding experimental transition strengths.

Isotope Level E_i(keV),I^π	Present Lifetime	Previous Results	Decay to E(keV),I^π	Multipole[a]	Exp.width $\Gamma(\Lambda)$ (eV)	Exp.Strength $\lvert M\rvert^2$ W.u.
^{45}Ti						
330, $3/2^+$	1.585±0.020 ns	1.72±0.10 ns (Bl 71)	37, $3/2^-$	E1	$(4.15\pm0.05)\times10^{-7}$	$(1.90\pm0.02)\times10^{-5}$
				M2 ($\delta=\infty$)	$(4.15\pm0.05)\times10^{-7}$	1033±13
^{47}Ti						
160, $7/2^-$	301±8 ps	300±100 ps (Ho 61) 25^{+16}_{-12} ps (We 72)	0, $5/2^-$	M1[b]	$(2.17\pm0.07)\times10^{-6}$	0.030±0.001
				E2	$(1.96\pm0.06)\times10^{-8}$	24±1
1795,$1/2^-$	<23 ps	>2 ps(We 72)	0, $5/2^-$	E2	$>1.29\times10^{-5}$	$0.09<\lvert M\rvert^2<0.98$
1825,$3/2^+$	<10 ps	>2 ps(We 72)	0, $5/2^-$	E1	$>6.58\times10^{-5}$	$1.23\times10^{-5}<\lvert M\rvert^2<6.16\times$ $\times10^{-5}$
^{49}Ti						
1381,$3/2^-$	<5 ps		0, $7/2^-$	E2	$>1.32\times10^{-4}$	>3.06
1585,$3/2^-$	<11 ps		0, $7/2^-$	E2	$>5.98\times10^{-5}$	>0.69
1762,$(\frac{5}{2}^- \frac{7}{2}^-)$	<14 ps		0, $7/2^-$	M1	$>4.70\times10^{-5}$	$>4.14\times10^{-4}$

a) Assumed $\delta = 0$ unless otherwise specified. b) $\delta = 0.095\pm0.03$.

previous results. The experimental transition widths are also shown with the transition strengths in Weisskopf units for both electric and magnetic γ-ray transition decay modes.

7.2d ^{47}V

Blasi et al (Bl 73) investigated the low lying levels in ^{47}V through the ^{47}Ti(p,n)^{47}V reaction with proton energies between 3.6 and 5.3 MeV and through the ^{40}Ca(^{10}B,2pn)^{47}V reaction at a beam energy of 25 MeV. Their level scheme is shown in fig. 57. The only lifetime measurements on the levels in ^{47}V have been performed by Blasi et al.(Bl 73) using the recoil distance technique to study the levels at 260 keV and above and a pulsed proton beam to obtain upper limits of <1ns for both the levels at 88 and 146 keV. Their results are also shown in fig. 57.

The level at 260 keV was studied using the ^{47}Ti foil and the ^{64}Ni-^{181}Ta foil combination as the second target. The ^{47}Ti(p,n)^{47}V reaction has a Q value of -3.690 MeV. An example of the experimental results is shown in fig. 54 of section 7.2b. The weighted mean of six experimental runs yielded a lifetime of 78±11 ps for the 260 keV level which is in agreement with the result of 90±12 ps obtained by Blasi et al. The spins of the 260 keV level and ground

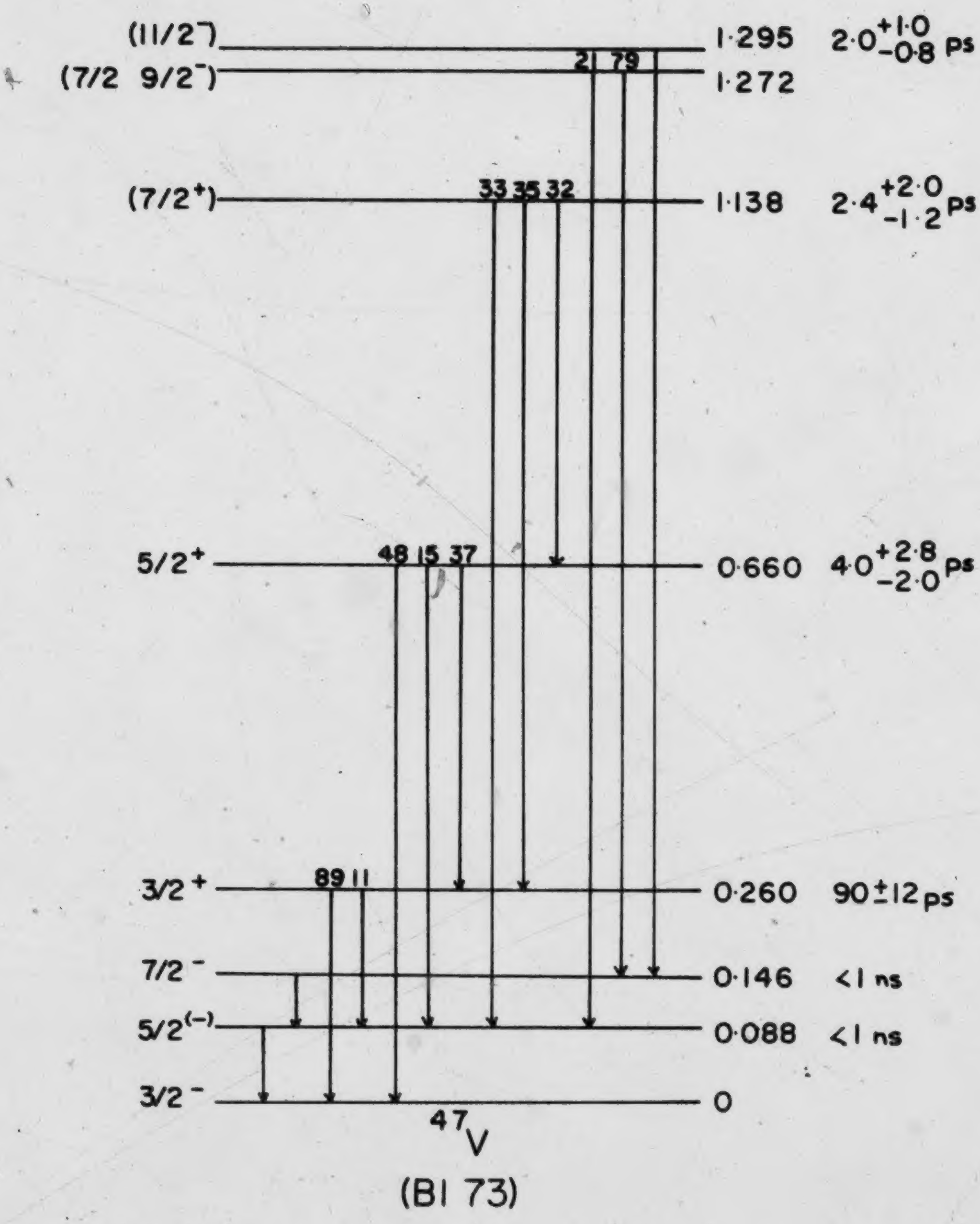
(11/2⁻)
(7/2 9/2⁻)
(7/2⁺)
5/2⁺
3/2⁺
7/2⁻
5/2⁽⁻⁾
3/2⁻
1·295
1·272
1·138
0·660
0·260
0·146
0·088
0
$2.0^{+1.0}_{-0.8}$ ps
$2.4^{+2.0}_{-1.2}$ ps
$4.0^{+2.8}_{-2.0}$ ps
90±12 ps
<1 ns
<1 ns
21 79
33 35 32
48 15 37
89 11
^{47}V
(BI 73)

Fig. 57. Experimental level scheme and previous lifetime results for ^{47}V.

state are $3/2^+$ and $3/2^-$, respectively, and hence assuming a pure E1 decay mode the present result leads to an E1 transition strength of 5.46×10^{-4} W.u.

The levels at 88 and 146 keV were studied using as the second target the ^{181}Ta-^{165}Ho foil combination and a 5.0 MeV pulsed proton beam. Typical experimental results are shown in fig. 58. The resulting lifetime of the 146 keV level observed by the 58 keV γ-ray transition to the 88 keV level is 786±95 ps. The centroid shift of the 88 keV γ-ray is equivalent to 1173±37 ps. However, the contribution to the centroid shift by the cascading 58 keV γ-ray must be established at the angle of observation in order to determine the lifetime of the 88 keV level.

To establish the contribution, an angular distribution of the 58 and 88 keV γ-rays was performed using a d.c. proton beam at an energy of 5.0 MeV. The results which have been corrected for absorption in the walls of the target chamber and the relative detector efficiency are shown in fig. 59. The angular distributions are seen to be nearly isotropic.

The angular distribution of nuclear γ-rays can be written in the form (Ro 67)

$$W(\theta) = \sum_{k \text{ even}} a_k P_k(\cos\theta) \quad . \qquad 7.1$$

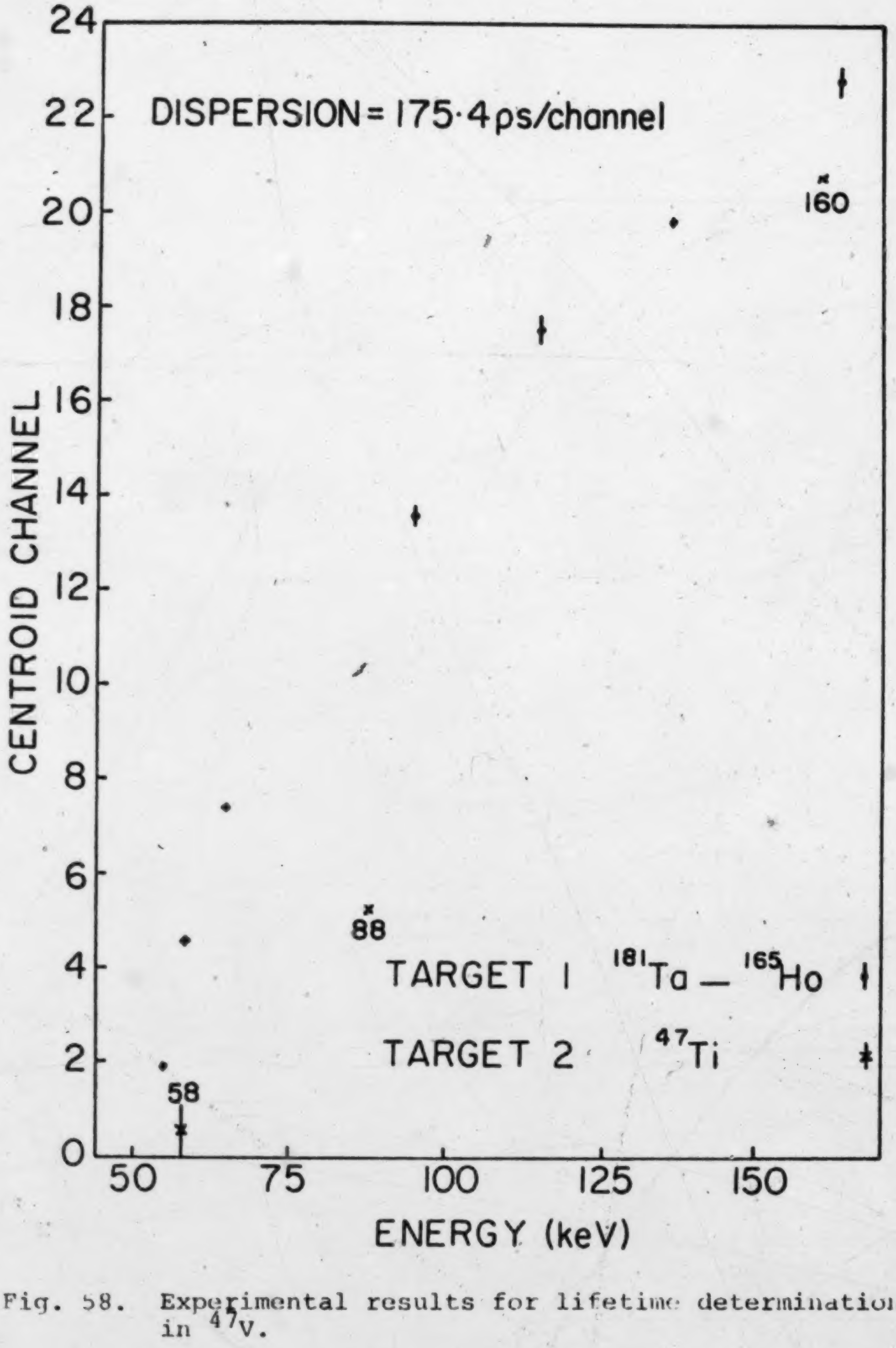

Fig. 58. Experimental results for lifetime determinations in ^{47}V.

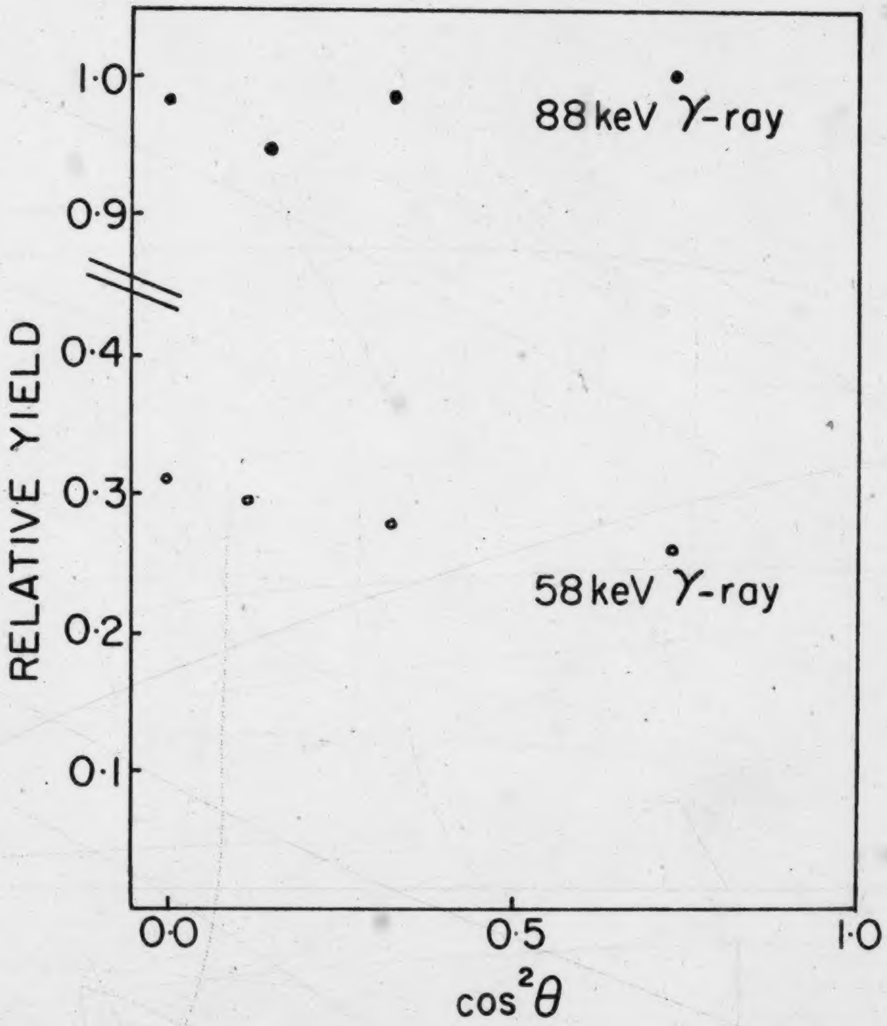

Fig. 59. Relative angular distributions for the 58 and 88 keV γ-ray transitions in ^{47}V.

Rose and Brink (Ro 67) have shown that, if only two multipolarities L and L' are present in the decay, the coefficients a_k can be written

$$a_k = \frac{B_k(J_1)}{1+\delta_{12}^2}\left[R_k(LLJ_1J_2) + 2\delta_{12}R_k(LL'J_1J_2) + \delta_{12}^2 R_k(L'L'J_1J_2)\right] \qquad 7.2$$

where J_1 is the spin of the decaying state, J_2 the spin of the final state, and δ_{12} is the mixing ratio of the radiation. The R_k coefficients are "geometric" factors containing vector coupling coefficients and are determined completely by the spins and multipolarities involved in the decay. The $B_k(J_1)$ coefficient contains the physics of the formation of the state J_1, and is related to the population parameters $P(m_1)$ of the substates of J_1.

$$B_k(J_1) = \sqrt{2J_1+1} \sum_{m_1=-J_1}^{J_1} (-)^{J_1-m_1}(J_1J_1m_1-m_1|k0)P(m_1) \quad . \qquad 7.3$$

The $B_k(J_1)$ coefficients have been calculated (Gr 71) using the Compound Nuclear Statistical Model (Sh 66) for the analysis of the (p,nγ) reaction. In this model the substates in the residual nucleus are almost equally populated to $m_1 = J(\text{target}) + 1$.

If the state of spin J_2 should cascade to another state spin J_3 and if this cascade is observed then the nuclear alignment parameters $B_k(J_1)$ in eq. 7.2 must be replaced by $B_k(J_1)U_k(J_1J_2)$ where

$$U_k(J_1J_2) = [U_k(LJ_1J_2) + \delta_{12}^2 U_k(L'J_1J_2)]/(1+\delta_{12}^2) \quad . \qquad 7.4$$

L, L' and δ_{12} refer to the cascade from state spin J_1 to state spin J_2 and $U_k(LJ_1J_2)$ are coefficients containing vector coupling coefficients determined completely by the spins and multipolarities involved in the decay. δ_{12} in eq. 7.2 must also be replaced by δ_{23}.

Assuming the maximum limit for E2 enhancements as used in Nuclear Data Sheets of 1000 W.u., an upper limit for the mixing ratio of $|\delta| < 0.08$ is obtained for the 146 → 88 keV γ-ray transition using the present result for the lifetime of the 146 keV level. Using this value and the slope of the 58 keV γ-ray angular distribution to obtain a value of a_2 [calculations yield $a_4 \approx 0$], eq. 7.2 gives $B_2(J_1) = -0.076$. This small value of $B_2(J_1)$ is expected since the target nucleus ^{47}Ti has a ground state spin $5/2^-$ and thus equal substate populations are expected up to $m_1 = 7/2^-$ which is the spin of the 146 keV state. Equal substate populations result in an isotropic angular distribution since $B_2(J_1) = 0$.

Because $B_2(J_1) \approx 0$, the angular distribution of the 88 keV γ-ray should also be isotropic and thus using the relative a_o coefficients as obtained from fig. 59 the lifetime for the 88 keV level was calculated to be 951±52 ps. Menti (Me 67) has done Internal Conversion Measurements on ^{47}V and according to him the 88 keV state decays 98% of the time via the M1 mode to the ground state. Hence assuming a pure M1 decay the present result corresponds to a M1 strength of 0.05 W.u. Again, assuming a pure M1 decay for the 146 →88 keV γ-ray transition, the present result of 786±95 ps for the lifetime of the 146 keV level yields a M1 strength of 0.21 W.u.

7.2e ^{49}V

The level scheme of ^{49}V is shown in fig. 60 from the work of Blasi et al (Bl 71A). The lifetimes of the levels above the second excited state have been studied using the Doppler Shift Attenuation method by Kiuru (Ki 72) using the $^{48}Ti(p,\gamma)^{49}V$ reaction at a maximum beam energy of 1.57 MeV and recently by Tabor and Zurmühle (Ta 74) using the $^{46}Ti(\alpha,p)^{49}V$ reaction at a beam energy of 10 MeV. Their results are shown in fig. 60. The lifetimes measured by Tabor and Zurmühle for the 748 and 1140 keV levels are substantially larger than those reported by Kiuru. However, most of the other

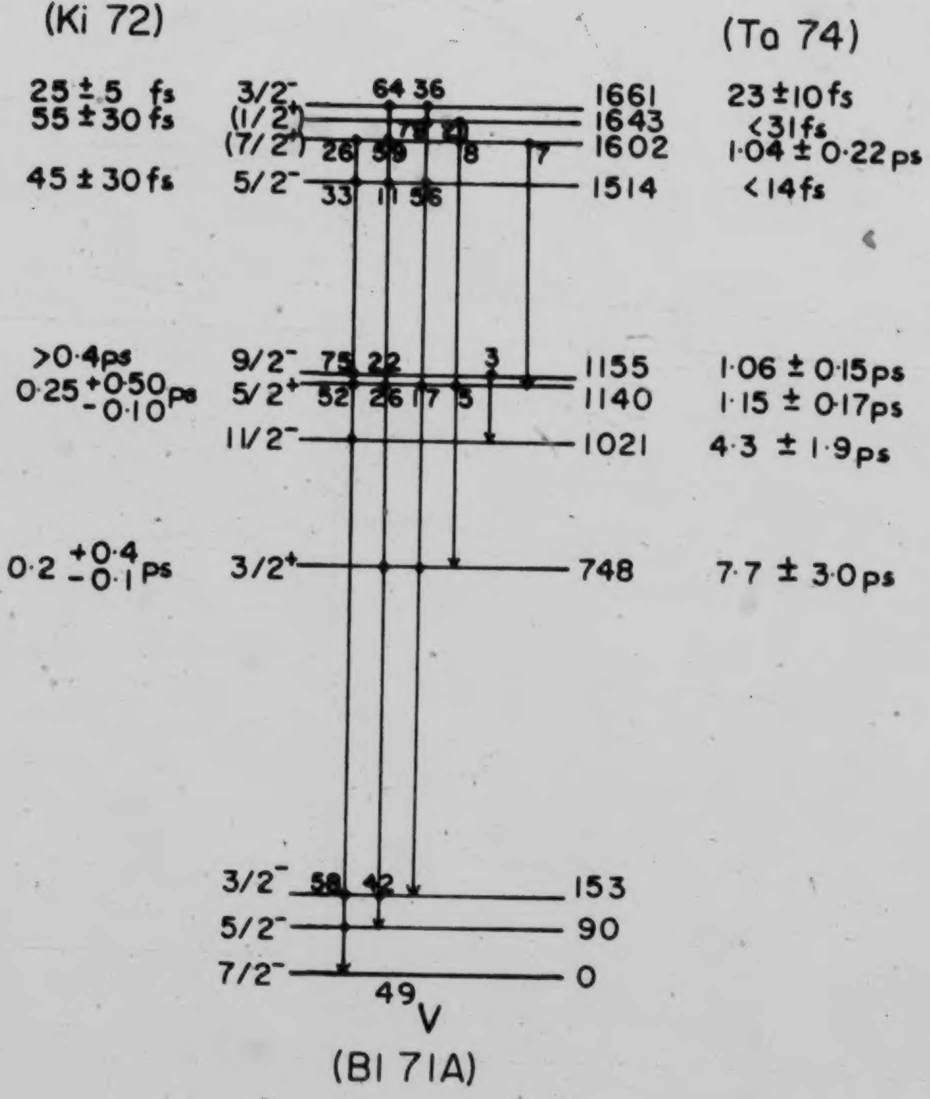
(Ki 72)
(To 74)
25 ± 5 fs
55 ± 30 fs
45 ± 30 fs
3/2⁻
(1/2⁺)
(7/2⁺)
5/2⁻
64 36
78 21
26 59 8 7
33 11 56
1661
1643
1602
1514
23 ± 10 fs
<31 fs
1.04 ± 0.22 ps
<14 fs
>0.4 ps
0.25 +0.50 -0.10 ps
9/2⁻
5/2⁺
11/2⁻
75 22 3
52 26 17 5
1155
1140
1021
1.06 ± 0.15 ps
1.15 ± 0.17 ps
4.3 ± 1.9 ps
0.2 +0.4 -0.1 ps
3/2⁺
748
7.7 ± 3.0 ps
3/2⁻
5/2⁻
7/2⁻
58 42
153
90
0
49V
(Bl 71A)

Fig. 60. Experimental level scheme and previous lifetime results for states in ^{49}V.

lifetimes are in reasonable agreement. Brown et al (Br 74) using the recoil distance technique and the $^{46}Ti(\alpha,p)^{49}V$ reaction at a beam energy of 11 MeV obtained a value of 5.1±1.0 ps for the 1021 keV level.

The lifetime of the level at 153 keV has been measured using several techniques. Currie (Cu 63) using a β^+-γ delayed coincidence technique obtained a value of 29.7±0.8 ns. Blasi et al (Bl 71A) using a pulsed proton beam obtained a lifetime of 28.9±2.9 ns and finally Vingiani et al (Vi 72) using a γ-γ delayed coincidence technique obtained a value of 28.7±0.5 ns.

Two measurements of the lifetime of the first excited state at 90 keV have been reported both using the β^+-γ delayed coincidence technique. Cheung and Mark (Ch 71) obtained the value of 620±29 ps while Okon et al (Ok 73) measured the lifetime to be 476± 29 ps. These results are seen to be in disagreement and a remeasurement of the lifetime of the 90 keV level would provide more information about this state.

The ^{49}Ti foil was used to study the levels in ^{49}V via the $^{49}Ti(p,n)^{49}V$ reaction which has a Q value of -1.384 MeV. Supplementary 'prompt' reference γ-rays were obtained using as the second targets the ^{181}Ta-^{165}Ho foil combination and the ^{64}Ni-^{181}Ta foil combination. Due to the long lifetime of the 153 keV level the Slope Method was used to calculate the lifetime. Fig. 61 shows

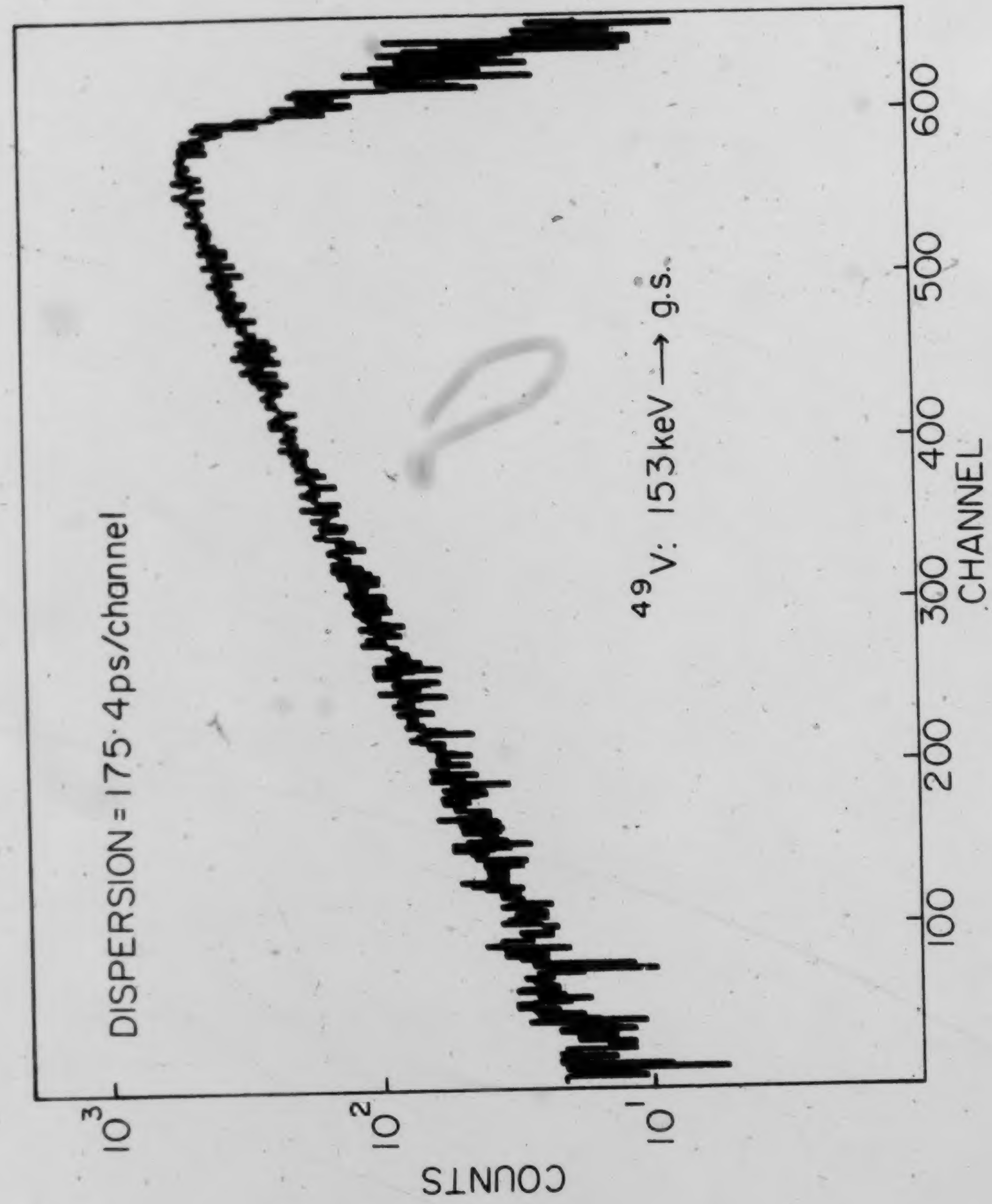

Fig. 61. Logarithmic plot of the delayed time distribution of the 153 keV →g.s. transition in ^{49}V.

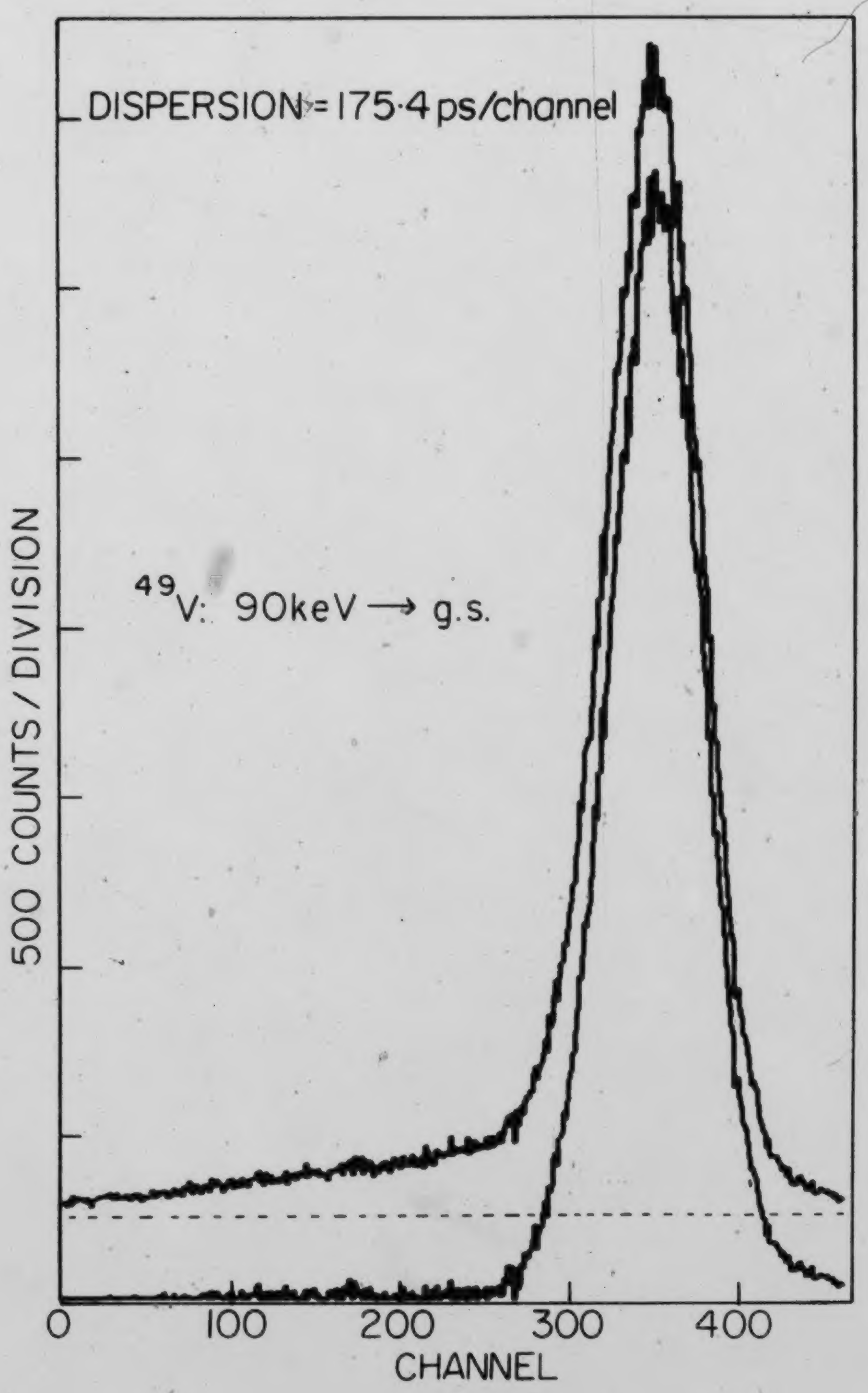

Fig. 62. The delayed time distribution for the 90 keV →g.s. transition in ^{49}V before and after the subtraction of the tail contrition due to the 153 → 90 keV decay.

a logarithmic plot (base 10) of the delayed time distribution obtained from the 153 keV → g.s. decay. A background subtraction has been performed on the result shown in fig. 61. A least squares fit to the slope from seven experimental runs yielded a lifetime of 28.71±0.35 ns. This result is in excellent agreement with the previous results.

The 153 keV transition is expected to be solely E2 in character since the transition proceeds from the $3/2^-$ 153 keV level to the $7/2^-$ spin ground state via a 58% branch. The experimental transition width for this decay is 1.33×10^{-8} eV and so our experimental determination of the lifetime corresponds to an E2 strength of 18.5 W.u.

The calculation of the lifetime of the 90 keV level is complicated by the 42% branch from the 153 keV level and thus the delayed time distribution for the 90 keV γ-ray transition has a tail as illustrated in fig. 62. The analysis entailed first the subtraction of the background contributions from ~~the~~ time distributions of the 90 and 153 keV γ-rays. Using the delayed time distribution of the 153 keV γ-ray, a fit was made to the tail of the time distribution for the 90 keV γ-ray and a subtraction performed. Account was taken of the walk with energy of the prompt time centroid curve between the two energies, 90 and 153 keV. The resulting time distribution for the 90 keV γ-ray is shown in fig. 62. Since the tail contribution is relatively small compared to the time contribution to the 90 keV γ-ray decay from direct population of the state by the (p,n) reaction, a 100% error in the determination of the walk of the prompt time centroid curve would only lead to an error of 15 ps in the final result.

Another point considered was the effect of the small change in FWHM between prompt time distributions at 90 and 153 keV. An investigation of this effect indicated that a maximum possible error of 20 ps could occur.

An example of the experimental results using a 5.0 MeV pulsed proton beam and the two targets, the ^{49}Ti foil and the ^{181}Ta-^{165}Ho foil combination, are shown in fig. 63. The weighted mean of six experimental runs yielded a lifetime for the 90 keV level of 329±19 ps. This result does not agree with either of the previous results.

The total internal conversion coefficient for the 90 keV transition has been measured by Menti (Me 67) to be 0.034. According to him the 90 keV state decays more than 99% of the time via the M1 mode to the ground state. Thus assuming a pure M1 transition the M1 strength for this transition is 0.13 W.u.

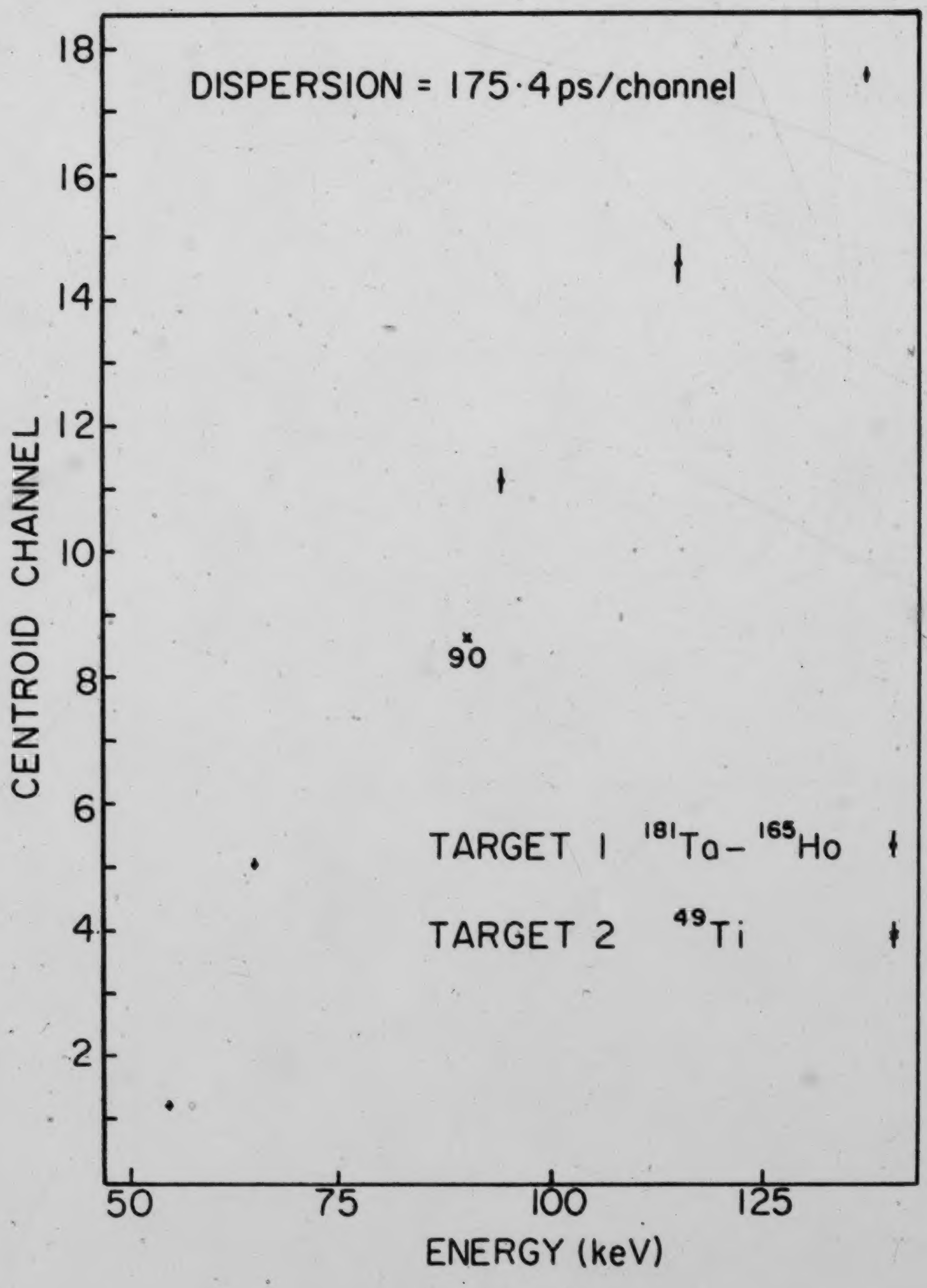

Fig. 63. Experimental results for the determination of the lifetime of the 90 keV level in ^{49}V.

7.2f ^{50}V

Very little experimental work has been reported for ^{50}V. However, Blasi et al (Bl 69A) studied the decay and level scheme of the low energy states and their results are shown in the insert to fig. 64. They found that there was no direct feeding of the levels at 226 and 320 keV using the (p,n) reaction at proton energies below 4.5 MeV and that these levels are fed by cascading γ-rays from the levels at 355 and 388 keV.

Both Temmer and Heydenburg (Te 56) and Fagg et al (Fa 56) obtained by Coulomb Excitation measurements a value for the reduced transition probability $B(E2)\uparrow$ of 110 e^2fm^4 for the 226 keV level which is equivalent to an E2 partial lifetime of $\tau(E2) = 10.6$ ns. Blasi et al (Bl 69A) using a pulsed beam gave an upper limit of 3 ns to this level, which suggests a strong magnetic dipole contribution.

Experimental investigations on the low lying energy levels of ^{50}V were performed using the 1 mg/cm^2 enriched ^{50}Ti foil and two second targets: The ^{64}Ni foil to study the 226 keV γ-ray transition and the ^{181}Ta-^{165}Ho foil combination to study the 94 keV transition. Pulsed proton beams of 4 to 4.4 MeV were used to excite the states in ^{50}V via the $^{50}Ti(p,n)^{50}V$ reaction which has a Q value of -2.997 MeV. Typical

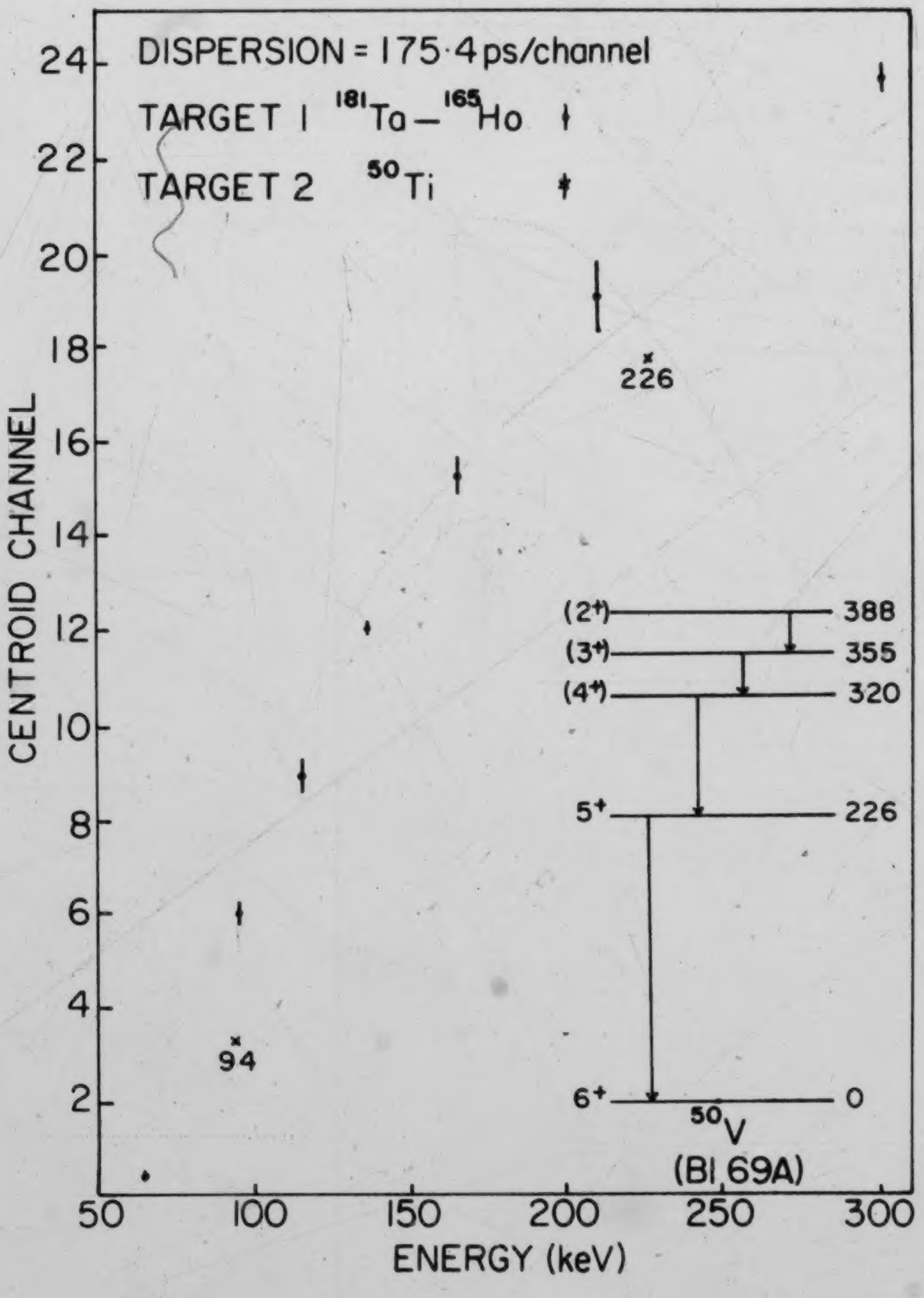

Fig. 64. Experimental results for lifetime determinations in ^{50}V. The insert shows the level scheme of ^{50}V.

results are shown in fig. 64. Within the error bars an identical centroid shift was observed for the 94 keV and 226 keV transitions in all experimental runs. Since the 226 keV level is fed entirely by the 94 keV γ-ray cascade from the 320 keV level the lifetime of the 226 keV level must be short. The present result is $\tau < 16$ ps which is the calculated error in the difference of the weighted means of the centroid shifts for the 94 and 226 keV transitions.

The 320 keV level is also fed entirely from γ-ray cascades from the 355 keV level and hence only an upper limit of <450 ps for lifetime of the 320 keV level could be calculated.

The Weisskopf estimate of the M1 partial lifetime for the 226 keV transition is $\tau_\omega(\mathrm{M1}) = 2.7$ ps and hence our result of <16 ps indicates a strong magnetic dipole contribution to this transition. The Weisskopf estimates of the M1 partial lifetimes for the 94 keV transition from the 320 keV level and the 35 keV transition from the 355 keV level are $\tau_\omega(\mathrm{M1}) = 38$ ps and $\tau_\omega(\mathrm{M1}) = 741$ ps, respectively. Our upper limit of <450 ps for the lifetime of the 320 keV level suggests that the apparent lifetime is mostly due to the feeding of the 320 keV level by the 35 keV γ-ray transition from the 355 keV state.

7.2g ^{51}V

^{51}V has received extensive experimental and theoretical study due to its closed shell of 28 neutrons. The level scheme shown in fig. 65 is from the work of Goodman and Donahue (Go 72) and Horoshko et al (Ho 70). Also shown are the lifetimes obtained by Goodman and Donahue using the Doppler Shift Attenuation technique. Only one measurement has been reported for the second excited state at 928 keV, that by Singh et al (Si 70), who obtained a lifetime of 101±36 ps using the delayed coincidence technique and recording the delays between the β^- rays from the 5·8 min ^{51}Ti feeding levels in ^{51}V and the following γ-rays. They also obtained a lifetime of 274±43 ps for the first excited state at 320 keV. Many other measurements on the lifetime of the first excited state have been reported and the results are shown in the insert to fig. 65. The weighted average of these results is 290±20 ps.

For our experiments a gloop ^{51}V target was prepared and the ^{64}Ni foil was used as the second target. One set of results is shown in fig. 66. A weighted mean of three experimental runs yielded a lifetime for the 320 keV level of 266±9 ps which is in agreement with the previous results.

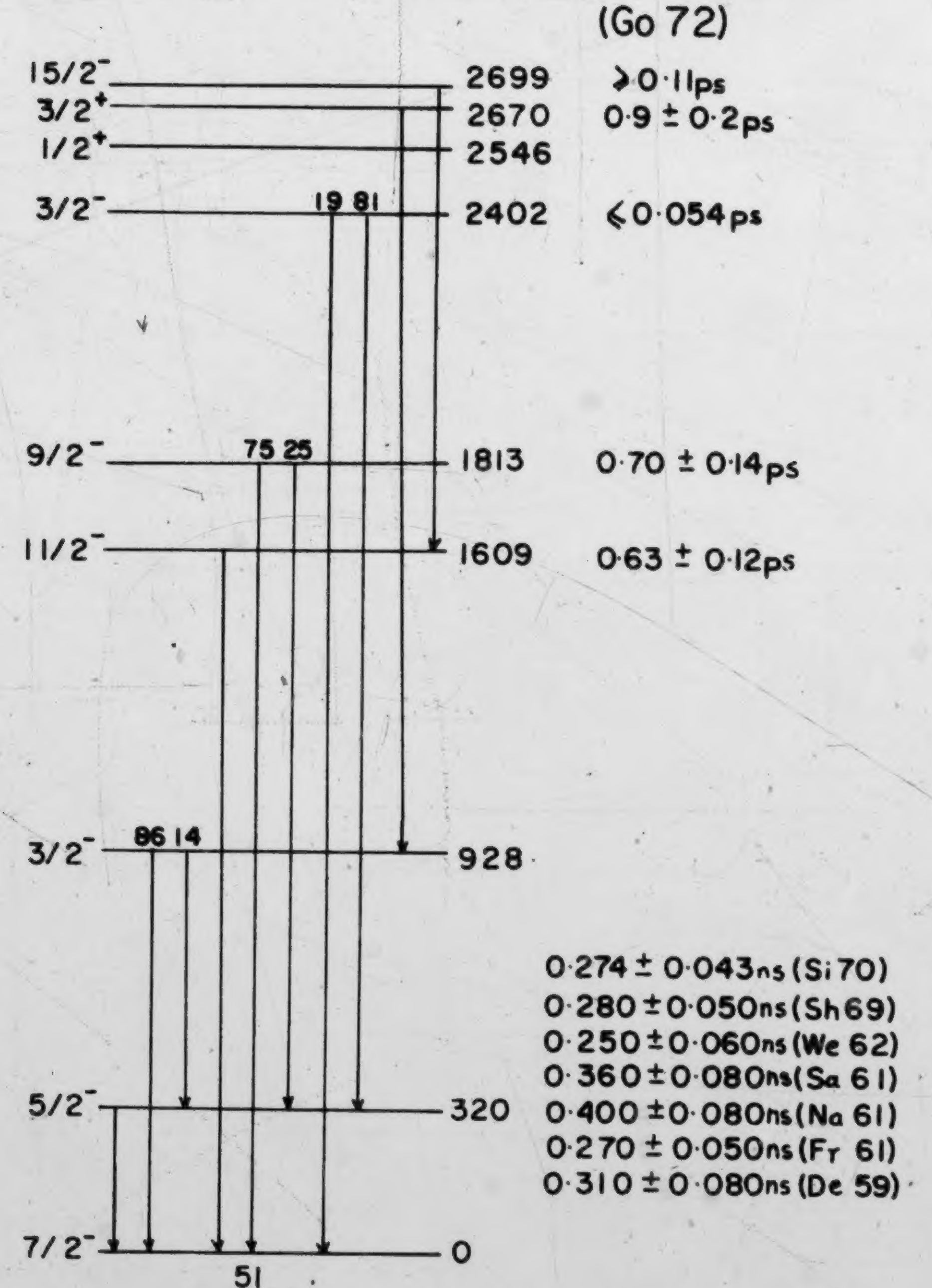
(Go 72)
15/2⁻
3/2⁺
1/2⁺
3/2⁻
9/2⁻
11/2⁻
3/2⁻
5/2⁻
7/2⁻
2699
2670
2546
2402
1813
1609
928
320
0
≥0·11ps
0·9 ± 0·2ps
≤0·054ps
0·70 ± 0·14ps
0·63 ± 0·12ps
19 81
75 25
86 14
0·274 ± 0·043ns (Si 70)
0·280 ± 0·050ns (Sh 69)
0·250 ± 0·060ns (We 62)
0·360 ± 0·080ns (Sa 61)
0·400 ± 0·080ns (Na 61)
0·270 ± 0·050ns (Fr 61)
0·310 ± 0·080ns (De 59)
51 V
(Ho 70) (Go 72)

Fig. 65. Experimental level scheme and previous lifetime results for ^{51}V.

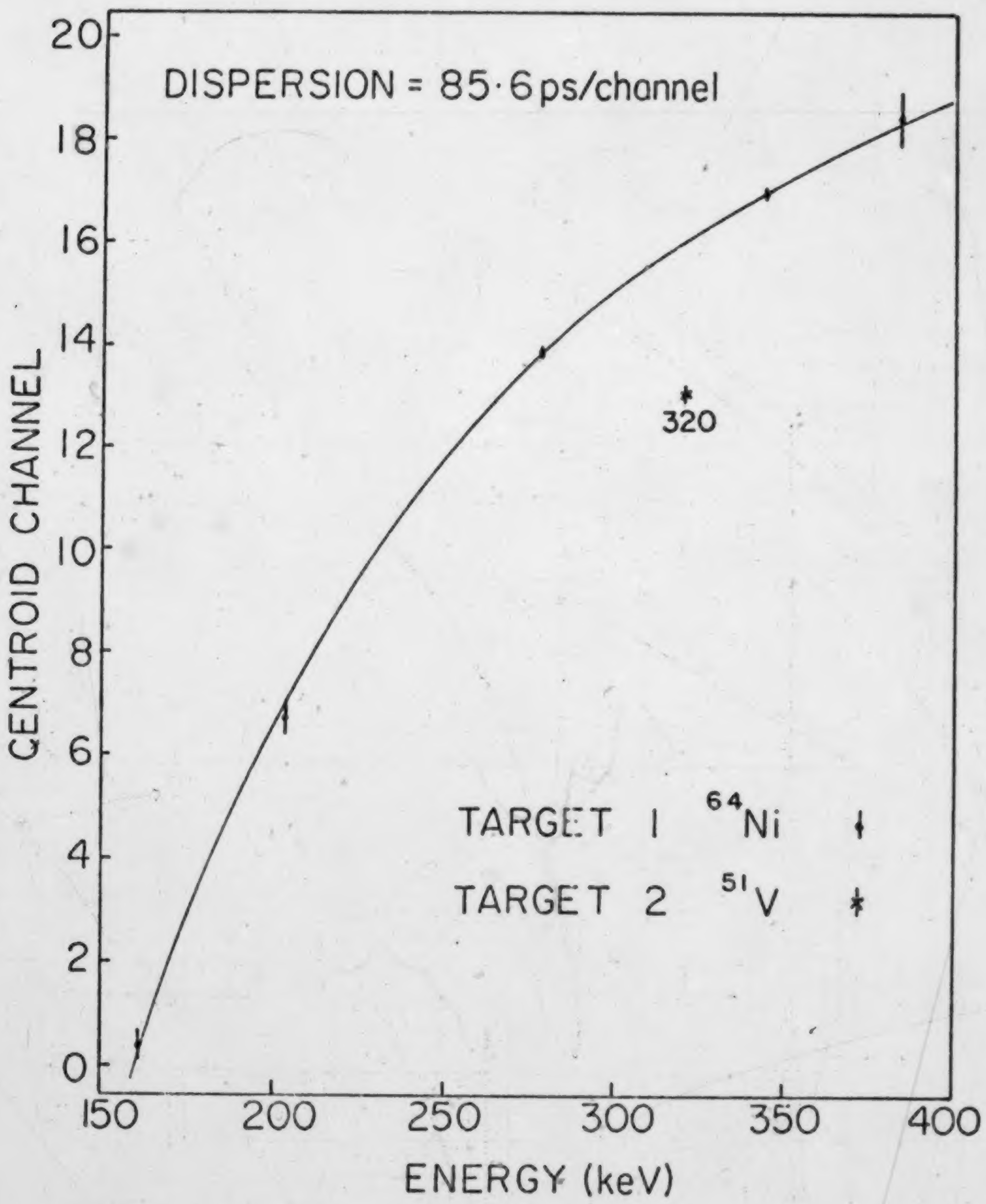

Fig. 66. Experimental results for the determination of the lifetime of the 320 keV level in ^{51}V. The solid line is a theoretical least squares fit to the experimental centroid points.

Horoshko et al (Ho 70) have calculated the weighted mean of the reduced transition probability B(E2)↓ from several Coulomb Excitation measurements and obtain a value of 154.0±7.6 e^2fm^4 for the 320 keV transition. Thus using this result and our lifetime result a value for the mixing ratio of $|\delta| = 0.45\pm0.02$ is obtained. The value is in agreement with the two experimental determinations of the mixing ratio; Ritter et al (Ri 62) obtained $\delta = -0.52\pm0.07$ from Coulomb Excitation measurements using 18 MeV ^{20}Ne ions, and Krause (Kr 63) obtained $\delta = -0.43\pm0.03$ from Resonance Fluorescence measurements. The experimental E2 and M1 transitions widths are $\Gamma(E2) = 4.16\times10^{-7}$ eV and $\Gamma(M1) = 2.04\times10^{-6}$ eV and hence our result corresponds to strengths of 13.7 W.u. and 3.0×10^{-3} W.u., respectively.

The 928 keV level was not observed from proton inelastic scattering so this state was investigated using a pulsed deuteron beam incident on the ^{50}Ti foil. Additional 'prompt' reference γ-rays were obtained using a second target, the ^{47}Ti foil, and the reaction ^{47}Ti(d,p)^{48}Ti. An illustration of the results is shown in fig. 67. No observable centroid shift was found for the 928 keV γ-ray decay and an upper limit of $\tau < 14$ ps was calculated for the lifetime. This result is in marked disagreement with that obtained by Singh et al (Si 70) who obtained a value of 101±36 ps.

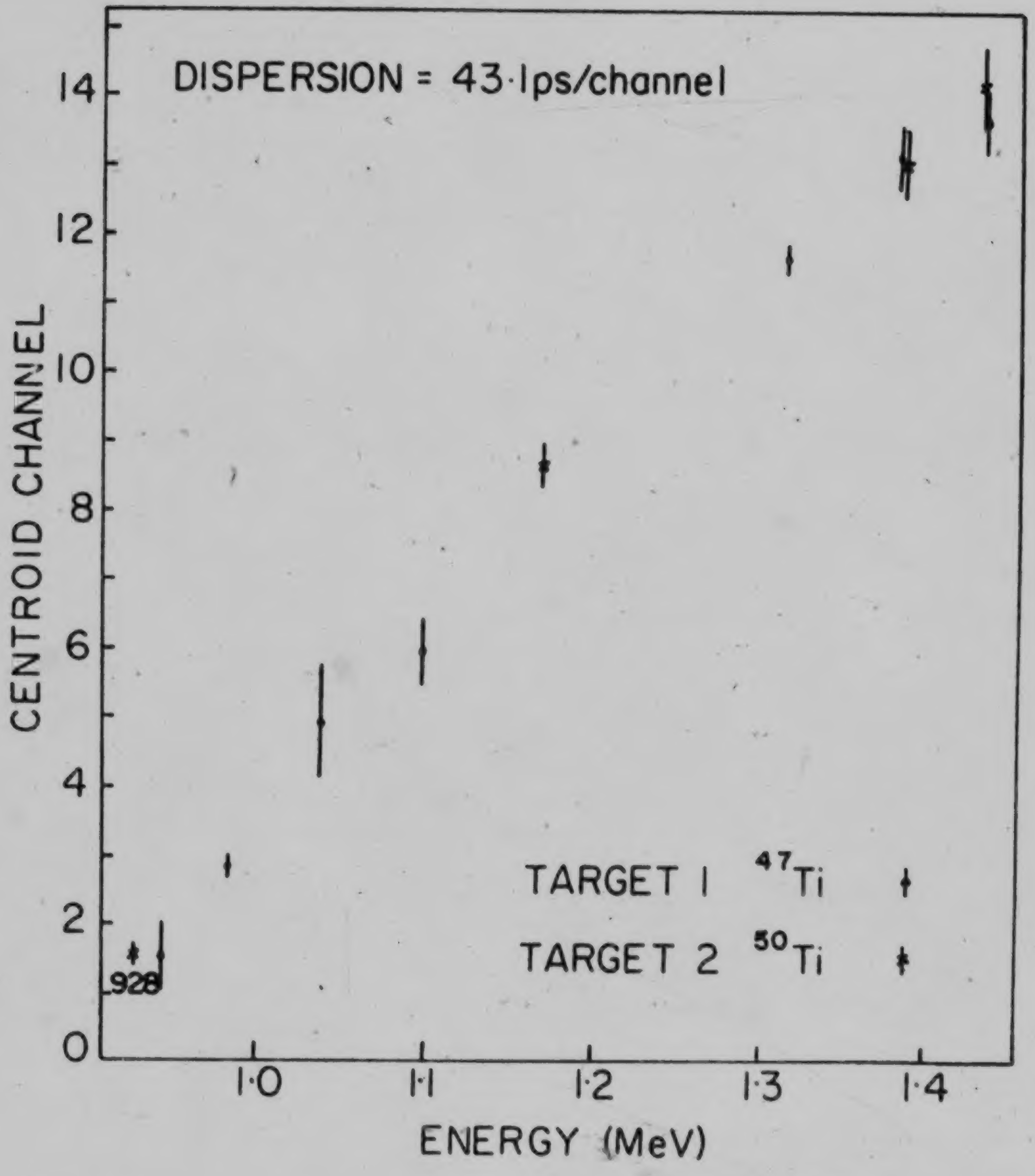

Fig. 67. Experimental results for the determination of the lifetime of the 928 keV level in ^{51}V.

Horoshko et al (Ho 70) have measured the reduced transition probability using the Coulomb Excitation Method to be B(E2)↓ = 76±5 e^2fm^4 for the 928 keV → g.s. transition. They also obtained a mixing ratio of $\delta = 0.03 \pm 0.09$ for this transition which indicates a pure E2 transition. Their measured branching ratio was 86%. Thus the calculated lifetime from these measurements is $\tau = 13.4 \pm 1.0$ ps which agrees with our upper limit.

For the $3/2^-$ 928 keV to the $5/2^-$ 320 keV level γ-ray transition Horoshko et al obtained two possible mixing ratios of $\delta = -0.33^{+0.11}_{-0.14}$ and $\delta = -8.8^{+4.1}_{-\infty}$ which are in qualitative agreement with the results of Robinson et al (Ro 63) who obtained the values of $\delta = -0.18 \pm 0.02$ and $\delta = +9 \pm 2$. From theoretical considerations Horoshko et al strongly favour the value of $\delta = -8.8^{+4.1}_{-\infty}$ which indicates nearly a pure E2 transition. They also found agreement between the measured and calculated B(E2) values only for $\delta = -8.8^{+4.1}_{-\infty}$. Using this value and the B(E2)↓ value of 107±9 e^2fm^4 calculated by Horoshko et al, the calculated value for the lifetime is $\tau = 12.7^{+3.3}_{-2.0}$ ps, again in agreement with our results.

Table 4 shows all the experimental results obtained for the Vanadium isotopes and a comparison with previous results. Also included in table 4 are the experiment transition widths and the transition

Table 4

Lifetime results for ^{47}V, ^{49}V, ^{50}V and ^{51}V and the corresponding experimental transition strengths.

Isotope Level E(keV), I^{π}	Present Lifetime	Previous Results	Decay to E(keV), I^{π}	Multipole^a	Exp.width $\Gamma(\Lambda)$ (eV)	Exp.Strength $\lvert M\rvert^2$ W.u.
^{47}V						
88, $5/2^-$	951±52 ps		0, $3/2^-$	M1	$(6.92\pm0.38)\times10^{-7}$	0.047±0.003
146, $7/2^-$	786±95 ps		88, $5/2^-$	M1	$(8.37\pm1.01)\times10^{-7}$	0.21±0.03
260, $3/2^+$	78±11 ps	90±12 ps(Bl 73)	0, $3/2^-$	E1	$(8.44\pm1.19)\times10^{-6}$	$(5.46\pm0.77)\times10^{-4}$
^{49}V						
90, $5/2^-$	329±19 ps	620±29 ps(Ch 71) 476±29 ps(Ok 73)	0, $7/2^-$	M1	$(2.00\pm0.12)\times10^{-6}$	0.13±0.01
153, $3/2^-$	28.71±0.35 ns	29.7±0.8 ns(Cu 63) 28.9±2.9 ns(Bl 71A) 28.7±0.5 ns(Vi 72)	0, $7/2^-$	E2	$(1.33\pm0.02)\times10^{-8}$	18.5±0.3
			90, $5/2^-$	M1	$(9.63\pm0.12)\times10^{-9}$	$(1.86\pm0.02)\times10^{-3}$
^{50}V						
226, 5^+	<16 ps	<3 ns (Bl 69A)	0, 6^+	M1	$>4.11\times10^{-5}$	>0.17
^{51}V						
320, $5/2^-$	266±9 ps	274±43 ps(Si 70) 290±20 ps(Sh 69)^b	0, $7/2^-$	M1^c	$(2.04\pm0.08)\times10^{-6}$	$(3.0\pm0.1)\times10^{-3}$
				E2^c	$(4.16\pm0.43)\times10^{-7}$	13.7±1.4
928, $3/2^-$	<14 ps	101±36 ps(Si 70)	0, $7/2^-$	E2	$>4.04\times10^{-5}$	>6.5
			320, $5/2^-$	M1^d	>0	> 0
				E2^d	$>6.3\times10^{-6}$	>8.36

Table 4 (cont'd)

a) Assumed $\delta = 0$ unless otherwise specified.

b) Weighted mean of several lifetime results quoted in (Sh 69).

c) $|\delta| = 0.45 \pm 0.02$.

d) $\delta = -8.8^{+4.1}_{-\infty}$ from (Ho 70).

strengths in Weisskopf units for both magnetic and electric decay modes.

7.3 ^{59}Ni and ^{65}Zn

These two isotopes were initially investigated to see whether they could be used as sources of 'prompt' reference γ-rays. However, both isotopes yielded low energy γ-ray transitions from states whose lifetimes were measurable by our technique. The level schemes for ^{59}Ni and ^{65}Zn from the work by Hutton et al (Hu 73) and Ezell and Scott (Ez 74), respectively, are shown in fig. 68.

7.3a ^{59}Ni

A gloop ^{59}Co target was prepared and the second target used was the ^{64}Ni foil. A 4.4 MeV pulsed proton beam was used to excite the states in ^{59}Ni and ^{64}Cu by the (p,n) reaction, the Q value being -1.858 MeV for the ^{59}Co(p,n)^{59}Ni reaction. Results obtained in one of the experimental runs are shown in fig. 69 which clearly show the centroid shifts of the 340 and 465 keV γ-ray transitions. The weighted mean of four experimental runs gave lifetime results for the 340 and 465 keV levels of 93±10 ps and 35±18 ps, respectively.

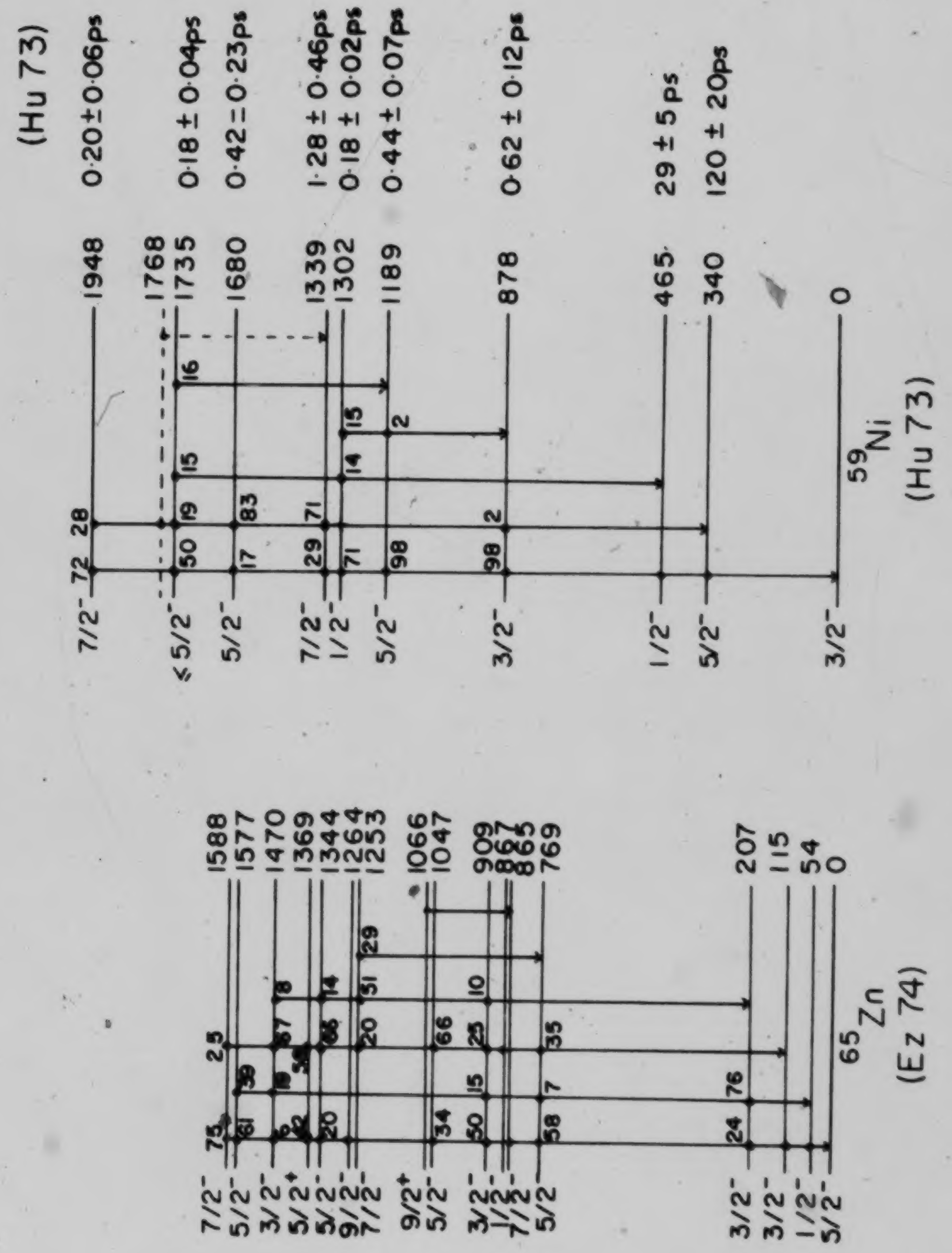
(Hu 73)
0·20±0·06ps
0·18 ± 0·04ps
0·42 ± 0·23ps
1·28 ± 0·46ps
0·18 ± 0·02ps
0·44 ± 0·07ps
0·62 ± 0·12ps
29 ± 5 ps
120 ± 20ps
1948
1768
1735
1680
1339
1302
1189
878
465
340
0
7/2⁻
≤5/2⁻
5/2⁻
7/2⁻
1/2⁻
5/2⁻
3/2⁻
1/2⁻
5/2⁻
3/2⁻
^{59}Ni
(Hu 73)
1588
1577
1470
1369
1344
1264
1253
1066
1047
909
867
865
769
207
115
54
0
7/2⁻
5/2⁻
3/2⁻
5/2⁺
5/2⁻
9/2⁻
7/2⁻
9/2⁺
5/2⁻
3/2⁻
1/2⁻
7/2⁻
5/2
3/2⁻
3/2⁻
1/2⁻
5/2⁻
^{65}Zn
(Ez 74)

Fig. 68. Experimental level schemes for ^{59}Ni and ^{65}Zn and previous lifetime results for excited states of ^{59}Ni.

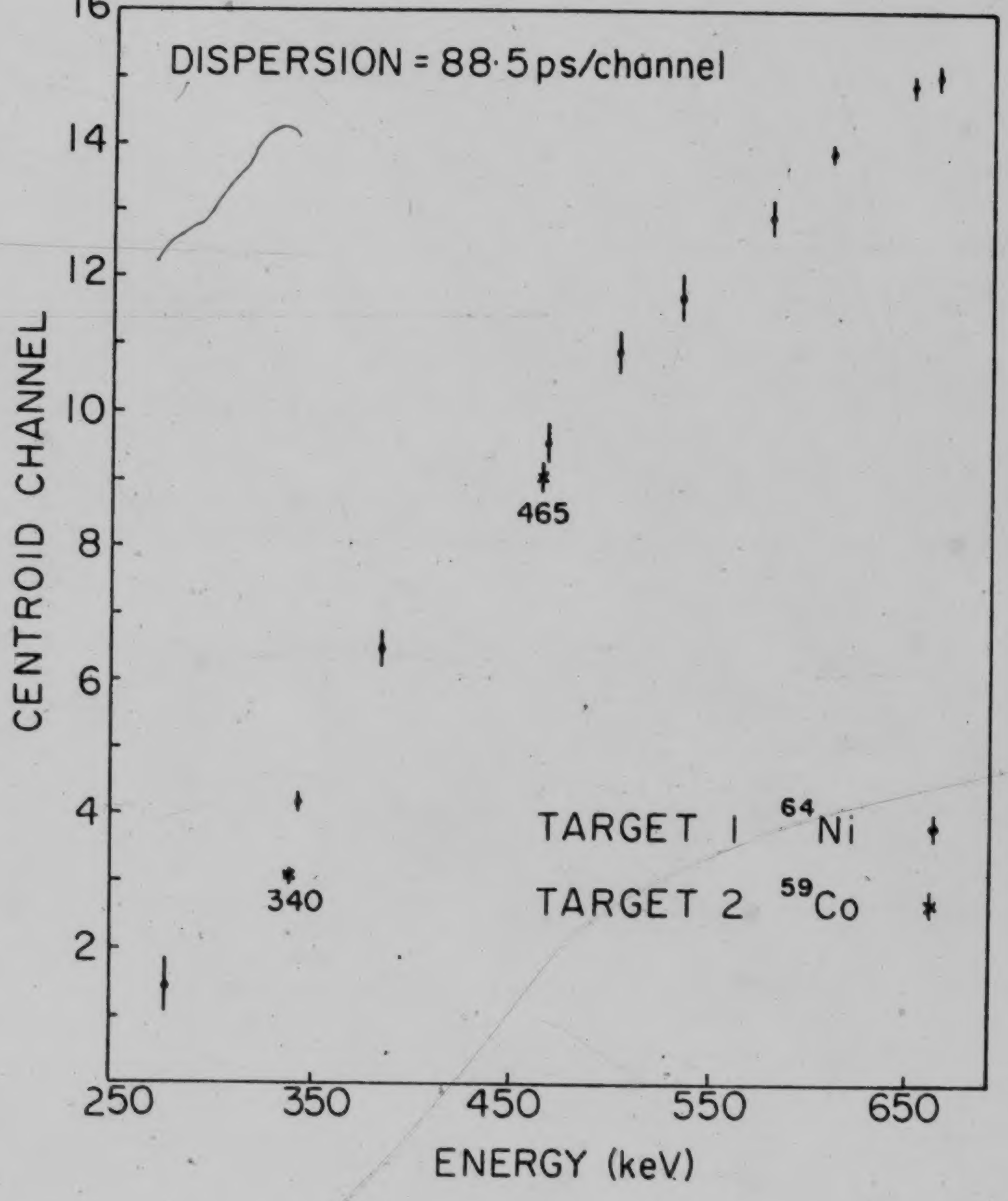

Fig. 69. Experimental results for lifetime determinations in ^{59}Ni.

Hutton et al (Hu 73) studied the lifetimes of ^{59}Ni using the ^{56}Fe(α,n)^{59}Ni reaction (E_α = 8.5-10.5 MeV) and the Doppler Shift Attenuation and Recoil Distance techniques. They obtained a lifetime of 120±20 ps for the 340 keV level and 29±5 ps for the 465 keV level. Within the experimental errors these results are in very good agreement with the present results. Both the levels at 340 keV and 465 keV are populated by cascading γ-rays from higher excited states. However, these higher energy levels have lifetimes less than 2 ps as illustrated in fig. 68 from the results obtained by Hutton et al (Hu 73), and therefore they have no effect on the measured lifetime values.

The mixing ratio of $\delta = -0.11 \pm 0.03$ was obtained by Hutton et al for the 340 keV γ-ray transition. Using our result for the lifetime, the experimental transition widths for the M1 and E2 modes of decay are $\Gamma(M1) = 6.99 \times 10^{-6}$ eV and $\Gamma(E2) = 8.46 \times 10^{-8}$ eV which correspond to a M1 and E2 strength of 0.009 W.u. and 1.7 W.u., respectively.

The mixing ratio has not been measured for the spin $1/2^-$ 465 keV level. If a pure M1 transition is assumed a M1 strength of 0.009 W.u. is obtained. Taking the other extreme of a pure E2 transition an E2 strength of 78 W.u. is obtained. This E2 enhancement is of much greater magnitude than generally found and thus this transition is expected to be mostly M1 in character.

7.3b ^{65}Zn

The lifetime of the first excited state at 54 keV has been measured by August and Friichtenicht (Au 60) to be 1.65±0.05 μs using a β^+-γ delayed coincidence technique. Using a γ-γ delayed coincidence technique Li-Scholz and Bakhru (Li 68) obtained a lifetime for the 115 keV level of 663±101 ps. The level at 207 keV has been assigned an upper limit of 500 ps by Tubbs (Tu 66) and hence this level was a candidate for our technique.

The target used was a natural copper foil, 48 mg/cm^2, which has a natural isotopic abundance of 30.9% ^{65}Cu, the rest being ^{63}Cu. A 4 MeV pulsed proton beam was used to excite the states of ^{65}Zn via the $^{65}Cu(p,n)^{65}Zn$ reaction which has a Q value of -2.13 MeV. The Q value of the $^{63}Cu(p,n)^{63}Zn$ reaction is -4.14 MeV so that no γ-ray transition in ^{63}Zn are observed. The second target used was either the ^{64}Ni-^{181}Ta foil combination or the ^{181}Ta-^{165}Ho foil combination. Two examples of the experimental results are shown in figs. 70 and 71.

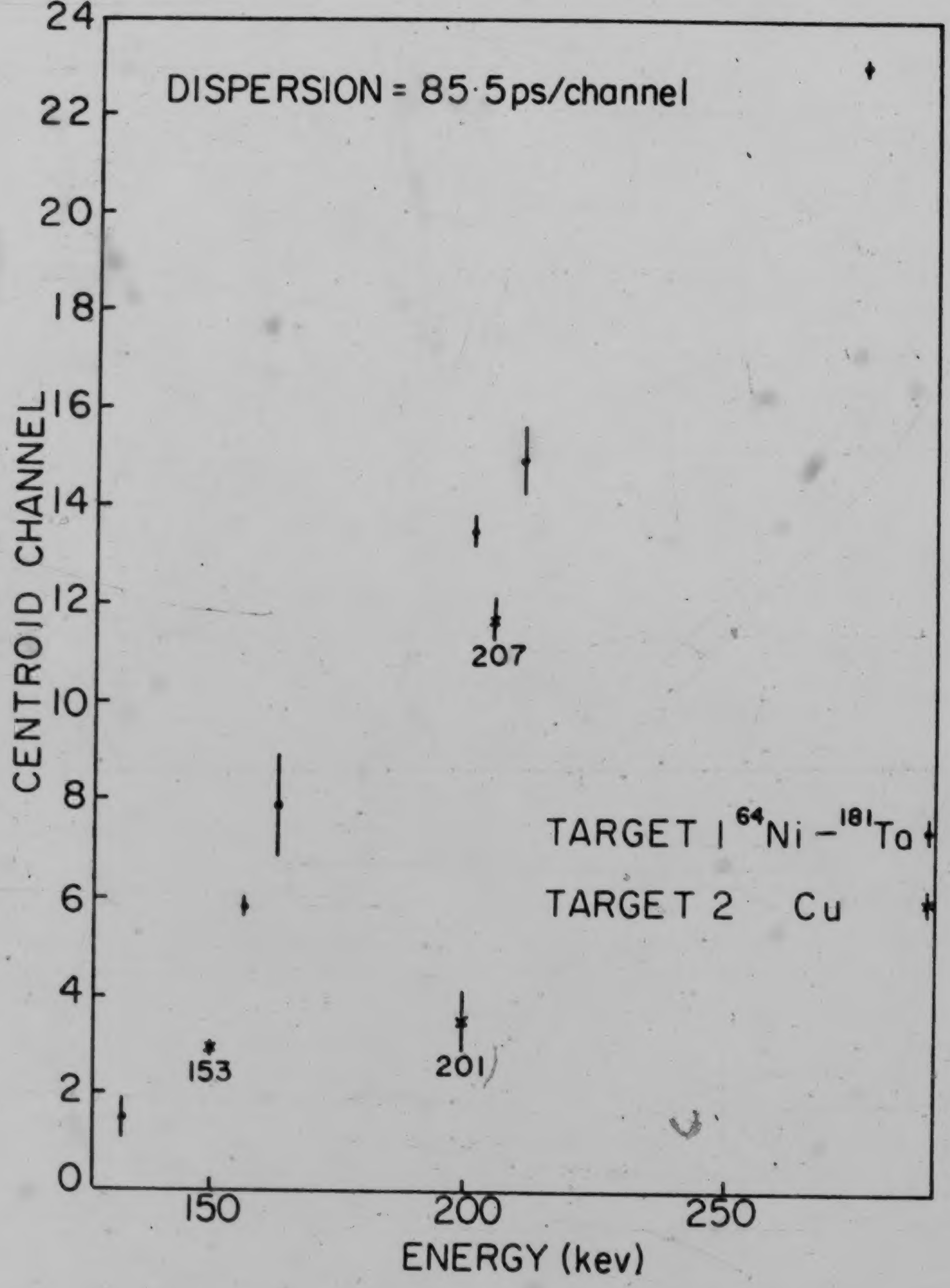

Fig. 70. Experimental results for lifetime determinations in ^{65}Zn, using a copper foil and the ^{64}Ni-^{181}Ta foil combination.

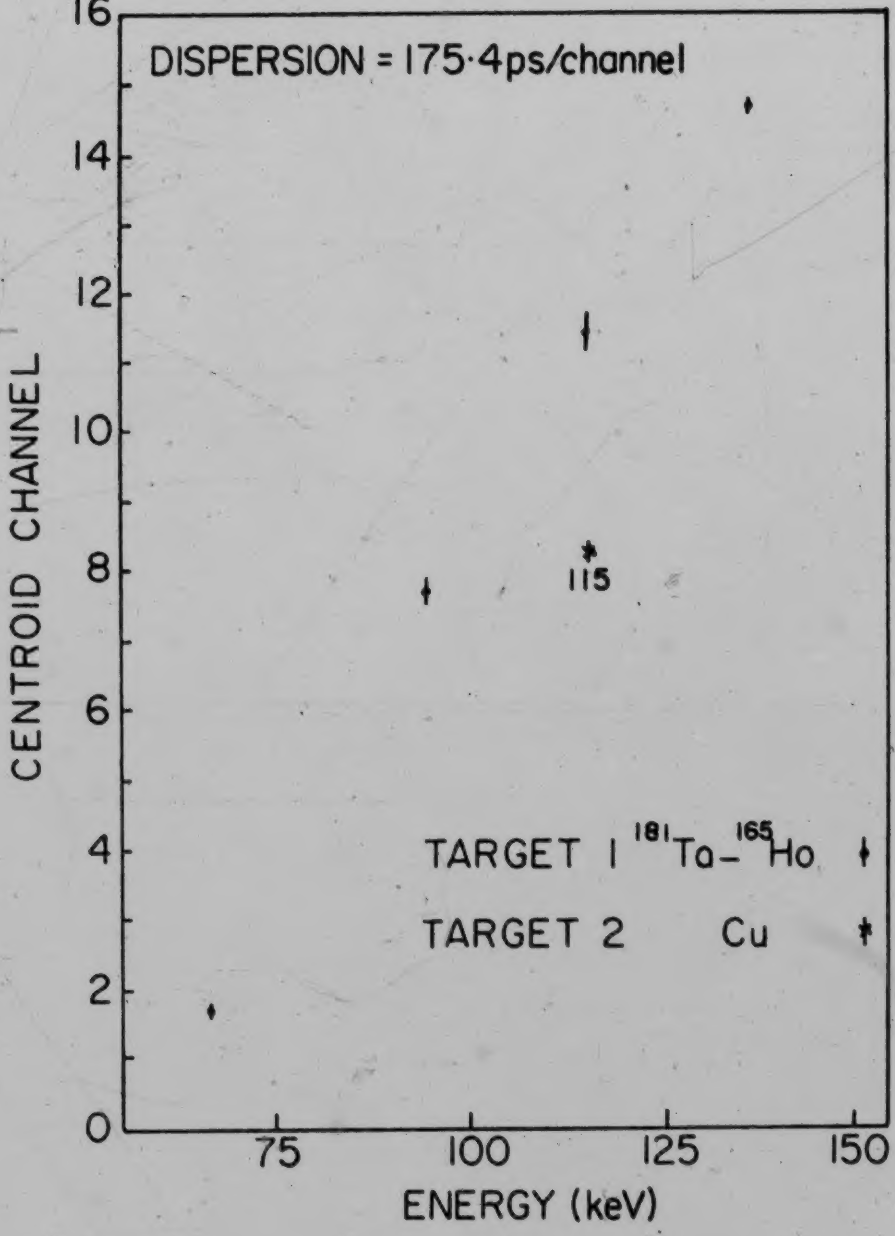

Fig. 71. Experimental results for lifetime determinations in ^{65}Zn using a copper foil and the ^{181}Ta-^{165}Ho foil combination.

An unexpected centroid shift was observed for the 201 keV γ-ray decay from the $9/2^+$ 1066 keV level to the $7/2^-$ state at 865 keV. The two decays at 202 and 212 keV in ^{64}Cu provide very good 'prompt' references for the 201 keV transition. The lifetime was found to be 829±37 ps for the 1066 keV level. Ezell and Scott (Ez 74) have assumed a pure E1 decay for this transition which has an experimental transition width of $\Gamma = 7.94\times10^{-7}$ eV using our lifetime result. This corresponds to an E1 strength of 9×10^{-5} W.u. Assuming a pure M2 transition a strength of 10^4 W.u. is calculated. Enhancements of this magnitude are not found so that an E1 decay mode is predominant for the 201 keV γ-ray transition.

The state at 207 keV decays by two branches; one via a 153 keV transition to the first excited state at 54 keV and a second to the ground state. The weighted mean of four experimental runs yielded lifetimes of 213±11 ps for the 153 keV transition and 227±22 ps for the 207 keV transition. The adopted lifetime for the 207 keV level was then calculated as the weighted mean of these two results which gives 216±10 ps. Robert et al (Ro 70A) have studied the low energy states of ^{65}Zn and deduce the mixing ratio of the 153 keV transition to be $\delta = 0.24\pm0.06$. Using this result and their branching ratios for the 207 keV state, our lifetime result leads to experimental transition widths of $\Gamma(M1) = 2.19\times10^{-6}$ eV and $\Gamma(E2) = (1.26\pm0.65)\times10^{-7}$ eV, respectively, for the 153 keV γ-ray transition. Hence the M1 and E2 strengths are 0.03 W.u. and 120±62 W.u., respectively.

The result for the lifetime of the 115 keV level was calculated to be 641±13 ps. The previous result by Li-Scholz and Bakhru (Li 67) of 663±101 ps is in agreement with the present result. Assuming a pure M1 decay mode for this transition a M1 strength of 0.03 W.u. is obtained.

The above levels are fed in part from cascading γ-rays from higher energy levels in ^{65}Zn. Thus a study of the higher excitation energy levels was performed. Two second targets were employed to provide the necessary 'prompt' reference γ-rays. These were the ^{47}Ti foil and the ^{49}Ti foil. The lifetimes of the levels in ^{47}Ti and ^{49}V are discussed in sections 7.2b and 7.2e, respectively. Using the natural copper foil to obtain the reaction ^{65}Cu(p,n)^{65}Zn, the reaction ^{63}Cu(p,p')^{63}Cu also provides 'prompt' reference γ-rays at energies 669, 962 and 1327 keV (Wo 70). An illustration of the experimental results is shown in fig. 72 for the case of the copper foil and the ^{47,49}Ti target.

No observable shifts were found except for the 865 keV γ-ray transition from the 865 keV level. This

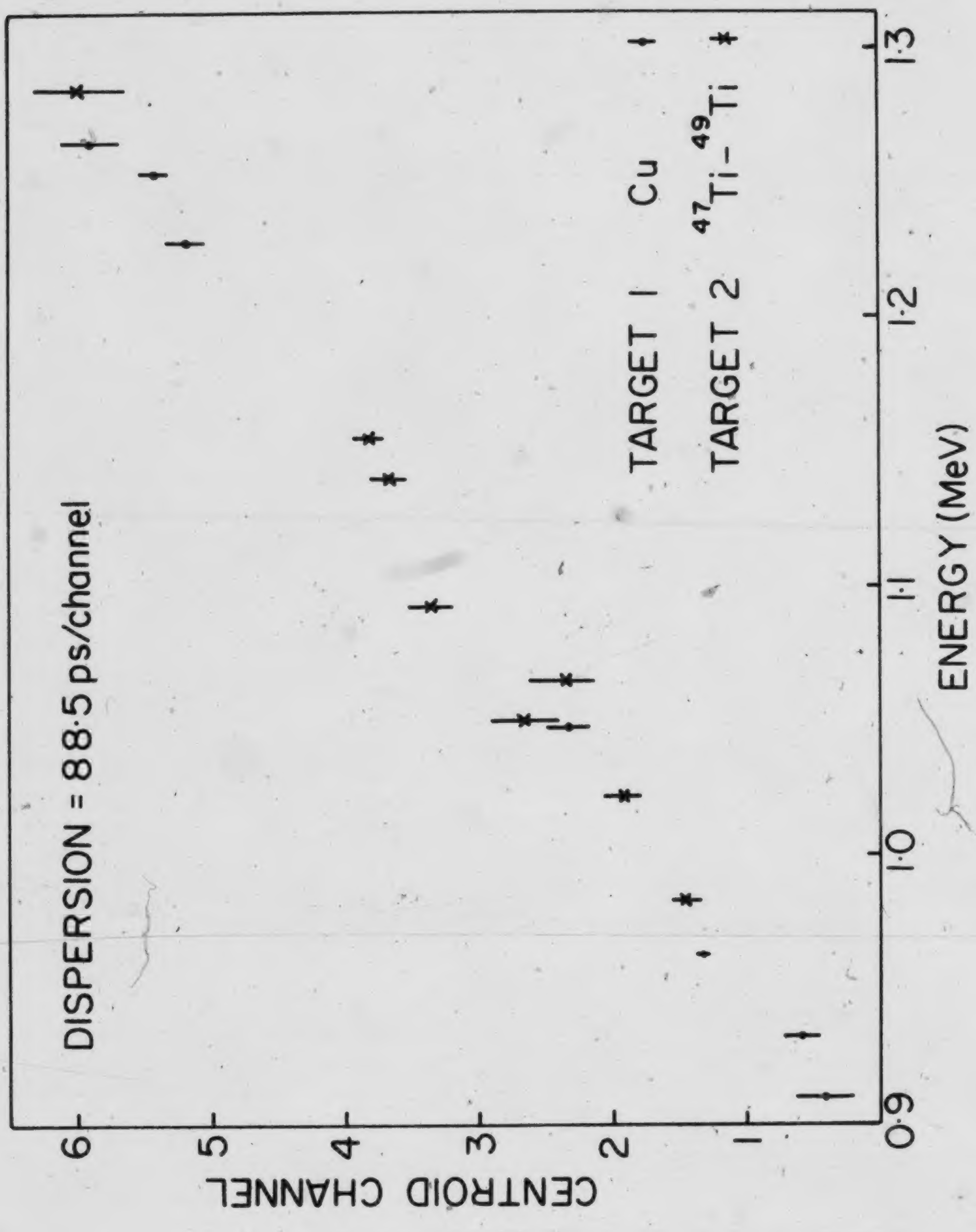

Fig. 72. Experimental results for lifetime determinations of the higher energy levels in ^{65}Zn.

level is fed by the 201 keV γ-rays from the 1066 keV level and it was found that the shift was entirely due to the feeding of the 865 keV level by cascading γ-rays from the 1066 keV level.

Table 5 shows the upper limits which have been assigned to the higher energy levels in ^{65}Zn plus the other results obtained for the low energy levels of ^{59}Ni and ^{65}Zn. Previous results are also given where applicable and the table also includes the experimental transition widths and the strengths in Weisskopf units for both electric and magnetic decay modes.

Table 5

Lifetime results for ^{59}Ni and ^{65}Zn and the corresponding experimental transition strengths.

Isotope Level E(keV), I^{π}	Present Lifetime	Previous Results	Decay to E(keV), I^{π}	Multipole[a]	Exp.width $\Gamma(\Lambda)$ (eV)	Exp.Strength $\|M\|^2$ W.u.
^{59}Ni						
340, $5/2^-$	93±10 ps	120±20 ps (Hu 73)	0, $3/2^-$	M1[b]	$(6.99\pm0.88)\times10^{-6}$	0.009±0.001
				E2[b]	$(8.46^{+6.78}_{-4.46})\times10^{-8}$	$1.7^{+1.36}_{-0.89}$
465, $1/2^-$	35±18 ps	29±5 ps (Hu 73)	0, $3/2^-$	M1	$(1.88^{+1.99}_{-0.64})\times10^{-5}$	$0.009^{+0.009}_{-0.003}$
				E2 ($\delta=\infty$)	$(1.88^{+1.99}_{-0.64})\times10^{-5}$	78^{+83}_{-26}
^{65}Zn						
115, $3/2^-$	641±13 ps	663±101 ps (Li 68)	0, $5/2^-$	M1	$(1.03\pm0.02)\times10^{-6}$	0.033±0.001
207, $3/2^-$	216±10 ps	<0.5 ns (Tu 66)	0, $5/2^-$	M1	$(7.01\pm0.31)\times10^{-7}$	0.0038±0.0002
			54, $1/2^-$	M1[c]	$(2.19\pm0.16)\times10^{-6}$	0.030±0.001
				E2[c]	$(1.26\pm0.65)\times10^{-7}$	120±62
1066, $9/2^+$	829±37 ps		865, $7/2^-$	E1	$(7.94\pm0.37)\times10^{-7}$	$(9.0\pm0.4)\times10^{-5}$

Lifetimes of higher energy levels in ^{65}Zn

769 keV, < 26 ps : 867 keV, < 37 ps : 909 keV, < 31 ps : 1047 keV, < 21 ps :

1252 keV, <19 ps : 1263 keV, <23 ps : 1343 keV, <18 ps : 1369 keV, <20 ps.

a) Assumed $\delta = 0$ unless otherwise specified.

b) $\delta = -0.11\pm0.03$ from (Hu 73).

c) $\delta = 0.24\pm0.06$ from (Ro 70).

CHAPTER 8

THEORETICAL INTERPRETATIONS

The 1 f $\frac{7}{2}$ shell region has been considered with particular interest since, following the shell model picture, nucleons are filling a fairly well isolated single particle level of quite large j and thus several simple shell model states are allowed. This argument was based on the relatively large energy gap between the 1 f $\frac{7}{2}$ and the neighbouring 2s-1d and 2 p $\frac{3}{2}$ shells, and by the presence of the doubly magic ^{40}Ca and ^{48}Ca cores which have been found to be particularly stable.

The properties of the nuclei in the 1 f $\frac{7}{2}$ shell have been studied by McCullen, Bayman and Zamick (Mc 64) [MBZ model] in terms of the spherical shell model with a suitable residual interaction between nucleons in a pure $(1f\,\frac{7}{2})^n$ configuration outside the closed shells. They assumed that the residual interaction was a two-body interaction where the matrix elements are completely determined by the interaction energy differences between the eight states $(1f\,\frac{7}{2})^2$, I = 0,1,...7. They presumed that these energy differences describe the observed states in ^{42}Ca, ^{42}Sc and ^{50}Ti.

Though many of the observed properties are accounted for by this model, there are serious discrepancies which cannot be avoided without more realistic assumptions. One test of the pure configuration assumption is a comparison of the spectra of cross-conjugate pairs of nuclei, that is nuclei with $Z = 20+a$, $N = 20+b$ and $Z = 28-b$ and $N = 28-a$. From particle-hole theorems these cross-conjugate pairs, e.g. ^{47}Ti and ^{49}V, should exhibit identical spectra. However, experimental level schemes are not identical. Equivalent nuclei which are nuclei having the same number of particles and holes i.e. ^{43}Ca, ^{45}Ca and ^{51}V, are also predicted to have approximately the same level spectrum but experimentally this is not so.

Probably the most serious weaknesses of the model are its inability to explain the ground state triplets exhibited by ^{45}Ti, ^{47}V and ^{49}V and that M1 transitions between states are forbidden although they occur between experimental levels. The inclusion of other configurations, including the $1f\frac{5}{2}$, $2p\frac{3}{2}$ and $2p\frac{1}{2}$ configurations, is expected to be important even in low lying states of nuclei in this region. Electromagnetic multipole matrix elements, particularly the B(M1) values, could be strongly affected by such admixtures. However, such configuration mixing has only been attempted with the Ca isotopes (Mi 61, Ra 65, En 66) and the N = 28 isotones (Au 67, Li 70, Li 71). Lips and McEllistrem (Li 70, Li 71) used a model which permits protons outside the closed ^{48}Ca core to occupy states of the configurations $(1f\frac{7}{2})^n$, $(1f\frac{7}{2}^{n-1}\ 1p\frac{3}{2})$ and $(1f\frac{7}{2}^{n-1}\ 1f\frac{5}{2})$ using a modified effective interaction calculation to obtain the eigenstates.

These calculations yielded appreciable improvements over the pure configuration model. However, although further admixtures of different configurations may explain other discrepancies, extensive computation is required as well as a large number of parameters. An increasing amount of evidence indicates that strong collective behaviour occurs in nuclei in the $1f\frac{7}{2}$ shell, so to overcome the problems of the shell model, Malik and Scholz (Ma 66, Sc 66, Sc 67) tried an alternative approach to the theoretical description of these nuclei. They used the Strong Coupling Symmetric Rotator model (RPC) including the Coriolis coupling between rotational bands.

Many of the difficulties encountered in the shell model are avoided in this treatment, namely the reproduction of the ground state triplets in ^{45}Ti, ^{47}V and ^{49}V, the correct number of levels below 2.5 MeV for nuclei in the upper half of the $1f\frac{7}{2}$ shell, and a better prediction of the spectra for cross-conjugate nuclei. They found that the Coriolis coupling strongly mixed the different bands so that the original band structure and the spacings of the single particle Nilsson levels is destroyed. Also the level schemes of the even-even adjacent nuclei of Titanium and Chromium (NDS 73A) as shown in fig. 73 do not exhibit the characteristic rotational J(J+1) type spectra with spin values 0^+ 2^+ 4^+ .... However, band mixing could destroy the rotational type spectra in these nuclei.

Recently evidence has been established that many of the odd-even nuclei in the $1f\frac{7}{2}$ shell have several low lying positive parity states which were considered as hole states by the excitation of a particle out of the 1d - 2s shell. Blasi et al (Bl 70, Bl 71) pointed out that the positive parity states of ^{45}Ti and ^{45}Sc show the characteristic J(J+1) sequence of a rotational band built on a $d\frac{3}{2}$ hole state. Similar rotational effects have been observed in ^{47}V and ^{49}V (Bl 71A, Bl 73). Fig. 74 shows the characteristic J(J+1) sequence for these nuclei where the energy of the positive parity levels are plotted against J(J+1).

Due to this strong evidence, the Symmetric Rotator model, as described in Appendix B, was used to compare the level schemes and electromagnetic transition rates of the odd-even isotopes of Titanium and Vanadium. A computer program written by Dr. D.A. Hutcheon at Oxford University was modified and corrected by myself and Dr. Hutcheon to run on the University of Alberta's IBM 360 computer. The model has several parameters, however, an attempt was made to develop a 'prescription' to obtain the parameters of the model from experimental

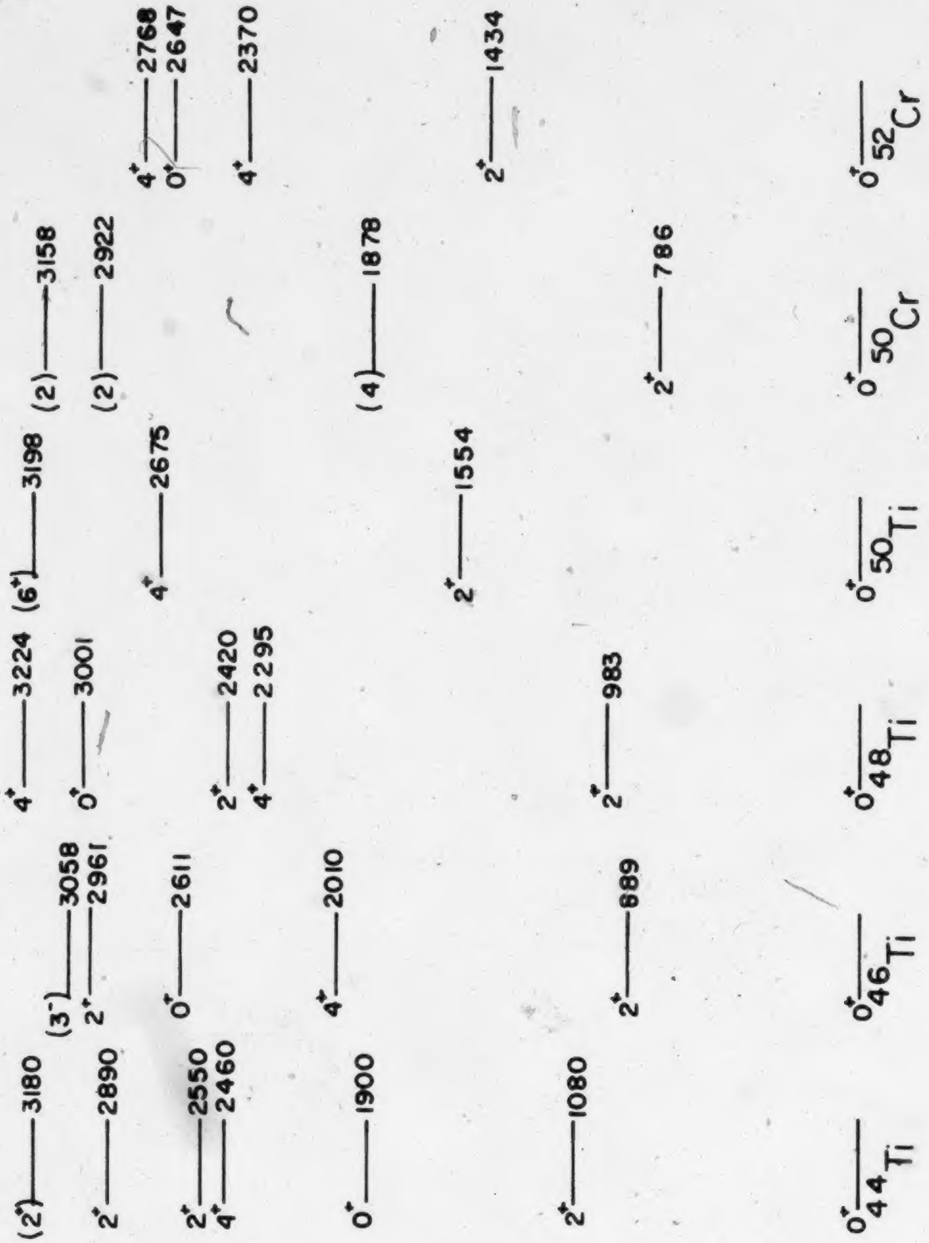
0^+ ^{44}Ti
2^+ 1080
0^+ 1900
2^+ 2550
4^+ 2460
2^+ 2890
(2^+) 3180
0^+ ^{46}Ti
2^+ 889
4^+ 2010
0^+ 2611
2^+ 2961
(3^-) 3058
0^+ ^{48}Ti
2^+ 983
4^+ 2295
2^+ 2420
0^+ 3001
4^+ 3224
0^+ ^{50}Ti
2^+ 1554
4^+ 2675
(6^+) 3198
0^+ ^{50}Cr
2^+ 786
(4) 1878
(2) 2922
(2) 3158
0^+ ^{52}Cr
2^+ 1434
4^+ 2370
0^+ 2647
4^+ 2768

Fig. 73. Experimental level schemes of the even-even Titanium and Chromium isotopes.

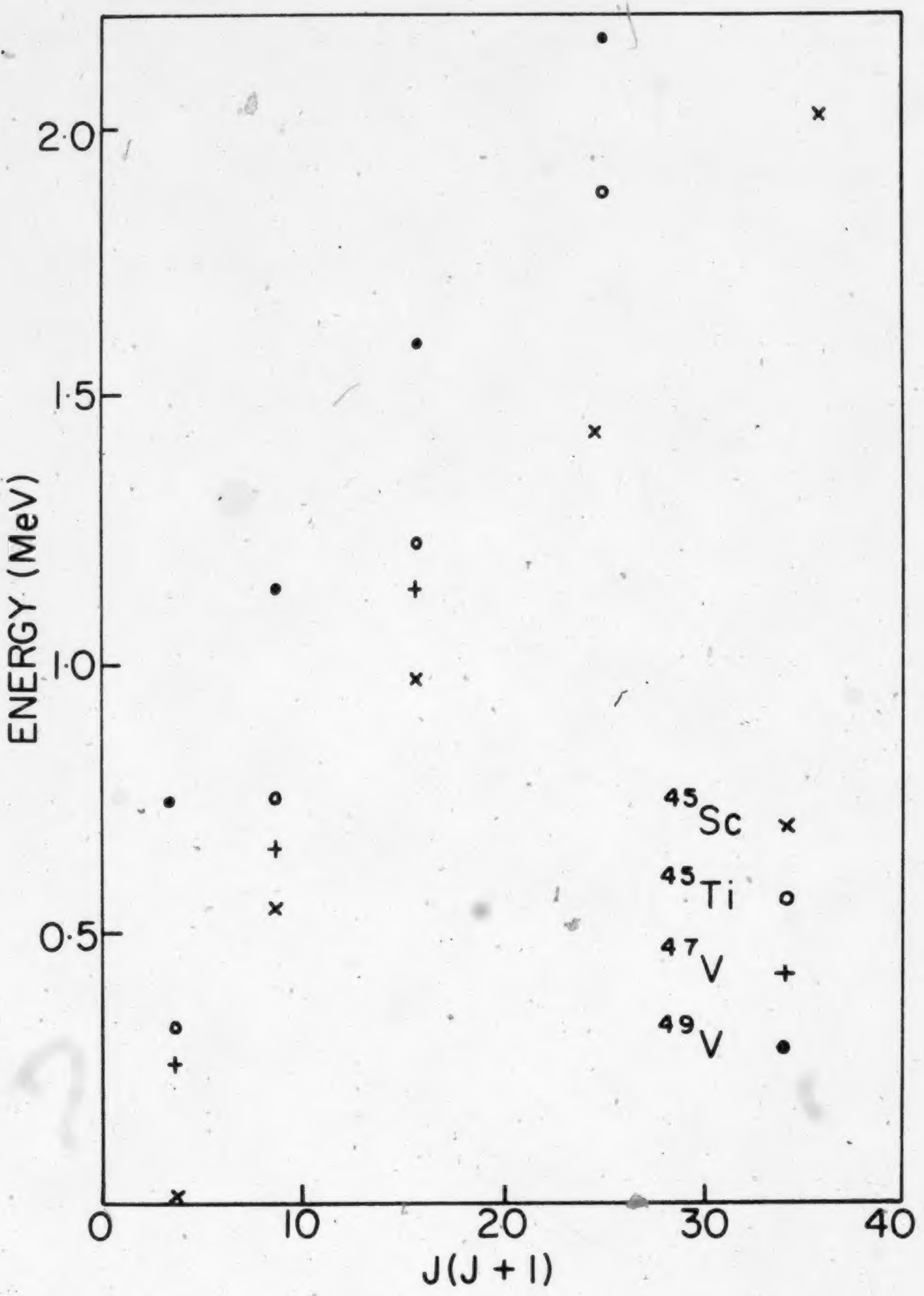

Fig. 74. The excitation energies of the positive parity levels in ^{45}Ti, ^{45}Sc, ^{47}V and ^{49}V plotted as a function of J(J+1).

data. Thus none of the parameters were allowed to vary, except the deformation parameter, δ. Hence it was felt that a meaningful test of the usefulness and validity of the model for reproducing the properties of the nuclei in the $1f\frac{7}{2}$ region, could be established.

Values of $\kappa = 0.066$ and $\mu = 0.32$ were obtained from the $^{48}\text{Ca}(^{3}\text{He},d)^{49}\text{Sc}$ data (NDS 70) by calculating the unperturbed single-particle energies $E_{\ell j}$ given by the centre-of-gravity relation

$$E_{\ell j} = \frac{\sum_i E_i\ S_i}{\sum_i S_i}$$

where E_i denote the excitation energy of a level belonging to the ℓj shell model states and S_i are the corresponding spectroscopic factors. These values are similar to those originally used by Nilsson (Ni 55) of $\kappa = 0.05$ and $\mu = 0.35$. The moment of inertia parameter $\hbar^2/2\mathscr{I}$ for each nucleus studied was calculated from the average energies of the first 2^+ state of the adjacent even-even nuclei, assuming a rotational character to these levels. For each nucleus only one rotational constant was used for all bands to eliminate further parametrization.

The computer program allows particle and hole excited states of the Nilsson model by permitting an unpaired nucleon to occupy any orbit in the $N = 3$ oscillator shell, with the remaining pairs occupying the lowest available orbitals. For the band mixing calculations, all bands based on the ten available single particle and hole states in the N = 3 shell have been included. However, overlap between bands based on the particle excited states and the hole excited states are not allowed.

The predicted spectra for the odd-even isotopes of Titanium and Vanadium are shown in figs. 75 to 80. Also shown in each figure are the corresponding experimental level schemes, only negative parity states being shown, and the theoretical predictions of the pure $(1f\frac{7}{2})^n$ configuration model, the MBZ model (Mc 64), where calculations have been done. The predicted spectra for ^{45}Ti, ^{47}V, ^{49}V and ^{51}V, each with three nucleons of the odd species outside the closed shell, are in good agreement with the experimental results. However, in ^{51}V the first excited $5/2^-$ state is predicted too high and the $9/2^-$ and $11/2^-$ spin states are predicted slightly low. In ^{45}Ti, ^{47}V and ^{49}V, the ground state triplets are very well reproduced by the theory with the correct spin assignments. The pure $(1f\frac{7}{2})^n$ configuration model is seen only to predict a doublet for these nuclei with incorrect spin assignments for the ground states of ^{45}Ti and ^{47}V. The Strong Coupling model is also seen to reproduce the large energy gap between the ground state triplets and the other excited states.

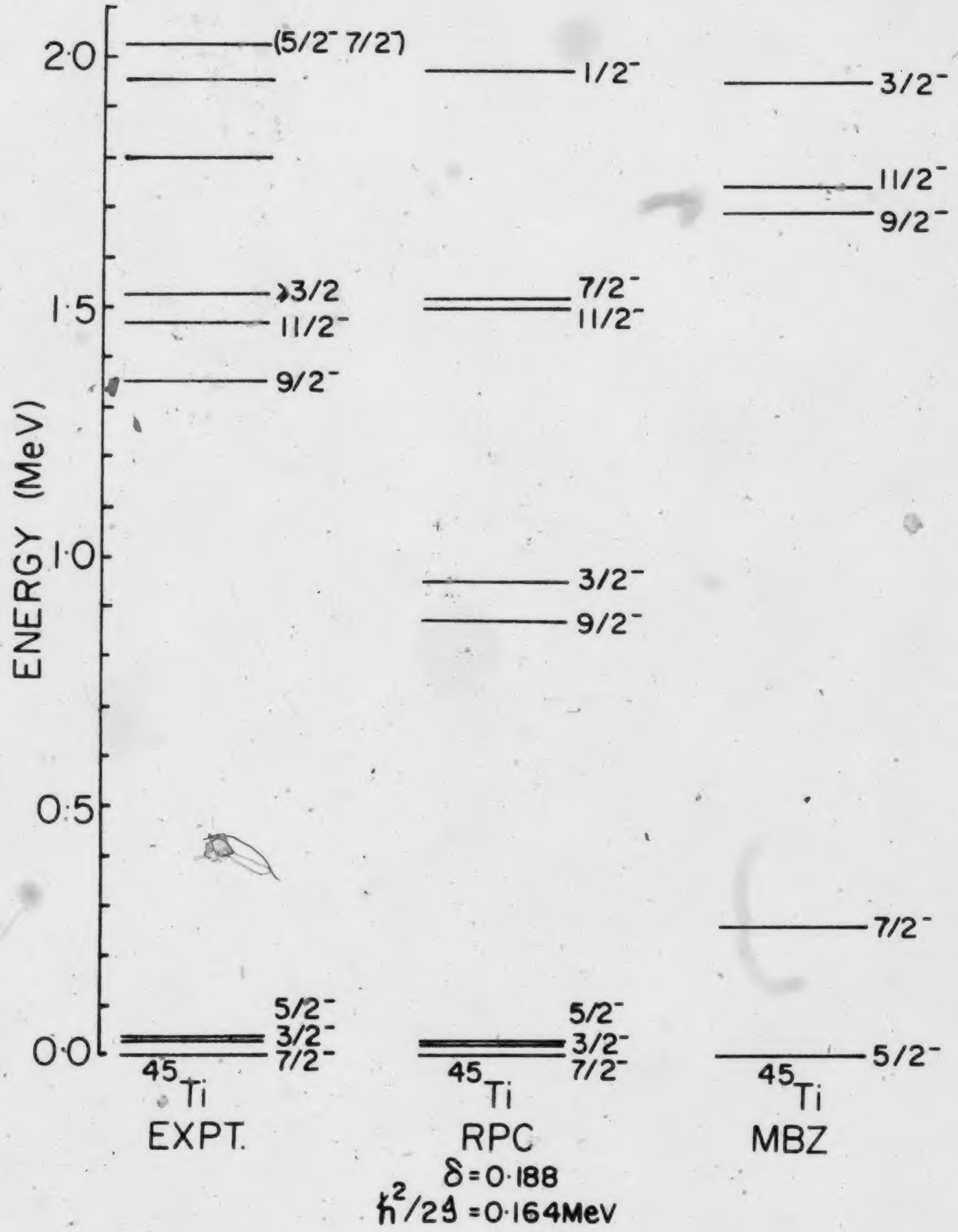
ENERGY (MeV)
2·0
1·5
1·0
0·5
0·0
(5/2⁻ 7/2⁻)
>3/2
11/2⁻
9/2⁻
5/2⁻
3/2⁻
7/2⁻
45 Ti
EXPT.
1/2⁻
7/2⁻
11/2⁻
3/2⁻
9/2⁻
5/2⁻
3/2⁻
7/2⁻
45 Ti
RPC
δ=0·188
ħ²/2ℐ =0·164MeV
3/2⁻
11/2⁻
9/2⁻
7/2⁻
5/2⁻
45 Ti
MBZ

Fig. 75. Experimental and theoretical level schemes of ^{45}Ti.

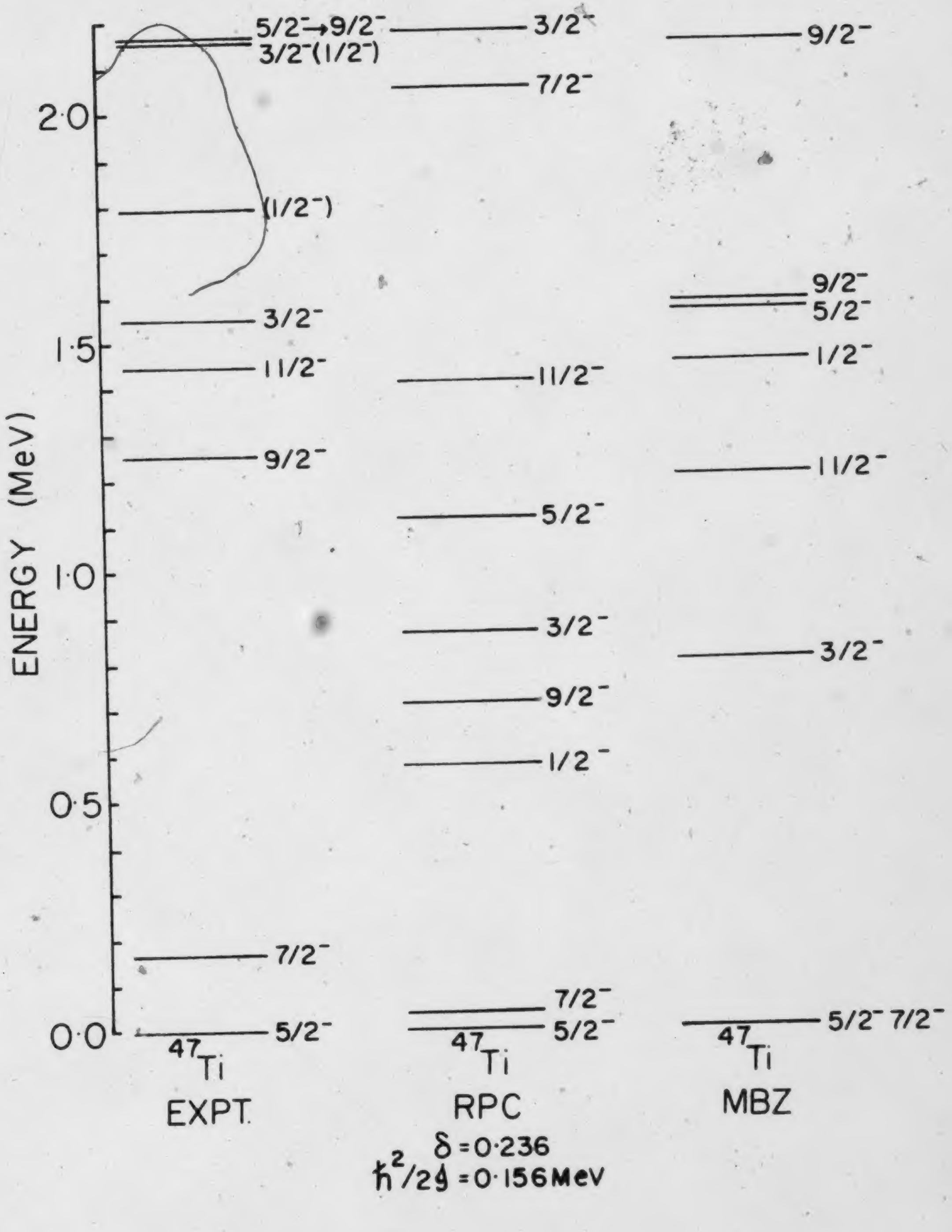
ENERGY (MeV)
2·0
1·5
1·0
0·5
0·0
5/2⁻→9/2⁻
3/2⁻(1/2⁻)
(1/2⁻)
3/2⁻
11/2⁻
9/2⁻
7/2⁻
5/2⁻
47 Ti
EXPT.
3/2⁻
7/2⁻
11/2⁻
5/2⁻
3/2⁻
9/2⁻
1/2⁻
7/2⁻
5/2⁻
47 Ti
RPC
δ = 0·236
ħ²/2ϑ = 0·156 MeV
9/2⁻
9/2⁻
5/2⁻
1/2⁻
11/2⁻
3/2⁻
5/2⁻ 7/2⁻
47 Ti
MBZ

Fig. 76. Experimental and theoretical level schemes of ^{47}Ti.

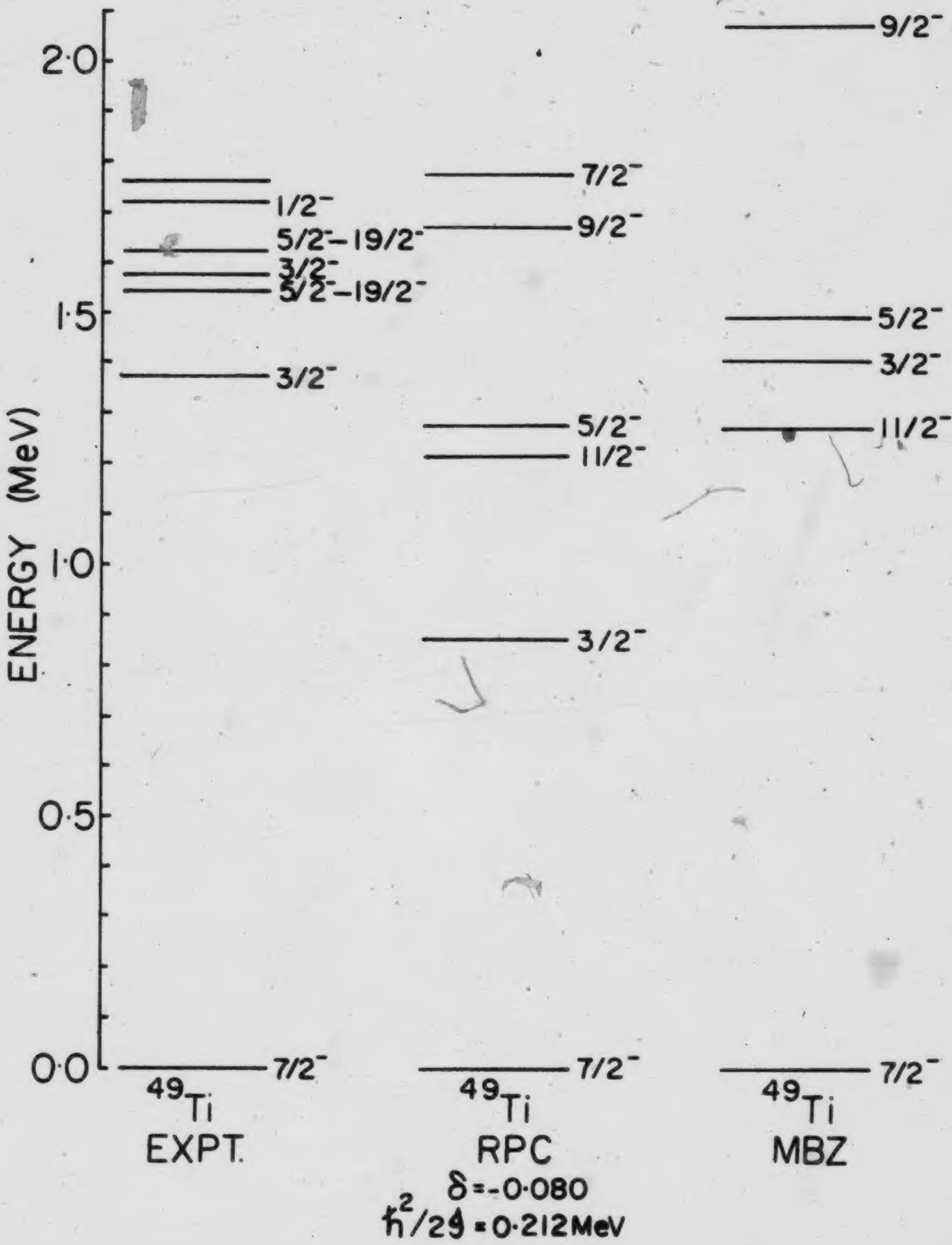

Fig. 77. Experimental and theoretical level schemes of ^{49}Ti.

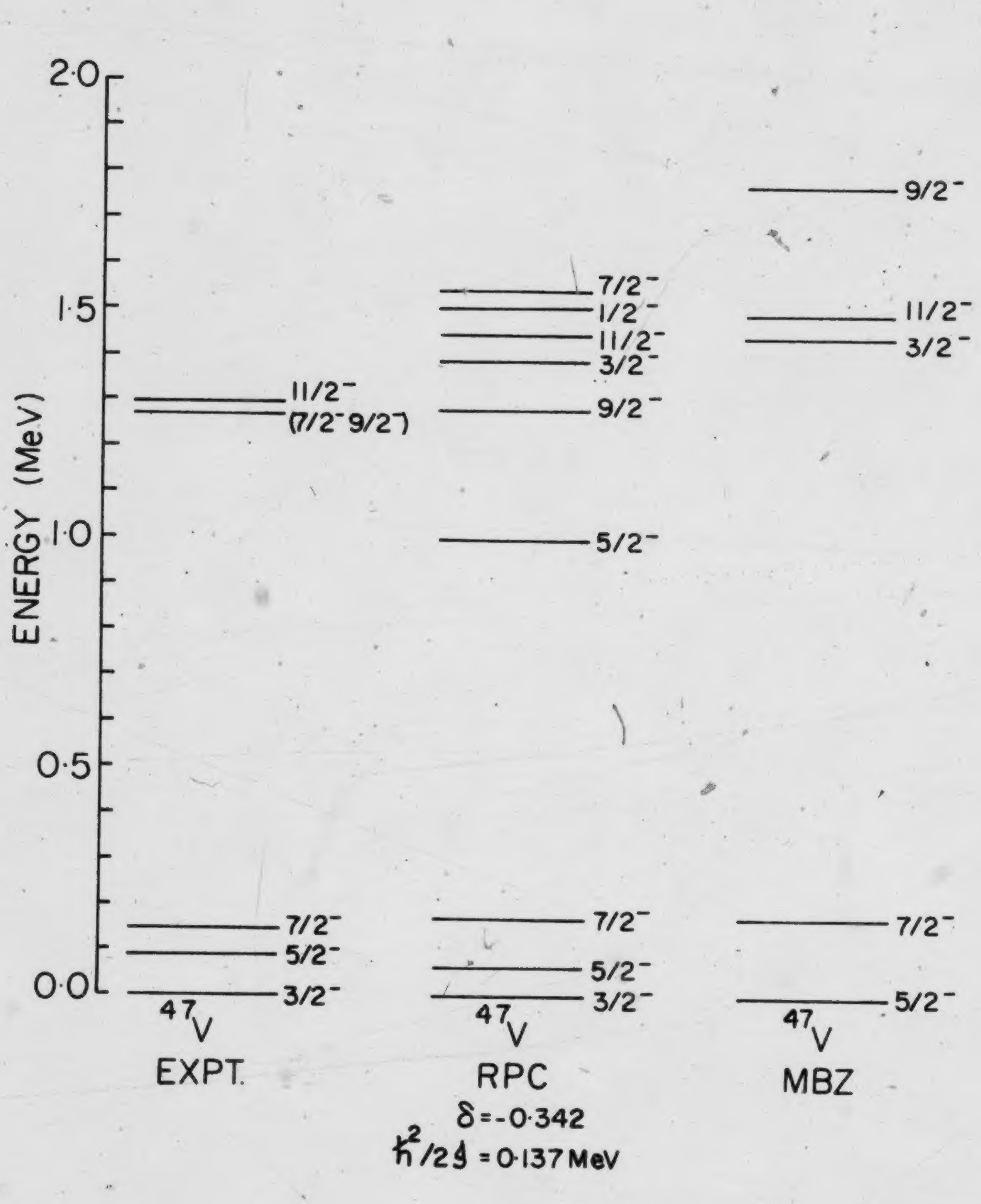
2.0
1.5
1.0
0.5
0.0
ENERGY (MeV)
11/2⁻
(7/2⁻ 9/2⁻)
7/2⁻
5/2⁻
3/2⁻
47V
EXPT.
7/2⁻
1/2⁻
11/2⁻
3/2⁻
9/2⁻
5/2⁻
7/2⁻
5/2⁻
3/2⁻
47V
RPC
δ=-0.342
ħ²/2ℐ =0.137 MeV
9/2⁻
11/2⁻
3/2⁻
7/2⁻
5/2⁻
47V
MBZ

Fig. 78. Experimental and theoretical level schemes of ^{47}V.

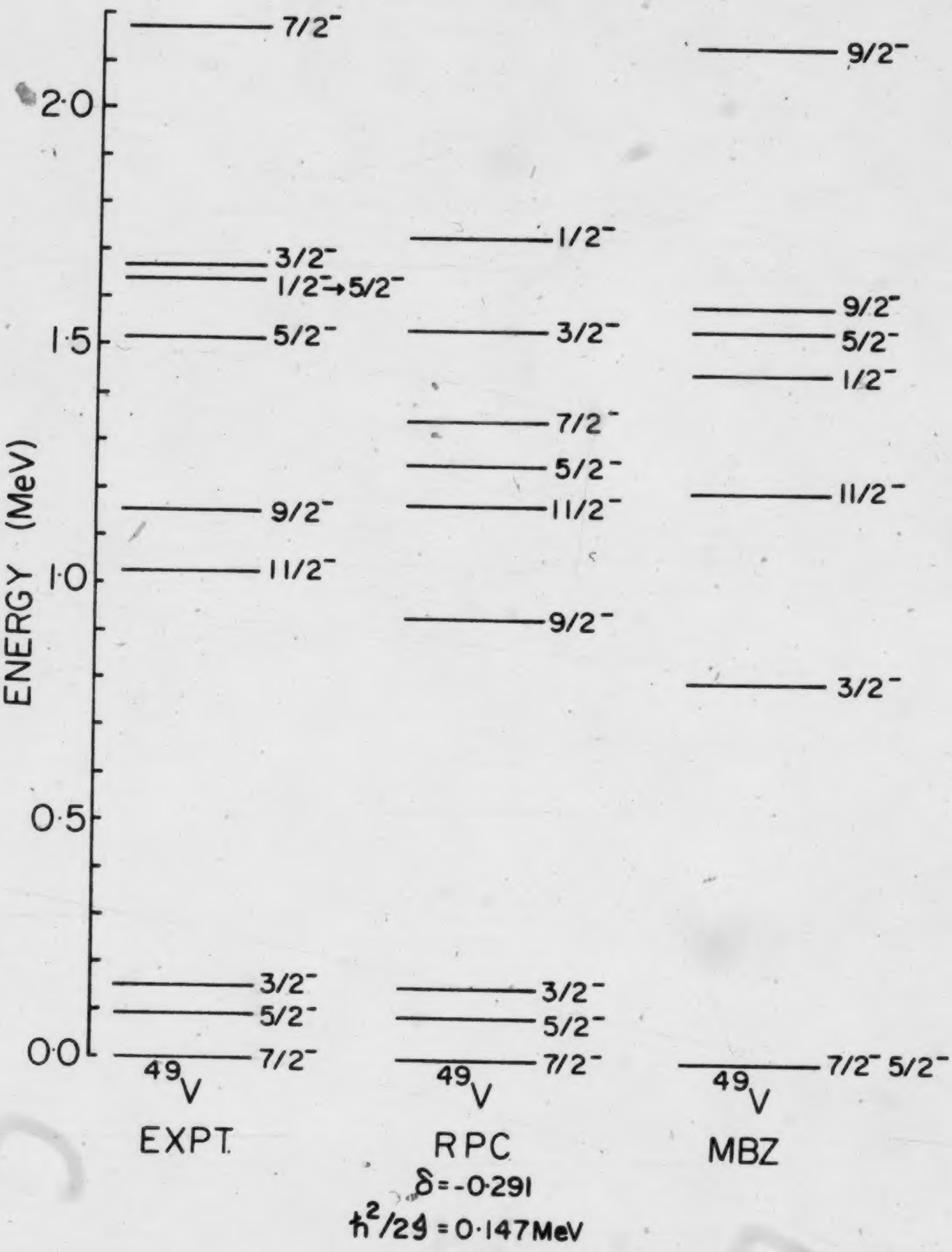
ENERGY (MeV)
2·0
1·5
1·0
0·5
0·0
7/2⁻
3/2⁻
1/2⁻→5/2⁻
5/2⁻
9/2⁻
11/2⁻
3/2⁻
5/2⁻
7/2⁻
49V
EXPT.
1/2⁻
3/2⁻
7/2⁻
5/2⁻
11/2⁻
9/2⁻
3/2⁻
5/2⁻
7/2⁻
49V
RPC
δ=-0·291
ħ²/2ℐ=0·147MeV
9/2⁻
9/2⁻
5/2⁻
1/2⁻
11/2⁻
3/2⁻
7/2⁻ 5/2⁻
49V
MBZ

Fig. 79. Experimental and theoretical level schemes of ^{49}V.

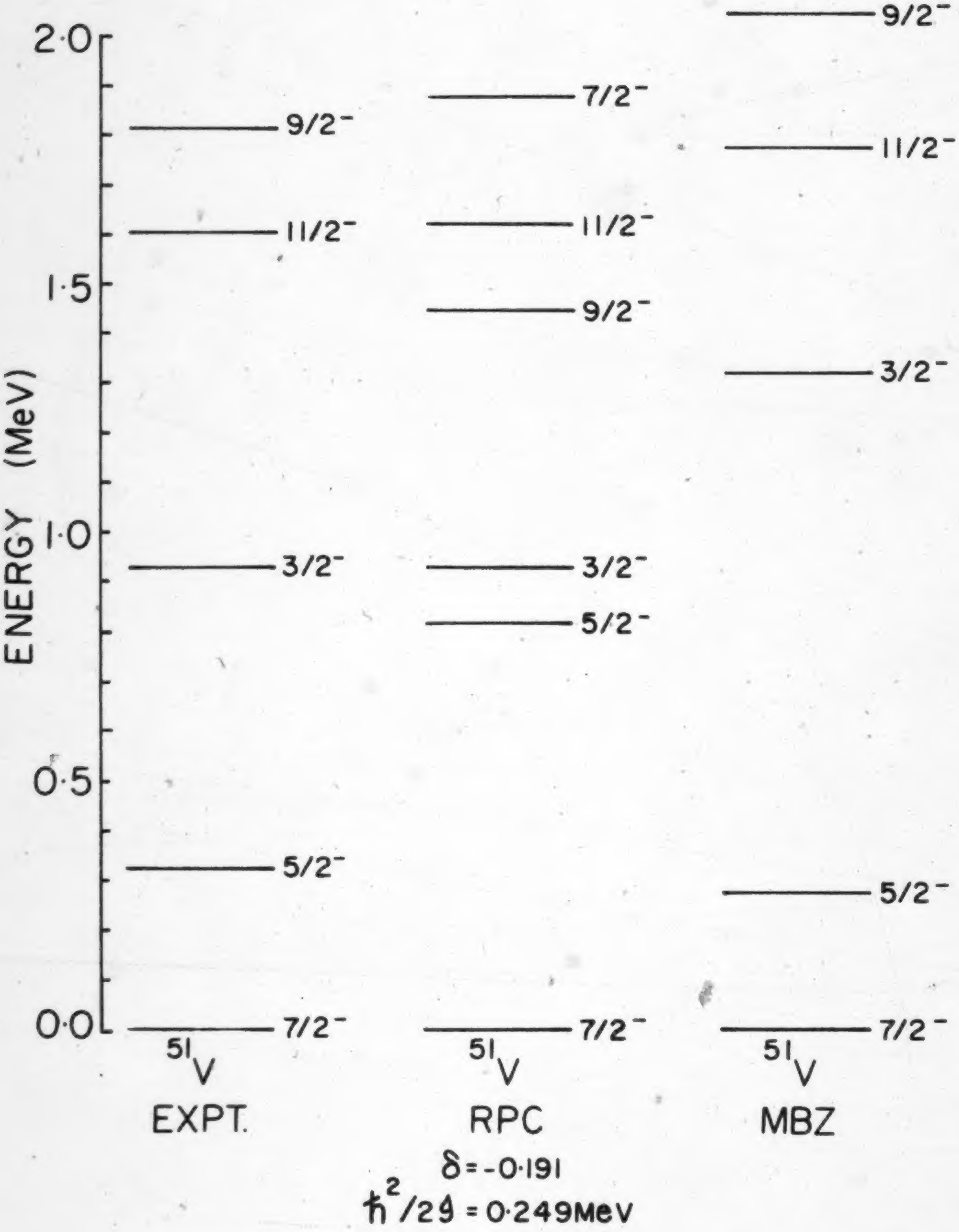
2·0
1·5
1·0
0·5
0·0
ENERGY (MeV)
9/2⁻
11/2⁻
3/2⁻
5/2⁻
7/2⁻
^{51}V
EXPT.
7/2⁻
11/2⁻
9/2⁻
3/2⁻
5/2⁻
7/2⁻
^{51}V
RPC
$\delta = -0{\cdot}191$
$\hbar^2/2\mathcal{J} = 0{\cdot}249$ MeV
9/2⁻
11/2⁻
3/2⁻
5/2⁻
7/2⁻
^{51}V
MBZ

Fig. 80. Experimental and theoretical level schemes of ^{51}V.

The Strong Coupling model produces only a fair fit to the experimental level scheme of ^{47}Ti. However, the anomalous 5/2$^-$ ground state spin is predicted plus the low lying 7/2$^-$ first excited state. The 9/2$^-$ second excited state as well as the 3/2$^-$ state are predicted too low. An extra state, spin 1/2$^-$, is also predicted at 558 keV which is not observed in the experimental level scheme.

For the case of ^{49}Ti, where there is little experimental data, the ground state spin of 7/2$^-$ is reproduced with the large energy gap to the first excited state.

The electromagnetic transition rates predicted by the model are shown in Tables 6 and 7, for the isotopes of Titanium and Vanadium, respectively. It is seen that good agreement between theory and experiment is obtained in most cases.

In conclusion, although only the deformation parameter, δ, was allowed to vary, the values used in the theoretical calculations are in good agreement with the values calculated from B(E2) measurements as listed by Wapstra (Wa 65) for even-even nuclei in this region. As shown by Davidson (Da 68), the B(E2) value for the ground state to 2$^+$ first excited state in even-even nuclei, as predicted by the Rotational model, is given by

Table 6

Comparison of experimental reduced transition probabilities with the Strong Coupling model calculations for ^{45}Ti, ^{47}Ti and ^{49}Ti.

Isotope	E_i(keV),$I_i^\pi \rightarrow$	E_f(keV),I_f^π	Multipole	B(Λ)[a] Experiment[b]	B(Λ)[a] Theory
^{45}Ti	37, 3/2⁻	0, 7/2⁻	E2	139±14[c]	129
	40, 5/2⁻	0, 7/2⁻	M1	0.052±0.003[c]	0.124
	1354, 9/2⁻	0, 7/2⁻	M1	$0.105^{+0.039}_{-0.034}$[d]	0.0002
			E2	322^{+280}_{-145}[d]	91
	1468,11/2⁻	0, 7/2⁻	E2	178±43[e]	127
	1521, 3/2⁻	37, 3/2⁻	M1	0.183±0.030[e]	0.103
^{47}Ti	160, 7/2⁻	0, 5/2	M1	0.0458±0.0001[f]	0.0281
			E2	239±41[g]	253
	1253, 9/2⁻	160, 7/2⁻	M1	$0.183^{+0.022}_{-0.019}$[h]	0.116
			E2	49^{+56}_{-33}[h]	258
	1253, 9/2⁻	0, 5/2⁻	E2	126±12[i]	88
	1445,11/2⁻	160, 7/2⁻	E2	146^{+36}_{-37}[i]	162
	1445,11/2⁻	1253, 9/2⁻	M1	0.32±0.08[i]	0.33
	1550, 3/2⁻	0, 5/2⁻	M1	$(1.4\pm0.4)\times10^{-4}$ [j]	0.225
			E2	$16.5^{+10.0}_{-2.6}$[j]	0.25
	1550, 3/2⁻	160, 7/2⁻	E2	39.8±11.4[i]	0.92
^{49}Ti	1381, 3/2⁻	0, 7/2⁻	E2	>32	24
	1585, 5/2⁻	0, 7/2⁻	M1	>0.0013	0.0506
			E2	>7.4	15
	1762, 7/2⁻	0, 7/2⁻	M1	>0.00074	0.0157

Table 6 (cont'd)

a) Units are μ_N^2 for B(M1) and e^2fm^4 for B(E2).

b) Assumed mixing ratio $\delta = 0$ except as noted

c) Lifetimes from (Ly 70) and for 37 keV transition $\alpha_T = 17.8$ (Je 68).

d) $\delta = +0.625^{+0.260}_{-0.159}$ from (Zu 72).

e) Lifetimes from (Zu 72).

f) $\delta = 0.095 \pm 0.003$ (see text).

g) Weighted mean of B(E2) values (Te 56, Ri 62).

h) $\delta = 0.15 \pm 0.06$ and lifetime from (We 72).

i) Lifetimes from (We 72).

j) $\delta = -4.4^{+1.2}_{-2.6}$ and lifetime from (We 72).

Table 7

Comparison of experimental reduced transition probabilities with the Strong Coupling model calculations for ^{47}V, ^{49}V and ^{51}V.

Isotope	E_i(keV), I_i^π →	E_f(keV), I_f^π	Multipole	B(Λ)[a] Experiment[b]	Theory
^{47}V	88, 5/2$^-$	0, 3/2$^-$	M1	0.088±0.005	0.0366
	146, 7/2$^-$	88, 5/2$^-$	M1	0.371±0.040	0.204
	1295, 11/2$^-$	146, 7/2$^-$	E2	204^{+135}_{-68}[c]	242
^{49}V	90, 5/2$^-$	0, 7/2$^-$	M1	0.230±0.013	0.0033
	153, 3/2$^-$	0, 7/2$^-$	E2	197±3	243
	153, 3/2$^-$	90, 5/2$^-$	M1	0.0035±0.0001	0.181
	1021, 11/2$^-$	0, 7/2$^-$	E2	172±59[d]	189
	1155, 9/2$^-$	0, 7/2$^-$	M1	0.016±0.004[e]	0.0454
			E2	106±28[e]	135
	1155, 9/2$^-$	90, 5/2$^-$	E2	126±17[f]	98
^{51}V	320, 5/2$^-$	0, 7/2$^-$	E2	154±7.6[g]	82
			M1	$0.006^{+0.0008}_{-0.0014}$[h]	0.0147
	928, 3/2$^-$	0, 7/2$^-$	E2	76±5[g]	41
	928, 3/2$^-$	320, 5/2$^-$	M1	> 0.0001[i]	0.5231
			E2	107±9[g]	44
	1609, 11/2$^-$	0, 7/2$^-$	E2	83±8[g]	59
	1813, 9/2$^-$	0, 7/2$^-$	M1	$2.96^{+25.30}_{-2.26}$[j]	0.0312
			E2	28±5[g]	48
	1813, 9/2$^-$	320, 5/2$^-$	E2	24±5[g]	48

Table 7 (cont'd)

a) Units are μ_N^2 for B(M1) and e^2fm^4 for B(E2).

b) Assumed mixing ratio $\delta = 0$ except as noted.

c) Lifetime from (Bl 73).

d) Lifetime from (Ta 74).

e) $\delta = -0.78^{+0.18}_{-0.22}$ and lifetime from (Ta 74).

f) Lifetimes from (Ta 74).

g) B(E2) from (Ho 70).

h) $\delta = -0.32^{+0.30}_{-0.57}$ from (Ho 70).

i) $\delta = -8.8^{+4.1}_{-\infty}$ from (Ho 70).

j) $\delta = +3.75^{+0.76}_{-0.51}$ from (Ho 70) and lifetime from (Go 72).

$$B(E2) = \frac{5}{16\pi^2} Q_o^2 \quad .$$

The intrinsic quadrupole moment Q_o is given by the relation

$$Q_o = \frac{32e}{\sqrt{5\pi}} R_o^2 \, \beta(1 + 0.16\beta)$$

and the deformation parameter β is related to δ

$$\delta \approx 0.95\beta \quad .$$

Using these formula, the average values of $|\delta|$ obtained from the two adjacent even-even isotopes are 0.35, 0.28 and 0.19 for ^{47}V, ^{49}V and ^{51}V, respectively. The corresponding values used in the theoretical calculations were 0.342, 0.291 and 0.191, respectively. These are in excellent agreement with the experimentally calculated values.

The agreement is not as good for the Titanium isotopes where the mean values obtained from the B(E2) measurements are 0.30, 0.28 and 0.21 for ^{45}Ti, ^{47}Ti and ^{49}Ti, respectively. The corresponding values used in the theoretical calculations were 0.188, 0.236 and 0.08, respectively.

As shown in fig. 73 the even-even isotopes of Titanium and Chromium (NDS 73) exhibit spectra typically associated with quadrupole vibrations of the core. The Vibrational model predicts a one phonon excited 2^+ state with energy $\hbar\omega$, and a degenerate two phonon excited state with energy 2hω and spins 0^+, 2^+ and 4^+. The level spectra in fig. 73 approximately show this type of spectra and thus it would seem that the Intermediate Coupling Model, as described in Appendix A, would be useful in reproducing the properties of the odd-even isotopes of Titanium and Vanadium. However, using the expected single particle energy separations for the $1f\frac{5}{2} - 1f\frac{7}{2}$, $2p\frac{3}{2} - 1f\frac{7}{2}$ and $2p\frac{1}{2} - 1f\frac{7}{2}$ orbitals a poor fit to the experimental data was obtained. Only for unreasonably large coupling parameters could the experimental level schemes and spectroscopic factors be reproduced with fair agreement. This is consistent with the use of the Strong Coupling model where large coupling parameters lead to permanent deformation of the core.

The Nickel isotopes have received much theoretical attention in recent years. Both Auerbach (Au 67A) and Glaudemans et al (Gl 72) described those isotopes in terms of strongly admixed spherical shell model configurations where neutrons occupy the $2p\frac{3}{2}$, $1f\frac{5}{2}$ and $2p\frac{1}{2}$ orbits outside the ^{56}Ni core. Glaudemans et al also calculated the electromagnetic transition rates using an effective neutron charge of $e_n = (1.70 \pm 0.08)e$ and neglecting any ^{56}Ni core excitations. In both calculations, the level scheme of ^{59}Ni is well reproduced for the first three excited states, however, for higher energy levels a poorer fit to experimental data was obtained.

Since the even-even adjacent Nickel isotopes (NDS 73A) exhibit spectra typical of the vibrational model, it was of interest to see whether the Intermediate Coupling Model could be applied to describe the properties of ^{59}Ni. Although there are several variable parameters within the model it was hoped that these could be fixed from experimental data and then only the coupling parameter, ξ, allowed to vary.

The one phonon core excitation energy, $\hbar\omega$ = 1.393 MeV, was obtained from the average of the energies of the first 2^+ states of the adjacent even-even Nickel isotopes (NDS 73A). The odd neutron has available to it the single particle orbitals $2p\frac{3}{2}$, $1f\frac{5}{2}$ and $2p\frac{1}{2}$. The single-quasiparticle energies of these shell model levels, $\varepsilon_{1f\frac{5}{2}} - \varepsilon_{2p\frac{3}{2}} = 0.48$ MeV and $\varepsilon_{2p\frac{1}{2}} - \varepsilon_{2p\frac{3}{2}} =$ 2.07 MeV, were obtained using the spectroscopic information from a (d,p) experiment (Ch 73). The energy levels and transition rates were then obtained using the computer program CORPAR (Ca 70) and the resulting level scheme is shown in fig. 81. Using up to a possible 3 phonon core excitations, the best fit to the experimental data was obtained for a coupling parameter $\xi = 2.135$. Also shown in fig. 81 are the experimental level scheme (Hu 73) and the two theoretical level schemes obtained by Auerbach (Au 67A) and Glaudemans et al (Gl 72) for comparison.

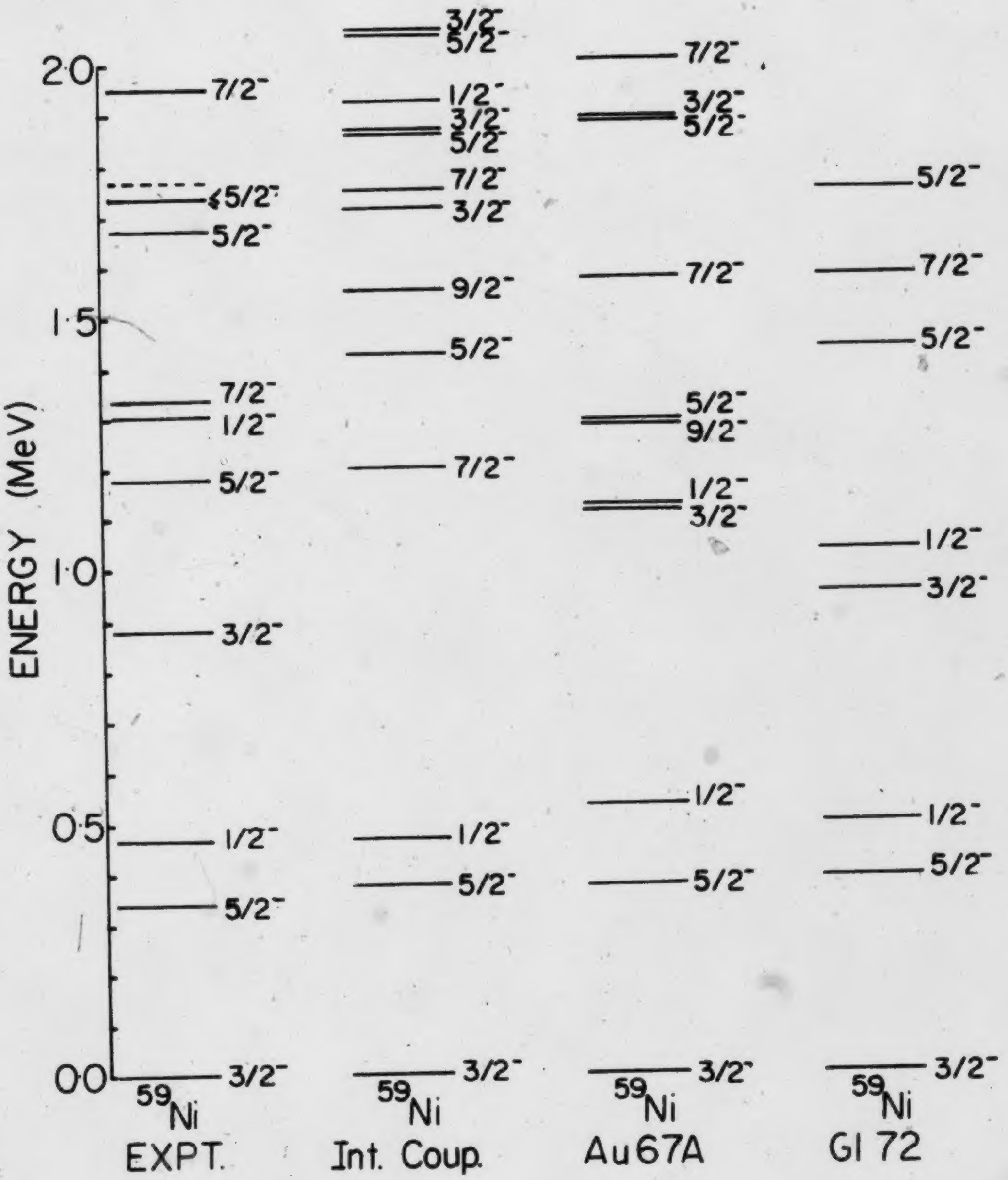

Fig. 81. Experimental and theoretical level schemes of ^{59}Ni.

The first three states are well reproduced by the Intermediate Coupling Model and although the fit is poorer for higher energy levels, corresponding experimental levels can be found for the predicted levels. The number of levels below 2.0 MeV is also in agreement with experimental results. Although no effective charge was used for the odd neutron, the electromagnetic transition rates are in fairly good agreement with experimental results as shown in Table 8.

No shell model calculations exist for ^{65}Zn. However, ^{65}Zn should be quite similar to ^{63}Ni, for which extensive theoretical studies are available (Au 67A, Gl 72). Both nuclei have seven neutrons outside the closed $1f\frac{7}{2}$ shell and although the proton shell is closed for ^{63}Ni, to a first approximation the two extra protons in ^{65}Zn may be assumed not to contribute to the structure of the low lying states in ^{65}Zn (We 70).

Weidinger et al (We 70) have done Weak Coupling Model calculations on ^{65}Zn considering ^{64}Zn as the core with a single neutron coupled to the core. Excited states of the core were restricted to a single phonon excitation and the core-particle interaction was the Thankappan and True (Th 65) spin-spin, quadrupole-quadrupole interaction. Since this model is similar to the Intermediate Coupling Model, it seemed worthwhile to apply the Intermediate Coupling Model to ^{65}Zn.

The single-quasiparticle energies of the shell model states $\varepsilon_{1p\frac{3}{2}} - \varepsilon_{1f\frac{5}{2}} = 0.130$ MeV and $\varepsilon_{1p\frac{1}{2}} - \varepsilon_{1f\frac{5}{2}} =$ 0.450 MeV, were obtained from the (d,p) data of Ehrenstein and Schiffer (Eh 67). A value of $\hbar\omega = 0.8$ MeV was used for the one phonon core excitation energy, which is slightly smaller than the average value of the energies of the first 2^+ states in ^{64}Zn and ^{66}Zn (NDS 73A). A best fit to the experimental data was obtained for a coupling parameter $\xi = 1.8$ and the predicted level scheme is shown in fig. 82. For comparison, the experimental level scheme (Ez 74) and the predicted level schemes of ^{63}Ni from the work of Auerbach (Au 67A) and Glaudemans et al (Gl 72), are also shown in fig. 82.

The first three levels are correctly reproduced, however, the $3/2^-$ level at 207 keV is not predicted. The experimental spectroscopic factor for this state is small (El 67) and hence the $3/2^-$ state produced by the coupling of the ground state $1f\frac{5}{2}$ level to the first excited state of the core may be the corresponding theoretical level. The large energy separation between the first set of states and the second which is characteristic of the Intermediate Coupling Model is also well reproduced.

The predicted electromagnetic transition rates are shown in Table 8. It is seen that for the low

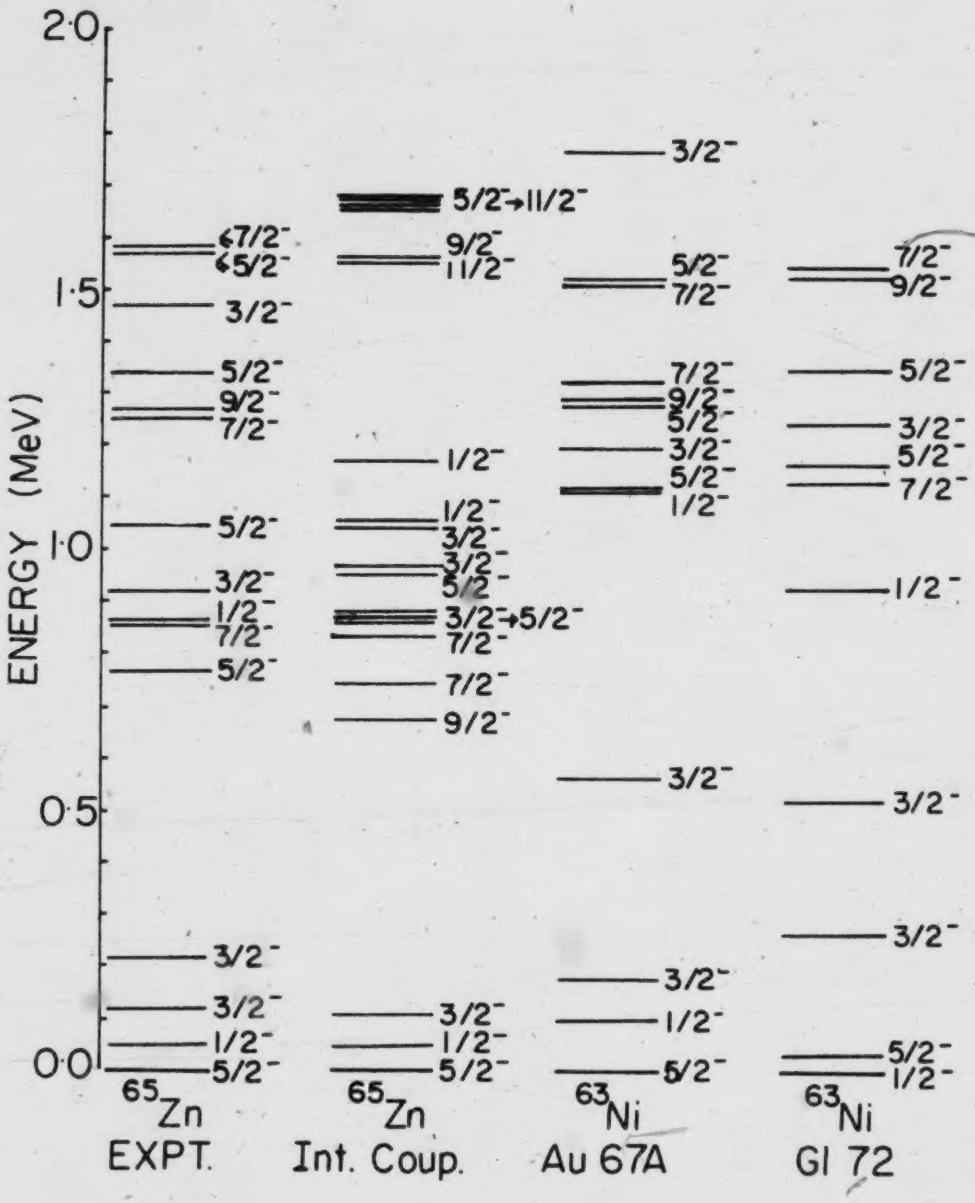

2.0
1.5
1.0
0.5
0.0
ENERGY (MeV)
⁶⁵Zn EXPT.
⁶⁵Zn Int. Coup.
⁶³Ni Au 67A
⁶³Ni Gl 72
7/2⁻
5/2⁻
3/2⁻
9/2⁻
1/2⁻
5/2⁻→11/2⁻
11/2⁻
3/2⁻→5/2⁻

Fig. 82. Experimental and theoretical level schemes of ^{65}Zn.

Table 8

Comparison of experimental reduced transition probabilities with the Intermediate Coupling model calculations for ^{59}Ni and ^{65}Zn.

Isotope			Multipole	$B(\Lambda)$[a]	
	E_i(keV), I_i^π →	E_f(keV), I_f^π		Experiment[b]	Theory
^{59}Ni	340, 5/2$^-$	0, 3/2$^-$	M1	0.0154±0.0016[c]	0.0019
			E2	23±12[c]	16
	465, 1/2$^-$	0, 3/2$^-$	M1	0.016±0.005	1.44
			E2($\delta=\infty$)	78±22	72
	878, 3/2$^-$	0, 3/2$^-$	M1	0.135±0.023[d]	0.091
			E2	20±17[d]	40
	1189, 5/2$^-$	0, 3/2$^-$	M1	0.065±0.041[e]	0.038
			E2	122^{+470}_{-122}[e]	62
	1302, 1/2$^-$	0, 3/2$^-$	M1	0.101±0.010[f]	0.124
	1339, 7/2$^-$	0, 3/2$^-$	E2	43±12	89
	1339, 7/2$^-$	340, 5/2$^-$	M1	0.0005±0.0005[g]	0.28
			E2	447^{+240}_{-116}[g]	0.76
^{65}Zn	54, 1/2$^-$	0, 5/2$^-$	E2	180^{+41}_{-30} [h]	27.9
	115, 3/2$^-$	0, 5/2$^-$	M1	0.0584±0.0012	0.00011
	207, 3/2$^-$	0, 5/2$^-$	M1	0.0071±0.0003	0.0023
	207, 3/2$^-$	54, 1/2$^-$	M1	0.053±0.002[i]	0.0004
			E2	1864±960[i]	21
	769, 5/2$^-$	0, 5/2$^-$	M1	>0.0035[j]	0.02
			E2	>1.69[j]	2.33
	1264, 9/2$^-$	0, 5/2$^-$	E2	>10	28

Table 8 (cont'd)

a) Units are μ_N^2 for B(M1) and e^2fm^4 for B(E2).

b) Assumed mixing ratio $\delta = 0$ except as noted.

c) $\delta = 0.11 \pm 0.03$ from (Hu 73).

d) $\delta = -0.09 \pm 0.04$ and lifetime from (Hu 73).

e) $\delta = 0.43 \pm 0.90$ and lifetime from (Hu 73).

f) Lifetime from (Hu 73).

g) $\delta = -8.1^{+2.6}_{-6.5}$ and lifetime from (Hu 73).

h) Lifetime from (Au 60) and $\alpha_T \approx \alpha_K = 6 \pm 1$ from (Ro 70).

i) $\delta = 0.24 \pm 0.06$ from (Ro 70).

j) $\delta = 0.20 \pm 0.06$ from (Ez 74).

lying energy levels, the transition rates are in poor agreement with the model predictions. However, the mixing ratios for these transitions are not known and assuming the lowest multipoles for the decay of these states may be incorrect. The use of an effective charge parameter will also change the predicted transition rates. However, for the higher energy γ-ray transitions, better agreement is obtained with experimental results. Hence the Intermediate Coupling Model cannot be completely ruled out in its application to ^{65}Zn since some of the properties of this isotope are reproduced by the model.

CHAPTER 9

CONCLUSIONS

This research has yielded a new method of improving the time resolution of Ge(Li) detectors by a pulse shape discrimination technique. The technique gives a significant improvement in the time resolution without seriously affecting the counting efficiency of the system. The results are considerably better than those of previous selection techniques. The improvement in the time resolution leads to greater accuracy in the determination of the centroids of the time distributions, which is the main limitation of the Centroid Shift technique for measuring lifetimes in the tens of picosecond region.

A further refinement of the technique was the development of the Triple Constant Fraction Discriminator which provides a convenient method of obtaining the improved time resolution. It also allows the experimenter to reject certain events which are mistimed by the electronics.

One of the greatest advantages of the present delayed coincidence technique is the simultaneous collection of data for both prompt and delayed time distributions. Thus errors are avoided that may occur due to electronic drifts and shifts between alternate experimental runs to obtain the time distributions separately. The use of two targets to obtain supplementary 'prompt' reference γ-rays in order to define the prompt time centroid curve, recognises the effect of the walk of the centroids of the prompt time distribution with the energy of the detected γ-ray.

The use of the two target rotating system to obtain these supplementary 'prompt' reference γ-rays is another advantage of the experimental method. The Target Discriminator, which allows the experimenter to separate the information obtained from each target, reduces errors in background subtractions since the peak to background ratio is not adversely affected by the presence of the second target.

The method of analysis where the centroid shifts of the delayed time distributions are measured relative to the prompt time centroid curve at the appropriate energy eliminates those errors that would occur due to the walk of the prompt time centroid curve. Analysis by this method ensures the accuracy of the present results and the validity of the technique.

The present delayed coincidence technique compares very favourably with other techniques to measure lifetimes in the picosecond region and in some cases distinct advantages can be seen. Using gas targets, the experimental upper limit for lifetime measurements by the

Doppler Shift Attenuation technique can be extended into the region of 10^{-11} secs. However, the use of gas targets is a distinct disadvantage and usually high energy heavy ion beams are required to obtain sufficient recoil velocities to observe a Doppler shift in energy of the emitted γ-ray. The method is also restricted to higher γ-ray energies so that measurable Doppler shifts are observed. In the analysis of Doppler shift experiments the function describing the energy loss of the residual recoiling nuclei is not accurately known and thus an important source of error occurs in the results.

The Recoil Distance technique is again generally restricted to reactions induced by high energy heavy ion beams since high recoil velocities are required to measure lifetimes of the order 10^{-11} secs. Recently, improvements in the technique have made lifetime measurements using ^{4}He beams, possible (Br 73). Another problem with this technique is the fabrication of thin targets to permit the residual nuclei to recoil freely into vacuum. The mounting of these targets to ensure an optically flat surface requires very precise engineering and measuring techniques.

The above problems are not encountered in the present delayed coincidence technique. However, there are a few major limitations to the technique. The first is the time resolution of Ge(Li) detectors which becomes increasingly worse with decreasing γ-ray energy. Thus lifetime measurements in the region of 50 ps or less become more difficult for low energy γ-ray transitions. Another problem is the availability of suitable 'prompt' reference γ-rays. However, once these have been established for a given energy region the problem is overcome to large extent. The third major limitation is the peak to background ratio. It was found that when this ratio decreased below 1:2 large uncertainties were introduced in background subtractions. Hence only γ-rays with reasonable intensities can be studied. This problem also occurs in the other two techniques mentioned above but to a lesser extent.

From the theoretical standpoint, the Strong Coupling Symmetric Rotator Model is seen to predict the level schemes of the odd-even Titanium and Vanadium isotopes very well, even though only the deformation parameter was allowed to vary. This provided a meaningful test of the model. The low lying ground state triplets in ^{45}Ti, ^{47}V and ^{49}V are all predicted and with the correct spin assignments. This was not possible with the pure $(1\ f\frac{7}{2})^n$ configuration shell model. The observed large energy gaps between these triplets and the next set of negative parity states are also well reproduced by the model. The only isotope where a relatively poor fit was obtained is ^{47}Ti although the predicted B(E2) transition rate for the 160 keV → g.s. transition is in very good agreement with the weighted mean of experimental results. Other electromagnetic transition rates predicted by the model are in fairly good agreement with experimental results.

Although little success was obtained using the Intermediate Coupling Model to predict the level schemes of the Titanium and Vanadium isotopes, the model is reasonably successful in its description of the properties of ^{59}Ni and ^{65}Zn. However, the predicted electromagnetic transition rates for the low energy transitions in ^{65}Zn are in poor agreement with experimental results.

In conclusion, there are two areas where further experimental investigations would be interesting using the present technique to study the Titanium and Vanadium isotopes. These are the two odd-odd isotopes of Vanadium, ^{48}V and ^{50}V. In ^{50}V the determination of the lifetimes of the 320, 355 and 388 keV levels would be possible if a suitable detector could be obtained for detecting the low energy γ-rays at 35 and 33 keV from the two levels at 355 and 388 keV, respectively. In the present work, it was found that although theoretically better timing of low energy γ-rays should be obtained with small volume planar Ge(Li) detectors as compared to coaxial Ge(Li) detectors, experimentally this was not the case. The problem here may be that at these low energies the noise is comparable in magnitude to the real event signals. The electrode area to detector volume is greater in planar detectors so noise contributions are larger in these detectors as compared to coaxial detectors.

For the case of ^{48}V several investigations into the lifetimes of the levels of this isotope have been reported (Ba 63, Au 67B, Bo 71, Hu 73A, Ha 73). The low energy level scheme shown in fig. 83 is from the work of Huber et al.(Hu 73A) with the lifetime results indicated with the appropriate references. The levels at 309,421 and 520 keV are obvious candidates for measurements by the present technique. Unfortunately, the Q value for the reaction ^{48}Ti(p,n)^{48}V is -4.795 MeV and it was found that using d.c. proton beams, beam energies greater than 6.0 MeV were required to excite these states to acceptable strengths. Although in principle, pulsed proton beams of this energy are obtainable from the University of Alberta's van da Graaff, many attempts to obtain such beams were unsuccessful due to deteriorating ion source characteristics and accelerator conditioning. Thus further investigations of this nucleus would be interesting using the pulsed beam (p,n) reaction.

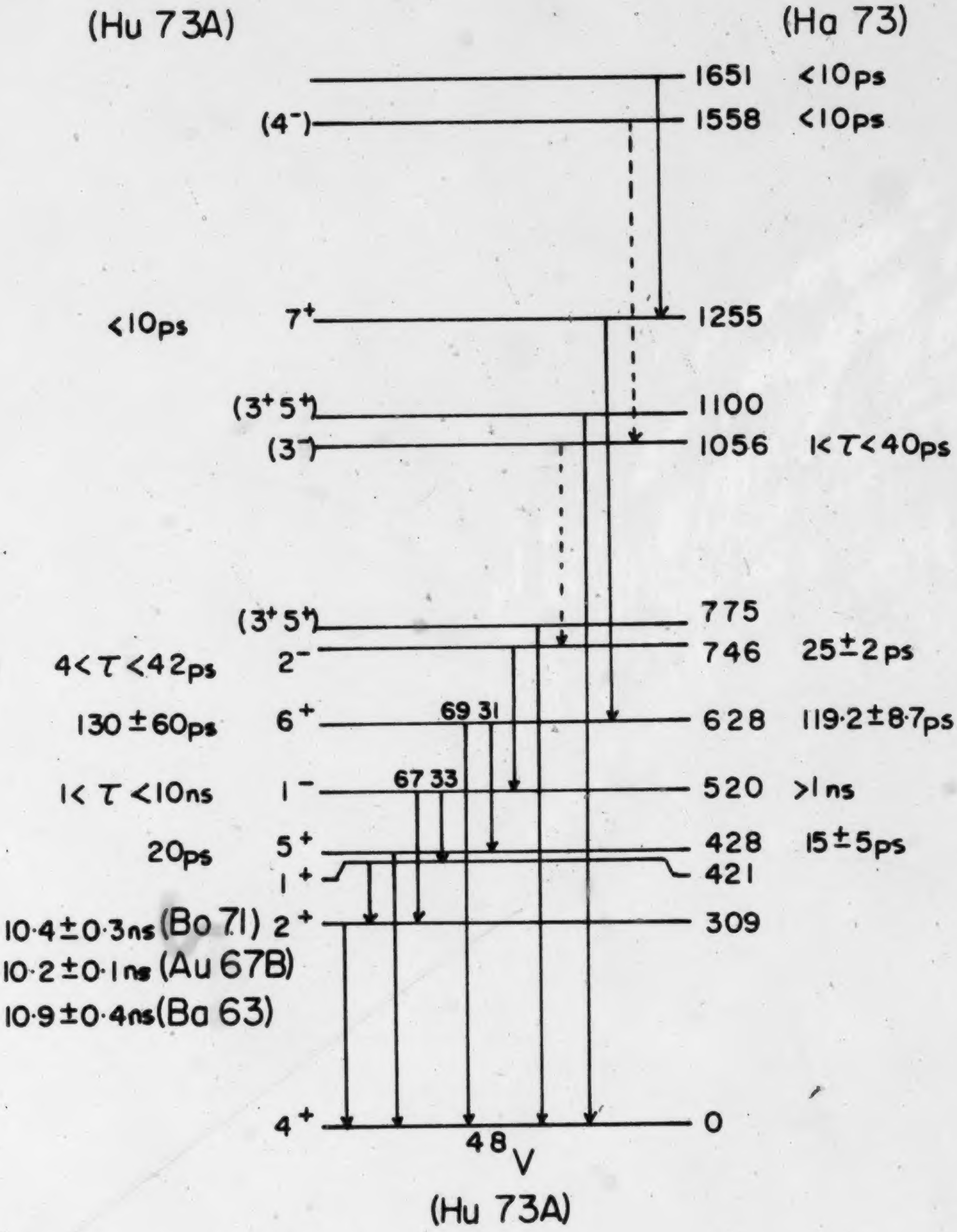
(Hu 73A)
(Ha 73)
1651 <10ps
(4⁻) 1558 <10ps
<10ps 7⁺ 1255
(3⁺5⁺) 1100
(3⁻) 1056 1<τ<40ps
(3⁺5⁺) 775
4<τ<42ps 2⁻ 746 25±2ps
130±60ps 6⁺ 628 119·2±8·7ps
69 31
1<τ<10ns 1⁻ 520 >1ns
67 33
20ps 5⁺ 428 15±5ps
1⁺ 421
10·4±0·3ns (Bo 71) 2⁺ 309
10·2±0·1ns (Au 67B)
10·9±0·4ns (Ba 63)
4⁺ 0
48V
(Hu 73A)

Fig. 83. Experimental level schemes and previous lifetime results for the states in ^{48}V.

REFERENCES

Al 65 T.K. Alexander and K.W. Allen, Can. J. Phys. 43 (1965) 1563.

Al 70 T.K. Alexander and A. Bell, Nucl. Inst. and Meth. 81 (1970) 22.

Ar 70 R. Armbruster, Y. Dar, J. Gerber, A. Macher and J.P. Vivien, Nucl. Phys. A143 (1970) 315.

Au 60 L.S. August and J.F. Friichtenicht, Phys. Rev. 120 (1960) 2072.

Au 67 N. Auerbach, Phys. Lett. 24B (1967) 260.

Au 67A N. Auerbach, Phys. Rev. 163 (1967) 1203.

Au 67B K. Auerbach, J. Braunsfurth, M. Maier, E. Bodenstedt and H.W. Flender, Nucl. Phys. A94 (1967) 427.

Ba 50 Z. Bay, Phys. Rev. 77 (1950) 419.

Ba 63 R.W. Bauer, J.D. Anderson and L.J. Christensen, Phys. Rev. 130 (1963) 312.

Be 68 G. Bertolini and A. Cocke, Semiconductor Detectors (North-Holland Publ. Co., Amsterdam, 1968).

Be 72 B. Bengtson and M. Moszyński, Nucl. Inst. and Meth. 100 (1972) 293.

Bl 60 A.E. Blaugrund, Y. Dar and G. Goldring, Phys. Rev. 120 (1960) 1328.

Bl 69 P. Blasi, P.R. Maurenzig and N. Taccetti, Nuovo Cim. Lett. 2 (1969) 174.

Bl 69A P. Blasi, P.R. Maurenzig, N. Taccetti and R.A. Ricci, Phys. Letts. 28B (1969)555.

Bl 70 P. Blasi, T.F. Fazzini, P.R. Maurenzig, N. Taccetti and R.A. Ricci, Nuovo Cim. 68A (1970) 49.

Bl 71 P. Blasi, M. Morando, P.R. Maurenzig and N. Taccetti, Nuovo Cim. Lett. 2 (1971) 63.

Bl 71A P. Blasi, M. Mandò, P.R. Maurenzig and N. Taccetti, Nuovo Cim. 4A (1971) 61.

Bl 73 P. Blasi, T. Fazzini, A. Giannatiempo, R.B. Huber and C. Signorini, Nuovo Cim. 15A (1973) 521.

Bo 52 A. Bohr, Dan. Mat. Fys. Medd. 26, No. 14 (1952).

Bo 53 A. Bohr and B.R. Mottelson, Dan. Mat. Fys. Medd. 27, No. 16 (1953).

Bo 71 P.D. Bond, J.D. McGervey and S. Jha, Nucl. Phys. A163 (1971) 571.

Br 65 R.T. Brockmeier, S. Wahlborn, E.J. Seppi and H. Boehm, Nucl. Phys. 63 (1965) 102.

Br 69 J.D. Brandenberger, Nucl. Inst. and Meth. 69 (1969) 271.

Br 73 F. Brandolini, M. de Poli and C. Rossi Alvarez, Nuovo Cim. Lett. Vol.8 No.6 (1973) 342

Br 74 B.A. Brown, D.B. Fossan, J.M. McDonald and K.A. Snover, Phys. Rev. C9 (1974) 1033.

Ca 70 T.P.G. Carola, Internal Report, Nuclear Research Centre, University of Alberta, UAE-NPL-24.

Ch 54 D.C. Choudhury, Dan. Mat. Fys. Medd. 28, No. 4 (1954).

Ch 67 D.C. Choudhury and T.F. O'Dwyer, Nucl. Phys. A93 (1967) 300.

Ch 68 R.L. Chase, Rev. of Sci. Inst. 39 (1968) 1318.

Ch 71 H.C. Cheung and S.K. Mark, Nucl. Phys. A176 (1971) 219.

Ch 72 Z.H. Cho and R.L. Chase, Nucl. Inst. and Meth. 98 (1972) 335.

Ch 72A Z.H. Cho and J. Llacer, Nucl. Inst. and Meth. 98 (1972) 461.

Ch 73 M.S. Chowdhury and H.M. Sen Gupta, Nucl. Phys. A205 (1973) 454.

Cu 63 W.M. Currie, Nucl. Phys. 47 (1963) 551.

Da 66 W.G. Davies, Ph. D. Thesis, University of Alberta, 1966.

Da 68 J.P. Davidson, Collective Models of the Nucleus (Academic Press Inc. (1968) page 107).

De 59 N.N. Delyagin and M. Preisa, JEPT 9 (1959) 1127.

Eh 67 D. von Ehrenstein and J.P. Schiffer, Phys. Rev. 164 (1967) 1374.

En 66 T. Engeland and E. Osnes, Phys. Lett. 20 (1966) 424.

En 73 P.M. Endt and C. van der Leun, Nucl. Phys. A214 (1973) 63.

Ez 74 R.L. Ezell and H.L. Scott, Nucl Phys. A218 (1974) 470.

Fa 56 L.W. Fagg, E.H. Geer and E.A. Wolicki, Phys. Rev. 104 (1956) 1073

Fo 55 K.W. Ford and C. Levinson, Phys. Rev. 100 (1955) 1.

Fr 61 R. Frauenfelder, W. Heer and F. Heinrich, Helv. Phys. Acta 34 (1961) 454.

Ge 67 D.A. Gedcke and W.J. McDonald, Nucl. Inst. and Meth. 55 (1967) 377.

Gl 72 P.W.M. Glaudemans, M.J.A. de Voigt and E.F.M. Steffens, Nucl. Phys. A198 (1972) 609.

Go 66 F.S. Goulding, Nucl. Inst. and Meth. 43 (1966) 1.

Go 72 A.S. Goodman and D.J. Donahue, Phys. Rev. C5 (1972) 875.

Gr 71 P.W. Green, B.C. Robertson and D.M. Sheppard, Internal Report, Nuclear Research Centre, University of Alberta UAE-NPL-1027.

Gr 73 P.W. Green, Ph. D. Thesis, University of Alberta, 1973.

Ha 73 B. Haas, P. Taras and R. Vaillancourt, University of Montreal, Nuclear Physics Annual Report, 1973.

He 54 W. Heitler, The Quantum Theory of Radiation (Oxford University Press, 3rd edition, 1954, page 188).

Ho 61 R.E. Holland and F.J. Lynch, Phys. Rev. 121 (1961) 1464.

Ho 70 R.N. Horoshko, D. Cline and P.M.S. Lesser, Nucl. Phys. A149 (1970) 562.

Hu 73 J.D. Hutton, N.R. Roberson, G.R. Gould and D.R. Tilley, Nucl. Phys. A206 (1973) 403.

Hu 73A R.B. Huber, C. Signorini, W. Kutschera and H. Morinaga, Nuovo Cim. 15A (1973) 501.

Hu 74 D.A. Hutcheon, D.C.S. White, W.J. McDonald and G.C. Neilson, Can. J. Phys. 52 (1974) 1090.

Iy 71 K.V.K. Iyengar and B.C. Robertson, Nucl. Phys. A171 (1971) 73.

Ja 69 J.M. Jaklevic, F.M. Bernthal, J.O. Radeloff and D.A. Landis, Nucl. Inst. and Meth. 69 (1969) 109.

Je 68 J.H. Jett, G.D. Jones and R.A. Ristinen, Phys. Letts. 28B (1968) 111.

Ka 69 C.D. Kavaloski and W.J. Kossler, Phys. Rev. 180 (1969) 971.

Ki 71 H.J. Kim and W.T. Milner, Nucl. Inst. and Meth. 95 (1971) 429.

Ki 72 A. Kiuru, Z. Physik 251 (1972) 93.

Kr 63 I.Y. Krause, Phys. Rev. 129 (1963) 1330.

Li 63 A.E. Litherland, M.J.L. Yates, M.B. Hinds and D. Eccleshall, Nucl. Phys. 44 (1963) 220.

Li 68 A. Li-Scholz and H. Bakhru, Phys. Rev. 168 (1968) 1193.

Li 70 K. Lips and M.T. McEllistrem, Phys. Rev. C1 (1970) 1009.

Li 71 K. Lips, Phys. Rev. C4 (1971) 1482.

Ly 70 F.J. Lynch, K.E. Nystén, R.E. Holland and R.D. Lawson, Phys. Lett. 32B (1970) 38.

Ma 66 F.B. Malik and W. Scholz, Phys. Rev. 150 (1966) 919.

Mc 64 J.D. McCullen, B.F. Bayman and L. Zamick, Phys. Rev. 134 (1964) B515.

Mc 71 F.K. McGowan, W.T. Milner, R.L. Robinson and P.H. Stelson, Ann. Phys. (N.Y.) 63 (1971) 549.

Mc 74 W.J. McDonald and D.C.S. White, To be published in Nucl. Inst. and Meth. Internal Report, University of Alberta, Nuclear Research Centre UAE-NPL-1062.

Me 67 W. Menti, Helv. Phys. Acta 40 (1967) 981.

Mi 61 H.E. Mitler, Nucl. Phys. 23 (1961) 200.

Mo 65 S.A. Moszkowski, Theory of Multipole Radiation, Alpha, Beta and Gamma Ray Spectroscopy (Vol. 2, North-Holland Publ. Co., Amsterdam, 1965).

Mo 70 M. Moszyński and B. Bengtson, Nucl. Inst. and Meth. 80 (1970) 233.

Mo 72A M. Moszyński and B. Bengtson, Nucl. Inst. and Meth. 100 (1972) 285.

Na 61 T.D. Nainan, Phys. Rev. 123 (1961) 1751.

NDS 70 Nuclear Data Sheets B, Vol. 4, Nos.3-4, July 1970.

NDS 72 Nuclear Data Sheets, Vol. 7, No. 2, February 1972.

NDS 73 Nuclear Data Sheets, Vol. 9, No. 4 (1973) 348.

NDS 73A Nuclear Data Sheets, Nuclear Level Schemes A=45 through A=257 (Academic Press, Inc., 1973).

NDS 74 Nuclear Data Sheets, Vol.11, No.2, February 1974.

Ne 50 T.D. Newton, Phys. Rev. 78 (1950) 490.

Ni 55 S.G. Nilsson, Dan. Mat. Fys. Medd. 29, No. 16 (1955).

Ok 73 O.B. Okon, H. Bakhru, M.K. Dewanjee and I.L. Preiss, Phys. Rev. C7 (1973) 239.

Ol 60 M.C. Olesen and B. Elbek, Nucl. Phys. 15 (1960) 134.

Ra 65 B.J. Raz and M. Soga, Phys. Rev. Lett. 15 (1965) 924.

Ri 62 R.C. Ritter, P.H. Stelson, F.K. McGowan and R.L. Robinson, Phys. Rev. 128 (1962) 2320.

Ro 57 M.E. Rose, Elementary Theory of Angular Momentum (John Wiley and Sons, Inc., 1957).

Ro 63 R.L. Robinson, N.R. Johnson and G.D. O'Kelley, Nucl. Phys. 47 (1963) 506.

Ro 67 H.J. Rose and D.M. Brink, Rev. Mod. Phys. 39 (1967) 306.

Ro 70 V.C. Rogers, L.E. Beghian, F.M. Clikeman and F.S. Mahoney, Nucl. Phys. A144 (1970) 81.

Ro 70A K.Q. Robert, J.R. Linn, B.J. Pellegrini and F.E. Durham, Nucl. Phys. A156 (1970) 553.

Ro 70B D.J. Rowe, Nuclear Collective Motion, Models and Theory (Methuen and Co., Ltd., 1970).

Sa 61 J. Samueli and A. Sarazin, J. Phys. Radium 22 (1961) 692.

Sa 69 E. Sakai, H.L. Malm and I.L. Fowler, Semiconductor Particle Detectors and Circuits (eds. W.L. Brown et al, Nat. Aca. of Sci., Washington, 1969).

Sc 66 W. Scholz and F.B. Malik, Phys. Rev. 147 (1966) 836.

Sc 67 W. Scholz and F.B. Malik, Phys. Rev. 153 (1967) 1071.

Sh 66 E. Sheldon and D.M. van Patter, Revs. Mod. Phys. 38 (1966) 143.

Sh 69 E.N. Shipley, R.E. Holland and F.J. Lynch, Phys. Rev. 182 (1969) 1165.

Si 61 P.C. Simms, N. Benczer-Koller and C.S. Wu, Phys. Rev. 121 (1961) 1169.

Si 70 H. Singh, B. Sethi and S.K. Mukherjee, Phys. Rev. C2 (1970) 2278.

Sk 66 S.J. Skorka, J. Hertel and T.W. Retz-Schmidt, Nucl. Data 2A (1966) 347.

Sp 66 P. Sparrman and F. Falk, Ark. Fys. 32 (1966) 447.

Sp 66A P. Sparrman, Nucl. Inst. and Meth. 41 (1966) 177.

St 67 M.G. Strauss and R.N. Larsen, Nucl. Inst. and Meth. 56 (1967) 80.

St 69 P. Steiner, E. Gerdau, W. Hautsch and D. Steenken, Z. Physik 221 (1969) 281.

Su 62 T. Sundström, Nucl. Inst. and Meth. 16 (1962) 153.

Sz 73 I.M. Szöghy, J.S. Forster and G.C. Ball, Nucl. Phys. A201 (1973) 433.

Ta 74 S.L. Tabor and R.W. Zurmühle, Phys. Rev. C10 (1974) 35.

Te 56 G.M. Temmer and N.P. Heydenburg, Phys. Rev. 104 (1956) 967.

Th 65 V.K. Thankappan and W.W. True, Phys. Rev. 137 (1965) B793.

Tu 66 N.A. Tubbs, Thesis, Oxford University, 1966.

Vi 72 G.B. Vingiani, C. Rossi-Alvarez, A. Buscemi and F. Brandolini, Phys. Letts. 40B (1972) 638.

Wa 63 E.K. Warburton, D.E. Alburger and D.H. Wilkinson, Phys. Rev. 129 (1963) 2180.

Wa 65 A.H. Wapstra, Nucl. Data, Vol. 1, No. 1, Dec. 1965.

Wa 70 R.A. Warner and J.E. Draper, Phys. Rev. C1 (1970) 1069.

We 60 R.S. Weaver and R.E. Bell, Nucl. Inst. and Meth. 9 (1960) 149.

We 62 R.S. Weaver and R. Barton, Can. J. Phys. 40 (1962) 660.

We 70 A. Weidinger, E. Finckh, U. Jahnke and B. Schreiber, Nucl. Phys. A149 (1970) 241.

We 72 J.J. Weaver, M.A. Grace, D.F.H. Start, R.W. Zurmühle, D.P. Balamuth and J.W. Noé, Nucl. Phys. A196 (1972) 269.

Wh 74 D.C.S. White and W.J. McDonald, Nucl. Inst. and Meth. 115 (1974) 1.

Wo 70 S.S.M. Wong, Nucl. Phys. A159 (1970) 235.

Ya 69 T. Yamazaki and G.T. Ewan, Nucl. Phys. A134 (1969) 81.

Zu 72 W.M. Zuk, W.F. Davidson, L.E. Carlson, M.R. Najam, Nucl. Phys. A187 (1972) 501.

APPENDIX A

A THEORETICAL DESCRIPTION OF THE ONE AND TWO PARTICLE INTERMEDIATE COUPLING MODEL

The Intermediate Coupling in the Unified Model was first outlined by Bohr (Bo 52) and Bohr and Mottelson (Bo 53). Later, it was elaborated by Choudhury and T.F. O'Dwyer (Ch 54, Ch 67) and Ford and Levison (Fo 55). The model is of considerable interest in the description of the low energy nuclear properties of the odd-mass nuclei whose doubly even neighbouring nuclei exhibit a vibrational spectrum. As described extensively in (Bo 53), the limiting cases of this model correspond either to weak coupling (for nuclei near double closed shells) or strong coupling (case of deformed nuclei).

1. One-Particle Theoretical Formulation

In this model, the odd-mass nucleus is treated as a coupled system comprising of a doubly even core capable of performing collective quadrupole oscillations of frequency ω and an extra-core nucleon which has several single particle levels available to it. The total Hamiltonian of the system can be expressed in the form

$$H_T = H_c + H_p + H_{int} \qquad 1$$

where H_c is the Hamiltonian for the core, H_p is the particle Hamiltonian, and H_{int} represents the interaction energy between the two systems.

The quadrupole oscillations of the nuclear surface of the core can be described by

$$R(\theta\phi) = R_o[1 + \sum_\mu \alpha_\mu\ Y_2^\mu(\theta,\phi)] \qquad 2$$

where α_μ are the dynamical variables of the collective motion. Provided the deviations from a spherical shape are small, the collective Hamiltonian can be expressed in the form (Ch 54)

$$H_c = \frac{1}{2} \sum_\mu \{B|\dot{\alpha}_\mu|^2 + C|\alpha_\mu|^2\} \qquad 3$$

which is the Hamiltonian of a system of harmonic oscillators with frequency

$$\omega = \sqrt{\frac{C}{B}} \quad . \qquad 4$$

The parameters B and C are, respectively, the collective mass and the nuclear deformability. Quantising the collective Hamiltonian by defining the momentum conjugate to α_μ and the commutation relations for α_μ and Π_μ

$$\Pi_\mu = \frac{\partial H_c}{\partial \dot{\alpha}_\mu} = B\dot{\alpha}_\mu^\dagger \qquad \begin{aligned} &[\alpha_\mu, \Pi_{\mu'}] = i\hbar\delta_{\mu\mu'} \\ &[\alpha_\mu, \alpha_{\mu'}] = [\Pi_\mu, \Pi_{\mu'}] = 0 \end{aligned}$$

the core Hamiltonian can be expressed in terms of creation and annihilation operators ($b_\mu^\dagger$ and b_μ) for spin 2 phonons which are defined by the equations

$$b_\mu^\dagger = \frac{1}{(2B\hbar\omega)^{\frac{1}{2}}} [B\omega\ \alpha_\mu^\dagger - i\Pi_\mu] \qquad b_\mu = \frac{1}{(2B\hbar\omega)^{\frac{1}{2}}} [B\omega\ \alpha_\mu + i\Pi_\mu^\dagger]$$

and solving for $\alpha_\mu^\dagger$ in terms of b_μ and $b_\mu^\dagger$ yields

$$\alpha_\mu^\dagger = \sqrt{\frac{\hbar}{2B\omega}}\ [b_\mu^\dagger + (-)^\mu b_{-\mu}] \qquad 5$$

The core Hamiltonian then becomes

$$H_c = \sum_\mu (b_\mu^\dagger b_\mu + \frac{1}{2})\ \hbar\omega \qquad 6$$

and has eigenvalues

$$E_N = (N + \frac{5}{2})\ \hbar\omega \qquad 7$$

where N can be interpreted as the number of phonons associated with a particular state.

For a given single particle orbital, the particle Hamiltonian H_p is a constant, having as its eigenvalues the single particle energy levels ε_j which are regarded as adjustable parameters in the theory.

The interaction Hamiltonian H_{int} can be written to first order in α_μ (Mi 54)

$$H_{int} = -k(r)\ \Sigma\ \alpha_\mu\ \ Y_2^\mu(\theta\phi) \qquad 8$$

where (r,θ,ϕ) are the coordinates of the particle. In calculating the matrix elements of 8 one needs the values of the radial matrix element

$$k \equiv \langle n'\ell'|k(r)|n\ell\rangle$$

which will depend in general on the quantum numbers n and ℓ describing the initial and final states of the particle. However, the dependence of k on these quantum numbers is not critical and so it is assumed to be constant. It is convenient to write the Hamiltonian in terms of phonon creation and annihilation operators,

$$H_{int} = -\sqrt{\frac{\pi}{5}}\,\hbar\omega\xi \sum_{\mu} (-)^{\mu}[b_{\mu} + (-)^{\mu}\, b^{\dagger}_{-\mu}]\; Y^{\mu}_{2}(\theta,\phi) \qquad 9$$

where the strength of the interaction is characterised by the dimensionless coupling parameter

$$\xi = \left(\frac{5}{2\pi\hbar\omega C}\right)^{\frac{1}{2}} k \quad . \qquad 10$$

It is convenient to work in an angular momentum representation. The basis states of the system are chosen as the eigenfunctions of $H_c + H_p$, the non-interacting system

$$|jNR;IM> = \sum_{m} (j\,R\,M{-}m\,m|IM)\,|j\;M{-}m>|Rm> \qquad 11$$

where j is the angular momentum of the odd nucleon, coupled to a core state characterised by N phonons coupled to a core spin R, to give a state of total angular momentum I and projection M.

The eigenfunctions of the total Hamiltonian (1) will be linear combinations of these basis states, of the form

$$|E_I;IM\rangle = \sum_{jNR} A(E_I;jNRI)\,|jNR;IM\rangle \quad . \qquad 12$$

The expansion coefficients $A(E_I;jNRI)$ and the corresponding energy eigenvalues in eq. 12 can be found by calculating the matrix elements of H_T, and diagonalising the resulting matrix. In this representation, both the core Hamiltonian H_c and the particle Hamiltonian H_p have only diagonal matrix elements

$$\langle jNR;IM|H_c + H_p|jNR;IM\rangle = (N + \tfrac{5}{2})\hbar\omega + \varepsilon_j \qquad 13$$

where $\hbar\omega$ is the phonon energy and ε_j the single particle energy for the particle in orbital j.

The matrix elements of the interaction Hamiltonian are:

$$\langle j'N'R';IM|H_{int}|jNR;IM\rangle = -\sqrt{\frac{\pi}{5}}\,\hbar\omega\xi\langle j'||Y_2||j\rangle$$

$$\sqrt{2j'+1}\;(-1)^{j'+R-I}\;W(jj'RR';2I)$$

$$\{(-1)^{R'-R}\;\sqrt{2R+1}\langle NR||b^\dagger||N'R'\rangle$$

$$+\sqrt{2R'+1}\;\langle N'R'||b^\dagger||NR\rangle\} \qquad 14$$

where the techniques of Racah algebra, using the Clebsch-Gordon and Racah coefficients, and the Wigner-

Eckart theorem[*] have been utilised in the derivation (Ro 57).

The reduced matrix elements for the spherical harmonic Y_2 and the boson creation operator $b^\dagger$ are the only terms left to be explicitly defined. The former is given by

$$\sqrt{2j'+1}\langle j'||Y_2||j\rangle = (-1)^{j'-\frac{1}{2}}\left[\frac{(2j+1)(2j'+1)}{4\pi}\right]^{\frac{1}{2}}(jj'\tfrac{1}{2}-\tfrac{1}{2}|20)$$

$$\tfrac{1}{2}[1+(-)^{\ell+\ell'}] \ . \qquad 15$$

---

[*] Since the interaction Hamiltonian must be a scalar, using the definition of the scalar product of two irreducible tensors (Ro 57)

$$H_{int} = -k(\tilde{Y}_2^\mu \cdot \tilde{\alpha}_\mu^*) = -k \sum_\mu (-)^\mu \alpha_{-\mu}^* Y_2^\mu$$

$$= -k \sum_\mu \alpha_\mu \quad Y_2^\mu \qquad 16$$

where since $R(\theta\phi)$, eq. 2, is real $\alpha_\mu^\dagger = (-)^\mu \ \alpha_{-\mu}$. Eq.16 is the form of the interaction Hamiltonian so both $\tilde{Y}_2^\mu$ and $\tilde{\alpha}_\mu^*$ are chosen as irreducible tensors in this calculation. From the definition of α_μ^*, $b_\mu^\dagger$ and $(-)^\mu b_{-\mu}$ are also irreducible tensors but not $b_{-\mu}$ alone. This fact is very important when using the Wigner-Eckart theorem which applies only to irreducible tensor operators. The definition of the Wigner-Eckart theorem used is that of Rose (Ro 57)

$$\langle j'M'|T_K^\kappa|JM\rangle = (JKM\kappa|J'M')\langle J'||T_K||J\rangle \quad .$$

Using coefficients of fractional parentage, detailed calculations of the method used in obtaining the reduced matrix elements of $b^\dagger$ can be found in (Ch 54) and (Fo 55). The result is:

$$\langle NR||b^\dagger||N'R'\rangle = \sqrt{N}\,[2^{N-1}(R')2R|\}2^N R] \qquad 17$$

where $[2^{N-1}(R')2R|\}2^N R]$ is the coefficient of fractional parentage, R' and R are the total angular momenta of the (N-1) and N phonon systems, respectively, and 2 is the angular momentum of each phonon. A list of the reduced matrix elements for $N \leq 3$ is given in Table 9.

Electromagnetic Transitions

The transition probability for radiation of a photon of multipole order L and frequency ω is

$$T(\sigma L) = \frac{8\pi(L+1)}{L[(2L+1)!!]^2}\frac{1}{\hbar}\left(\frac{\omega}{c}\right)^{2L+1} B(\sigma L) \qquad 18$$

where σ is the mode of the transition, either electric or magnetic, and $B(\sigma L)$ is the reduced transition probability.

$$B(\sigma L) = \frac{1}{2J_i+1}\sum_{M_i M_f} |\langle f|M^\sigma_{LM}|i\rangle|^2 \qquad 19$$

The values of the multipole operators, M^σ_{LM}, used are those introduced by Bohr and Mottelson (Bo 53) for

Table 9

Reduced matrix elements for the boson creation operators.

N	R	N'	R'	$\langle NR\|\|b^{\dagger}\|\|N'R'\rangle$
1	2	0	0	1
2	0	1	2	$\sqrt{2}$
2	2	1	2	$\sqrt{2}$
2	4	1	2	$\sqrt{2}$
3	2	2	0	$\sqrt{7/5}$
3	0	2	2	$\sqrt{3}$
3	2	2	2	$\sqrt{4/7}$
3	3	2	2	$\sqrt{15/7}$
3	4	2	2	$\sqrt{11/7}$
3	2	2	4	$\sqrt{36/35}$
3	3	2	4	$-\sqrt{6/7}$
3	4	2	4	$\sqrt{10/7}$
3	6	2	4	$\sqrt{3}$

the system resulting from the coupling of a single particle to the quadrupole oscillations of the core surface. In this formulation only the electric quadrupole and magnetic dipole transitions will be considered. These multipole operators are:

i) Electric quadrupole operator:

$$M^E_{2\mu} = (e_p - \frac{Ze}{A^2})r^2 \; Y_2(\theta\phi) + \frac{3}{4\pi} Ze \; R_o^2 \; \alpha^\dagger_\mu \qquad 20$$

where e_p is equal to e for protons and 0 for neutrons, r is the radial coordinate and R_o the nuclear radius. The term $-Ze/A^2$ has been introduced (Bo 53) to account for the orbital motion of the core around the centre of mass of the whole nucleus which will give a matrix element for electric transitions. However, this will be replaced by e_{eff}, which is an effective charge parameter.

ii) Magnetic dipole operator:

$$M^M_{1\mu} = \mu_o \sqrt{\frac{3}{4\pi}} \; (g_s \; s_\mu + g_\ell \; \ell_\mu + g_R \; R_\mu) \qquad 21$$

where $\mu_o = e\hbar/2Mc$ is the nuclear magneton, g_ℓ and g_s are the orbital and spin gyromagnetic ratios, respectively, and g_R is the effective gyromagnetic ratio of the core taken as equal to Z/A. R_μ is the Z-component of angular momentum of the core.

The initial and final state wavefunctions, $|i\rangle$ and $|f\rangle$ are given by

$$|i\rangle = |E;IM\rangle = \sum_{jNR} A(E;jNRI)\,|jNR;IM\rangle$$

and

$$|f\rangle = |E';I'M'\rangle = \sum_{j'N'R'} A(E;j'N'R'I')\,|j'N'R'I'M'\rangle .$$

In the formulation the matrix elements of r^2 are assumed independent of the quantum numbers and are given by the constant density approximation

$$\langle r^L\rangle = \frac{3}{3+L}\, R_o^L$$

where the equilibrium nuclear radius R_o is given by

$$R_o = 1.2A^{1/3}\ \text{fm} .$$

Defining χ_1 and χ_2 as follows

$$\chi_1 = (e + e_{eff})\,\frac{3}{5}\, R_o^2$$

$$\chi_2 = \frac{3}{4\pi}\sqrt{\frac{\hbar\omega}{2c}}\ Ze\ R_o^2$$

then for the electric quadrupole operator of the reduced transition probability, the calculations yield

$$\begin{aligned} B(E2)_{I\to I'} = (2I'+1)\Big| \sum_{\substack{jNR\\ j'N'R'}} & A(E,jNRI)A(E'j'N'R'I') \\ & \{\delta_{NN'}\delta_{RR'}(-)^{I'+j-R}\,\chi_1\langle j'||Y_2||j\rangle\sqrt{2j'+1}\;W(j'jI'I;2R) \\ & + \chi_2\,\delta_{jj'}\delta_{\ell\ell'}\sqrt{2R'+1}\;W(R'RI'I;2j)(-)^{I-j+R'} \\ & [\langle N'R'||b^\dagger||NR\rangle + (-)^{R'-R}\sqrt{\frac{2R+1}{2R'+1}}\,\langle NR||b^\dagger||N'R'\rangle]\}\Big|^2 . \end{aligned}$$

22

The reduced transition probability for magnetic dipole operator is:

$$\underset{I\to I'}{B(M1)} = \frac{3}{4\pi}\mu_o^2(2I'+1)\Big|\sum_{jj'NR} A(E;jNRI)A(E';j'NRI')$$

$$\{g_R(-)^{R+I-j-1}\delta_{jj'}\delta_{\ell\ell'}\sqrt{R(R+1)(2R+1)}\,W(RRI'I;1j)$$

$$+\,g_\ell(-)^{\ell+j-j'-I'-R-\frac{1}{2}}\delta_{\ell\ell'}\sqrt{(2j+1)(2j'+1)}$$

$$\sqrt{\ell(\ell+1)(2\ell+1)}\,W(j'jI'I;1R)W(\ell\ell j'j;1\tfrac{1}{2})$$

$$+\,g_s(-)^{\ell-\frac{1}{2}+I'-R}\,\delta_{\ell\ell'}\sqrt{\frac{3}{2}}\sqrt{(2j+1)(2j'+1)}\,W(j'jI'I;1R)$$

$$W(\tfrac{1}{2}\tfrac{1}{2}jj;1\ell)\}\Big|^2 \quad . \qquad 23$$

2. The Two-Particle Theoretical Formulation

In this section we consider a system of A nucleons composed of a collective core of (A-2) nucleons, coupled to a single proton and neutron outside the vibrating core. The total Hamiltonian is

$$H_T = H_c + H_p + H_n + H_{int}(p) + H_{int}(n) + V_{pn} \quad . \qquad 24$$

The notation is same as in section 1 but the extra term V_{pn} is the residual interaction between the two extra particles. Again it is convenient to work in the angular momentum representation and choose as the basis states, the eigenfunctions of the core-plus-particles Hamiltonian, $H_c + H_p + H_n$, and represent these eigenfunctions by $|j_p\, j_n\, J;\, NR;IM>$ where

$$|j_pj_nJ;NR;IM> = \sum_{\rho}(JRM-\rho\,\rho|IM)\,|j_pj_nJ\,M-\rho>|NR\rho>$$

and

$$|j_pj_nJ\,M-\rho> = \sum_{m}(j_pj_n m\, M-\rho-m|J\,M-\rho)\,|j_pm>|j_n\, M-\rho-m> \;.$$

The eigenfunctions of the total Hamiltonian will be a linear combination of the basis states and are represented as

$$|E;IM> = \sum_{\substack{j_pj_n\\ JNR}} A(E;j_pj_nJNRI)\,|j_pj_n\,J;NR;IM> \;. \qquad 25$$

In this representation both the core and particle Hamiltonians have only diagonal matrix elements.

$$<j_pj_nJ;NR;IM|H_c+H_p+H_n|j_pj_nJ;NR;IM> = (N+\tfrac{5}{2})\hbar\omega + \varepsilon_j^p + \varepsilon_j^n \qquad 26$$

where ε_j^p and ε_j^n are the single particle energies for a particle in the orbital j.

The matrix elements of the interaction Hamiltonian $H_{int}(p)$ are

$$<H_{int}(p)> = -\sqrt{\frac{\pi}{5}}\,\hbar\omega\xi\{<NR||b^{\dagger}||N'R'> + (-)^{R'-R}$$

$$\sqrt{\frac{2R'+1}{2R+1}}\,<N'R'||b^{\dagger}||NR>\}<j_p'||Y^2||j_p>$$

$$[(2j_p'+1)(2J'+1)(2J+1)(2R+1)]^{\frac{1}{2}}\,W(JJ'RR';2I)$$

$$W(JJ'j_pj_p';2j_n)\,\delta_{II'}\,\delta_{MM'}\,\delta_{j_nj_n'}\,(-)^{I-R'-j_n+j_p} . \qquad 27$$

A similar result holds for $H_{int}(n)$ except that the subscripts p are replaced by n and the whole result is multiplied by the phase factor

$$(-)^{j_p+j_n-J+j_p'+j_n'-J'} .$$

This extra phase factor comes from the relation

$$(j_pj_nm_pm_n|JM) = (-)^{j_p+j_n-J}\,(j_nj_pm_nm_p|JM) .$$

The residual interaction Hamiltonian V_{pn} is assumed to be a sum of the scalar products of two tensors, one of which acts on the proton coordinates and the other acting on the neutron coordinates (Sh 63)

$$\text{i.e.}\quad V_{pn} = \sum_{k=0}^{\infty} (\tilde{T}^k(p)\cdot\tilde{T}^k(n))$$

$$= \sum_{k=0}^{\infty} \Sigma_{\kappa}(-)^{\kappa}\,T^k_{-\kappa}(p)\,T^k_{\kappa}(n) . \qquad 28$$

Using this relationship the matrix elements of the residual interaction are

$$\langle V_{pn}\rangle = \delta_{NN'}\delta_{RR'}\delta_{JJ'}\delta_{MM'}\delta_{II'} \sum_k \sqrt{(2j_p'+1)(2j_n'+1)}$$

$$W(j_p j_p' j_n j_n';kJ)\langle j_p'||T^k(p)||j_p\rangle\langle j_n'||T^k(n)||j_n\rangle(-)^{j_p+j_n-J} . \qquad 29$$

However this term can be assumed to be small and can be neglected in most calculations.

Electromagnetic Transitions

As with the single particle case the following constants are defined:

$$\langle r^2\rangle = \frac{3}{5} R_o^2 ,$$

$$\chi_1^i = (e_i + e_{eff}^i)\frac{3}{5} R_o^2 \qquad i = p,n$$

and

$$\chi_2 = \frac{3}{4\pi}\sqrt{\frac{\hbar\omega}{2c}}\ Ze\ R_o^2 .$$

The electric quadrupole operator for the two particle system then becomes

$$M_{2\mu}^E = \chi_1^p\ Y_2(\theta_p\phi_p) + \chi_1^n\ Y_2(\theta_n\phi_n) + \chi_2\sqrt{\frac{2c}{\hbar\omega}}\ \alpha_\mu^\dagger \qquad 30$$

and the magnetic dipole operator

$$M_{1\mu}^M = \mu_o\sqrt{\frac{3}{4\pi}}\ (g_s^p s_\mu^p + g_s^n s_\mu^n + g_\ell^p \ell_\mu^p + g_R R_\mu) . \qquad 31$$

The reduced transition probabilities can then be calculated to give the two horrendous formulae

$$\begin{aligned}
\underset{I\rightarrow I'}{B(E2)} = (2I'+1) \Big| & \sum_{\substack{JNRj_pj_n \\ J'N'R'j'_pj'_n}} A(E;j_pj_nJNRI)A(E';j'_pj'_nJ'N'R'I') \\
& \chi_1^p \delta_{NN'}\delta_{RR'}\delta_{j_nj_n'}<j'_p||Y_2||j_p>W(j'_pj_pJ'J;2j_n)W(I'IJ'J;2R) \\
& [(2j'_p+1)(2J+1)(2J'+1)]^{\frac{1}{2}}(-)^{j_p-j_n+J-J'+R-I'} \\
& + \chi_1^n \delta_{NN'}\delta_{RR'}\delta_{j_pj_p'}<j'_n||Y_2||j_n>W(j'_nj_nJ'J;2j_p)W(I'IJ'J;2R) \\
& [(2j'_n+1(2J+1)(2J'+1)]^{\frac{1}{2}}\ (-)^{2j_n-j'_n-j_p+R-I'} \\
& + \chi_2 \delta_{j_pj_p'}\delta_{j_nj_n'}\delta_{JJ'}(-)^{I-J+R'}\sqrt{(2R'+1)}\,W(R'RI'I;2J) \\
& [<N'R'||b^\dagger||NR> + (-)^{R'-R}\sqrt{\frac{2R+1}{2R'+1}}<NR||b^\dagger||N'R'>]\}\Big|^2
\end{aligned} \tag{32}$$

and

$$\begin{aligned}
\underset{I\rightarrow I'}{B(M1)} = \frac{3}{4\pi}\mu_o^2(2I'+1) \Big| & \sum_{\substack{JNRj_pj_n \\ J'j'_pj'_n}} A(E;j_pj_nJNRI)A(E';j'_pj'_nJ'NRI') \\
& \{g_R\sqrt{R(R+1)(2R+1)}\ W(RRI'I;1J)(-)^{R+I-J-1}\delta_{JJ'}\delta_{j_pj_p'}\delta_{j_nj_n'} \\
& + g_s^p\ W(\tfrac{1}{2}\tfrac{1}{2}j'_pj_p;1\ell_p)W(j'_pj_pJ'J;1j_n)W(I'IJ'J;1R) \\
& [\tfrac{3}{2}(2j_p+1)(2j'_p+1)(2J+1)(2J'+1)]^{\frac{1}{2}}(-)^{j_n-J-J'+R-I'-\frac{1}{2}-\ell_p} \\
& \delta_{\ell_p\ell_p'}\delta_{j_nj_n'} + g_s^n\ W(\tfrac{1}{2}\tfrac{1}{2}j'_nj_n;1\ell_n)W(j'_nj_nJ'J;1j_p)W(I'IJ'J;1R) \\
& [\tfrac{3}{2}(2j_n+1)(2j'_n+1)(2J+1)(2J'+1)]^{\frac{1}{2}}(-)^{j'_n-j_n+j_p-2J'+R-I'-\ell_p-\frac{1}{2}} \\
& \delta_{\ell_n\ell_n'}\delta_{j_pj_p'} + g^pW(\ell_p\ell_pj'_pj_p;1\tfrac{1}{2})W(j'_pj_pJ'J;1j_n)W(I'IJ'J;1R) \\
& [\ell_p(\ell_p+1)(2\ell_p+1)(2j_p+1)(2j'_p+1)(2J+1)(2J'+1)]^{\frac{1}{2}} \\
& (-)^{J'+J-R+I'-\ell_p-j_p+j'_p-j_n-\frac{1}{2}}\}\Big|^2 \ .
\end{aligned} \tag{33}$$

APPENDIX B

THE STRONG-COUPLING SYMMETRIC ROTATOR MODEL

Some nuclei show an energy spectrum characteristic of a rotator and appear to have a non-spherical equilibrium shape. Such nuclei have been described successfully by the Unified Model, which exhibits both collective and individual particle aspects of nuclear structure. The basis of the model is the strong-coupling model of Bohr and Mottelson (Bo 53) where, in odd-A nuclei, the unpaired nucleon moves in a field generated by the deformed core. The total Hamiltonian consists of the rotational energy of the core and the single particle Hamiltonian H_p and is given by

$$H = H_{rot} + H_p \qquad 1$$

where

$$H_{rot} = \sum_{k=1}^{3} \frac{\hbar^2}{2\mathcal{J}_K} R_K^2$$

R_1, R_2 and R_3 and $\mathcal{J}_1$, $\mathcal{J}_2$ and $\mathcal{J}_3$ are respectively, the components of the rotational angular momentum *R* , and the components of the moments of inertia $\mathcal{J}$ in the body fixed coordinate system. In general *R* is not equal to the total angular momentum *I* of the system but is given by

$$I = R + j \tag{3}$$

where j is the intrinsic angular momentum of the extra core nucleon. The total angular momentum will be a constant of motion, however, R and j will not be because of the deformation. The projection of I upon the laboratory z axis is M; its projection on the body-fixed 3 axis is taken as K whereas the projection of j on this axis is denoted by Ω.

If the system possesses an axis of symmetry which is taken as the 3 axis, then K and Ω will also be good quantum numbers. For an axial symmetric deformation we take

$$\mathfrak{J}_1 = \mathfrak{J}_2 = \mathfrak{J}$$

and then the total Hamiltonian may be expressed in terms of the total angular momentum

$$H = \frac{\hbar^2}{2\mathfrak{J}} (I^2 - 2I \cdot j + j^2) + H_P \tag{4}$$

or

$$H = \frac{\hbar^2}{2\mathfrak{J}} (I^2 + j^2 - 2I_3 j_3) - \frac{\hbar^2}{2\mathfrak{J}} (I_+ j_- + I_- j_+) + H_P \tag{5}$$

where the quantities $I_\pm$ and $j_\pm$ are the operators $I_1 \pm iI_2$ and $j_1 \pm ij_2$, respectively. In the last two equations use has been made of the fact that since a quantal system cannot rotate about an axis of symmetry because it is impossible to define an azimuthal angle for the system, the angular momentum R_3 of the rotator about its axis of symmetry is zero and hence also $K = \Omega$ (Ro 70B).

The second term in eq. 5 is the Rotation-Particle-Coupling term or the Coriolis interaction. In its absence the particle would be unaware of the rotational motion of the axes and so the effect of such an interaction is to decouple the particle from the core. In general this term possesses only off-diagonal matrix elements except for the case $K = \Omega = \frac{1}{2}$ for which the diagonal matrix elements are nonvanishing. This follows from the fact that since the nucleus is assumed to possess axial symmetry the levels are degenerate in the sign of K and Ω.

The eigenfunctions of the operator $(\hbar^2/2\mathcal{J})\, \mathcal{I}^2$ are the normalised D-functions $D(\alpha\beta\gamma)$ which are the transformation functions for the spherical harmonics under finite rotations. These satisfy the following relations

$$
\begin{aligned}
\mathcal{I}^2\, D^I_{MK} &= I(I+1)\, D^I_{MK} \\
I_z\, D^I_{MK} &= M\, D^I_{MK} \qquad\qquad 6 \\
I_3\, D^I_{MK} &= K\, D^I_{MK} \quad .
\end{aligned}
$$

We define the normalised intrinsic wave function as $\chi_{\Omega\alpha}$ ($\equiv|\Omega\alpha>$) where α is an additional index to distinguish between states of the same projection quantum number Ω. Because the potential is not spherically symmetric, the average force on the particle is not central and the operator j^2 in eq. 5 is not a constant of motion and can be absorbed in the particle Hamiltonian. Thus it is simpler to deal with states of a constant angular momentum as a basis

$$\chi_{\Omega\alpha} = \sum_{j} c_{j\Omega\alpha}\, \chi_{j\Omega} \quad . \qquad 7$$

There is an alternative representation for $\chi_{\Omega\alpha}$ in which the constants of motion are the orbital angular momentum ℓ, its component Λ on the 3-axis, and Σ, the component of spin on the 3 axis

$$\chi_{\Omega\alpha} = \sum_{\ell\Lambda} a_{\ell\Lambda\Omega\alpha}\, \chi_{\ell\Lambda\Omega} \quad (\chi_{\ell\Lambda\Omega} \equiv |N\ell\Lambda\Omega>) \quad . \qquad 8$$

The coefficients $c_{j\Omega\alpha}$ are connected to the coefficients $a_{\ell\Lambda\Omega\alpha}$ by the angular momentum addition relations

$$c_{j\Omega\alpha} = \sum_{\ell\Lambda} (\ell\tfrac{1}{2}\Lambda\Sigma|j\Omega)\, a_{\ell\Lambda\Omega\alpha} \quad . \qquad 9$$

In the absence of the Coriolis coupling the total wavefunction Φ is a properly symmetrized product of the D-function and single particle wavefunction $\chi_{\Omega\alpha}$

$$\Phi = \left(\frac{2I+1}{16\pi^2}\right)^{\frac{1}{2}} [D^I_{MK}\, \chi_{\Omega\alpha} + (-)^{I-\frac{1}{2}}\, D^I_{M-K}\, \Pi_x\, \chi_{-\Omega\alpha}] \qquad 10$$

where $\Pi_x = (-)^{\ell}$ is the parity of χ (Pr 62). Φ is not an adequate wavefunction when the Coriolis interaction is included in the model Hamiltonian. This couples states which differ by one unit in K and hence K is no longer a good quantum number. One may use Φ as a suitable basis and expand the total wave function

$$\psi(I,M;\upsilon) = \left(\frac{2I+1}{16\pi^2}\right) \sum_{K\alpha} A_\upsilon(\alpha K;I)\left[D^I_{MK}\chi_{r\alpha} + (-)^{I-\frac{1}{2}} D^I_{M-K}\Pi_x\chi_{-\Omega\alpha}\right] \qquad 11$$

where υ is an additional index to define the state.

The problem remaining is that of the extra nucleon moving in the potential well of the deformed, but symmetric, core. It should be expected that the form of the potential should go over in a continuous fashion to the shell-model potential when the deformation goes to zero and that the well-known magic numbers at nucleon number 2, 8, 20, 50, 82, 126 are reproduced. This last condition is an important restriction on the form of the potential. In our case the Nilsson (Ni 55) model Hamiltonian was used to describe the single particle motion

$$H_p = H_o + C\,l\cdot s + D\,l^2$$

$$= -\frac{\hbar^2}{2M}\Delta + \frac{1}{2}M(\omega_1^2x_1^2 + \omega_2^2x_2^2 + \omega_3^2x_3^2) + C\,l\cdot s + D\,l^2 \qquad 12$$

$C\,l\cdot s$ is the usual spin orbit term and the $D\,l^2$ term gives a correction to the oscillator potential especially at large distances. C and D are parameters adjusted to reproduce the shell model states when the deformation vanishes.

Axial symmetry is assured by taking $\omega_1 = \omega_2 = \omega$, which with ω_3 is parameterized by

$$\omega^2 = \omega_o^2(1 + \frac{2}{3}\delta)$$

$$\omega_3^2 = \omega_o^2(1 - \frac{4}{3}\delta) \qquad 13$$

where δ gives the degree of deformation, the oscillator potential becoming spherically symmetric when $\delta = 0$. Requiring the volume enclosed by any given spheroidal equipotential surface to remain constant under changes of δ leads to

$$\omega_1^2 R_1^2 = \omega_2^2 R_2^2 = \omega_3^2 R_3^2 = \frac{2}{\mu} V_o$$

and

$$R_1^2 R_2^2 R_3^2 = \text{const}$$

where R_i are the semi axes of the surface. Hence

$$\omega_1^2 \omega_2^2 \omega_3^2 = \text{const}$$

and

$$\omega_o(\delta) = \mathring{\omega}_o \left(1 - \frac{4}{3}\delta^2 - \frac{16}{27}\delta^3\right)^{-1/6} \qquad 14$$

where $\mathring{\omega}_o$ is the value of $\omega_o(\delta)$ for $\delta = 0$ and is related approximately to the nuclear mass by $\hbar\mathring{\omega}_o = 41A^{1/3}$ MeV.

Introducing new coordinates

$$\rho_i = \sqrt{\frac{M\omega_o}{\hbar}}\, x_i \qquad i = 1,2,3$$

the Hamiltonian becomes

$$H_p = H_o + H_\delta + C\, \mathit{l}\cdot s + D\, \mathit{l}^2 \qquad 15$$

where H_o is a spherically symmetric harmonic oscillator Hamiltonian

$$H_o = \hbar\omega_o\, \frac{1}{2}(-\Delta + \rho^2) \qquad 16$$

and

$$H_\delta = -\frac{4}{3}\sqrt{\frac{\pi}{5}}\,\hbar\omega_o\, \rho^2\, Y_2^o(\theta\phi) \quad . \qquad 17$$

The representation chosen by Nilsson was with H_o diagonal, together with ℓ^2, ℓ_3 and s_3, which all commute with H_o. The corresponding quantum numbers are denoted by ℓ, Λ and Σ. The base vectors used are $|N\ell\Lambda\Sigma>$ where N represents the total number of oscillator quanta. One has

$$H_o|N\ell\Lambda\Sigma> = (N + \frac{3}{2})\hbar\omega_o|N\ell\Lambda\Sigma> \quad . \qquad 18$$

Nilsson further parameterised the total Hamiltonian eq. 15:

$$H_p = H_o + \kappa\hbar\overset{\circ}{\omega}_o R \qquad 19$$

where

$$\kappa = -\frac{1}{2}\,\frac{C}{\hbar\overset{\circ}{\omega}_o}$$

and

$$R = \eta U - 2\, \boldsymbol{l}\cdot\boldsymbol{s} - \mu\, \boldsymbol{l}^2 \qquad 20$$

with

$$\mu = \frac{2D}{C} \quad \text{and} \quad \eta = \frac{\delta}{\kappa}\, \frac{\omega_o(\delta)}{\mathring{\omega}_o} \, .$$

U is obtained from

$$H_\delta = -\delta\hbar\omega_o \frac{4}{3}\sqrt{\frac{\pi}{5}}\, \rho^2\, Y_2^o(\theta\phi) = \kappa\hbar\mathring{\omega}_o \eta U \quad . \qquad 21$$

The diagonalisation of the dimensionless matrix R is then carried out in the chosen representation. R is treated as a function of η and is diagonalised for a sequence of η-values giving eigenvalues $r^{N\Omega}(\eta)$ where Ω is the eigenvalue of $j_3 = \ell_3 + s_3 = \Lambda + \Sigma$. The corresponding energy eigenvalues of the total Nilsson Hamiltonian are thus

$$E_{Nilsson} = (N + \tfrac{3}{2})\, \hbar\omega_o(\delta) + \kappa\hbar\mathring{\omega}_o\, r^{N\Omega} \quad . \qquad 22$$

The eigenvectors are then an expansion in terms of the basis vectors

$$\chi_{\Omega\alpha} \equiv |\Omega\alpha\rangle = \sum_{\ell\Lambda} a_{\ell\Lambda\Omega\alpha} |N\ell\Lambda\Sigma\rangle \quad . \qquad 23$$

Associated with each level are a much used set of numbers, the asymptotic quantum numbers $[Nn_3\Lambda]\Omega$ and the parity where n_3 is the number of oscillator quanta along the 3-axis. Although n_3 is not a constant of motion it becomes very nearly so for large deformations.

Incorporating these eigenvalues with those of the rotational Hamiltonian, the diagonal terms of the total Hamiltonian H, eq. 5, are:

$$\langle IMK\alpha|H|IMK\alpha\rangle = \frac{\hbar^2}{2\mathscr{I}}\,[I(I+1) - 2K^2 + \sum_j |C_{j\Omega\alpha}|^2\, j(j+1) - \delta_{K,\frac{1}{2}}(-)^{I+\frac{1}{2}}(I+\tfrac{1}{2})a] + E_{\mathrm{Nilsson}} \qquad 24$$

and the off diagonal terms are

$$\langle IMK'\alpha'|H|IMK\alpha\rangle = -\frac{\hbar^2}{2\mathscr{I}} \sum_j C_{j\Omega'\alpha'} C_{j\Omega\alpha} \{[\delta_{K',K-1} + (-)^{I-j}\delta_{K',-(K-1)}]\, [(I+K)(I-K+1)(j+K)(j-K+1)]^{\frac{1}{2}} + \delta_{K',K+1}[(I-K)(I+K+1)(j-K)(j+K+1)]^{\frac{1}{2}} - \delta_{K',K}\, j(j+1)\} \qquad 25$$

where use has been made of the following matrix relations

$$\langle IMK|I_{\pm}|IMK\pm 1\rangle = [(I\mp K)(I\pm K+1)]^{\frac{1}{2}}$$

$$\langle j\Omega|j_{\mp}|J\Omega\pm 1\rangle = [(j\mp\Omega)(j\pm\Omega+1)]^{\frac{1}{2}} \quad .$$

The last term in the diagonal matrix elements arises from the Coriolis coupling term for $K = \frac{1}{2}$. This serves to define the "decoupling parameter" a

$$a \equiv \sum_j (-)^{j+\frac{1}{2}}\,(j+\tfrac{1}{2})\,|C_{j\frac{1}{2}\alpha}|^2 \quad . \qquad 26$$

The decoupling parameter can have a very strong influence on the appearance of a $K = \frac{1}{2}$ rotational band. If it is small the band will display the usual I(I+1) spacing; however, for larger values the band will have an anomalous behaviour.

Electromagnetic Transitions

Brockmeier et al (Br 65) and Nilsson (Ni 55) have discussed electromagnetic transition probabilities with and without the band mixing Coriolis coupling term, respectively. The formalism of Brockmeier is now presented for the reduced transition probabilities of (σ,L) radiation between the band mixed states (υ I) and (υ'I'), where υ is an additional index to label the state

$$B(\sigma L;\upsilon I\rightarrow\upsilon'I') = C(\sigma L)^2\left|\sum_{\substack{\alpha\ K\\ \alpha'K'}} F_{\sigma L}(\alpha'K';\upsilon'I'||\alpha K;\upsilon I)\right|^2 \qquad 27$$

where C(σL) is a constant and

$$F_{\sigma L}(\alpha'K';\upsilon'I'||\alpha K;\upsilon I) \equiv A_{\upsilon}(\alpha K;I)A_{\upsilon'}(\alpha'K';I')G_{\sigma L}(\alpha'K';\alpha K)$$

$$[(IL,K\ K'-K|I'K')+(-)^{I'+K'}(IL,K\ -K'-K|I'-K')b_{\sigma L}(\alpha'K';\alpha K)] \qquad 28$$

$A_{\upsilon}(\alpha K;I)$ are the coefficients of expansion of the band mixed states in terms of the basis states eq. 11.

i) Magnetic dipole transitions:

In this case the constant C(σL) is

$$C(M1) = \frac{e\hbar}{2MC}\sqrt{\frac{3}{4\pi}}$$

and $G_{\sigma L}$ and $b_{\sigma L}$ are calculated to be

$$G_{M1}(\alpha'K';\alpha K) = \delta_{KK'}[-\delta_{\alpha\alpha'}g_R K + \sum_{\ell\Lambda} a_{\ell\Lambda\Omega\alpha}a_{\ell\Lambda\Omega\alpha'}(g_s\Sigma + g_\ell\Lambda)]$$

$$+ \delta_{|K'-K|,1}\frac{K-K'}{\sqrt{2}}\sum_{\ell\Lambda\Lambda'} a_{\ell\Lambda\Omega\alpha}a_{\ell\Lambda'\Omega'\alpha'}$$

$$[\delta_{\Lambda\Lambda'}(g_s-g_R) + \delta_{\Sigma\Sigma'}(g_\ell-g_R)\sqrt{(\ell-\Lambda_<)(\ell+\Lambda_>)}] \qquad 29$$

$$b_{M1}(\alpha'\tfrac{1}{2};\alpha\tfrac{1}{2})G_{M1}(\alpha'\tfrac{1}{2};\alpha\tfrac{1}{2}) = \frac{(-)^{1+N}}{\sqrt{2}}\sum_{\ell\Lambda\Lambda'} a_{\ell\Lambda\frac{1}{2}\alpha}a_{\ell\Lambda'\frac{1}{2}\alpha'}$$

$$[\delta_{\Lambda o}\delta_{\Lambda' o}(g_s-g_R) + (\delta_{\Lambda o}\delta_{\Lambda' 1}+\delta_{\Lambda 1}\delta_{\Lambda' o})(g_\ell-g_R)\sqrt{\ell(\ell+1)}]. \qquad 30$$

As before $K = \Omega$ and $K' = \Omega'$.

ii) Electric quadrupole transitions:

In the case the constant $C(\sigma L)$ is

$$C(E2) = \beta^2(e + e_{eff})\sqrt{\frac{5}{4\pi}}$$

where

$$\beta = \sqrt{\frac{\hbar}{M\omega_o}} \quad .$$

The calculated relations for $G_{\sigma L}$ and $b_{\sigma L}$ are

$$G_{E2}(\alpha'K';\alpha K) = G_{E2}^{sp}(\alpha'K';\alpha K) + G_{E2}^{coll}(\alpha K)\delta_{\alpha\alpha'}\delta_{KK'} \qquad 31$$

where $G_{E2}^{coll}(\alpha K) = \frac{1}{2\beta^2}Q_o$ and Q_o is the intrinsic quadrupole moment given by

$$Q_o = 0.8\, z\, R_o^2\, \delta(1 + 0.5\, \delta) \qquad 32$$

where $R_o = 1.2\ A^{1/3}$ fm, δ is the deformation parameter and z is the atomic number.

$$G^{sp}_{E2}(\alpha'K';\alpha K) = \sum_{\substack{\ell\ \Lambda \\ \ell'\Lambda'}} \delta_{\Sigma\Sigma'} a_{\ell'\Lambda'\Omega'\alpha'} a_{\ell\Lambda\Omega\alpha} (N\ell'/\rho^2/N\ell) \sqrt{\frac{2\ell+1}{2\ell'+1}}$$

$$(\ell 2\Lambda\Lambda'-\Lambda|\ell'\Lambda')(\ell 200|\ell'0) \qquad 33$$

and

$$b_{E2}(\alpha'K';\ K)G^{sp}_{E2}(\alpha'K';\alpha K) = (-)^{K'+\frac{1}{2}+N'} \sum_{\substack{\ell\ \Lambda \\ \ell'\Lambda'}} \delta_{\Sigma_1-\Sigma'} a_{\ell'\Lambda'\Omega'\alpha'} a_{\ell\Lambda\Omega\alpha}$$

$$(N\ell'/\rho^2/N\ell) \sqrt{\frac{2\ell+1}{2\ell'+1}} (\ell 2\Lambda-\Lambda'-\Lambda|\ell'-\Lambda')(\ell 200|\ell'0)$$

$$34$$

where $\rho = r/\beta$ and a supplementary condition that b_{E2} may be non-zero only if one of the following conditions is fulfilled:

1) $K = \frac{1}{2}$, $K' = \frac{3}{2}$ or vice versa

2) $K = K' = \frac{1}{2}$ and $\alpha \neq \alpha'$.